Laser wakefield acceleration of electrons

Lewis Dickson

université PARIS-SACLAY

Laser wakefield acceleration of electrons

Accélération d'électrons par sillage laser-plasma

Thèse de doctorat de l'université Paris-Saclay

École doctorale n° 572, Ondes et Matière (EDOM)
Spécialité de doctorat : Physique
Graduate School : Physique. Référent : Faculté des sciences d'Orsay

Thèse préparée au **Laboratoire de Physique des Gaz et des Plasmas** (Université Paris-Saclay, CNRS), sous la direction de **Brigitte CROS**, directrice de recherche

Thèse soutenue à Paris-Saclay, le 29 mars 2023, par

Lewis DICKSON

Composition du jury

Membres du jury avec voix délibérative

Jaques ROBERT Professeur, LPGP, Université Paris-Saclay	Président
Laura CORNER Maître de conférences (éq. HDR), University of Liverpool (Liverpool, United Kingdom)	Rapporteur & Examinatrice
Patric MUGGLI Professeur associé (éq. HDR), Max Planck Institute for Physics (München, Germany)	Rapporteur & Examinateur
Emmanuel d'HUMIÈRES Professeur, CELIA, Université de Bordeaux	Examinateur

THESE DE DOCTORAT
NNT : 2023UPASP037

université PARIS-SACLAY

ÉCOLE DOCTORALE
Ondes et matière (EDOM)

Titre : Accélération d'électrons par sillage laser-plasma
Mots clés : sillage laser plasma, accélération d'électrons, expériences laser plasma, optimisation numérique, diagnostic plasma

Résumé : L'accélération par sillage laser plasma fournit des gradients accélérateurs plusieurs ordres de grandeur au dessus de ceux des accélérateurs actuels, mais la stabilité et la qualité des faisceaux d'électrons accélérées doivent être améliorées. Ce travail est centré sur l'étude d'injecteurs laser-plasma (LPI) à basse ($150\,\mathrm{MeV}$) et haute énergie ($1\,\mathrm{GeV}$) créés en cellule de gaz. Des outils expérimentaux et numériques ont été développés pour l'optimisation et le diagnostic de l'interaction laser-plasma. Une nouvelle méthode de mesure monocoup de la densité plasma en cellule de gaz a été mise au point et utilisée. Des méthodes d'intelligence artificielles ont été mises en oeuvre pour l'automatisation, le diagnostic et l'optimisation d'une expérience de sillage laser plasma. Les effets du front d'onde du laser, de la position focale, et de la densité du plasma ont été mesurés et comparés à des simulations. Des profils laser réalistes, utilisés comme données d'entrée, ont permis d'améliorer fortement la précision des simulations et d'expliquer l'impact de l'asymétrie du laser sur les propriétés des électrons. Une expérience de qualification utilisant une cellule à gaz dans la zone focale longue de l'installation laser Apollon a permis d'obtenir des électrons jusqu'au GeV. Une deuxième campagne a permis d'améliorer la stabilité et la qualité des faisceaux d'électrons jusqu'à 1.8 GeV.

Title : Laser wakefield acceleration of electrons
Keywords: laser plasma wakefield, electron acceleration, laser plasma experiments, optimisation by machine learning, plasma diagnostic

Abstract: Laser Wakefield Acceleration (LWFA) provides orders of magnitude higher accelerating gradients than current accelerator designs, but the stability and quality of the accelerated electron bunches require improvement. This work focuses on the development of low ($150\,\mathrm{MeV}$) and high energy ($1\,\mathrm{GeV}$) laser-plasma injectors (LPI) in gas cells. Experimental and numerical tools have been developed for the optimisation and diagnosis of the laser-plasma interaction. A novel method for single-shot plasma density measurement in a gas cell was developed and implemented. Bayesian optimisation and automation of an LWFA experiment were completed. The effect of laser wavefront and focal position and plasma density in a low-energy LPI were explored experimentally and compared to simulations. Realistic laser profiles were used as input data and shown to explain otherwise overlooked effects on electron properties arising from laser asymmetry. The first gas cell experiment in the long focal area of the Apollon laser facility achieved electron bunches with energy up to 1 GeV. A second experiment at Apollon was performed leading to $1.8\,\mathrm{GeV}$ electrons with improved stability and quality.

Table des matières

Liste des figures

Liste des tableaux

Acknowledgments

It is a privilege to be able to complete a PhD and an even greater privilege to get to work with so many interesting people during this time. In these acknowledgements, I hope to convey the gratitude that I hold for all of those that have helped me throughout the last few years.

I would first like to extend my gratitude to the reporters and members of my jury that have made this process possible. I want to thank the reporters Laura Corner and Patric Muggli who provided their valuable and detailed feedback on the manuscript and their questions during the defence, which helped me to centre the work that has been completed within this thesis both technically and within the broader scientific field. Emmanuel d'Humières gave significant time to both the defence and reading of the manuscript, and I also want to thank you for your kind words during this process. Jacques Robert, j'ai essayé de suivre ton conseil selon lequel un doctorat ne devrait pas être stressant et je pense que j'y suis arrivé (au moins jusqu'à la rédaction !) donc merci pour ta gentillesse depuis le début.

I have been given a fantastic environment for my academic development thanks to my group, Interaction et Transport de Faisceaux Intenses dans les Plasmas. My supervisor and colleagues have always warmly welcomed me and my broken French. Je voudrais remercier ma directrice de thèse, Brigitte Cros. Je suis heureuse de t'avoir eu comme superviseur au cours des trois dernières années et demie, et j'apprécie combien tu m'as aidée à grandir en sachant quand me donner plus de responsabilités et quand me laisser explorer dans mon travail. Ce qui a été une expérience fantastique, c'est que j'ai beaucoup appris à tes côtés. Je te remercie de ton aide et tes conseils. Thanks to my office mate and soundest guy, Ioaquin Moulanier. We've clicked from the start, and I'll struggle to find someone as enjoyable to talk to. Francesco Massimo has helped me so much during the writing of this manuscript and, even though it's not his responsibility, has taken significant time going through this manuscript, making it what it is now. Je voudrais également exprimer ma gratitude à Gilles Maynard qui a toujours fait en sorte que mes idées soient valorisées et qui m'a beaucoup aidé dans mes processus de réflexion sur la physique des lasers et des plasmas. In the laboratory, Laboratoire de physique des gaz et des plasmas, I have received significant support from Charles Ballage, to whom no request is ever a problem and Ovidiu Vasilovici, who has helped implement the many experiments presented in this thesis. Je tiens également à remercier Nicolas Dessaints et Bérénice Saidi pour leur aide pendant et avant la thèse. The four experiments presented in this manuscript allowed me to meet and work with researchers and staff from all over the world. The many collaborators I have worked with over the years have shown me kindness and support throughout many challenging experiments and some painfully late nights. There are far too

many to thank, but I would like to give a special thanks to the few I have worked with the most. Sandrine Dobosz Dufrénoy tu as été présent tout au long de mon doctorat et tu m'as toujours soutenu dans mon travail. Cornelia Gustafsson, you've answered my incessant questions - always with a smile - and helped make some of the most enjoyable work that I've completed during the thesis. Thanks to Michael Backhouse, I have the house playlist that still fuels my coding, and you gave so much support throughout and after the automation experiment. Francesco Filippi, your good mood and relaxed persona is always a pleasure to be around – and I won't tell anyone about the kebab pizza. Working with you, Matt Streeter, has shown me the truly enjoyable side of science and I'm grateful for all of your help with questions and articles during the last three years.

Whilst the academic support has been fantastic, time with family and friends has been equally important in the completion of this work. Sol, you've been a fantastic friend and made the last few years really special. I'll really miss hanging out with you. I want to thank my friends Fabi, Lucas, Lu, Jo, Lena, Flo, Rémy, Mara, and Gaelle for all the picnics, brunches and beers that have made my time in Paris so much more special. The PhD would also have been a lot tougher without my mates in Glasgow providing weekly quiz sessions during the pandemic and welcoming us back like no time had passed. I look forward to at least one more rosé filled visit before we leave Hector, Ruaraidh, Ryan, Gav, Rob, Lauren and Megan. Susie, you've always encouraged my education as if you were my own mum, and I've enjoyed our physics chats more than you'd ever know. Thank you for all of your support and, most importantly, the golden mars bar. A big thanks to my big sister (not really) Juliane and Chris for their visits and ferry rides and for always making me feel cared for and loved. My parents, Lynn and Richard, have always given me the opportunity to carve my own path, and I appreciate that so much. I wouldn't have the confidence to complete something like this without you two - thank you both so much. Owen, you're the coolest guy, and your belief in me is always so motivating. Thanks for everything bro.

Finally, to my fiancée Kyrie. From being clueless teenagers to slightly less clueless adults, you have supported me and been my best friend throughout the last 12 years of my life, throughout high school, university and now a PhD (which I can say with certainty wouldn't have happened without you!) You have made my life full, and for that, I am more grateful than I can write here. I cannot wait for what the future holds for us.

Résumé de la Thèse

Résumé de la Thèse en Français

L'interaction entre un faisceau laser à impulsion courte et un plasma sous-dense permet de produire de forts gradients accélérateurs et de focalisants dans le plasma, par un processus appelé accélération par sillage laser plasma (LWFA). Ces structures accélératrices transitoires peuvent être utilisées pour piéger les électrons du plasma et les accélérer à des énergies ultra-relativistes sur de courtes distances. La théorie de l'accélération par champ de sillage laser est née avec l'article fondateur de Tajima et Dawson en 1979[1], dans lequel il était prédit que les impulsions laser pouvaient générer des ondes de plasma relativistes dans un plasma et, par conséquent, fournir une structure d'accélération utile pour l'accélération d'électrons à très haute énergie. Les premiers résultats expérimentaux étaient limités en raison de la puissance crête des lasers et de la durée des impulsions beaucoup plus longues que la longueur d'onde du plasma. Avec l'avènement de l'amplification d'impulsions étirées, il est devenu possible d'amplifier et de comprimer les impulsions laser à des intensités beaucoup plus élevées qu'auparavant, ce qui a entraîné une révolution dans les systèmes laser disponibles avec les caractéristiques requises pour le LWFA. Des travaux approfondis ont été réalisés à l'échelle mondiale pour comprendre l'interaction non linéaire entre le laser et le plasma et la dynamique des électrons qui en résulte. Le domaine vise maintenant à fournir des sources d'électrons pour les futurs collisionneurs linéaires de particules, des paquets d'électrons pour les lasers à électrons libres et des sources de rayonnement secondaire à partir des particules accélérées pour des applications médicales et industrielles.

Alors que de grands progrès ont été réalisés dans la compréhension théorique et la production expérimentale de spectres d'électrons avec un sous-ensemble des paramètres requis pour les futures applications, l'obtention de tous les paramètres du faisceau tels que la charge, la dispersion de l'énergie, l'émittance, etc. et la stabilité de tous ces paramètres simultanément est un effort continu. Une méthode proposée pour améliorer la qualité des paquets d'électrons consiste à séparer les étapes d'injection et d'accélération. L'étape de l'injecteur fournirait un paquet d'électrons relativistes grâce à l'interaction non linéaire du laser et du plasma, qui serait ensuite accéléré à des énergies plus élevées en utilisant une approche par étapes, où le reste des processus d'accélération est réalisé dans un régime quasi-linéaire où toute autre injection d'électrons est bloquée.

Cette thèse est consacrée à l'étude des mécanismes physiques permettant le développement des injecteurs laser-plasma (LPI) envisagés dans le cadre du projet EuPRAXIA, avec des énergies de paquets d'électrons de $150\,\mathrm{MeV}$ et $1\,\mathrm{GeV}$.

Les expériences sur l'injecteur à "faible" énergie ($150\,\mathrm{MeV}$) ont été réalisées

au Lund Laser Centre (LLC) en Suède, où le couplage du laser et du plasma a été exploré en détail et où les résultats ont été comparés à des simulations utilisant des paramètres laser réalistes, ce qui a permis d'obtenir un bon accord et d'interpréter les observations expérimentales. Ces résultats ont permis d'identifier et de quantifier l'impact de la qualité du faisceau laser sur les propriétés des électrons accélérés.

Une deuxième expérience au LLC a mis en oeuvre l'apprentissage automatique (ML) au moyen d'une optimisation bayésienne (BO) pour explorer efficacement l'espace des paramètres expérimentaux et optimiser une fonction de mérite définie telle que l'énergie du faisceau d'électrons ou la densité spectrale des électrons. Ensuite, un réseau neuronal a été mis en œuvre pour la reconstruction du point focal à l'aide d'une caméra de diagnostics, utilisée comme référence pendant les tirs à haute intensité, ce qui permet de reconstruire la tache focale équivalente au niveau du plasma à chaque tir.

Enfin, cette expérience a permis de mettre au point une nouvelle méthode monocoup de détermination de la densité du plasma basée sur un capteur de front d'onde, utilisant une suppression de la phase de fond auto-référencée, permettant de négliger les variations de la phase du faisceau sonde.

Ces deux expériences ont permis d'améliorer notre compréhension de l'interaction laser-plasma grâce à une analyse fine et précise des spectres obtenus et des paramètres d'entrée expérimentaux.

Des spectres d'électrons avec des valeurs proches des cibles de l'injecteur EuPRAXIA $150\,\mathrm{MeV}$ ont été produits mais nécessitent une augmentation de la charge spectrale.

Les expériences $1\,\mathrm{GeV}$ Les expériences LPI ont été réalisées avec l'installation de recherche nationale Apollon, qui fournira à terme des faisceaux laser de classe PW et multi-PW. L'augmentation de l'énergie disponible, multiplée par 10 au niveau du plasma, permet de focaliser faisceau laser sur de plus longues distances tout en fournissant une force pondéromotrice suffisante pour créer une onde de sillage de grande amplitude, permettant d'atteindre des énergies électroniques de l'ordre de $1\,\mathrm{GeV}$.

Deux expériences ont été menées avec Apollon. Une première expérience mise en service et de qualification du faisceau laser et des équipements expérimentaux, a permis de valider la génération d'électrons dans cellule de gaz dans la salle longue focale. La première expérience accueillant des utilisateurs externes a généré et utilisé des spectres d'électrons ultra-relativistes pour produire des positrons par le biais d'une cascade de rayonnement créée lors de l'interaction du faisceau d'électrons et d'une cible solide.

Ces deux expériences ont permis de produire des spectres d'électrons de l'ordre de $1\,\mathrm{GeV}$, mais la stabilité du système laser lors de l'expérience de mise en service a limité la stabilité et la reproductibilité des faisceaux d'électrons. Le diagnostic des propriétés du faisceau laser proche de la zone d'interaction avec le plasma a

été mise en place dans les deux expériences. L'analyse des résultats a été entreprise pour comprendre comment les fluctuations de la stabilité du laser d'entrée affectent l'accélération des électrons. les premiers résultats de simulations ont permis d'interpréter la forme des distributions en énergie et les charges des électrons accélérés.

En résumé, cette thèse a développé de nouvelles méthodes pour l'analyse du laser à l'entrée du plasma et le diagnostic de la densité du plasma, ainsi que le ML et la mise en œuvre de BO pour améliorer les spectres d'électrons résultants et récupérer des paramètres autrement négligés dans les expériences précédentes. Nous avons ensuite utilisé ces méthodes pour explorer et comprendre les processus physiques qui soutendent les modifications des spectres d'électrons. Les résultats et les conclusions de ces travaux sont présentés, ainsi que l'état actuel de la recherche et la manière dont ce travail s'appuie sur celui-ci.

Ce travail n'aurait pas été possible sans l'aide de notre équipe à l'ITFIP et des nombreux collaborateurs et membres du personnel/chercheurs des deux installations expérimentales.

Thesis Summary in English

Interaction between short-pulse lasers and under-dense plasma allows for strong accelerating and focusing gradients to be produced within the plasma through a process called laser-wakefield acceleration (LWFA). These transient accelerating structures can be used to trap electrons from the background plasma and accelerate them to ultra-relativistic energies over short distances. The theory of laser-wakefield acceleration was born with the seminal paper of Tajima and Dawson in 1979[1] where it was predicted that laser pulses could drive density perturbations in plasmas and, in turn, provide an accelerating structure useful for electron acceleration. Initial experimental results were limited due to laser peak power and pulse durations which were much longer than the plasma wavelength.

With the advent of chirped pulse amplification, it became possible to amplify and compress laser pulses to much higher intensities bringing about a revolution in available laser systems with the characteristics required for LWFA. Extensive work has been completed globally to understand the nonlinear interaction between the laser and plasma and the resulting electron dynamics. The field now aims to provide electron sources for future linear particle colliders, electron bunches for Free-Electron Lasers and secondary radiation sources from the accelerated particles for medical and industrial applications. Whilst there has been great progress in the theoretical understanding and experimental production of electron spectra with a sub-set of the required parameters for future applications, achieving all bunch parameters such as charge, energy spread, emittance, etc., and the stability of all of these simultaneously, is an ongoing effort.

A proposed method for improving the quality of the electron bunches is the

separation of the injector and accelerator stages. The injector stage would provide a relativistic electron bunch through the nonlinear interaction of the laser and plasma, which would then be accelerated to higher energies using a staged approach where the remainder of the accelerating processes are performed in a quasi-linear regime where further electron injection is blocked.

This thesis focuses on the development of laser-plasma injectors (LPIs) envisioned within the EuPRAXIA framework[2] with electron bunch energies at $150\,\mathrm{MeV}$ and $1\,\mathrm{GeV}$. The "low" energy ($150\,\mathrm{MeV}$) injector experiments were performed at the Lund Laser Centre (LLC) in Sweden, where the coupling of the laser and plasma were explored in great detail and the results compared against simulations using realistic laser parameters allowing for an improved agreement. A second experiment at the LLC applied Bayesian Optimisation (BO) to efficiently search the experimental parameter space and optimise a defined merit function such as total charge or spectral density of the electrons. Secondly, a neural network was implemented for focal spot reconstruction using a spatially separated camera allowing for on-target focal spot reconstruction on each shot. Further, this experiment implemented a novel wavefront sensor based, single-shot, plasma density retrieval method using a self-referenced background phase removal technique. This allowed for a dynamic phase background to be calculated which retrieves the plasma-induced phase shift for wavefront sensors using probe lines without phase stabilisation. Both of these experiments improved our understanding of the laser-plasma interaction through careful analysis of the resulting spectra and experimental input parameters. Electron spectra with values approaching the EuPRAXIA $150\,\mathrm{MeV}$ injector targets were produced but require an augmentation of the spectral charge.

The $1\,\mathrm{GeV}$ LPI experiments were performed at the Apollon Petawatt Laser Facility. The increase in available on-target laser energy by a factor of 10 compared to the LLC allows the laser to be focused over longer distances whilst providing a sufficient ponderomotive potential for driving the plasma wakes, allowing for $1\,\mathrm{GeV}$ electron energies to be achieved. Two experiments were conducted at Apollon: the first commissioning experiment to implement a gas cell plasma target in the long focal area and the first external user experiment aimed at using ultra-relativistic electron spectra to produce positrons through a radiation cascade created during the interaction of the electron bunch and a solid target. Both of these experiments successfully produced electron spectra in the $1\,\mathrm{GeV}$ range; however, the stability of the laser system in the commissioning experiment limited the stability and the reproducibility of the electron bunches. Diagnostic of the laser properties in the focal volume was implemented in both experiments and has been analysed to understand how the fluctuations in the input laser stability affect the resulting electron acceleration.

In summary, this thesis provides novel methods for the analysis of the laser on target through machine learning and diagnosis of the plasma density, along with and implementation of BO for improving the resulting electron spectra. We then

used these techniques to uncover the underlying physical processes which result in alterations of the electron spectra. The results and conclusions are presented alongside the current state-of-the-art research and how this work builds on this.

This work would not have been possible without the help of our team at ITFIP and the many collaborators and staff/researchers at both experimental facilities.

List of Abbreviations

RF	Radio-Frequency
LWFA	Laser Wakefield Acceleration
CCD	Charge-Coupled Device
BSI	Barrier Suppression Ionaisation
QED	Quantum Electrodynamics
UHI	Ultra-High Intensity
ELISA	ELectron Injector for compact Staged high energy Accelerator
FWHM	Full-Width Half-Maximum
HWHM	Half-Width Half-Maximum
LPI	Laser-Plasma Injector
LPA	Laser-Plasma Accelerator
GSA	Gerchberg–Saxton Algorithm
LLC	Lund Laser Centre
PIC	Particle-in-cell
FBPIC	Fourier-Bessel Particle-In-Cell
CPA	Chirped Pulse Amplification
OPCPA	Optical Parameteric Chirped Pulse Amplification
AO-PDF	Acousto-optic Programmable Dispersive Filter
AO	Adaptive Optic
DC	Direct Current
GD	Group Delay
GDD	Group Delay Dispersion
TOD	Third Order Dispersion
FOD	Fourth Order Dispersion
LFA	Long Focal Area (Apollon laser facility)
SFA	Short Focal Area (Apollon laser facility)
XPW	Cross-Polarised Wave
DPSSL	Diode-Pumped Solid State Laser
FROG	Frequency-Resolved Optical Gating
RASP	Radial Asymmetry Parameter
RMS	Root Mean Sqaure
TTL	Transistor-Transistor Logic

CW	Continuous wave
MZ	Mach-Zehnder (interferometer)
RPM	Revolutions Per Minute
FFT	Fast Fourier Transform
WFS	Wavefront Sensor
SRWFS	Self-Referenced Wavefront Sensor
RMZ	Rapid Mach-Zehnder (interferometer)
YAG	Yttrium Aluminum Garnet
ICT	Integrating Current Transformer
(c)GAN	(Conditional) Generative Adversarial Model
ML	Machine Learning
NN	Neural Network
BO	Bayesian Optimisation
RBF	Radial Basis Function
EI	Expected Improvement
MAD	Median Absolute Deviation
CAL	Complex Amplitude of the Laser electric field
HG	Hermite-Gauss
LG	Laguerre-Gauss
FPS	Flat Phase Setting
SE	Short Exit
LE	Long Exit
ICC	Interaction Chamber Centre
UCB	Upper Confidence Bound

List of Symbols

$\vec{E}$	Electric Field
E_0	Maximum Electric Field
$\vec{B}$	Magnetic Field
$\vec{A}$	Vector Potential
A_0	Maximum Vector Potential
a_0	Normalised Peak Vector Potential
I_0	Peak Laser Intensity
ϕ	Scalar Potential
ω_0	Laser Angular Frequency
λ_0	Laser Wavelength
$\vec{k}_0$	Laser Wavevector
w_0	Laser Waist
τ	Laser Pulse Duration
$\mathcal{E}$	Laser Pulse Energy
z_R	Rayleigh length
ω_p	Plasma Angular Frequency
λ_p	Plasma Wavelength
n_e	Plasma Electron Density
n_c	Critical Electron Density
ρ	Density
c	Speed of Light in Vacuum
$\vec{J}$	Vector Current
μ_0	Permeability of Free Space
ϵ_0	Permittivity of Free Space
m_e	Electron Mass
e	Electron Charge
f	Focal Length
Z	Atomic Number
v_{ph}	Phase Velocity
v_g	Group Velocity
γ	Lorentz Factor
η	Refractive Index
$\mathcal{R}$	Bubble Radius

General Introduction

High-energy particles and their associated secondary radiation are used in many applications from medical imaging, to defect detection in manufacturing, and at high energies, for fundamental particle physics research. The current highest accelerating gradients used for applications are achieved in radio-frequency cavities, however, these are limited to 10s of MeV/m due to surface breakdown on the metallic cavity walls. Limitations in the accelerating gradients that can currently be achieved lead to large, and expensive accelerator facilities. The development of novel technologies with stronger accelerating fields could improve access to particle and photon beams for hospitals, universities and research facilities. One such novel acceleration method is laser wakefield acceleration. It was predicted by Tajima and Dawson in 1979[1] that the use of plasmas - a state of matter which is already "broken down" into electrons and ions – could be excited by laser pulses to create accelerating structures for electron acceleration.

The field of laser wakefield acceleration encompasses laser, plasma and accelerator physics along with the nonlinear interactions between all of these fields, providing a rich and evolving field of study. Laser plasma accelerators produce their accelerating capabilities through transient and dynamic electron structures created through density perturbations from short-pulse laser-plasma interactions[1]. This transient structure, or plasma wake, produces its own challenges but provides many benefits.

As the plasma structure is incapable of the same surface break-down problems prevalent in radio-frequency (RF) cavities, accelerating gradients up to three orders of magnitude[3] greater can be achieved, allowing for extreme miniaturisation of the accelerator. These strong accelerating fields are created by the large charge separation and short distances within the wake. This miniaturisation could be used in future linear colliders to reduce the footprint of an accelerator facility by orders of magnitude or allow smaller facilities to create $\mathcal{O}(100\,\mathrm{MeV})$ electron accelerators using off-the-shelf laser systems. Further, as the electron bunch length is on the order of the plasma wavelength, bunch lengths on the micrometre scale (equivalently fs scale in duration) are produced[4], allowing for electron currents on the kilo-ampere scale[5]. These are well suited for next-generation free-electron lasers as they will require higher peak currents and shorter bunch duration than what is currently available from RF accelerators and without the requirement of bunch compressors[6]. These ultra-short bunches also provide a unique opportunity for QED experiments[7, 8], where interaction between the high-current electron bunch and a secondary ultra-intense laser ($I > 10^{20}\mathrm{W\,cm^{-2}}$) can be used to probe the QED threshold and provide experimental validation of the quantum corrections to the laser-electron interaction at very high intensities.

As the electrons are accelerated, they oscillate in the strong transverse fields of the plasma wake, producing x-ray radiation, commonly referred to as betatron radiation[9]. The electrons, and their betatron radiation, are intrinsically temporally synchronised to the drive laser[10] due to their injection and acceleration dynamics. This can be used in pump-probe studies[11] where the radiation (electrons or x-rays) produced during the laser-wakefield acceleration is used to probe the excited matter, which can be pumped by either the original laser or a secondary laser temporally synchronised to the first.

Electrons, betatron radiation, and interaction of the accelerated electrons with solid targets to produce γ-radiation through Bremsstrahlung[12] and positrons through the resulting radiation cascade[13] can be used for medical and diagnostic studies[14]. The production of relativistic positrons could also have applications in future lepton-lepton colliders which will require a positron injector[15].

All of these applications, however, require a high-quality electron source. Laboratories around the world have been successful in creating electron sources through laser wakefield acceleration that approach RF linear accelerators with regard to peak bunch energy[16], bunch charge[17, 18], and energy spreads approaching the per mille (‰) level[19]. Achieving these parameters simultaneously, however, and in a repeatable way remains a challenge and a topic of study. One suggested approach for simultaneously improving the electron parameters and stabilising the interaction is the separation of the injection and accelerating regimes. This approach is detailed in the EuPRAXIA design study[2], which aims to produce an electron injector with either a 'low energy' of $150\,\mathrm{MeV}$ or 'high energy' of $1\,\mathrm{GeV}$ electron bunch peak energy, $30\,\mathrm{pC}$ of charge and an energy spread of less than 5%, which is then subsequently injected into another stage for acceleration to higher energies[20].

Further challenges arise from the highly nonlinear interaction between the laser and the plasma, which produces the injection and accelerating processes for the electron bunches. The small source size of the electron bunches - on the order of the plasma wavelength - leads to large emittances that will require strong magnetic or plasma-based optics to collimate and transport the bunches. As the electric field of the electron bunch can also drive a plasma wake, the amount of charge that can be loaded into the wakefield is limited. This effect, termed beam-loading, can lead to large energy spreads if improperly matched through amplification of the bunch's energy chirp. Finally, the laser systems which drive the plasma density perturbation typically have poor wall-plug efficiency meaning that the conversion between input energy and electron energy is poor before the accelerating process begins. Work is underway to improve the efficiency of drive lasers through pumping with diode-pumped solid-state lasers or the combination of many fibre lasers, for example[21].

In this work, we explore the development of such injectors by investigating the experimental parameters responsible for the accelerated electron characteris-

tics, by developing plasma and laser diagnostics to improve measurements of the experimental parameters, and by applying optimisation methods to find optimum experimental configurations.

The chapters within this thesis are ordered as follows, with specifications on the work completed by the author:

Chapter 1: Introduction to Laser-Plasma Interaction in Underdense Plasmas

1. Presentation of theoretical descriptions of laser, plasmas, laser-plasma interaction, and acceleration of electrons
2. Presentation of the state-of-the-art in laser-wakefield acceleration

Chapter 2: Experimental Instruments: Lasers, Plasma Devices, and Electron Detectors

1. Overview of laser systems and their associated diagnostics, including presentation of the rotational asymmetry parameter
2. Development of a temporally resolved Mach-Zehnder interferometer
3. Presentation of plasma diagnostics and the development of a single shot self-reference wavefront sensor plasma density diagnostic
4. Overview of electron diagnostics and definition of electron parameters used throughout the presentation of the results

Role of author: Development of rotational asymmetry parameter, development of single-shot self-referenced wavefront sensor plasma density diagnostic, development of temporally resolved Mach-Zehnder interferometer
Role of others: Ovidiu Vasilovici (LPGP): development of gas injection control. Francesco Filippi (CNR): set-up, acquisition and analysis of Mach-Zehnder during Bayesian optimisation experiment ; Romain Cadas(LPGP): electron-spectrometer electron tracking code

Chapter 3: Introduction to Numerical Tools: Machine Learning and Simulation

1. Introduction to generative adversarial networks and Bayesian optimisation
2. Focal spot analysis methods including the calculation of complex laser electric field from fluence images and focal spot reconstruction using generative adversarial networks
3. Introduction to particle-in-cell simulations

Role of author: Development of focal spot reconstruction method, acquisition of focal spot images for focal spot reconstruction (aided by Michael Backhouse, ICL)
Role of others: Gilles Maynard (LPGP): development of modified GSA algorithm for complex laser electric field retrieval. Ovidiu Vasilovici (LPGP): development of dual camera 10Hz acquisition software

Chapter 4: Low Energy Laser-Plasma Injector

1. Exploration of laser-plasma coupling and control of electron parameters through density downramp, focal position, and laser wavefront
2. Comparison of electron parameters to simulations using realistic laser profiles
3. Bayesian optimisation of laser-wakefield acceleration experiment and resulting spectra
4. Application of Bayesian optimisation to offline data sets for hyper-parameter optimisation

First laser-plasma coupling experiment: *Role of author*: Experimental planning and set-up, data acquisition, analysis of results
Role of others: Gilles Maynard (LPGP)- laser complex electric field retrieval, PIC simulations and analysis. Jonas Björklund Svensson (Lund University) - calibration of electron spectrometer, The results of the first experiment at the LLC presented in this chapter are based on the published article *Mechanisms to control laser-plasma coupling in laser wakefield electron acceleration* L.T.Dickson (2022)[22].
Second Bayesian optimisation experiment: *Role of author*: Experimental planning and set-up, data acquisition, analysis of electron spectra, development of Bayesian optimisation and automation code (in collaboration with Michael Backhouse, ICL), development of off-line Bayesian optimisation code, focal spot analysis, wavefront sensor plasma density implementation and analysis
Role of others: Cornelia Gustafsson (Lund University): calibration of electron spectrometer, acquisition of laser temporal measurements

Chapter 5: High Energy Laser-Plasma Injector: Apollon Experiments

1. Commissioning experiment at Apollon laser facility
2. Analysis of Apollon laser energy, pointing, and radial profile stability
3. Long focal length experiment for the development of high-quality multi-GeV electron spectra

Commissioning experiment: *Role of author*: Experimental planning and set-up, data acquisition, analysis of electron spectra (in collaboration with Ioaquin Moulanier, LPGP), focal spot analysis (in collaboration with Ioaquin Moulanier, LPGP), plasma density analysis
Role of others: Ioaquin Moulanier (LPGP): focal spot analysis, complex electric laser field extraction and simulations (appendix). Arnd Specka (LLR): Design and implementation of electron spectrometer. Gilles Maynard (LPGP): electron spectrometer spatial calibration
Long focal length experiment: *Role of author*: experimental set-up and data acquisition, analysis of electron spectra, analysis of laser parameters
Role of others: Matthew Streeter (QUB): calibration of electron spectrometer, electron spectra calibration code

Chapter 6: Conclusions

1. Summary of results from the low and high energy electron injector experiments
2. Future prospects for further improvements in laser-plasma injector development

1 - Introduction to Laser-Plasma Interaction in Underdense Plasmas

Contrary to the metallic components of radio-frequency cavities used for particle acceleration, the accelerating structure in laser wakefield acceleration (LWFA) is composed of a transient electron structure excited by the ponderomotive force of a short pulse laser on the plasma electrons. Here, we will first describe the physics and mathematical description of short pulse lasers which provide the perturbative radiation force responsible for LWFA. We will then present plasmas and their parameters which affect the interaction with the laser and its nonlinear evolution within this medium. The interaction between the laser and the plasma, resulting in the expulsion of electrons from the laser axis, and the electric fields/accelerating dynamics of the plasma wake are explained. They will then be presented alongside their different regimes. The relevant state-of-the-art physics is then presented.

1.1 . Description of Short-Pulse Lasers in Vacuum

Laser wakefield acceleration requires high-intensity, short-pulse lasers to provide the perturbative force required to create the accelerating structures in the plasma. Modern commercially available laser systems can provide terawatt ($10^{12}\mathrm{W}$) powers with pulse duration on the 10s of femtosecond ($10^{-15}\mathrm{s}$) scale. These are defined as high-peak power as they deliver intense light over a very short duration, leading to the power over the temporal duration of the laser pulse is high but the average output power is much lower. For example, a laser with $50\,\mathrm{TW}$ peak power operating with a pulse energy of $1\,\mathrm{J}$, pulse duration of $20\,\mathrm{fs}$, at a repetition rate of $10\,\mathrm{Hz}$ provides an average power of $10\,\mathrm{W}$. We will begin by using the Maxwell equations to derive useful quantities to describe the laser-plasma interaction.

Starting from the Maxwell equations in the Lorenz Gauge[23] allows us to develop useful equations for understanding the laser-plasma interaction. Laser pulses are electromagnetic waves which can be described in terms of electric, $\vec{E}$, and magnetic, $\vec{B}$, fields and, equivalently, their description in terms of potentials. We can then write:
Gauss's Law as:

$$\nabla \cdot \vec{E} = \nabla^2\phi - \frac{1}{c^2}\frac{\partial^2\phi}{\partial t^2} = -\frac{\rho}{\epsilon_0}\,, \tag{1.1}$$

Gauss's Law for Magnetism as:

$$\nabla \cdot \vec{B} = \nabla \cdot \left(\nabla \times \vec{A}\right) = 0\,, \tag{1.2}$$

Faraday's Law of Induction as:

$$\nabla \times \vec{E} = -\frac{\partial \nabla \times \vec{A}}{\partial t}\,, \tag{1.3}$$

and **Ampere's Law** as:

$$\nabla \times \vec{B} - \frac{1}{c^2}\frac{\partial \vec{E}}{\partial t} = \nabla^2\vec{A} - \frac{1}{c^2}\frac{\partial^2\vec{A}}{\partial t^2} = -\mu_0\vec{J}\,. \tag{1.4}$$

In all the above equations $\vec{A}$, ϕ are the vector and scalar field potentials, respectively, defined from:

$$\vec{E} = -\nabla\phi - \frac{\partial\vec{A}}{\partial t}\,, \tag{1.5}$$

and,

$$\vec{B} = \nabla \times \vec{A}\,. \tag{1.6}$$

A reminder for the reader that the Lorentz Gauge in SI units specifies that: .

$$\nabla \cdot \vec{A} + \frac{1}{c^2}\frac{\partial\phi}{\partial t} = 0 \tag{1.7}$$

Further, c, ρ, ϵ_0, μ_0, $\vec{J}$ are the speed of light in vacuum, charge density, permittivity and permeability of free space, and the current vector, respectively. Using the Coulomb gauge instead, $\nabla \cdot \vec{A} = 0$, and Gauss's law allows us to retrieve the Poisson equation:

$$\nabla \cdot \left(-\nabla\phi - \frac{\partial \vec{A}}{\partial t} \right) = \frac{\rho}{\epsilon_0} \tag{1.8}$$

$$\therefore \nabla^2 \phi = -\frac{\rho}{\epsilon_0} \,. \tag{1.9}$$

We can categorise the nonlinearity of the laser-plasma interaction by the "normalised peak vector potential" which is defined as the maximum of the normalised vector potential:

$$a_0 = \max(\vec{a}) = \frac{eA_0}{m_e c} = \frac{eE_L}{mc\omega_0} \,, \tag{1.10}$$

which is defined from the electron's maximum velocity in the laser's electric field, eA_0/m_e, normalised to the speed of light c. This electron velocity is also called the "quiver" velocity since the electron rapidly oscillates back and forth in the fast oscillating electric field of the laser pulse, whose carrier angular frequency is ω_0. This dimensionless quantity allows us to identify the degree of relativistic corrections that must be applied to an electron's motion during the interaction with the laser pulse and separate the laser-plasma interaction broadly into linear ($a_0 \ll 1$) and nonlinear ($a_0 \gtrapprox 1$) regimes as discussed below in section 1.4. From Eq. 1.10, the peak electric field amplitude can be calculated[3], for a case with $a_0 = 1 \,, \lambda_0 = 2\pi c/\omega_0 = 800\,\mathrm{nm}$, to be 4 TV/m indicating that the electric fields of the laser pulse are extremely large.

The Gaussian beam description is a solution of the above Maxwell equations under the paraxial beam assumption. It is a good approximation for short pulse lasers in the spatial and temporal domains[24]. We can define the complex spatial profile of a Gaussian laser pulse as[25]:

$$\vec{E}(r,z,t) = \vec{E}_0 \frac{w_0}{w(z)} \exp\left(-\frac{r^2}{w(z)^2} \right) \exp\left(-ik_0 \frac{r^2}{R(z)} \right) \exp\left(i\phi(z) \right), \tag{1.11}$$

where $\vec{E}_0$ determines the polarization and the amplitude of the transverse electric field. We can define the beam properties from the above components of the Gaussian solution, starting with the **beam waist**[25]:

$$w(z) = \sqrt{w_0^2 \left[1 + \left(\frac{z}{z_R} \right)^2 \right]} \,, \tag{1.12}$$

the **Rayleigh length** as:

$$z_R = \frac{\pi w_0^2}{\lambda_0} \,, \tag{1.13}$$

the **beam divergence**:

$$\theta = \lim_{z \to \mathrm{inf}} \frac{w(z)}{z} = \frac{\lambda_0}{\pi w_0}\,, \tag{1.14}$$

the **radius of curvature** as:

$$R(z) = z\left[1 + \left(\frac{z_R}{z}\right)^2\right], \tag{1.15}$$

and finally the **Gouy phase** as:

$$\phi(z) = \arctan\left(\frac{z}{z_R}\right). \tag{1.16}$$

In the above equations, we defined the beam waist, w_0, as the radius where the electric field is equal to $1/e^2\,(\approx 0.135)$ times its peak value. Geometrically the Rayleigh length describes the distance along the propagation axis where beam waist increases by a factor $\sqrt{2}$. It is also important to note that for a given pre-focusing beam diameter, D, and focal length of focusing optic, f, we can calculate the beam waist at focus, assuming zero aberration, as:

$$w_0 = \frac{f\lambda_0}{\pi D}\,. \tag{1.17}$$

When modelling a drive laser for laser-plasma interaction as a Gaussian beam, we can define power, fluence and intensity of the pulse from the temporal, spatial, and temporal *and* spatial properties of the laser pulse energy, respectively. Fluence is defined as the energy density per unit area of the laser and is in fact what is measured when a transverse image of a laser is taken with a charge-coupled device (CCD) as the measurement is temporally integrated. Using the generalised formula for the relation between peak and radially dependent fluence for super-Gaussian beams, we can then set n = 1 for a Gaussian case retrieving:

$$F(r) = F_0\left[-2\left(\frac{r}{w_0}\right)^{2n}\right] = F_0\left[-2\left(\frac{r}{w_0}\right)^{2}\right] \tag{1.18}$$

where w_0 is the transverse laser waist at focus and F_0 is the peak fluence defined as the maximum energy density per unit area of the pulse. The peak fluence for a Gaussian laser profile is defined as:

$$F_0 = \mathcal{E}\frac{2^{\frac{1}{n}}n}{\pi w_0^2 \Gamma\left(\frac{1}{n}\right)} = \mathcal{E}\frac{2}{\pi w_0^2} \tag{1.19}$$

Here we have used the definition for the gamma function, $\Gamma(1) = 1$. The total beam energy can be retrieved by integrating the fluence over the surface transverse to the laser propagation as:

$$\mathcal{E} = \int F(r)dS \tag{1.20}$$

We can similarly describe the power, defined as the energy per unit time of the pulse, as:

$$P = \kappa \frac{\mathcal{E}}{\tau_0} \tag{1.21}$$

where κ is a constant value equal to 0.94 or 0.88 for Gaussian and sech^2 pulses, respectively.

From the peak fluence, we can also calculate the peak intensity of the pulse, which is more relevant for understanding the dynamics of laser-plasma and laser-electron interactions:

$$I_0 = \frac{2F_0}{\tau} \times \sqrt{\frac{\ln 2}{\pi}} \approx \mathcal{E} \frac{2}{\pi \tau w_0^2}\,, \tag{1.22}$$

where τ is the full-width at half-maximum pulse duration. Whilst this description is useful for calculating the intensity from images of the laser pulse, we can also characterise the intensity from the electric and magnetic fields. The intensity is defined as the energy per unit area per unit time, equivalent to the magnitude of the Poynting vector (the vector describing the energy flux of the laser pulse.) Starting from the definition of the Poynting vector, $\vec{S} = \vec{E} \times \vec{H}$, where $\vec{E}$ is the electric field and $\vec{H}$ the magnetic field auxiliary vector, we can derive a measure defined as intensity to describe the power per unit area per unit time, which will be referred to throughout this manuscript. Taking the modulus of the pointing vector, using the relation $|\vec{A} \times \vec{B}| = |\vec{A}||\vec{B}| \sin\theta$, the relation between the magnetic field auxiliary vector and the electric field in vacuum $|\vec{H}| = \sqrt{\frac{\epsilon_0}{\mu_0}}|\vec{E}|$, and using the definition for the speed of light in vacuum as $c = \frac{1}{\sqrt{\epsilon_0 \mu_0}}$ we find:

$$I \triangleq |\vec{S}| = |\vec{E}| \times |\vec{H}| = \sqrt{\frac{\epsilon_0}{\mu_0}} |\vec{E}|^2 = c\epsilon_0 |\vec{E}|^2\,. \tag{1.23}$$

Substituting an arbitrary plane wave function to describe the electric field, arbitrarily linearly polarised in the y-direction, $\vec{E} = E_0 \sin\omega_0 t \hat{\mathrm{y}}$, gives the intensity averaged over one period:

$$I \triangleq |\vec{S}| = c\epsilon_0 E_0^2 |\sin\omega_0 t|^2 = \frac{1}{2} c\epsilon_0 E_0^2\,. \tag{1.24}$$

As the intensity is described in terms of the peak electric field, and therefore the peak vector potential, we can define the normalised vector potential of Eq. 1.10 by substituting Eq. 1.24 into Eq. 1.10 giving:

$$a_0 \approx 0.86 \times \lambda_0[\mu\mathrm{m}] \sqrt{I_0[10^{18}\mathrm{W\,cm^{-2}}]}\,. \tag{1.25}$$

We can further describe the electric field of a short pulse laser in the temporal domain with a Gaussian function of the form:

$$E(t,0) = E_0 \exp\left[-2\ln(2)\frac{t^2}{\tau_0^2}\right] \cdot \exp\left[i\omega_0 t\right], \tag{1.26}$$

where τ_0 is the pulse duration at full-width half-maximum of the peak laser intensity in time. Equivalently, through Fourier transform, we can extract the frequency dependence around the central laser frequency, ω_0, as[26]:

$$\tilde{E}(\omega) = \frac{E_0 \tau_0}{2\sqrt{\ln(2)}} \exp\left[-\frac{\tau_0^2}{8\ln(2)}\Big(\omega - \omega_0\Big)^2\right] . \tag{1.27}$$

Short pulse lasers require a bandwidth of frequencies around the central frequency where the frequency bandwidth is related to the pulse duration through the duration-bandwidth product. From the uncertainty principle, in this case, using the Cauchy-Schwarz inequality for time and energy (equivalently frequency), the required duration-bandwidth product for a given pulse duration of a Gaussian temporal profile is[27]:

$$\Delta\omega\tau_0 \geq 2.77 \tag{1.28}$$

This indicates that, for example, a $40\,\mathrm{fs}$ laser must have a frequency bandwidth of $6.9 \times 10^{13}\,\mathrm{rad\,s^{-1}}$ (FWHM) corresponding to a wavelength bandwidth of $16.9\,\mathrm{nm}$ (FWHM).

1.2 . Plasma Description

The plasma transforms a fraction of the large transverse electric fields of the laser pulse into accelerating and focusing fields. Further, the plasma alters the laser evolution in ways beneficial for sustained wake creation. We will therefore discuss the key principles and equations for the plasma, which will lay the basis for understanding the more complex phenomena.

Plasma is a state of matter where the atomic constituents are partially or fully ionised, resulting in a conductive medium capable of sustaining and reacting to electric and magnetic fields whilst being globally neutral due to Debye shielding[28]. Laser ionisation, which will be discussed in further detail in the section 1.2.3, typically results in the creation of cold plasmas due to electron tunnelling from atomic potential-well deformation induced by the strong electric fields of high-intensity lasers, being the dominant mechanism of ionisation. The cold plasma electrons can then oscillate at the plasma (or Langmuir[29]) frequency, ω_p, defined by the plasma density and mass of the electrons and assuming infinite ion mass:

$$\omega_p = \sqrt{\frac{n_e e^2}{m_e \epsilon_0}} \approx 5.64 \times 10^4 \left(n_e[\mathrm{cm^{-3}}]\right)^{1/2} \mathrm{rad\,s^{-1}} , \tag{1.29}$$

where e and m_e are the charge and rest mass of the electron, respectively, and n_e is the electron density in units of $\mathrm{cm^{-3}}$. This frequency corresponds to the resonance of the plasma electrons arising from the dielectric function of the electron gas[30].

From this value, we can define the plasma wavelength:

$$\lambda_p = 2\pi c/\omega_p \,, \tag{1.30}$$

where c is the speed of light in vacuum, providing us with the typical time, ω_p, and length scales, λ_p of the plasma motion.

1.2.1 . Dispersion of Electromagnetic Waves in Plasma

By examining an electromagnetic wave in the plasma, we can derive the critical plasma density, defined as the density at which an incoming wave becomes evanescent, i.e. the wave number, k, becomes imaginary for a given frequency, ω. Combination of Eqs. 1.3 and 1.4 gives:

$$\nabla \times (\nabla \times \vec{E}) = -\frac{\partial(\nabla \times \vec{B})}{\partial t} \tag{1.31}$$

$$\nabla(\nabla \cdot \vec{E}) - \Delta\vec{E} = \frac{1}{c^2}\left(\frac{1}{\epsilon_0}\frac{\partial \vec{j}}{\partial t} + \frac{\partial^2 \vec{E}}{\partial t^2}\right) \tag{1.32}$$

where we can expand the left-hand side using the vector identity: $\nabla \times \nabla\vec{C} = \nabla(\nabla\cdot\vec{C}) - \Delta\vec{C}$ where Δ is the Laplace operator defined as $\nabla\cdot\nabla$. Using an arbitrary plane wave of the form $\vec{E} = E_0 \sin(k_0 \cdot z - \omega_0 t)\hat{\mathrm{y}}$, where we have assumed the wave-vector is along the axis of propagation z, and substituting the current in the fluid view $\vec{j} = -en_e\vec{v}$, we can then write the terms in the above expression (from left-to-right) as:

$$\nabla(\nabla \cdot \vec{E}) = 0\,\hat{\mathrm{x}} + 0\,\hat{\mathrm{y}} - k_0^2\vec{E}\hat{\mathrm{z}} = 0\,, \qquad \Delta\vec{E} = -k_0^2\vec{E}\,, \tag{1.33}$$

$$\frac{\partial \vec{j}}{\partial t} = -en_e\frac{\partial \vec{v}}{\partial t}\,, \qquad \frac{\partial^2 \vec{E}}{\partial t^2} = -\omega_0^2\vec{E}\,. \tag{1.34}$$

$$\tag{1.35}$$

The first term equals zero due to the orthogonality of the unit vectors from the plane wave definition. We can find $\partial\vec{v}/\partial t$ by taking the time derivative of the non-relativistic Lorentz equation w.r.t time giving:

$$\frac{\partial \vec{v}}{\partial t} = \frac{-e\vec{E}}{m_e} \tag{1.36}$$

Where we can then finally cancel the electric field, leaving the dispersion relation:

$$\omega_0^2 = k_0^2c^2 + \omega_p^2\,. \tag{1.37}$$

Eq. 1.37 shows a cut-off frequency, the plasma frequency ω_p, below which the laser light can no longer propagate in the plasma, as the magnitude of the wave vector would become imaginary. Rearranging our Eq. 1.29 and defining the density that creates this condition as the critical density, we retrieve:

$$n_c = \frac{\epsilon_0 m_e}{e^2}\omega_0^2 \tag{1.38}$$

In engineering units this becomes: $n_c = \frac{1.1\times10^{21}}{\lambda_0(\mu\mathrm{m})}\mathrm{cm}^{-3}$. Laser wakefield acceleration relies on the laser pulse traversing the plasma to drive the wake, and therefore the plasma is 'underdense', i.e. $n_e < n_c$ as would be expected. Conversely, plasmas where $n_e > n_c$ (such as in solid target experiments for laser ion acceleration) are termed 'over-dense'.

1.2.2 . Plasma Fluid Equations

In addition to the equations in section 1.1, we can include the electron momentum from the Lorentz force and the continuity equation for the plasma electrons to complete the Maxwell-Vlasov equations in the fluid description of the plasma where quantities are average quantities over the particles. Where the **continuity equation** is:

$$\frac{\partial n_e}{\partial t} + \nabla \cdot (n_e \vec{v}) = 0\,, \tag{1.39}$$

and the **fluid momentum equation** is:

$$\frac{d\vec{p}}{dt} = \frac{\partial \vec{p}}{\partial t} + (\vec{v}\cdot\nabla)\vec{p} = -q(\vec{E} + \vec{v}\times\vec{B}) \tag{1.40}$$

where $\vec{v}$ is the particle species' vectorial velocity. The above equations are only valid for non-collisional plasmas. Starting from the Debye length, λ_D, defined as a characteristic length scale for the electrostatic screening effects in plasma, we can define the so-called plasma parameter, g, to extract the regime of collisionality[30]:

$$\lambda_\mathrm{D} = \left(\frac{\varepsilon_0 k_\mathrm{B} T_\mathrm{e}}{e^2 n_\mathrm{e}}\right)^{1/2} = 743\left(\frac{T_\mathrm{e}}{\mathrm{eV}}\right)^{1/2}\left(\frac{n_\mathrm{e}}{\mathrm{cm}^{-3}}\right)^{-1/2}\mathrm{cm}. \tag{1.41}$$

$$g \coloneqq \frac{1}{n_e \lambda_D^3} \tag{1.42}$$

The definition of g corresponds to the inverse of the number of plasma electrons contained in a cube with side λ_D. For typical experimental parameters of laser wakefield acceleration experiments in underdense plasmas, with low electron temperatures due to the ionisation method discussed in the following section 1.2.3, $g \ll 1$ which implies that collective plasma effects dominate over particle collisions[31]. We can therefore neglect the effect of particle collisions and use the Maxwell-Vlasov equations to describe the plasma evolution.

1.2.3 . Plasma Production Through Ionisation of Gases

The ionisation of a gas into a plasma using high-intensity laser pulses occurs through several processes independent of the photovoltaic effect[32] due to typical laser wavelengths being longer than the required wavelength for single photon electron ejection. Instead, multi-photon ionisation and deformation of the atomic binding potential (to varying degrees) due to the large electric fields of the laser occur. The dominant mode of ionisation is related to the laser intensity, described by Eq. 1.24.

Distinctions of the dominant ionisation regimes are described by the Keldysh parameter[33], Γ_k:

$$\Gamma = \omega_0 \sqrt{\frac{2\Phi_i}{I_0}} \tag{1.43}$$

where ω_0, I_0 are the laser angular frequency and intensity, and Φ_i the ion binding potential. When Γ is large, the ion binding potential is unperturbed by the laser field, and so multi-photon ionisation dominates. This occurs when an electron absorbs n photons, where n is dependent on the binding potential and frequency of the laser pulse. When Γ is close to unity, the ion binding potential is perturbed, reducing the barrier for electron tunnelling out of the atom. The rate at which electrons tunnel from the atomic potential is proportional to the deformation of the potential and the duration of the deformation. Finally, total suppression of the ionic binding potential is achieved for small Γ where the electrons are no longer bound to the ion through Barrier Suppression Ionisation (BSI).

For BSI, we can use the binding potential of a given atomic species as the minimum required potential deformation and calculate the intensity required for the gas species used during this thesis to be instantly ionised. We can begin by writing the potential experienced by the electron as a sum of the atomic and laser potentials gives:

$$V(r) = -\frac{e^2 Z}{4\pi\epsilon_0 r} - q|E_0|r\,, \tag{1.44}$$

where Z is the charge number of the atom in its current ionisation state, and e is the electron charge. This allows us to find the position where the potential experienced by the electron is maximal by taking the derivative w.r.t r and setting it to zero. From this, we find that the apparent potential is maximum for:

$$r = \pm\sqrt{\frac{eZ}{4\pi\epsilon_0|E_0|}}\,. \tag{1.45}$$

Using Eq. 1.24, we can write the maximum electric field in terms of intensity, set the apparent potential to zero, and substitute r from Eq. 1.45 to find the required laser intensity for instantaneous ionisation, I_i:

$$I_i \;= \frac{c\varepsilon_0^2\pi^2 E_i^4}{2Z^2e^6} \approx 4\times10^9 \frac{(E_i[eV])^4}{Z^2}\mathrm{Wcm}^{-2}\,. \tag{1.46}$$

From Eq. 1.46 it can be seen that for a hydrogen atom ($Z = 1$) with a binding energy of $13.6\,\mathrm{eV}$, this would correspond to BSI at an intensity of $1.4\times10^{14}\mathrm{Wcm}^{-2}$. As typical laser intensities in LWFA experiments regularly exceed $10^{18}\mathrm{Wcm}^{-2}$, ionisation is performed at the beginning of the rising edge of the laser pulse (termed the "foot"), meaning that the bulk of the laser is propagating in an already formed plasma. The ionisation intensity gap between the first five, and the final two electrons, of nitrogen in table 1.1 will be discussed further in section 1.5.1.2 as a method for controlling electron injection into the plasma wake.

Species	$\mathcal{E}_{ion}$(eV)	I_r(W/cm^2)
H^+	13.6	1.4×10^{14}
N^{5+}	97.9	7.5×10^{15}
N^{6+}	552.1	7.6×10^{18}
N^{7+}	667.1	1.6×10^{19}

Table 1.1 – Atomic binding energies, $\mathcal{E}_{ion}$, and the required intensity, I_r, for barrier suppression ionisation for different gas species and ionisation states used during experiments for this thesis.

1.3 . Laser Propagation in Plasma

Significant nonlinear and relativistic effects must be accounted for when discussing the propagation of high-intensity lasers in underdense plasmas. Here we will begin by discussing the ponderomotive force arising from the inhomogeneous laser intensity profile. We will then explore the spatial and temporal evolution of the laser in the plasma.

1.3.1 . Laser Phase and Group Velocity in Plasmas

From Eq. 1.37 we can derive the group and phase velocity of the plasma and use this to define the plasma's refractive index. From the definition of the phase, v_{ph}, and group, v_g, velocity we have:

$$v_{ph} = \frac{\omega_0}{k} = \sqrt{c^2 + \frac{\omega_p^2}{k^2}}\,, \tag{1.47}$$

$$v_g = \frac{d\omega_0}{dk} = \frac{c^2}{v_{ph}} = \frac{c^2 k}{\sqrt{c^2 k^2 + \omega_p^2}} \tag{1.48}$$

Calculation of the refractive index requires that we take into account the relativistic corrections of the plasma frequency i.e $\omega_{p\gamma} = \omega_p / \sqrt{\gamma_\perp}$, where $\gamma_\perp$ is the electron γ-factor perpendicular to the laser propagation defined as $\gamma_\perp = 1 + \vec{a}^2/2$. Here $\vec{a}$ is the normalised vector potential and we have assumed that the quiver momentum is much greater than the electron's momentum before interaction with the laser allowing us to neglect the transverse momentum dependence of $\gamma_\perp$[34]. The refractive index of light is defined as $\eta = \frac{c}{v_{ph}}$ which therefore gives:

$$\begin{aligned} \eta &= \sqrt{1 - \frac{\omega_p^2}{\gamma_\perp \omega_0^2}} \\ &\approx 1 - \frac{1}{2}\frac{n_e}{\gamma_\perp n_c}\,, \end{aligned} \tag{1.49}$$

where the plasma density, n_e, and refractive index η, can vary both spatially and in time.

1.3.2 . Ponderomotive Force

The Ponderomotive force, arising from the time-averaged effects of an inhomogeneous oscillating electromagnetic field of a pulsed laser, is the perturbative force which cavitates the plasma resulting in the accelerating structures that make laser wakefield acceleration possible. Qualitatively, it can be thought of as the low-frequency action arising from the high-frequency field of the laser[35]. As the electron rapidly oscillates in the electric and magnetic field of the laser, the inhomogeneity of the laser pulse, in both the temporal and transverse axis, leads to an electron experiencing varying field strengths during the oscillation period. The resulting instantaneous force, which alternates its sign during the oscillations, is not compensated after one oscillation period due to the inhomogeneous amplitude of the laser envelope. This results in a net force acting on the electron. This then shifts the centre of the particle's oscillation producing a second-order motion of the particle where it is shifted as well as oscillated in the lasers electric field.

To begin our description of the interaction between laser and matter, we first consider the case of electron motion induced by an electromagnetic wave where we consider the interaction to be in the linear regime where $a_0 \ll 1$. Writing the fluid momentum equation (Eq. 1.40) in potential notation gives:

$$\frac{d\vec{p}}{dt} = \left(\frac{\partial}{\partial t} + \vec{v}\cdot\nabla\right)\vec{p} = -e(\vec{E} + \vec{v}\times\vec{B}) \tag{1.50}$$

$$= -e\Big(-\frac{\partial\vec{A}}{\partial t} - \nabla\phi + \vec{v_e}\times(\nabla\times\vec{A})\Big)\,. \tag{1.51}$$

From the Poisson equation in Eq. 1.8, the laser does not provide charge and therefore the scalar potential, ϕ, describes the potential of the wake from the charge separation. Further, considering Eq. 1.38 and the relativistic correction to the plasma frequency $\omega_{p\gamma} = \omega_p/\gamma_\perp$, we can see that for underdense plasma densities, the plasma frequency $\omega_p \ll \omega_0$. Therefore the vector potential descriptions of the electric field in Eq. 1.5 indicate that the vector potential will predominantly describe the laser field. Considering only the effects of the laser on the electron motion, i.e neglecting the effects of the $\nabla\phi$ term and considering $\vec{A} = \vec{A}_{laser}$, and separating Eq. 1.51 into linearised ("1" subscript) and second order ("2" subscript) components we find, first for the linear term:

$$\frac{\partial\vec{p}_1}{\partial t} = e\frac{\partial\vec{A}}{\partial t}\,, \tag{1.52}$$

which describes the fast oscillations, or quiver momentum of the electrons. We can use this to solve for $\vec{B}$ where we have replaced $\vec{A}$ with the normalised vector potential from Eq. 1.10:

$$\vec{B} = \nabla\times\vec{A} = \frac{m_e c}{e}\nabla\times\vec{a} = \frac{1}{e}\nabla\times\vec{p}_1\,, \tag{1.53}$$

$$\therefore \vec{p_1} = m_e c\vec{a}\,. \tag{1.54}$$

Using our linear solution, separating the time derivative into first and second-order momenta, rewriting the velocity terms as $\vec{v} = \vec{p}/m_e\gamma$, substituting Eq. 1.54, and replacing $\vec{A}$ with the normalised vector potential, $\vec{a}$, we find from Eq. 1.51:

$$\frac{\partial \vec{p_1}}{\partial t} + \frac{\partial \vec{p_2}}{\partial t} + \frac{1}{m_e\gamma}(\vec{p_1}\cdot\nabla)\vec{p_1} - e\Big(-\frac{m_e c}{e}\frac{\partial \vec{a}}{\partial t} + \frac{1}{m_e\gamma}\vec{p_1}\times\Big(\frac{m_e c}{e}\nabla\times\vec{a}\Big)\Big)\,, \quad (1.55)$$

which yields :

$$m_e c\frac{\partial \vec{a}}{\partial t} + \frac{\partial \vec{p_2}}{\partial t} + \frac{m_e c^2}{\gamma}(\vec{a}\cdot\nabla)\vec{a} = m_e c\frac{\partial \vec{a}}{\partial t} - \frac{m_e c^2}{\gamma}\vec{a}\times\nabla\times\vec{a} \quad (1.56)$$

$$\therefore \frac{\partial \vec{p_2}}{\partial t} = -\frac{m_e c^2}{\gamma}\left(\vec{a}\times\nabla\times\vec{a} + \vec{a}\cdot\nabla)\vec{a}\right)\,. \quad (1.57)$$

We can use the vector identity, $\nabla|C|^2 = 2\left[(\vec{C}\cdot\nabla)\vec{C} + \vec{C}\times\left(\nabla\times\vec{C}\right)\right]$, to find:

$$\vec{F}_p \triangleq \frac{\partial \vec{p_2}}{\partial t} = -\frac{m_e c^2}{2\gamma}\nabla|\vec{a}|^2 = -\frac{e^2}{2m_e\gamma}\nabla|\vec{A}|^2, \quad (1.58)$$

which is the ponderomotive force of the laser pulse on the electrons leading to the second-order motion. From this equation, it can be seen that the ponderomotive force is proportional to the gradient of the absolute square of the vector potential. This indicates that a spatially (and/or temporally) inhomogeneous electromagnetic waves are required to produce a non-zero average displacement of the electrons during the interaction with the laser. The ponderomotive force will push particles out of regions where the intensity of the laser is higher (i.e. particles will experience a force in the direction opposite to the gradient of the intensity). Another interesting point is that this force is independent on the sign of the charge of the particle and is inversely proportional to the mass of the particle (hence its name). Electrons will thus experience a larger effect of the ponderomotive force compared to ions. This then leaves an ion core after the laser has passed and produces electron sheaths which are created from the expelled electrons. The restoring force of the ions on the electrons then induces an oscillation around the ion core, which we term the plasma wake.

For the relativistic case of nonlinear laser-plasma interaction when $a_0 \geq 1$ we must include the cross-product term and relativistic corrections to the Lorentz factor of the electrons, which then gives[36]:

$$\vec{F}_{pnl} = -\frac{e^2}{2m_e\gamma_p}\nabla|\vec{A}|^2, \quad (1.59)$$

where the ponderomotive Lorentz factor is defined as $\gamma_p = \sqrt{1 + \frac{|\vec{p}|^2}{m_e^2c^2} + \frac{e^2|\vec{A}|^2}{m_e^2c^2}}$. The inverse scaling of the electron momenta indicates that the nonlinear ponderomotive force will provide a stronger force to low-energy electrons.

1.3.3 . Self-Focusing

Since the energy gain of the electrons is limited to the existence of the wake structure, it could be assumed that the diffraction of the laser would limit the acceleration to few Rayleigh lengths (specifically $L = \pi z_R$, where z_R is the Rayleigh length[37]) before the intensity decreases to below the critical value for driving electron expulsion. However, the nonlinear effect of self-focusing produces a focusing of the laser which allows for the pulse intensity to be maintained over many Rayleigh lengths without the need for external guiding. These nonlinear relativistic effects occur once the laser power crosses a threshold termed the critical power for relativistic self-focusing defined as[23]:

$$P_c = 3.851 \frac{2\pi c^3 m_e}{\mu_0 e^2} \left(\frac{\omega_0}{\omega_p}\right)^2 \approx 1.68 \times 10^{-2} \left(\frac{\omega_0}{\omega_p}\right)^2 [\mathrm{TW}] \tag{1.60}$$

For a laser to be self-focused, $\partial\eta(r)/\partial r$ must be negative[38]. This implies also that the phase velocity of the laser pulse on axis will be slower than the phase velocity off-axis leading to wavefront curvature of the laser pulse. This curvature acts to focus the laser radially towards the principal axis of propagation.

Multiple effects are simultaneously responsible for inducing the refractive index structure required for self-focusing, namely: relativistic self-focusing, ponderomotive self-focusing, and thermal self-focusing. On the temporal scale of short pulses, we can neglect the effect of thermal self-focusing due to the plasma ion's collisional timescale being significantly longer than the temporal scale of the laser evolution ($\mathcal{O}(\mathrm{ns})$ for hydrodynamic plasma expansion against $\mathcal{O}(\mathrm{fs})$ pulses). Accounting for the effects of relativistic and ponderomotive self-focusing during the propagation of high-intensity lasers in plasmas, requires relativistic corrections to the refractive index of the plasma and inclusion of the local plasma density profile alterations induced by the nonlinear ponderomotive force. We will assume a Gaussian intensity distribution for the following discussion.

Using the refractive index of a plasma from Eq. 1.49 we see that an increase in $\gamma_\perp$ of the plasma electrons will increase η. As the laser vector potential is highest on-axis for a Gaussian beam, electrons at locations closer to the axis will gain a higher quiver momentum and therefore an increased $\gamma_\perp$ factor than those further from the axis. This effect is referred to as relativistic self-focusing.

Ponderomotive self-focusing relies on the cavitation of plasma electrons due to the ponderomotive force. Reduction of the on-axis electron density will increase the refractive index on-axis. As the electron density increases again further from the principal axis the refractive index does to.

1.3.4 . Pulse Temporal Evolution

In addition to the radial spatial compression of the laser pulse through self-focusing presented above in section 1.3.3, the temporal envelope of the laser pulse is also altered during the propagation in the plasma. A model of pulse compression

is presented by Pathak et al.[39] for the linear and nonlinear interaction regimes. They present the following equation to describe the evolution of the refractive index with variations in the plasma density and laser frequency as:

$$\eta = \left[1 - \frac{\omega_{\mathrm{p}}^2}{2\omega_0^2}\left\{1 + \frac{\delta n}{n_0} - \frac{\langle a^2\rangle}{2} - 2\frac{\delta\omega}{\omega_0}\right\}\right], \tag{1.61}$$

where $\langle a^2\rangle$, is the time average normalised vector potential over one laser period, and δn, $\delta\omega$ are variations in the density and laser frequency, respectively. From this equation, we can interpret the physical mechanisms leading to the shortening of the laser pulse in the plasma. During the laser-plasma interaction, the electron density at the front of the pulse is increased and decreased at the rear of the pulse through the ponderomotive force. This leads to a reduction in the group velocity at the front of the laser pulse and an increase at the rear. Therefore during propagation, the distance between the front and rear edge of the laser pulse decreases, shortening the laser's duration.

A secondary effect that can reduce the pulse duration is pulse etching that results from the local depletion of the laser pulse[40]. The pulse etching velocity was derived, in units of c, as[34]:

$$v_{etch} = \frac{\omega_p^2}{\omega_0^2}\,. \tag{1.62}$$

Resulting in the velocity of the front end of the laser, again in units of c, being:

$$v_f \approx 1 - \frac{3}{2}\frac{\omega_p^2}{\omega_0^2} \tag{1.63}$$

From geometric reasoning, a given laser pulse duration, τ, sets a limit on the length the laser can propagate in the plasma before full depletion as[41]:

$$L_{depletion} \approx (\omega_0^2/\omega_p^2)\tau c\,. \tag{1.64}$$

1.4 . Regimes of Laser Wakefield Excitation

We can characterise the laser-plasma interaction, and the resulting wakefield dynamics, through a_0 of equation 1.10. For $a_0 < 1$, linear interaction is produced due to the electron momenta being non-relativistic (or weakly relativistic) and the resulting wake excitation being far from cavitated, i.e., whilst there is a density perturbation, electrons remain within the ion region. When $a_0 \gtrapprox 1$, electrons become ultrarelativistic from the quiver momentum imparted by the fast oscillations of the lasers' electric field over a single laser cycle. First, we will explain the process of wakefield generation qualitatively before defining the interaction in the linear and nonlinear regime to extract the relevant physics for understanding the resulting plasma and electron dynamics.

1.4.1 . Qualitative Picture of Laser Wakefield Acceleration

During the interaction of the UHI short-pulse laser with an underdense plasma, plasma wakes are created that can sustain large accelerating and focusing fields. As discussed in section 1.2.3, typical laser intensities used during LWFA experiments significantly exceed the intensity required to ionise the gas into a plasma instantly. As this process occurs at the foot of the laser, the laser pulse can be considered to be propagating within a plasma. The ponderomotive force from the intensity profile of the laser pulse then expels plasma electrons off-axis from the laser volume. During the time scale of a short pulse, the ions are immobile due to their inertia. The ejected electrons from the laser volume form dense sheaths around the laser axis as they are pulled radially towards the positively charged ion cavity. This plasma density perturbation then sustains the large accelerating and focusing fields. Electrons trapped in this wake are then accelerated and travel with the wake, gaining energy and oscillating in the plasma wake due to the transverse fields. At the end of the plasma, these electrons then exit with the depleted laser pulse and continue to propagate freely.

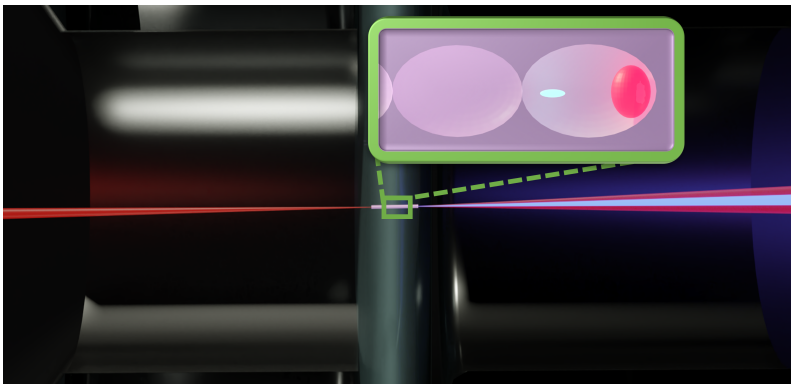

Figure 1.1 – Illustration of laser wakefield acceleration in the ELISA gas cell with $500\,\mu\mathrm{m}$ plasma plateau to demonstrate the scale of processes. Laser enters from the left, electrons are trapped and accelerated and leave the cell in bright blue alongside the diffracted laser. The plasma column is visible across the gas volume in line with the laser. Gas injection arrives from the top of the cell. The gas cell has been extruded to show the internal setup. Gas leakage through the entrance and exit face has been omitted for clarity. Zoomed inset shows the laser pulse in red, travelling to the right, creating a rarefied region of electrons surrounded by the background plasma. The trapped electron bunch is shown in blue at the back of the first wave bucket.

A typical interaction between the laser and plasma during an LWFA experiment is displayed in Fig. 1.1, not shown to scale for clarity. Electron density wakes are displayed in the plasma volume where the electrons are trapped and accelerated.

1.4.2 . Linear Plasma Waves

In the linear interaction regime, the electrons are perturbed by the ponderomotive force of the laser pulse without gaining sufficient quiver momentum to be considered relativistic. This is the case when the laser's normalised vector potential, $a_0 < 1$, and we can define the electron density perturbation due to the laser as some small value around the background plasma density value as: $n_e - n_0 = \delta n_e \ll n_0$. In this case, the density perturbation, or plasma waves, are sinusoidal and can be derived in 3D using the Poisson (Eq. 1.8), continuity (Eq. 1.39) and fluid momentum (Eq. 1.51)[3] equations.

Writing Eq. 1.39 and Eq. 1.8 for the case of small charge density perturbation where we can linearise these equations, we find:

$$\frac{\partial \delta n_e}{\partial t} + \nabla \cdot (\delta n_e \vec{v}) = 0 \text{ (Continuity Eq.)}, \tag{1.65}$$

$$\Delta\phi = -\frac{\rho}{\epsilon_0} = -e\frac{n_e - n_0}{\epsilon_0} = -e\frac{\delta n_e}{\epsilon_0} \text{ (Poisson Eq.)}. \tag{1.66}$$

We have defined the Laplace operator as $\Delta = \nabla \cdot \nabla$ and the density perturbation $\delta n_e = n_e - n_0$ from the uniform initial density n_0. Differentiating Eq. 1.65 with respect to time gives us:

$$\frac{\partial^2 \delta n_e}{\partial t^2} + \nabla \cdot \left(\delta n_e \frac{\partial \vec{v}}{\partial t} \right) = 0 \tag{1.67}$$

We can find $\partial\vec{v}/\partial t$ by combing our linear (Eq. 1.52) and second-order motion (Eq. 1.58) fluid momentum solutions, adding back the gradient of the scalar potential to account for the non-zero net charge, and dividing by the electron mass to give:

$$\frac{\partial \vec{v}}{\partial t} = \frac{1}{m_e}\left(\frac{\partial \vec{p}_1}{\partial t} + \frac{\partial \vec{p}_2}{\partial t} \right) = \frac{e}{m_e}\nabla\phi + c\frac{\partial \vec{a}}{\partial t} - \frac{c^2}{2\gamma}\nabla\vec{a}^2 \tag{1.68}$$

Inserting Eq. 1.68 into Eq. 1.67 then substituting the linearised Poisson equation (Eq. 1.66) in the Coulomb gauge such that $\nabla \cdot \vec{A} = 0$ (equivalently $\nabla \cdot \vec{a} = 0$) gives:

$$\frac{\partial^2 \delta n_e}{\partial t^2} + \delta n_e \left(\frac{e}{m_e}\Delta\phi + c\frac{\partial \nabla \cdot \vec{a}}{\partial t} - \frac{c^2}{2\gamma}\Delta\vec{a}^2 \right) = 0, \tag{1.69}$$

$$\frac{\partial^2 \delta n_e}{\partial t^2} \left(\frac{-e^2}{m_e \epsilon_0}\delta n_e - \frac{c^2}{2\gamma}\Delta\vec{a}^2 \right) = 0, \tag{1.70}$$

which can be rearranged to find the equation for plasma wave generation:

$$\left(\frac{\partial^2}{\partial t^2} + \omega_p^2 \right) \frac{\delta n_e}{n_{e0}} = \frac{c^2}{2\gamma}\Delta\vec{a}^2 . \tag{1.71}$$

The form of this equation is recognisable as a forced oscillator where the driving force is provided by the ponderomotive force of the laser on the right-hand side and

the term $\omega_p^2 \delta n_e / n_{e0}$ represents the space charge. The form of the plasma wave in the linear case is a sinusoidal oscillation of the plasma electrons where the solutions in the linear regime for Gaussian pulses have been calculated to be[42]:

$$E_z(r,z,t) = \mathcal{F}(r)\cos(k_0 z - \omega_0 t)\,, \tag{1.72}$$

$$E_r(r,z,t) = -\mathcal{F}(r)\frac{4c}{\omega_p}\frac{r}{\omega_0^2} sin(k_0 z - \omega_0 t)\,, \tag{1.73}$$

where the radially dependent function $\mathcal{F}(r)$ is given by:

$$\mathcal{F}(r) = \frac{m_e c \omega_p}{e}\sqrt{\frac{\pi}{2}} a_0^2 \frac{\omega_p \tau}{4\sqrt{2\ln 2}} \exp\left(-\frac{\omega_p^2 \tau^2}{16 \ln 2}\right) \exp\left(-\frac{2r^2}{w_0^2}\right)\,. \tag{1.74}$$

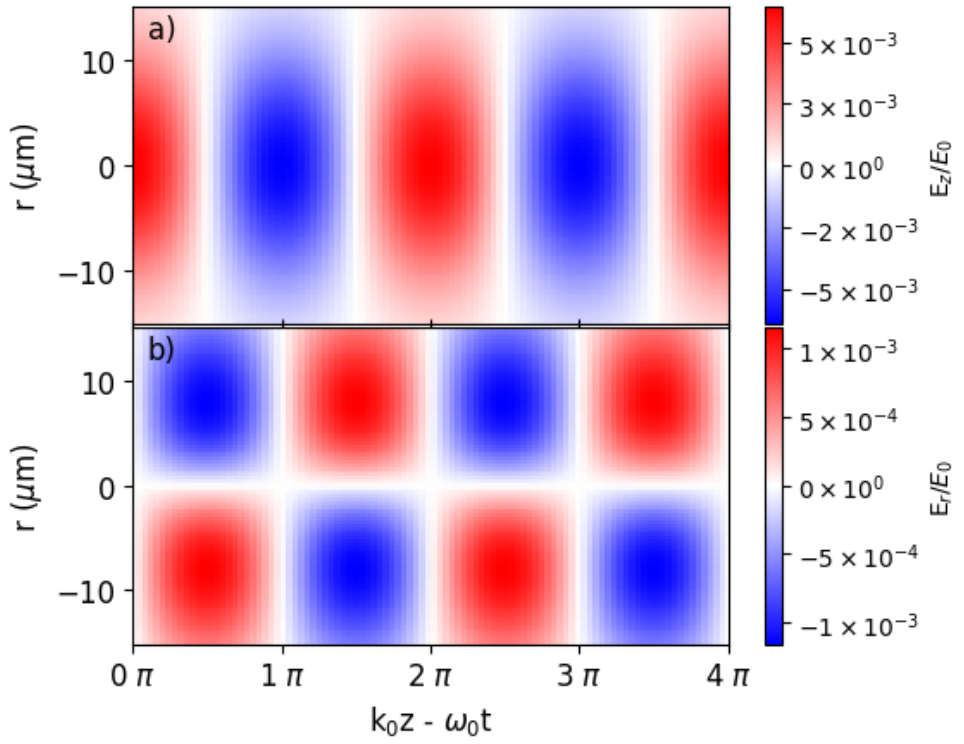

Figure 1.2 – Wake electric fields in the a) longitudinal and b) radial direction calculated from equations 1.72 and 1.73, respectively, for a linear plasma perturbation induced by a laser pulse with $a_0 = 0.2$, $\tau = 38\,\mathrm{fs}$, $w_0 = 16\,\mu\mathrm{m}$ and for an ambient plasma density of $n_e = 5 \times 10^{18}\mathrm{cm}^{-3}$. Longitudinal and radial fields are normalised to the cold wave-breaking electric field, E_0, defined by equation 1.76.

Solving these equations allows us to plot the longitudinal and radial electric fields produced by the density perturbation as shown in Fig. 1.2. Figure 1.2 shows the $\pi/2$ phase shift between the longitudinal and radial fields described by Eqs. 1.72 and 1.73. This phase shift results in four distinct regions of the plasma wake,

Phase	0-$\pi/2$	$\pi/2$ - π	π - $3\pi/2$	$3\pi/2$-2π
Accel./Decel.	Decel.	Accel.	Accel.	Decel.
Foc./Defoc.	Foc.	Foc.	Defoc.	Defoc.

Table 1.2 – Acceleration/deceleration and focusing/defocusing regions of the linear plasma wave as a function of phase.

presented in table 1.2, where accelerating and decelerating regions are $\pi/2$ out of phase with the focusing and defocusing fields.
The ideal phase region for laser wakefield acceleration in Fig. 1.2 is between $\pi/2$ and π modulo 2π where the fields are both accelerating and focusing. From Eq. 1.73 we see that the radial fields are zero on axis where r = 0.

From Eq. 1.72, we see that the longitudinal accelerating field scales $\propto a_0^2$, indicating that the accelerating field scales quadratically with the a_0. However, when $a_0 \approx 1$, our assumptions on small density perturbations and non-relativistic electron energies are no longer valid as the interaction enters the nonlinear regime.

1.4.3 . Nonlinear Plasma Waves

When the quiver momentum of the electrons becomes relativistic, characterised by $a_0 > 1$, driver-induced density perturbations can no longer be assumed to be small, and Eq. 1.71 is no longer valid. Whilst the 3D equations can only be solved numerically, solving the nonlinear dynamics in 1D is possible under some assumptions.

This well-known 1D model of the dynamics of an electron in a plasma wave[3, 43-46] still gives an insight into the nonlinear plasma wave excitation and electron trapping. The presentation of this 1D model is based mainly on that in[45, 46].

The assumptions of the model include a plasma of constant density n_0 in the cold relativistic fluid limit, with immobile ions and a linearly polarized laser pulse with carrier wavelength λ_0, in the quasi-static approximation[47] described by a transverse vector potential $A(\xi = x - v_g t) = a_0 \exp(-\xi^2/\sigma)\cos(\xi)$, where $\sigma = 0.5(L_{\mathrm{FWHM}})^2/\ln 2$ (L_{FWHM} is the laser pulse FWHM duration in field) and v_g is the group velocity of the laser pulse. The electrostatic potential of the wakefield excited by the laser is denoted by Ψ and the longitudinal electric field by $E_z = -\partial_\xi \Psi$. This electrostatic potential can be found by solving numerically the nonlinear differential equation[48-50]

$$\partial_\xi^2 \Psi = \left[\beta_p \left(1 - \frac{(1+A^2)}{\gamma_p^2 (1+\Psi)^2} \right)^{-1/2} - 1 \right], \tag{1.75}$$

where $\gamma_p = (1-\beta_p^2)^{-1/2} = (n_0/n_c)^{-1/2}$ is the Lorentz factor associated to the plasma wave phase/group normalized velocity β_p.

In the linear regime ($a_0 < 1$), Eq. 1.75 becomes the equation of a forced linear oscillator, yielding sinusoidal waves. Departing from the linear regime, the plasma

electron acquires a relativistic velocity and thus increased inertia, changing the electric field wave profile. The period of the plasma oscillations elongates, and the waveform departs from a sinusoid, approaching a triangular wave as a_0 increases. For example, Fig. 1.3 was obtained with $a_0 = 2.15$, and the electric field (blue line) has a waveform which is closer to a triangular wave than to a sinusoidal wave.

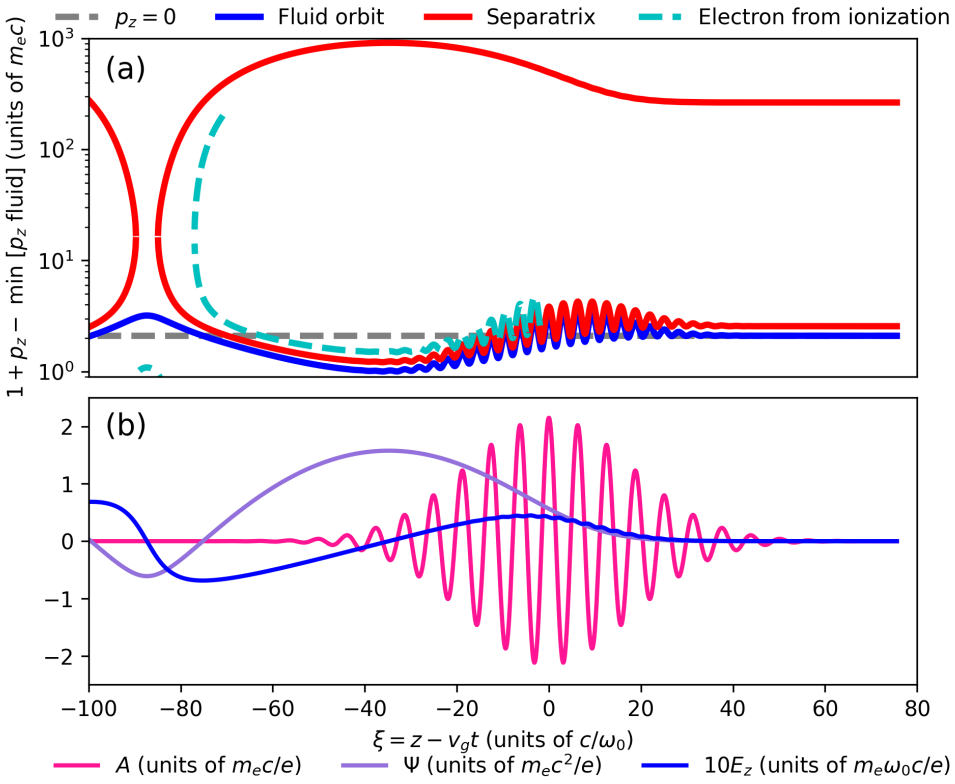

Figure 1.3 – Figure adapted from[46], which was adapted from Figs. 2, 5 of[45]. The laser and plasma parameters used for the Figure are $a_0 = 2.15$, $\tau = 42$fs, and $n_e = 6.7 \times 10^{18}$cm^{-3} corresponding to the Lund Laser Centre laser results presented in chapter 4. a) Displays phase space trajectories of test electrons, including a fluid orbit, the separatrix and the trajectory of an electron stripped from its atom/ion through ionization. (b) illustrates the laser vector potential A, electrostatic potential Ψ and scaled longitudinal electric field E_z.

Increasing a_0 has been shown to lead to a regime termed the "bubble" regime where full cavitation occurs, and the ion cavity is void of electrons[3]. In this regime, a 1D cold fluid model is not sufficient to describe the involved phenomena, and full kinetic numerical techniques like the Particle in Cell (PIC) method[51] are necessary.

1.5 . Electron Dynamics

To accelerate plasma electrons, we must first trap them within the plasma wake. Here we present how electrons are injected into the plasma wave and their resulting acceleration and oscillation dynamics during their propagation with the plasma wave. We then describe the limiting factors to the energy gain of the electrons and how these effects can be mitigated.

1.5.1 . Electron Trapping

The large electric fields of the wake have a phase velocity approaching c. For electrons to become trapped, they require a relativistic velocity along the same axis and be temporally synchronised with the wake. When these conditions are met, and the electrons are injected into the correct phase of the wakefield, the electron becomes trapped and propagates with the plasma wave, driven forward and constrained by the longitudinal and focusing fields, respectively.

Referring to the 1D model of the previous section, once Eq. 1.75 is solved, a Hamiltonian function H can be defined to describe the dynamics of a test electron in this system. Given a value H_0 of the Hamiltonian, the evolution of the test electron momentum for each value of ξ can be found by inverting the expression of H and finding p_x, as shown in[43, 45, 46]. Fig. 1.3 demonstrates the application of the Hamiltonian method for laser and plasma parameters used during the experimental campaign presented laser in chapter 4, namely $a_0 = 2.15$, $\tau = 42\text{fs}$, and $n_e = 6.7 \times 10^{18}\text{cm}^{-3}$. The curves of constant H in the phase space $\xi - p_x$ describe the evolution of the momentum of a test electron and give insightful information on its trapping.

Electrons with low initial longitudinal momentum are not trapped in the plasma wave and perform fluid orbits where their trajectories oscillate with the passing of the plasma wave, as can be seen by the blue line in Fig. 1.3 a). As the plasma wave propagates, electrons with a trajectory bounded by the plasma wave are trapped and accelerated. From Fig. 1.3, it is clear that these electrons must have an initial longitudinal momentum sufficient to be trapped by the wave. The bounding region between trapped and untrapped trajectories is referred to as the separatrix, shown by the red line in Fig. 1.3. This encloses the phase space region where electrons have sufficient momentum, and positions inside of the plasma wave, to avoid phase slippage out of the wave. The cyan curve in Fig. 1.3 is the trajectory of an electron stripped from a partially ionized ion by the intense laser field. From Fig. 1.3 it is clear that this electron slips behind the laser and is accelerated near the end of the first plasma wave bucket. This process of trapping electrons created through ionisation injection will be discussed in section 1.5.1.2.

1.5.1.1 . Self-Injection

At the rear of the cavity, the electron trajectories cross, providing very strong longitudinal electric fields allowing for electrons to be accelerated to the phase

velocity of the cavity and therefore be trapped in the wake. This requires very high laser intensity to provide a large enough charge separation to produce these strong fields for self-injection with full cavitation of the electrons. Self-injection of electrons from the plasma background into the wakefield within the LPI requires high laser intensities to induce wave breaking in the nonlinear regime[3]. The wave-breaking process leading to self-injection of plasma electrons into the plasma wake requires an $a_0 > 4$[52] therefore requiring intense laser pulses from either smaller focal spots, higher laser energies for a given spot size, or shorter pulses. Self-injection reduces the complexity of the plasma source but sets more stringent requirements for the laser system due to the higher a_0 required. The highly nonlinear and often continuous self-injection phenomenon leads to electron beams with high energy spread and high divergence[3]. A sudden increase in the cavity's size, e.g. caused by sudden self-focusing of the laser pulse or a reduction in the plasma density to increase the plasma wavelength, can trigger the injection of some energetic electrons in the right phase of the accelerating field.

1.5.1.2 . Ionisation Injection

We can reduce the required laser intensity for injection, and augment trapped charge, through a process called ionisation injection[53-55]. The ionisation of the innermost electrons from dopant heavier atoms (e.g. nitrogen) occurs only in phase with the peak laser intensity as this provides a sufficient electric field to suppress the ionic binding potential. Comparison to the laser intensity requirements for a gas mixture of hydrogen and nitrogen, shown in table 1.1 indicates that a large intensity gap is present between H^+/N^{1-5+} and the innermost electrons of the nitrogen atoms, $N^{6/7+}$. The background plasma is comprised primarily of light atoms (e.g. hydrogen or helium) ionised at the leading edge of the laser pulse. The intensity gap allows the inner shell electrons to be ionised only at locations with sufficiently high laser intensity. This occurs in phase with the peak of the laser pulse, thus ionising the electrons inside of the ion cavity, contrary to the self-injection process where the electrons traverse the ion cavity before being injected at the rear of the bubble.

Chen *et al.*[53] derived the process of electron trapping with atomic species of separated binding potentials. Whilst his work originally envisioned using a secondary transverse laser to localise the ionisation region (a technique later termed "trojan horse" injection[56]), the idea of using plasma in its mid-charge state was presented in their work. Experimental validation and further generalisation of the theory of ionisation injection in the nonlinear regime was presented by Pak *et al.*[55], and McGuffey *et al.*[54].

From the barrier suppression ionisation process, the electrons are ionised at rest inside the plasma wake and therefore slip towards the rear of the plasma cavity as the laser passes. During this phase slippage, they may gain sufficient energy from the longitudinal electric field of the wake and can be accelerated to the phase velocity of the wake and become trapped. The electrons then continue to gain

energy until the energy gain limitations - outlined in section 1.5.2.1 - are reached.

During ionisation injection schemes, continuous injection of electrons can occur when the laser intensity remains sufficiently high to ionise the inner shell electrons. To mitigate this effect, a process called self-truncated ionisation injection[57] is implemented. This process requires controlling the evolution of self-focusing of the laser within the plasma to localise regions of high intensity. This can be completed through structured plasma density profiles and alteration of the focal position of the laser such that the laser is unmatched to the plasma and is not continually self-focused to intensities beyond the ionisation threshold for the inner shell electrons. Further, as the laser's self-focusing depends on the plasma density, as discussed in section 1.3.3, we can create a plasma structure which allows for the control of the evolution of the laser intensity within the plasma.

1.5.2 . Electron Acceleration

Laser wakefield acceleration transforms a fraction of the transverse electric fields of the laser pulse into longitudinal accelerating and transverse focusing fields of the plasma wake, which is then used for particle acceleration[58]. The process of electron energy gain will be presented alongside the limitations of this and how it can be overcome. During the accelerating process, the electrons quickly become relativistic due to their relatively small mass ($0.511\,\mathrm{MeV}$). Therefore we discuss acceleration in terms of energy and relativistic mass corrections, which are important for the discussion on electron spectrometers in section 2.3.1.

1.5.2.1 . Energy Gain

The longitudinal electric field sustained by the plasma wake is responsible for the energy gain of the injected electrons. Simulation results obtained with a Gaussian driver in an underdense plasma are shown in Fig. 1.4 before electron injection to demonstrate the typical longitudinal electric field structure across the plasma wake in the nonlinear regime. Further details on particle-in-cell simulations are discussed in section 3.3.

The change in relativistic momentum of the electron is linearly proportional to the negative of the electric field (due to the electron's charge state.) We can therefore decompose the ion cavity into regions of acceleration ($E < 0$) and deceleration ($E > 0$). Electrons are typically injected at the back of the wake as discussed in section 1.5.1, meaning that they will experience a strong longitudinal electric field near the electron sheath crossing region when they have sufficient momenta in the longitudinal direction to avoid immediate phase slippage. Due to their small mass, the electrons will be quickly accelerated to relativistic velocities and propagate with the wake gaining energy until the limiting circumstances discussed in the following section (1.5.2.2) are met.

The maximum longitudinal electric field before wavebreaking, which can be used for particle acceleration, is often estimated as a function of the ambient

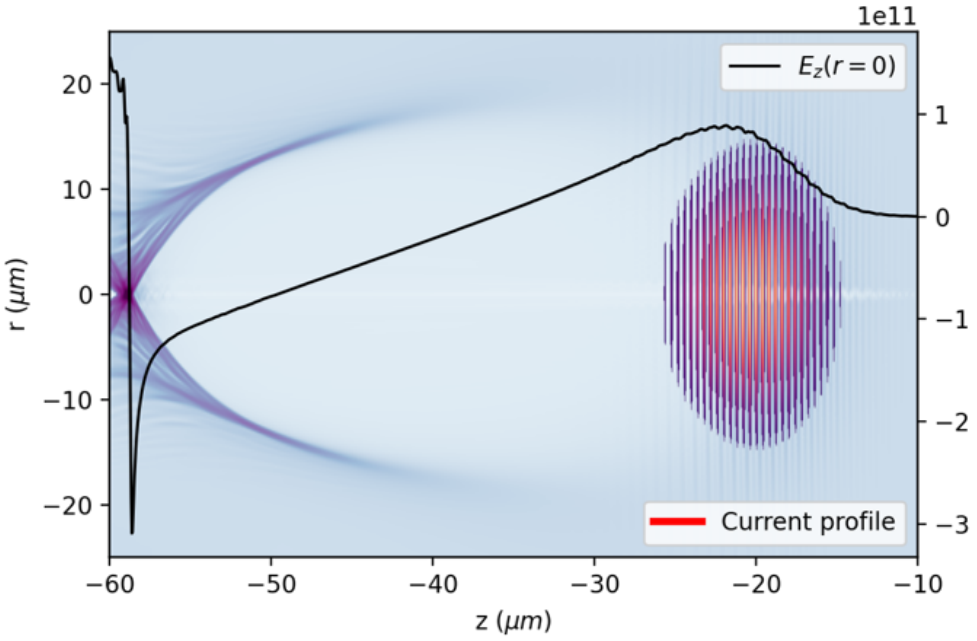

Figure 1.4 – Simulation results show the creation of an ion cavity in the bulk plasma induced by a Gaussian drive laser propagating from left to right with the longitudinal electric field, E_z, in units of $\mathrm{V\,m^{-1}}$. The electron density is displayed in blue, where darker colours indicate higher densities. This snapshot is extracted before electron injection, as shown by the lack of trapped electron current. The longitudinal electric field is illustrated with the solid black line.

plasma density, n_0, through[3, 59]:

$$E_0 = \frac{m_e \omega_p c}{e} \tag{1.76}$$

$$E_0(\mathrm{GV\,m^{-1}}) = 96\sqrt{n_0\,[10^{18}\mathrm{cm^{-3}}]} \tag{1.77}$$

However, more accurate calculations in nonlinear regimes must be carried out with PIC simulations since relativistic and thermal effects can correct this estimation[3].

1.5.2.2 . Limitations and Mitigation

The electron energy gain is limited by three main phenomena: laser driver depletion due to wake generation, diffraction of the laser pulse and dephasing of the accelerated relativistic electrons. Optimising electron energy gain for a given experimental set up requires optimising the experimental parameters to match interaction length to the shortest limiting length, be it dephasing, depletion, or diffraction of the driver.

The dephasing of the electron can be qualitatively understood from Fig. 1.3 b). The group velocity of the laser pulse is sub-luminal due to propagation in the plasma ; therefore, the phase velocity of the plasma wave will also be sub-luminal. A trapped electron with relativistic velocity $v_z \approx c$ will progress with respect to

the co-moving frame of the plasma wave and enter a region in which the sign of the longitudinal electric field changes, which occurs after a one-half period of the plasma wave[3]. The particle is then decelerated. In the linear regime, the distance over which this phase slippage occurs is referred to as the linear dephasing length:

$$L_{dephase} = \frac{\lambda_p}{2(1 - v_{pp}/c)} \,. \tag{1.78}$$

This equation is derived from half the plasma wavelength, $\lambda_p/2$, divided by the relative velocity of the phase velocity of the plasma wave, v_{pp}, and the velocity of an ultra-relativistic electron $v_e \approx c$. From this equation, it is clear that increasing the plasma wavelength or increasing the phase velocity of the plasma wave will increase the length of interaction before dephasing, which can be achieved by reducing the ambient plasma density from equation 1.30. However, a reduction of the plasma density will also limit the energy gain, as seen in equation 1.76.

The phase velocity of the plasma wave in the nonlinear case is given by $v_{ppnl} \approx c[1 - 3\omega_p^2/(2\omega_0^2)]$[40]. In this case, the dephasing length can be calculated as:

$$L_{nldephase} \approx \frac{c}{c - v_{ppnl}} \mathcal{R} \approx \frac{2}{3} \frac{\omega_0^2}{\omega_p^2} \mathcal{R} \,, \tag{1.79}$$

where $\mathcal{R}$ is the radius of the cavity.

Laser pump depletion occurs when the laser energy is deposited into the wake and no longer contains sufficient intensity for continued wake generation. The distance over which this process occurs can be estimated by comparing the etching velocity and the laser's pulse duration. We can further use the equations presented above in section 1.3.4 on laser pulse etching to demonstrate that when etching continues, the laser becomes depleted after a finite amount of time. The etching velocity in the nonlinear regime ($a_0 \geq 1$) was estimated as[34]:

$$v_{etch} \approx c \frac{\omega_p^2}{\omega_0^2} \,, \tag{1.80}$$

from arguments based on the depletion time for the density spike at the leading edge of the laser pulse to deplete the laser's energy fully. In the 3D nonlinear regime the depletion length is given by[40]:

$$L_{depletion} \approx \frac{c}{v_{etch}} c\tau_{FWHM} \approx \frac{\omega_0^2}{\omega_p^2} c\tau_{FWHM} \tag{1.81}$$

where τ_{FWHM} is the pulse duration measured at Full-Width Half-Maximum intensity.

Optimising the energy gain, therefore, requires maximising the interaction length, L_i, to the minimum limiting distance, i.e:

$$L_i = \begin{cases} L_{depletion} & \text{if } L_{depletion} < L_{dephase} \\ L_{dephase}, & \text{otherwise} \end{cases} \tag{1.82}$$

1.5.2.3 . Beam Loading

The electron bunch's space charge field can alter the wave's form and thus the wakefield surrounding the bunch. This leads to changes in the longitudinal electric field of the plasma resulting in an effect termed beam loading[60]. The alteration of the wake structure can limit the injection and acceleration of electrons by locally flattening the wake potential through the bunch charge, compensating for the ion cavity charge. This limits the amount of charge that can be injected but can also reduce the energy spread of the bunch. The superposition of the wakefield and the secondary plasma wave driven by the electron bunch can be used to flatten the accelerating gradient such that electrons in different regions of the bunch experience approximately the same accelerating field, leading to a lower energy spread for an electron bunch with different longitudinal positions and equivalent energies[61].

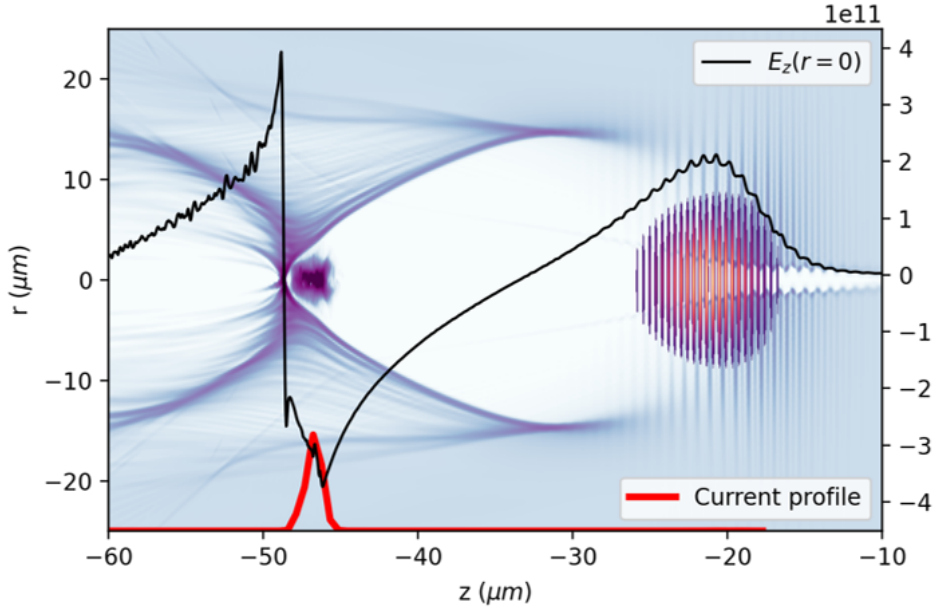

Figure 1.5 – Transverse slice of laser wakefield acceleration with Gaussian laser driver simulation performed in particle in cell code FBPIC. The injected electron current profile and longitudinal electric field are displayed with solid red and black lines, respectively.

It can be seen from Fig. 1.5 that the beam-loading effect is not well optimised as the differences in the accelerating gradient in different parts of the beam result in a stronger acceleration at the front than the back of the electron bunch. Electron bunches in LWFA from self-injection are typically negatively chirped in energy (i.e. electrons at the longitudinal rear of the bunch have lower energy than the head of the bunch) due to injection occurring at the rear of the bunch before the electrons move forward in the cavity region due to the subluminal velocity of the plasma wave. This means that the beam loading demonstrated here will lead to a growth

of energy spread where the front of the bunch with already higher energies continue to increase their energy faster than the rear of the bunch.

1.5.2.4 . Transverse Dynamics

During the acceleration of electrons within the plasma cavity, the strong transverse fields act on the electron bunch similarly to an undulator in a free-electron laser, creating betatron radiation[62].

Similar to the decomposition of the ion cavity in accelerating and decelerating regions in section 1.5.2.1, regions of focusing and defocusing fields are also present and defined similarly for $E_\perp < 0$ and $E_\perp > 0$ respectively. In equation 1.78, we considered only the accelerating portion of the longitudinal field. However, there is only a quarter of the total ion cavity volume where the electric fields of the plasma wave are both accelerating *and* focusing.

1.6 . Laser-Plasma Electron Sources: State-of-the-Art

After the conception of laser wakefield acceleration in 1979[1], the first results of peaked distribution electron beams - in contrast to the Maxwellian distributions achieved in the interim - the so-called "dream beams", arrived in the early 2000s[63-65]. The demonstration that LWFA could be used to create peaked electron spectra indicated that the fascinating physical interaction of laser and plasma could also produce electron spectra with desirable properties. The following two decades of research have refined our theory, experimental, and simulation capabilities to produce LWFA sources capable of high energy[16, 66], high charge[17, 18], low energy spread[19] and high repetition rate[67, 68] electron sources. However, achieving all of these parameters simultaneously remains a challenge and requires an improved understanding of the nonlinear physical processes during the electron injection and acceleration and novel techniques for electron parameter control to reach comparable bunch properties of current radio-frequency (RF) accelerator technology.

In this section, we describe the state-of-the-art research in LWFA that has been completed by many groups worldwide. Many groups are actively targeting solutions to these problems through various approaches, including advanced control of the laser and plasma parameters and their resulting interaction and understanding of the physical processes which control the electron dynamics, multi-staging of all optical systems, multi-sectioned gas targets or laser-plasma to particle-plasma hybrid accelerators and novel injection mechanisms for example.

The use of machine learning (ML) for optimisation and prediction of accelerator parameters has begun to be implemented in laser-plasma experiments and is discussed in detail in sections 3.1.3.4 and 3.1.1 respectively.

A proposed method for improving the stability and control of electron parameters is the separation of the injection and accelerating regimes. EuPRAXIA targets

two classes of laser-plasma injectors (LPIs): a 'low energy' injector capable of producing electron bunches with energy of $150\,\mathrm{MeV}$, and a 'high energy' injector with a bunch energy of $1\,\mathrm{GeV}$ both with $30\,\mathrm{pC}$ of charge and energy spread $\leq$5%[20].

1.6.1 . Laser Plasma Injectors for Multi-Stage Acceleration

Separation of the injection and acceleration dynamics has been simulated[69] and implemented[70] by spatially constraining the gas mixtures. Using the ionisation injection method, the first region consists of a low-Z gas doped with high-Z atoms and a second region of pure low-z gas to act as an accelerator stage for the electrons. Further injection is reduced in the second compartment by the high a_0 requirement of self-injection. Laser-wakefield accelerated electrons have been injected into a second region where the laser is extracted, and the particle bunch acts as the drive beam[71-73]. As the particle driver traverses the plasma at approximately luminal velocity, issues with dephasing are mitigated for a trailing witness bunch which experiences the wake driven by the particle driver.

Injection of relativistic electrons into a secondary accelerating stage is challenging due to the plasma wave scales being on the order of 10s of $\mu\mathrm{m}$ and the strong focusing forces of the plasma wave leading to high divergence of the beams between the stages[74]. An energy gain of $100\,\mathrm{MeV}$ in a second stage has been demonstrated in 2016[75], however the energy spread induced by the chromaticity of the electron bunch leads to energy spreads $> 60\%$. Methods for reducing the energy spread and improving the coupling between the stages have been suggested by rotating the phase space of the electron bunches using a magnetic chicane[76]. An initially negatively chirped electron bunch will then be positively chirped as it enters the second stage, which compensates for the energy chirp.

1.6.2 . Laser Spatial and Temporal Manipulation

The assumption of a Gaussian laser driver - in terms of both temporal duration and spatial intensity - is typically taken in LWFA experiments and simulations. This allows for simplification of the interaction dynamics to understand experimental results and a speed-up in simulations by reducing the number of angular modes required to describe the laser pulse and, therefore, the required resolution of the simulation. Recent experimental work in gas jets has uncovered the effects of beam halo[77] and non-Gaussian laser profile[78] at low and intermediate laser intensity, respectively, on the LPI electrons. Including non-Gaussian laser properties in simulations requires the implementation of realistic intensity and phase maps of the laser pulse. This was achieved in the cited work by Ferri *et al.*[78] by imaging the laser at focus, and $5\,\mathrm{mm}$ after, on each shot and using the Gerchberg-Saxton algorithm[79] (GSA) (a modification of this method is discussed in further detail in section 3.2.1) for the phase retrieval from the two fluence images. Accounting for the realistic phase evolution of the laser improved the retrieval of the achieved normalised photon number within the error of the experimental measurements, indicating that including realistic laser parameters can improve the accuracy of the

simulated results.

In their work, verification of the phase retrieval efficacy was limited to comparing the output of simulated results as only two images were taken in the focal volume. Both were used for the GSA algorithm for intensity-phase retrieval, meaning that they could not be propagated to check for the efficacy of the retrieval. In this work, we present the GSA algorithm applied to fluence images of the laser focal volume to describe the complex amplitude of the laser at different wavefront phase settings controlled by a deformable mirror. Simulated results for the electron parameters agree with the experimental measurements when realistic laser parameters are included.

Similarly, control of the laser spatial phase leads to improvements in electron dynamics. The first documented application of spatial phase control on the acceleration dynamics of electrons was performed by He *et al.*[80] who used a genetic algorithm to improve electron beam charge density through alteration of adaptive optic piston control. They found through their work that the laser phase profile, which produced the densest electron spectra, was not simply the pulse with the highest symmetry through the focal volume but was far from the perfect Gaussian intensity distribution. Control of the spectral phase (discussed further in section 2.1.1.4) of the driving laser pulse allows for alterations in the temporal duration of the laser pulse and the spectral chirp. Previous work has demonstrated that the temporal rise gradient of the laser pulse plays a stronger role than the alteration in the temporal duration arising from the addition of chirp[81].

The first application of Bayesian optimisation to LWFA by Shalloo *et al.*[81] (discussed in detail in section 3.1.3.4) altered the spatial phase of the laser using a deformable mirror to control the position of the laser focus within the plasma. These results indicated possible control of the electron bunch dynamics by altering the spatial phase of the drive laser described experimentally and in simulations in section 4.1.3.3.

1.6.3 . Development of Secondary Radiation Sources

While relativistic electrons can be used directly in QED experiments, future lepton colliders, etc., their secondary radiation, produced during their acceleration, and particles/radiation created through their interaction with solid matter, can provide further useful radiation sources.

Due to the strong transverse wakefields described in section 1.5.2.4, the electrons inherently produce X-ray radiation during the acceleration process. This radiation duration is on the order of the bunch size leading to fs x-ray pulse duration. Laser wakefield accelerators have been used to perform imaging of car fuel injector nozzles[82] via tomography using the betatron radiation, studies on future use for radiotherapy[83], and 3D imaging of human bones to demonstrate the capabilities of medical imaging applications[84].

Interaction of an ultra-relativistic electron bunch with high-Z material has been

demonstrated to create positrons through the resulting radiation cascade induced by γ-rays from inverse Compton scattering of the electron bunch with the atomic nuclei[85]. These positrons have energies and divergence associated with the parent electron bunch energy and divergence, respectively[15].

In this thesis in chapter 4, we examine the mechanisms resulting in electron bunch deflection from the laser axis: an understudied but essential parameter for multistage acceleration[86] or high-intensity QED experiments requiring precise electron bunch and secondary laser pulse alignment[7, 8].

1.6.4 . High Energy Electron Sources

Production of electron bunches at the multi-GeV-scale in a single accelerator stage has been experimentally achieved. $7.8\mathrm{GeV}$[16] electron bunches with total charges of hundreds pC and peak charges of tens pC, were created using external guiding in a $20\mathrm{cm}$ plasma capillary for a $0.85\mathrm{PW}$ peak laser power. The laser pulse was guided in the plasma channel using a dual laser set-up. An initial long-pulse laser heated a discharge-induced pre-formed plasma inside the capillary, creating a region of low plasma density on-axis through the hydrodynamic expansion of the plasma. This acted as a waveguide for a secondary short-pulse laser to perform laser wakefield acceleration. This dense guiding structure allowed for the long propagation distance of the laser pulse whilst reducing the on-axis plasma density. This allowed for an increase in the electron dephasing length whilst also increasing the depletion length by guiding the laser pulse.

Using nanoparticle injection, where a secondary laser ablates a metal target creating small particles within the gas mixture to increase the injected charge, leads to the production of multi-nC total charges and electron energies up to $10\,\mathrm{GeV}$[66] at laser powers of $0.75\mathrm{PW}$. In their scheme, they also show that it is possible for accelerated electrons to gain energy from direct laser acceleration in the region close to the laser pulse, where typically, the electrons are decelerated by the longitudinal electric field.

Work by Lu *et al.*[40] uncovered phenomenological scaling laws for the energy gain of electrons accelerated in the bubble regime related to the laser power and plasma density as:

$$\Delta E[\mathrm{GeV}] \simeq 1.7\left(\frac{P[\mathrm{TW}]}{100}\right)^{1/3}\left(\frac{10^{18}}{n_e[\mathrm{cm}^{-3}]}\right)^{2/3}\left(\frac{0.8}{\lambda_0[\mu\mathrm{m}]}\right)^{4/3}. \tag{1.83}$$

We can therefore see that reaching high electron energies in a single accelerator stage requires very large powers. For example, energy gain for a PW-class laser operating at a plasma density of $1\times10^{18}\mathrm{cm}^{-3}$ and a central wavelength of $800\mathrm{nm}$ would provide a theoretical electron energy gain of $3.7\,\mathrm{GeV}$.

Increasing the spot size is also known to increase the amount of total injected charge by increasing the injection volume[87]. Operating with longer focal lengths to increase the transverse spot size at focus reduces the peak intensity for a given

pulse energy, as seen from Eq. 1.22. It therefore requires increased peak powers to compensate for the larger focal spot.

As stated in section 1.5.2.1, the dephasing and depletion lengths of the electron-laser-plasma interaction limit electron energy gain. We can increase these length scales through the reduction in the plasma density (equations 1.78 and 1.81). However, this will also reduce the accelerating fields' energy gain per unit distance (as in equation 1.76). To increase the energy of the electrons we therefore require that the interaction length be increased, which can be achieved through increasing the focal length of the final optic. Neglecting the effects of self-focusing, which can further contain the laser, the unguided interaction length, L_{ug}, is related to the Rayleigh length by a factor π, and therefore the F-number of the focusing optic by:

$$L_{ug} = Z_r \pi = F^2 \lambda_0 \,, \tag{1.84}$$

where $F = f/D$ is the F-number of the focusing optic, f the focal length, and D the beam aperture diameter. From Eq. 1.84, we can see that even without self-focusing or external guiding, the interaction length scales favourably with the F-number.

In this work, we present the development of a high-energy electron source at Apollon. Using f $= 3$ and 9 m spherical mirror focal lengths, we explore the stability of the laser system and its effect on the production of high-quality electron beams. Energies up to $1.8\,\mathrm{GeV}$, with low energy spread, are produced without external guiding using the f$= 9$ m spherical mirror with an F-number of 75 (for a beam aperture of $120\mathrm{mm}$). Since we rely solely on the self-focusing mechanisms (discussed above in section 1.3.3), only regions of the laser above the critical power threshold will have sufficient a_0 for longer than a few Z_r, reducing the depletion length of the laser driver. Therefore, this peak-power limitation on the laser system requires custom-built laser systems in the PW regime to provide high electron energy gain in the unguided regime.

Whilst longer focal lengths lead to larger focal spots and therefore a more diffuse transverse energy distribution, the available pulse energy at Apollon allows for the focal spot to contain ample energy for the production of plasma wakes and perform electron acceleration over cm-scale plasmas. The effect of the focal length on the energy of the electron spectra is presented in chapter 5.

2 - Experimental Instruments: Lasers, Plasma Devices and Electron Detectors

Accurate control and measurement of the lasers and plasma sources used to study laser wakefield acceleration of electrons require precise and reliable diagnostics. In this chapter, we present the main instruments and techniques used during this thesis. The layout and operation of high peak-power laser systems, specifically the Lund Laser Centre Terawatt Laser and the Apollon Laser System used during this work, and their associated diagnostics for characterising laser pulses, are presented. A novel method for characterising the rotational symmetry of a focal spot is also presented. The ELectron Injector for compact Staged high energy Accelerator (ELISA) gas cell, used throughout experiments during this thesis, and its characteristics, are described. Methods for measuring the plasma density within the gas cell, an important parameter for tuning the non-linear interaction between the laser and plasma for an LPI, are discussed, including the development of a self-referenced wavefront sensor-based plasma density measurement. A method using a fast camera applied to a Mach-Zehnder interferometer to measure temporal filling rates of the gas cell is described. Finally, the general implementation of dipole-based electron spectrometers and their imaging systems are discussed.

2.1 . Laser Systems

The availability of laser systems with short duration and high-peak power initially limited the study of laser wakefield acceleration physics, proposed by Tajima and Dawson[1], due to laser pulse duration being significantly longer than the plasma period. Today, laser systems capable of driving laser-plasma acceleration in the non-linear regime are available 'off-the-shelf'[88, 89] due to the advances in both laser technology and diagnostics. We present in this section the major characteristic components (CPA, OPCPA) and systems of high peak-power laser and techniques used to achieve high-quality focal spots due to spectral and wavefront corrections (AO-PDFs, adaptive optics). The layout of the lasers used during the work of this thesis and the differences between these systems are presented.

2.1.1 . Overview of Major Components

2.1.1.1 . Chirped-Pulse Amplification

Chirped-Pulse Amplification (CPA)[90, 91] allows for the production of high-intensity laser pulses through the amplification of a stretched pulse before re-compression. Amplification of the stretched pulse allows for the pulse energy to be amplified whilst keeping the peak power below the critical power defined by Eq. 1.60 for a given amplifier aperture. When this condition is not met, the laser can self-focus within the amplifier medium causing damage to the crystal [25] and lowering the quality of the focal spot due to filamentation [92]. In addition, to avoid self-focusing and amplifier damage, the effect of the pulse intensity is related to the non-linear phase shift through the B-integral defined as[93]:

$$B = \frac{2\pi}{\lambda} \int \eta_2 I(z)\, dz \tag{2.1}$$

where λ, η_2, $I(z)$ are the central laser wavelength, the non-linear refractive index of the amplification medium and pulse intensity, respectively. The reduction in intensity through pulse stretching reduces the B-integral and correspondingly the influence of non-linear phase shift on the pulse, which would otherwise degrade the pulse compression through increased phase shift in regions of the pulse with higher intensity.

Figure 2.1 illustrates a simplified layout of a typical CPA system. An initially short pulse is extracted from a mode-locked oscillator[26]. In the original CPA proposition, the pulse was then stretched using single-mode fibres to linearly chirp the pulse. This utilised the group delay dispersion arising from the chromatic dispersion of the medium, and the self-phase modulation due to the optical Kerr effect[25] where the short pulse intensity produces a modulation of the non-linear refractive index[90]. Modern systems typically use a stretcher-compressor pair, as shown in Fig. 2.1, where the initial stretcher has positive dispersion to impart a longer path length for the higher frequency light, and an inversely matched negative dispersion for the compressor to recompress the pulse after amplification. Note that the

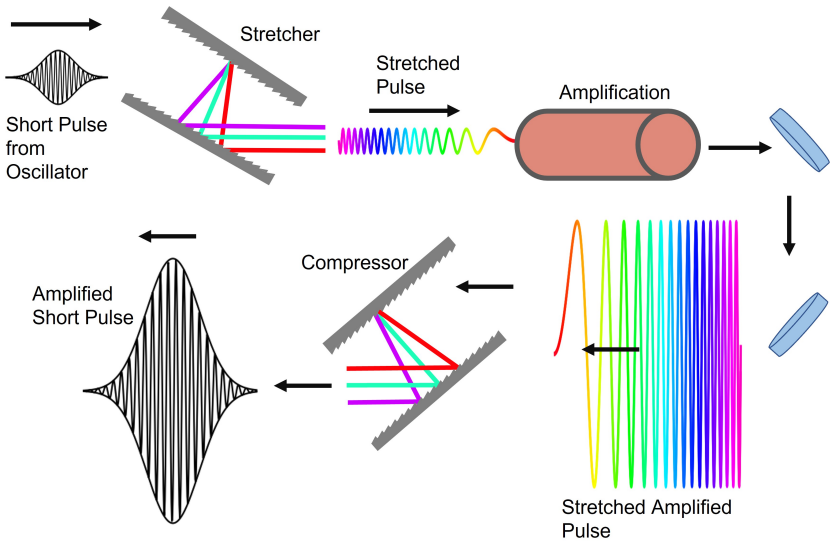

Figure 2.1 – Illustration of the process of chirped pulse amplification. A short pulse enters from the top left into a stretcher where positive dispersion results in a strongly positively chirped pulse elongating the pulse. This pulse is then amplified before being recompressed in the compressor with an inverted dispersion from the stretcher. Note that the amplification and stretching ratios are not to scale, and the pulse envelope of the stretched pulses has been omitted for clarity.

telescopic imaging set-up required for the stretcher to provide positive dispersion has been omitted for clarity. The stretcher provides up to five orders of magnitude increase in the pulse length from the fs to ns scale allowing for the intensity to be significantly reduced[26]. The pulse is strongly positively chirped (lower frequencies at front of pulse) on the exit of the stretcher. The magnitude of compression and energy gain is reduced for clarity in Fig. 2.1. After amplification and compression, the peak intensity of the output pulse is up to 10^6 times greater than at input to the CPA system.

The choice of compressor configuration will affect the laser system's achievable pulse energy and repetition rate. Compressors require both high spectral bandwidth and high damage threshold to be capable of compressing the amplified pulse. The damage threshold of gold-based compressor gratings is $0.25\mathrm{J cm}^{-2}$ meaning that, for example, for next generation $10\,\mathrm{PW}$ laser systems, gratings on the order of $1\,\mathrm{m}$ are required, leading to high costs and stringent manufacturing requirements. The gratings must also be sufficiently large that no spectral clipping occurs which would increase the pulse duration due to the reduced spectral bandwidth.

2.1.1.2 . Optical Parametric Chirped-Pulse Amplification

Optical Parametric Chirped-Pulse Amplification (OPCPA) uses the stretched pulses of a CPA system to improve the efficiency and pump simplicity of an optical parametric amplifier. Optical parametric amplification (OPA) uses two-photon

input with pump and signal frequencies ω_{pump} and ω_s respectively, into a non-linear crystal. The pump energy is then converted into the much weaker signal pulse whilst also producing a lower frequency photon, ω_i, as illustrated in Fig. 2.2 through parametric amplification.

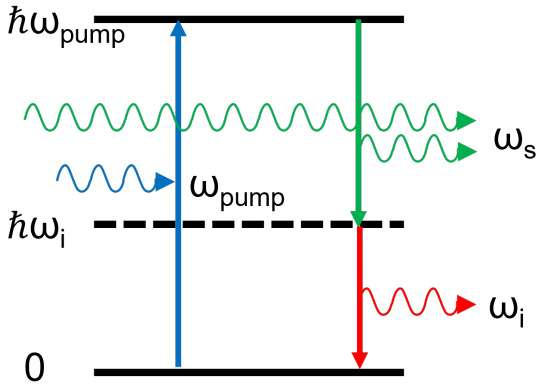

Figure 2.2 – Illustration of the process of optical parametric amplification in a nonlinear crystal. Pump photon (ω_{pump}), signal photon (ω_s), and idler photon (ω_i) are displayed in blue, green and red, respectively. Ground and excited state and denoted by solid horizontal lines for $\hbar\omega_{pump}$ and 0.

This method is beneficial to employ as a front end of the laser system to increase the contrast and quality of the pulse temporal envelope[94] due to the non-linear amplification process and the high bandwidth that can be achieved with OPCPA, respectively. The non-linear amplification process improves the pulse contrast as the gain process is constrained to the short time over which pump and signal pulses interact in the crystal[25]. Combining OPA with CPA stretches the input pulses for the parametric amplification and allows them to be pumped with ns-scale pumps. This increases the amount of pump energy, and therefore amplification of the input pulse, that can be achieved[95].

2.1.1.3 . Adaptive Optics

Adaptive Optics (AO), or deformable mirrors, allow for the control of the laser wavefront by changes in the mirror curvature that is modified through actuator control of the mirror sub-structure. A general layout for an adaptive optic system for wavefront correction is illustrated in Fig. 2.3. This allows for aberrations, induced by the optical system, thermal loading on the optical components and gratings[96], air turbulence[97], etc. to be corrected, producing higher quality focal spots and resulting in a larger partition of the pulse energy contained within the central spot. This subsequently has been shown to lead to more efficient wakefield generation for a given pulse energy by reducing the loss of energy surrounding the focal spot during the interaction[98].

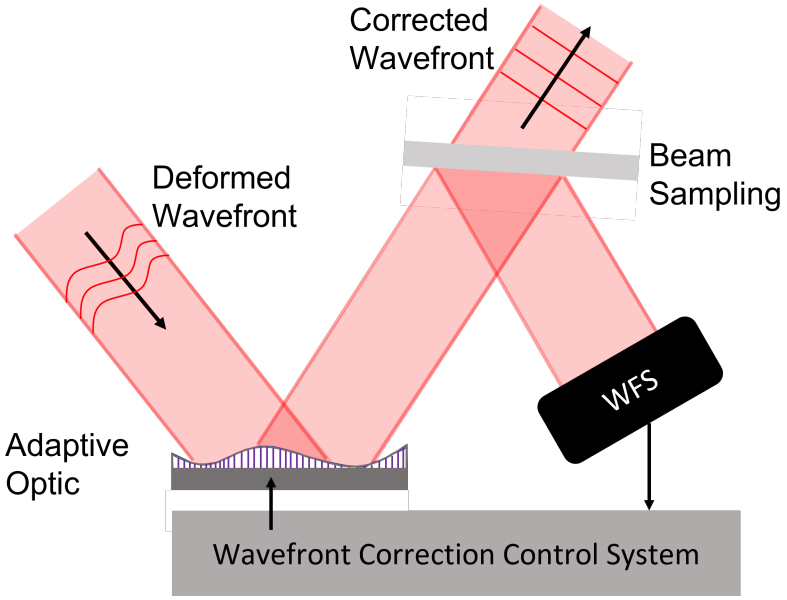

Figure 2.3 – Overview of a typical adaptive optic set-up. A pulse with a deformed wavefront enters from the top left onto the adaptive optic. The mirror curvature is altered with the pistons displayed as small purple lines.

Figure 2.3 illustrates the typical functioning of a closed-loop wavefront correction set-up. A pulse with a deformed wavefront enters from the top-left and reflects from the adaptive optic. The surface of the adaptive optic is a membrane whose curvature is controlled by voltage-actuated pistons. The reflected beam is then sampled and the wavefront is measured by a wavefront sensor (discussed further in section 2.2.3). The required wavefront correction is then calculated by the control software and the corresponding pistons actuated. The pulse with a corrected wavefront then propagates further down the laser chain or towards the interaction point.

Typically, the deformations in the focal spot can be described using the Zernike polynomials basis[99]. These are a complete basis of orthogonal functions over the unit disk which is therefore well suited to describe focal spots in the transverse plane due to their typically circular nature. Similar to the way Fourier series expansion provides an orthogonal basis for periodic functions, the Zernike polynomials can be used to describe a smooth phase map, G, such that[100]:

$$G(r,\theta) = \sum_{m,n} \left[a_{m,n} Z_n^m(r,\theta) + b_{m,n} Z_n^{-m}(r,\theta) \right] , \tag{2.2}$$

where a and b are scaling coefficients, and n and m are the radial order and angular order numbers, respectively, and Z the corresponding Zernike polynomial retrieved from the recursion relation in Cartesian coordinates as:

$$Z_n^m(x,y) = \sum_{i=0}^{q} \sum_{j=0}^{M} \sum_{k=0}^{M-J} (-1)^{i+j} \binom{n-2M}{2i+p} \binom{M-j}{k} \times \frac{(n-j)!}{j!(M-j)!(n-M-j)!} x^{\xi} y^{\eta}\,, \tag{2.3}$$

where:

$$M = \frac{n}{2} - |m - \frac{n}{2}|\,, \qquad p = \frac{|s|}{2}(s+1)\,, \qquad s = sgn(d)\,,$$
$$d = n - 2m\,, \qquad q = (d - s \times Mod[n,2])\,\frac{s}{2}\,, \qquad \xi = 2(i+k) + p\,,$$
$$\eta = 2(i+j+k) - p\,.$$

In this expression the Mod is the modulo operator and $sgn()$ operation finds the sign of a real number defined as $s(x) = 1$, for $x > 1$; $s(x) = 0$, for $x = 0$; $s(x) = -1$, for $x < 1$. The two vector notation terms inside the brackets are binomial coefficients where $\binom{h}{f} = \frac{h!}{f!(h-f)!}$.

From Eq. 2.3 we can calculate the first five non-zero Zernike polynomials in Cartesian coordinates to describe tip/tilt ($n = 1, m = \pm 1$) and astigmatism/defocus ($n = 2, m = 0, \pm 2$) to illustrate how higher order Zernike polynomials describe increasingly complex wavefront deformations. The Cartesian representation of the Zernike polynomials over the unit disk is illustrated alongside their equations and Zernike notation in table 2.1. The Cartesian equation is plotted over the unit circle to produce the Cartesian representation of the corresponding Zernike polynomial. We omit bias ($n = 0, m = 0$) in table 2.1 as it is the simple DC component of the wavefront description, which acts to shift the focal plane of the laser.

Calculation of the relative coefficients of each mode then allows for the inverse distortion on the phase to be applied using the adaptive optic resulting in an improved focal spot. During the laser wavefront correction illustrated in Fig. 2.3 the phase map of the wavefront is extracted using the wavefront sensor. The coefficients of the Zernike polynomials are then calculated from the wavefront map, commonly completed with a least squares fit, and the pistons controlling the adaptive optic used to remove these aberrations. Due to non-ideal piston motion (i.e. hysteresis effects) and a finite number of pistons, the process is completed in a loop to converge on the flattest wavefront possible for the measurement and control set-up.

2.1.1.4 . Spectral Phase: Acousto-Optic Programmable Dispersive Filters

The spectral phase describes the relative phases of the frequencies composing a short-pulse laser. A spectral description of a short pulse laser is given by equation 1.27. We introduce a frequency-dependent refractive index $\eta(\omega)$ which will

Descriptor	Z_n^m	Cartesian Equation	Cartesian Representation
Tip	Z_1^{-1}	x	
Tilt	Z_1^1	y	
Astigmatism	Z_2^{-2}	2xy	
Astigmatism	Z_2^2	-x^2 + y^2	
Defocus	Z_2^0	1 - 2x^2+2y^2	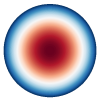

Table 2.1 – Zernike polynomials and their corresponding Cartesian representations. All Cartesian representations are scaled between [-1,1] and illustrated with red to blue respectively.

induce a spectrally dependent phase shift, termed the spectral phase[26]:

$$\phi(\omega, z) = \omega\, \eta(\omega)\, \frac{z}{c}\,, \tag{2.4}$$

for propagation in the homogeneous medium for a distance of z. As full experimental spectral phase functions are typically not tractable, we expand equation 2.4 as a Taylor series to examine the effects of the lower order terms on the laser pulse.

$$\begin{aligned}\phi(\omega, z) = \phi(\omega_0, z) + \left.\frac{d\phi(\omega, z)}{d\omega}\right|_{\omega_0} \cdot (\omega - \omega_0) + \frac{1}{2}\left.\frac{d^2\phi(\omega, z)}{d\omega^2}\right|_{\omega_0} \cdot (\omega - \omega_0)^2 \\ + \frac{1}{6}\left.\frac{d^3\phi(\omega, z)}{d\omega^3}\right|_{\omega_0} \cdot (\omega - \omega_0)^3 + \frac{1}{24}\left.\frac{d^4\phi(\omega, z)}{d\omega^4}\right|_{\omega_0} \cdot (\omega - \omega_0)^4 + \ldots\end{aligned} \tag{2.5}$$

The derivatives in the above equation are typically termed Group Delay (GD), Group Delay Dispersion (GDD), Third Order Dispersion (TOD) and Fourth Order Dispersion (FOD) for the first, second, third and fourth order derivative terms above, respectively. As we are interested in parameters which change the laser-plasma interaction, we can neglect the GD from our discussion as it introduces a constant shift for all frequencies resulting in only a temporal shift of the laser pulse whilst the frequency spectrum remains unchanged.

Following the derivation of the effects of the group delay dispersion (GDD) on an arbitrary Gaussian short pulse laser by Borzsonyi *et al.*[26], we illustrate the effect of GDD on a short pulse laser and the resulting chirp in Fig. 2.4.

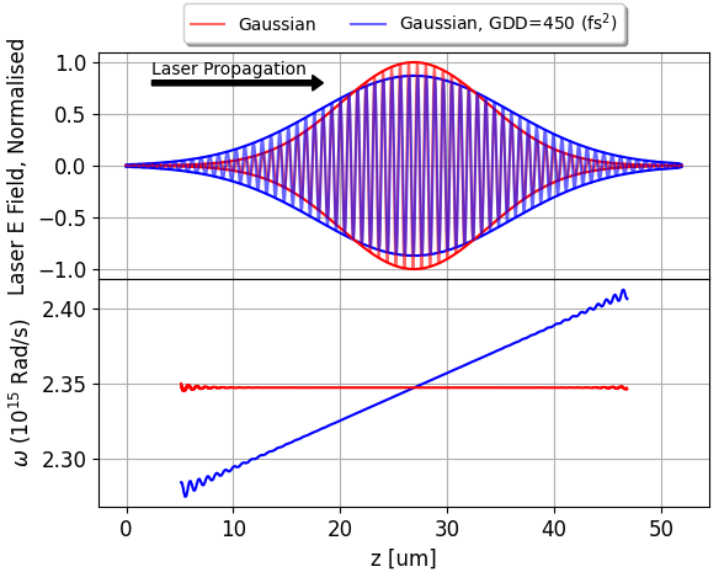

Figure 2.4 – Comparison between a chirped (blue) and unchirped (red) laser pulse with their temporally dependent dominant frequency (instantaneous frequencies), below for a $38\,\mathrm{fs}$ pulse duration and a central frequency of $2.35 \times 10^{15}\ \mathrm{rad\,s^{-1}} (800\,\mathrm{nm})$. The oscillating electric field and envelope are displayed for both pulses. The pulse moves from left to right.

Figure 2.4 shows the effect of introducing GDD into the laser pulse. In this case, the GDD is > 1, leading to a spectrally negatively linearly-chirped[101] laser pulse, where the blue light is at the front of the pulse. The oscillations at the end of the instantaneous frequency plots arise from the comparatively small oscillation amplitude of the laser envelope and are, therefore, numerical artefacts. It is clear from the comparison between the chirped and unchirped laser fields that the introduction of a chirp reduces the peak electric field, correspondingly the experimental interaction intensity, due to the spreading of the spectral energy in time from energy conservation. This is related to the initial pulse duration and GDD for

a laser pulse with a Gaussian temporal profile through[26]:

$$E^* = E_0 \frac{\tau_0}{\sqrt[4]{\tau_0^4 + (4\ln(2)\cdot GDD)^2}}, \tag{2.6}$$

where E_0 and E^* are the original and re-scaled peak envelope electric fields, respectively. For the example in Fig. 2.4 with a pulse duration $\tau_0 = 38\,\mathrm{fs}$ and a GDD of 450 fs^2, this corresponds to a reduction in the peak electric field of 15%. From Fig. 2.4, it is also clear that there is an increase in the pulse duration due to the linear chirp, which can be described by[26]:

$$\tau^* = \tau_0 \sqrt{1 + \left(\frac{4\ln(2)\cdot GDD}{\tau_0^2}\right)^2}; \tag{2.7}$$

for the above example, the pulse is stretched to $50\,\mathrm{fs}$. The above scaling also indicates that the percentage change in pulse characteristics from the addition of GDD is pulse duration dependent, indicating that shorter pulses will be more strongly altered (in terms of peak electric field and pulse duration) for a given value of GDD.

The spectral phase of the laser pulse is modified through an acoustic-optic programmable dispersive filter (AO-PDF). We have limited the expansion to the fourth order derivative in Eq. 2.5 as this is typically the limit of the spectral phase control from an AO-PDF. In the experiments in chapters 4 and 5 a Fastlite DAZZLER[102] brand AO-PDF was used. The principle of using acoustic waves with crystal birefringence properties for controlling the spectral phase of pulsed lasers was developed by P. Tournois[103]. Paratellurite crystals are used in AO-PDFs operating on laser pulses in the visible to the near-infrared range, such as the titanium:sapphire amplified lasers used in the majority of high peak power, short pulse lasers. AO-PDFs are typically used post-oscillator to pre-compensate the spectral dispersion associated with the amplification chain. This allows for the pulse dispersion at the output of the oscillator to be recovered at the exit of the amplification chain before compression[103] leading to an optimally temporally compressed pulse.

Figure 2.5 demonstrates the principle of operation of an AO-PDF for pulse shaping. The input pulse enters through the left where the laser polarisation is aligned to a principal axis of the bulk crystal[25]. In the absence of acoustic waves, the pulse will propagate through the crystal and be blocked by the polarisation filter set on the perpendicular axis. An acoustic transducer creates acoustic waves within the bulk crystal. These waves locally stress the crystal allowing mixing between the input and orthogonal polarisation axis, which alter the refractive index in a frequency-dependent manner, leading to a description which is applicable with Eqs. 2.4 and 2.5. The form of this acoustic wave is a superposition of different frequencies producing a time-varying waveform allowing for a propagating short pulse to be shaped. Modification of the temporal phase in comparison to the case

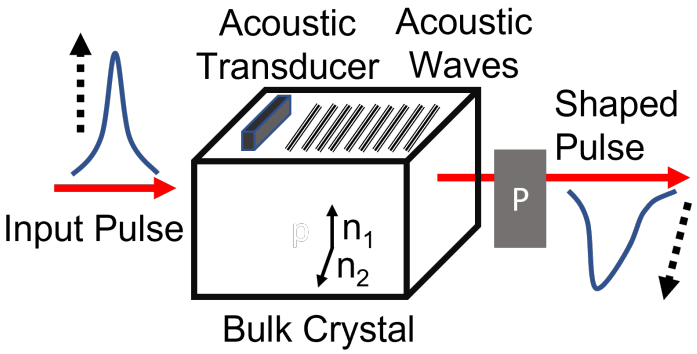

Figure 2.5 – Layout of a typical an acoustic-optic programmable dispersive filter set-up in a collinear geometry. An input pulse enters from the left, polarised along one of the principal axes of the birefringent crystal. An acoustic transducer converts radio-frequency waveforms into acoustic waves in the crystal. The polarization plate, denoted by "P", allows only polarised light in the n_2 axis. The shaped output pulse then exits to the right.

for optimum compression allows for control over the pulse duration, pulse envelope, and chirp of the laser pulse. The laser pulse can be imparted with a chirp, or a more complex higher-order phase function with TOD and FOD, leading to altered interaction between the laser and the plasma. For example, the chirped pulse in Fig. 2.4 would lead to the initial interaction between the laser and plasma of a higher frequency light with a shallower intensity gradient than in the unchirped case.

2.1.2 . Lund Laser Centre: Terawatt Laser System

The Lund Laser Centre High Power Laser located at the University of Lund, is a titanium:sapphire-based laser system utilising CPA[104]. Four amplification stages provide an at-focus energy of $\approx 1\,\mathrm{J}$ with a pulse duration of $38\,\mathrm{fs}$. A $775\,\mathrm{mm}$ off-axis parabola was used as the final focusing optic providing a focal spot with $16\,\mu\mathrm{m}$ FWHM. The phase front of the laser pulse was controlled with a 32 actuator NightN (opt) Ltd. brand adaptive optic (AO)[105] in tandem with a Phasics SID4 wavefront sensor[106] which uses the full beam attenuated before compression and extracted in the interaction area to correct aberrations in the wavefront. This was completed using a correction procedure designed to flatten the phase front at focus provided by Phasics software. Corrections in the wavefront are then applied by altering the actuators of the AO. A detailed description of the laser system, before the user area, is presented in the thesis of Svendsen[107] and will be summarised here with an overview in Fig. 2.6.

An initially low energy short pulse is extracted from a mode-locked oscillator before a Pockels cell is used to extract pulses at $10\,\mathrm{Hz}$. These pulses are then pre-amplified to the μJ level and an AO-PDF is used for pre-compensating the dispersion of the amplification system. The AO-PDF is set to pre-compensate the

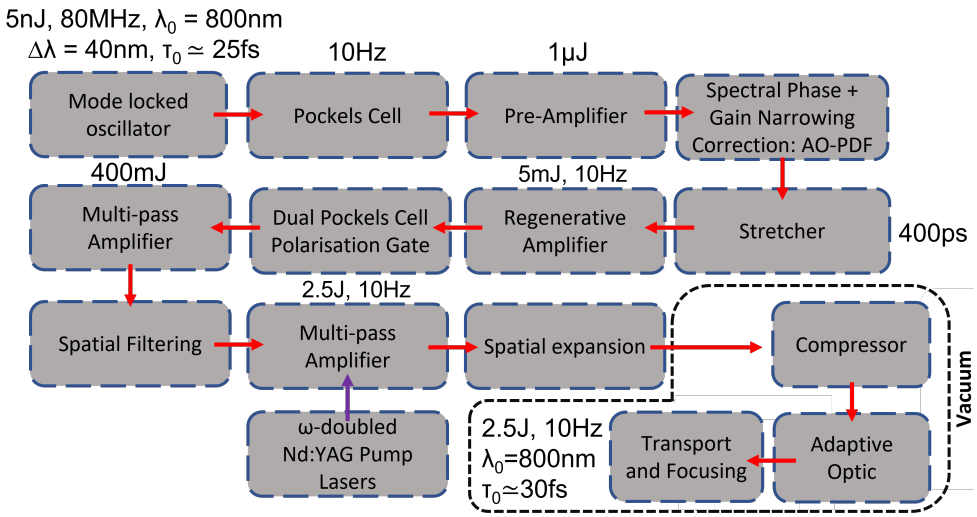

Figure 2.6 – Overview of the LLC Terwatt laser system from initial pulse creation to fully amplified and compressed pulse in the interaction chamber. Numeric values indicate the nominal values at the output of the corresponding laser component. When values differ from the nominal values they are stated in the text. The final three sections - compression, wavefront correction and transport and focusing are completed in vacuum due to high laser intensity. The energy at interaction will be reduced from the $2.5\,\mathrm{J}$ due to transmission of the compressor and transport line.

spectrally dependent gain profile of the amplification system such that the relative intensities at the end of amplification are similar to the input spectra, thus conserving the short pulse of the laser. This is done by reducing the relative intensities of the central wavelength which is optimally amplified. A two-grating stretcher with a telescopic imaging system is used to stretch the pulse to approximately $400\,\mathrm{ps}$ before amplification. Between the second and third amplification stages, a dual Pockels cell set-up is used to act as a polarisation gate with an opening duration on the ns-level allowing for the reduction of pre- and post-pulse laser signal. Spatial filtering is then applied to the pulse by focusing the beam through an aperture, allowing for energy outside of the main volume to be removed.

The final amplification stage then brings the pulse to the nominal energy of $2.5\,\mathrm{J}$ where the beam must then be spatially expanded to reduce the intensity on the compressor gratings. The compressor has the inverse dispersion of the stretcher allowing for the pulse to be recompressed to approximately its initial pulse duration. Compression and the following wavefront correction are completed under vacuum due to the pulse intensity now being sufficiently high to experience non-linear effects in air, such as self-focusing, filamentation, and non-linear phase shift of the pulse. The adaptive optic is then used to correct for spatial aberrations in the pulse allowing for improved Strehl ratio and reduction of focal spot asymmetry. The beam is then transported to the experimental chamber through vacuum piping where it is focused by the off-axis parabola. An automated laser position control system

is implemented using piezo motorised mirrors throughout the transport chain to stabilise laser-pointing drifts at focus.

Figure 2.7 – Experimental room at the Lund Laser Center with an interaction chamber at the centre and optical tables for the pre-interaction laser diagnostics on the right. The black lead-shielded door was in place during the experimental runs.

2.1.3 . Apollon Petawatt Laser System

The Apollon facility represents over a decade of work within the French physics community and a large collaborative effort between many groups on the Saclay Plateau. This world-class laser system is built underground inside a portion of a decommissioned linear accelerator facility at *Orme des Merisiers*, to study the next generation of particle acceleration schemes using laser-matter interaction. The Apollon laser facility currently houses a 1 PW-scale beam (designated F2) with a planned 10 PW beamline (designated F1) along with a probe beam extracted from a holed turning mirror of the F2 beam. During the following presentation of the experimental campaigns for high-energy laser-plasma injector investigation in chapter 5, the F2 beam was used. Apollon is separated into two experimental rooms: long and short focal areas (LFA and SFA respectively) where the principal difference is the focal length of the final focusing optic ; $\mathcal{O}(\mathrm{m})$ vs $\mathcal{O}(\mathrm{cm})$.

The length of the focusing optic for the F2 beam can be selected in the LFA area from 3 and 9 m. A 6 m focal length is also available, however, it is not currently possible to use the nominal interaction point with this configuration due to spherical mirror mounting constraints. Therefore the 3 and 9-meter focusing optics were used during the exploration of the high-energy laser plasma injector. The choice of focusing optic sets the focal spot size and the corresponding Rayleigh

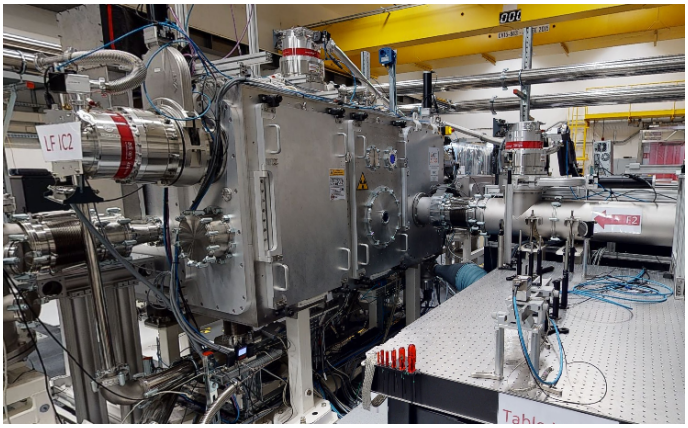

(a) Long focal area experimental chamber. F2 beam enters from right.

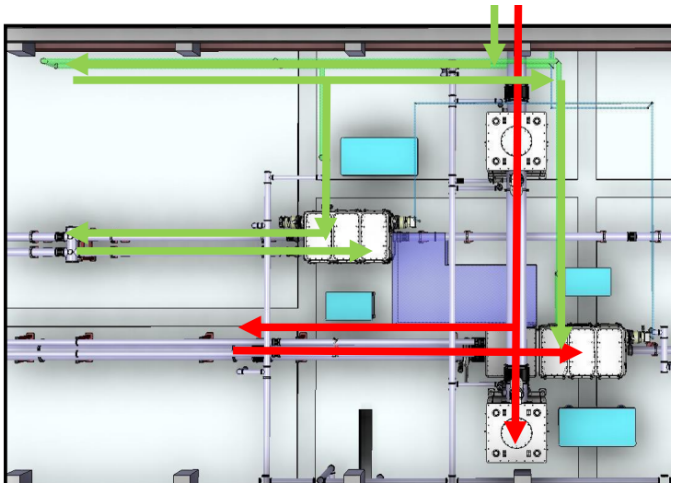

(b) LFA experimental layout. F2 beam is shown in green and F1 in red.

Figure 2.8 – a) F2 Interaction chamber in the long focal area of Apollon and b) overview of the Long focal area showing the two high power beam paths and main vacuum chamber implantation. Images are extracted from 3D scan of Apollon facility produced by AlphaScan3D[108].

length of the laser, increasing the interaction length with longer focal lengths, and reducing the requirements of active/passive plasma-based laser guiding. The LFA was used in all presented analyses as the laser parameters at focus are well suited for electron acceleration through LWFA.

The interaction chamber and the floor plan of the LFA experimental area, are displayed in Fig. 2.8 a) and b), respectively. The experimental chamber and room provide extensive shielding from the ionising radiation generated by the high flux of electrons and secondary radiation caused by electron-matter and laser-matter interactions. Diagnostics are EMP and radiation protected through the use

of shielded cables, off-axis detectors, and lead shielding where applicable. The LFA currently houses two experimental vacuum chambers for the F1 (future) and F2 beams where the experimental results were acquired. All experimental control is performed remotely, from a dedicated LFA control room.

The Apollon laser chain is presented in references[109] by Zou and[94, 110] by Papadopoulos *et al.* A composite layout of the laser chain from these articles is presented in Fig. 2.9 along with the component descriptions. Throughout the laser chain measurements on the laser profile, spectra and energy are measured allowing for detailed tracking of the laser parameters and quick identification of issues throughout the laser chain. Calorimetry measurements are performed at the end of each component section: OPCPA front end, each amplification stage, input and output of compressor and a final measurement using a calibrated leak on a portion of the main beam in the interaction chamber. Spectral measurements are taken before and after the OPCPA process, and after the compressor. The spectral transmission of the post-compressor mirror was out with the central region bandwidth of the F2 beam which limited the use of this diagnostic in stability tracking of the laser pulse. Measurements of the near and far field images of the laser pulse are acquired at each amplification stage, at the beam steering between the two experimental areas, and pre- and post-compressor. This laser data is provided for each experimental shot allowing correlations between fluctuations in the laser parameters and the accelerated electrons to be deduced such as reduced charge when the energy drops within the laser chain.

The Apollon laser system uses an OPCPA front end to ensure a large spectral bandwidth and high contrast pulses[94]. The output from a commercial titanium:sapphire oscillator (Rainbow, Femtolasers) produces a broad spectrum that is extracted at 800 and 1030 nm. The 800 nm portion is spectrally broadened, and contrast is increased by more than two orders of magnitude in a cross-polarised wave (XPW)[111]. This beam then enters a ps stretcher consisting of bulk BK7 and is then pulse-shaped using a FASTLITE DAZZLER in a double pass configuration. The OPCPA pump beam is produced through the chirped pulse amplification and second harmonic generation of the 1030 nm portion in a BBO crystal. Diode-pumped solid-state laser (DPSSL) allows for $100\,\mathrm{Hz}$ repetition rate operation for the OPCPA pump beam. The output of the OPCPA is then stretched to the ns-level producing a pulse train of $1\,\mathrm{ns}$ pulses at $30\,\mathrm{mJ}$ with a repetition rate of greater than $10\,\mathrm{Hz}$.

The shot picker provides a single shot per minute to the amplification chain from the OPCPA front end. Four multi-pass titanium:sapphire amplifiers bring pulses to a nominal $30\,\mathrm{J}$ corresponding to the F2 beam. A final amplifier, not used during this work, provides $300\,\mathrm{J}$ at the output corresponding F1 beam. A flat gain profile is modulated using an AO-PDF at 1 shot/min. Wavefront control is performed using a 52-actuator adaptive optic before compression to improve the laser wavefront both at focus and to limit damage on the compressor gratings due

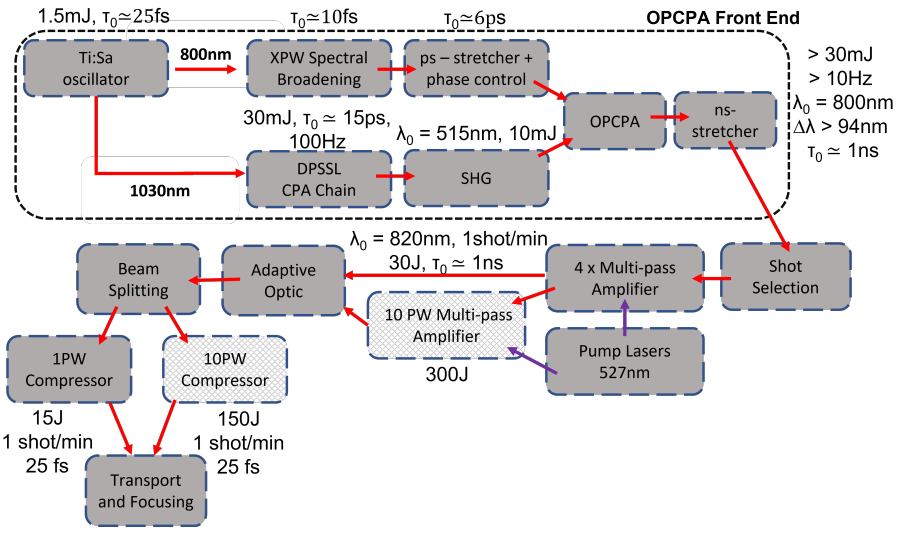

Figure 2.9 – The layout of the Apollon laser chain, including the OPCPA-based front end and two amplification paths for the 1PW and 10PW beamlines with their nominal pulse parameters. Hashed boxes indicate that these components are not currently in use. This figure is created as a composite from descriptions in references[94, 109, 110].

to high-intensity regions in a deformed expanded beam. The beam at the entrance of the compressors is designed to be at most 140 and 400 mm, respectively, for the F2 and F1 beams. The pulse is then compressed using gold coated dual-grating compressor layout.

The beam is then transported to the experimental chamber under vacuum where the spherical mirror provides the final focusing of the laser pulse at interaction. The turning mirror is holed allowing for a circular centre portion of the beam to be extracted and used as a probe beam for the transverse plasma density measurements. All plasma density measurements taken at the Apollon facility in this thesis use this beam that is attenuated, delayed for synchronisation with the main pulse, and then aligned transversely through the gas cell using two vacuum-compatible tip/tilt-mirror motors.

Currently, the only laser available is the F2 beam providing $15\,\mathrm{J}$ with a pulse duration of $25\,\mathrm{fs}$. The probe beam used for transverse plasma density measurements is extracted from the centre portion of this beam at the turning mirror.

2.1.4 . Limitations from Laser System Design

Differences in the laser chain designs between LLC and Apollon define the amount of control that can be obtained over each laser system. The AO was placed before the compressor in the Apollon design as it is shared between the long and short focal area beamlines due to size and cost. Due to the AO being before the compressor (unlike at the LLC detailed in section 2.1.2), alterations on the focal spot are strongly limited to avoid high spatial frequencies and peak intensities

on the compressor gratings. This limits the degree to which aberrations can be corrected, or artificially introduced, to study asymmetric focal spots for example. As this is not the case at the LLC the wavefront can be arbitrarily deformed allowing for the study of the effect of the wavefront on electron acceleration as explored in section 4.1.3.3.

Exploration of the effect of the GDD, TOD, and FOD on electron spectra is limited in the case of the Apollon experiment as the spectral phase control is set during the OPCPA chain limiting the effect of the AO-PDF at focus, as can be seen in Fig. 2.9. This strongly limits the safe bounds on pulse deformation due to the interaction required in the OPCPA stage. Since the amplification in OPCPA is strongly related to the intensity, strong deformations in the temporal envelope would strongly reduce the intensity and correspondingly the output energy of the front end.

2.1.5 . Laser Diagnostics

Measurements of the laser system pulse duration, spectral chirp, pointing, and stability of these parameters are required to decouple the effects of laser fluctuations on the interaction between laser and plasma. Here we present measurements of the laser pulse duration and spectral phase, and finally a novel description of the asymmetry of the measured focal spots.

2.1.5.1 . Pulse Duration

Understanding and accurately simulating the interaction between the short laser pulse and plasma requires an accurate description of the pulse duration. Self-referenced methods such as autocorrelators[112] and frequency-resolved optical gating (FROG)[113] techniques to extract the pulse duration and the pre- and post-peak intensity, duration, and spectral chirp respectively. These methods are classified as self-referenced as they use the incoming pulse to interfere with itself in a non-linear crystal to produce a higher-order pulse containing information on the pulse duration[27]. These pulse duration measurements were implemented during the development of the low-energy LPI in section 4.

We can define a minimum physical limit on the pulse duration from a given laser spectrum measurement as defined by Eq. 1.28 that is useful for verifying the more complex pulse duration measurements to follow. When the pulse is bandwidth-limited (or Fourier Limited), Eq. 1.28 is instead an equality allowing us to set the lower physical limit. For the example a laser spectrum plotted in red in Fig. 2.10 was measured using a spectrometer at Apollon facility at the entrance of the amplification chain, the values of λ and $\Delta\lambda$ (FWHM in spectral intensity) can be extracted by applying a Gaussian fit to the spectrum, displayed here as the dashed blue line. For this example, the spectral bandwidth is measured as $\Delta\lambda = 51\,\mathrm{nm}$ from $2\sqrt{2\ln 2}\sigma$ where σ is the standard deviation is of the Gaussian fit.

We can combine the transformation between wavelength-bandwidth and frequency-

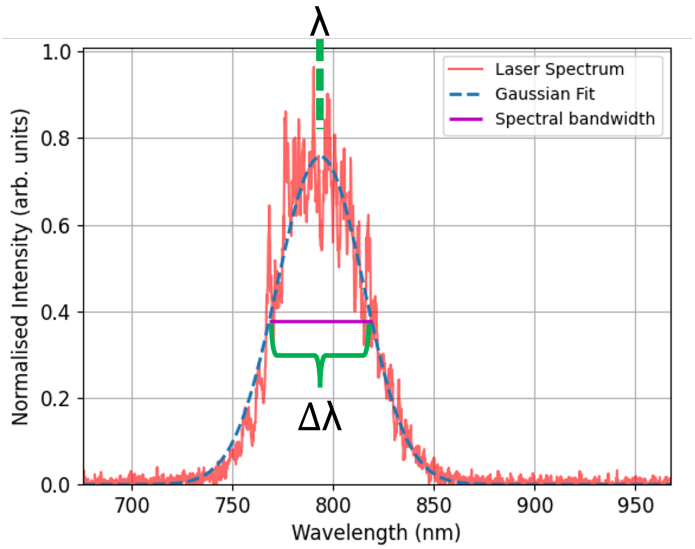

Figure 2.10 – Extraction of spectral bandwidth from spectrometer after the shot selection stage at Apollon (see Fig. 2.9). Normalised and baseline shifted spectrum is shown in red with the fitted Gaussian function in blue. The central wavelength and bandwidth are marked by the vertical green dashed line and purple horizontal line respectively.

bandwidth and Eq. 1.28 to find:

$$\Delta v = 2\pi \frac{c\Delta\lambda}{\lambda^2} \tag{2.8}$$

$$\tau_{min} = \frac{0.441}{\Delta v} \tag{2.9}$$

as defined for Gaussian pulses assuming no spectral chirp. For the above example, this results in a minimum pulse duration of $18\,\mathrm{fs}$.

2.1.5.2 . Radial Asymmetry Parameter: RASP

As will be shown in chapter 4, asymmetries of the laser driver lead to asymmetries in the accelerating and focusing fields and resulting electron dynamics[114]. Asymmetric accelerating fields can drive electron beams off-axis[22], induce larger betatron oscillations due to cavity deformation[115] and alter the electron parameters[77, 78]. Here we describe a new method for quantifying the rotational symmetry of a laser pulse through the focal volume in the transverse plane. This allows for quantification of the quality of the focal spot and its evolution through focus, using the rotational asymmetry parameter, or RASP, of the laser pulse. This is a useful comparative tool when comparing focal spots with altered wavefront settings.

For a given transverse laser fluence map, $\mathcal{E}(r,\theta)$ in cylindrical coordinates, where r is the radius with origin at the centre of mass and θ the azimuthal angle in the transverse plane, we define a projection $\mathcal{P}_i(r)$ for each $\theta = \theta_i$, where

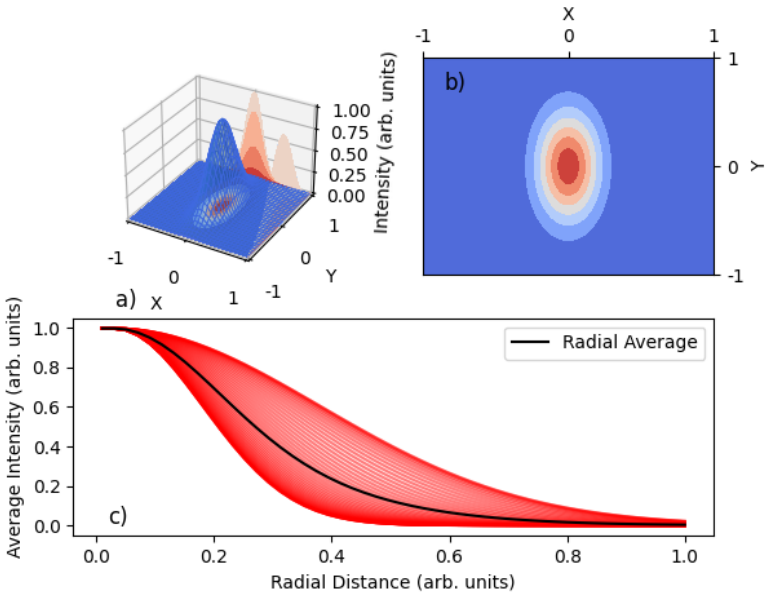

Figure 2.11 – Illustration of the method to calculate the radial asymmetry parameter for a toy 2D Gaussian model. a) 2D Gaussian function with axial projections b) Transverse distribution of Gaussian model c) Radial average is displayed in black alongside each radial projection.

'i' is a given projection angle index, for the laser energy map in $0 < r < R$, where R is the maximum radial limit. We then calculate the average radially dependent energy distribution from the centre-of-mass of each image which we call $A(r) = \left\langle \sum_{i=0}^{i} P_i(r) \right\rangle$. Finally, $\mathcal{R}$, the normalised rotational asymmetry parameter (RASP), is obtained by calculating the normalised mean absolute variation between the rotational average and each projection:

$$\mathcal{R} = \frac{\int_0^R \left(\overline{|\mathcal{A}(r) - \mathcal{P}_i(r)|} \right) dr}{\int_0^R \mathcal{A}(r) dr} \,. \tag{2.10}$$

Experimentally, images are first taken in the transverse plane through the focal volume at known displacements around the focal plane. These images are then cleaned and the background is removed to reduce camera and measurement noise effects on the calculation. Images are then centred with reference to their centre-of-mass and cropped to a box of constant size allowing sufficient space around the energy distribution to not crop the numerically interpolated image at any angle of rotation. We take a projection every 3.6° around the centre of mass as a compromise between accuracy of $\mathcal{R}$ and image interpolation induced noise, which for this method was found to be of the order 10^{-5} using the scipy ndimage rotate function[116]. From Eq. 2.10 we see that the RASP for a perfect rotationally symmetric distribution - such as a Gaussian or Airy distribution where each projection

is equal to the average projection - would give $\mathcal{R} = 1$ and a perfectly asymmetric one would correspond to a value of $\mathcal{R} = 0$.

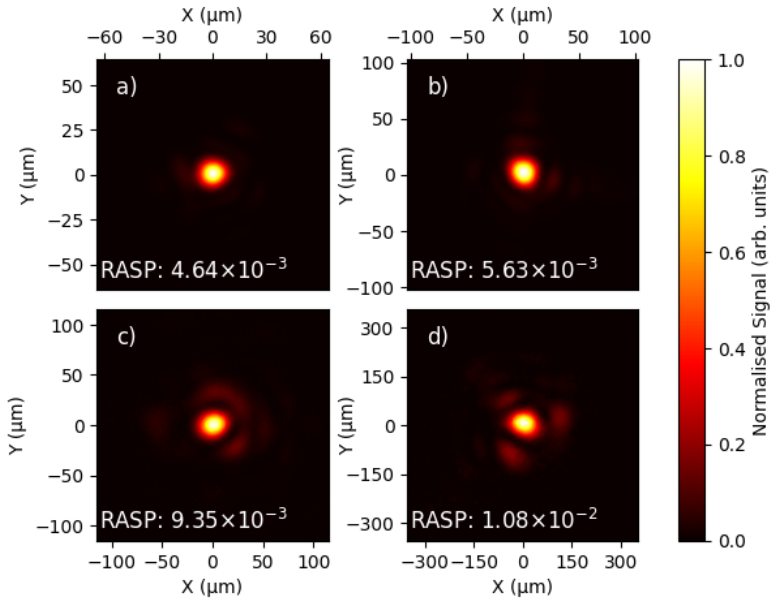

Figure 2.12 – Normalised focal spot images used for the calculation of the radial asymmetry parameter for the four experimental campaigns: a) LLC 2019 (section 4.1) , b) LLC 2021 (section 4.2), c) Apollon 2021 (section 5.1.2), d) Apollon 2022 (section 5.2). Images are cropped to an $8\times$FWHM box around the peak intensity for each focal spot image and spatially calibrated. RASP values are inset for each image.

Using a 2D Gaussian with a sigma ratio of 2.33 between σ_y and σ_x the calculation of the RASP method is demonstrated in Fig. 2.11. Figure 2.11 a) and b) show the Gaussian profile in 3D with X and Y projections and a top-down view, respectively. In Fig. 2.11 c) we have plotted the average radial projection, in black, from each projection in red. The RASP value is then calculated using the above method, retrieving a value of 7×10^{-2}. This process can then be repeated for images around the focal plane to calculate the change in RASP through focus.

To illustrate typical values of the radial asymmetry parameter, we apply the above method to images of the transverse laser profile taken at focus. Figure 2.12 illustrates the focal spot images taken during the four campaigns completed during this thesis with a cropping of $8\times$FWHM in intensity for each image where the FWHM is the RMS of the x and y FWHMs. The RASP value is inset for each focal spot image where the radial symmetry is best for a), then b) then c) then d) corresponding to increasing RASP value. As can be seen from the spatial scaling of the transverse laser focal spot images, the RASP value allows for the comparison of focal spot symmetry between laser systems with different focal spot sizes. Qualitatively it can also be seen that the RASP parameter describes well the focal spots with the increased rotational symmetry where pseudo-Gaussian (a)),

to pseudo-Airy (b), c)), to modulated pseudo-Airy function(d)) are described by increasing asymmetry values. Increasing the asymmetry of the focal spot, along with an asymmetric distribution of laser energy surrounding the main spot, leads to a higher value of RASP. These results indicate that this parameter can provide a useful tool when optimising focal spots through adaptive optics or performing comparative analysis between focal spot configurations. In section 4.1.3.3 we use this calculation of RASP through the focal volume to compare the effect of laser wavefront settings on the accelerated electrons.

2.2 . Plasma Characteristics and Diagnostic

2.2.1 . ELISA Gas Cell

Gas cells are small containers set inside a larger vacuum chamber containing gas in a prescribed volume around the interaction point with the high-intensity laser. Gas cells[2] allow for increased stability and reliability of the plasma density profile and control of the gradients for the density up and downramps which are challenging to implement in gas jets[117-119]. Further, the process of ionisation injection must be spatially localised to limit the continuous injection of electrons throughout the plasma volume, which otherwise results in large energy spread[120]. This can be achieved in gas cells by tailoring the entrance and exit structures such that the plasma density profile can control the laser evolution in the plasma and thus the a_0 during propagation. The majority of experimental results presented during this thesis were obtained with the ELISA (ELectron Injector for compact Staged high energy Accelerator) gas cell. Here we present the layout of the gas cell, the pressure control system and the density profile, which is implemented through mechanical alterations of the entrance and exit cell face geometry.

The ELISA cell, developed by LPGP in collaboration with LIDYL, is a gas cell where the gas density profile is controlled via geometric settings of the internal face displacement to set the plateau length and aperture diameter and length of the entrance and exit faces to control the up and down ramp characteristics, respectively. Demonstration of typical operation of the cell where a short-pulse, high-intensity laser enters from the left, ionises the gas into a plasma, drives a plasma wake, traps electrons in this wake through ionisation injection and accelerates the electrons throughout the plasma volume, is shown in Fig. 2.13. The laser and electrons then exit the cell to the right whilst propagating through the expanded volume of the exit portion of the gas cell before entering the vacuum under free propagation. The global coordinate system is displayed where the origin is set at the internal side of the gas cell's entrance face located at the plasma region's left-most side in Fig. 2.13. A typical experimental set-up of the gas cell mounted on an XYZ and tip-tilt correction stage in the Apollon LFA experimental chamber is shown in Fig. 2.14. The gap between the cell faces where the plasma plateau region is located, and the region where the transverse probing of the plasma density is per-

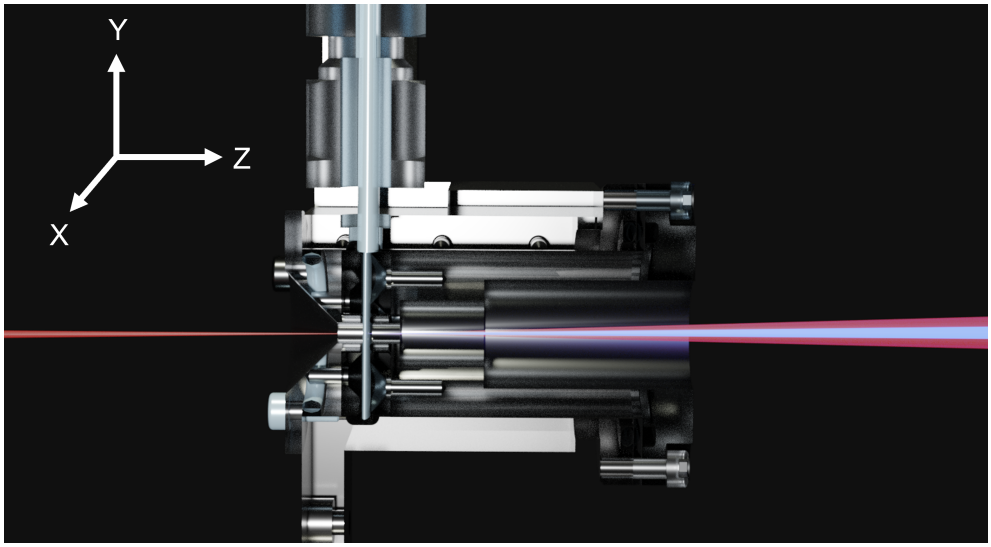

Figure 2.13 – Fixed length version of the ELISA gas cell with $500\,\mu\mathrm{m}$ plasma plateau. The laser enters from the left; electrons are trapped and accelerated, leaving the cell in bright blue alongside the diffracted laser. Gas injection arrives from the top. The gas cell has been extruded to show the internal setup. The global Cartesian coordinate system used in all following analyses is inset.

formed is visible on the right-hand side of the window where the white LED light traverses the cell.

The gas density gradients in the up and downramp regions are controlled through the hydrodynamic flow of the gas through an aperture of variable diameter and length, allowing for a controllable plasma density up and down ramp to be produced. The gradient and length of the plasma density upramp are responsible for coupling the laser pulse into the plasma plateau through self-focusing, where the density is sufficient for the injection process.

The downramp profile is responsible for coupling the accelerated electrons between the plasma and vacuum after the gas cell. The effects of this are discussed further in section 4.1.3.1 where a $100\,\mathrm{MeV}$ increase in electron energy is seen with a $1\,\mathrm{mm}$ increase in the length of the plasma down-ramp.

Fig. 2.15 illustrates the plasma density profile in the ELISA gas cell. Entrance and exit face aperture and length control the gradients between a) to b) and c) to d), respectively, and the separation between the faces alters the plasma length b) to c).

The gas injection system, illustrated in Fig. 2.16, consists of a Bronkhorst pressure regulator - to control the gas flow rate to reach a set target pressure - mounted between the gas bottle and a reservoir that stabilised the backing pressure of the injection system. The pressure inside the reservoir is monitored by an MKS absolute gauge. Pressure reduction, and full venting of the reservoir, are controlled by a butterfly valve mounted between the reservoir and the vacuum backing system.

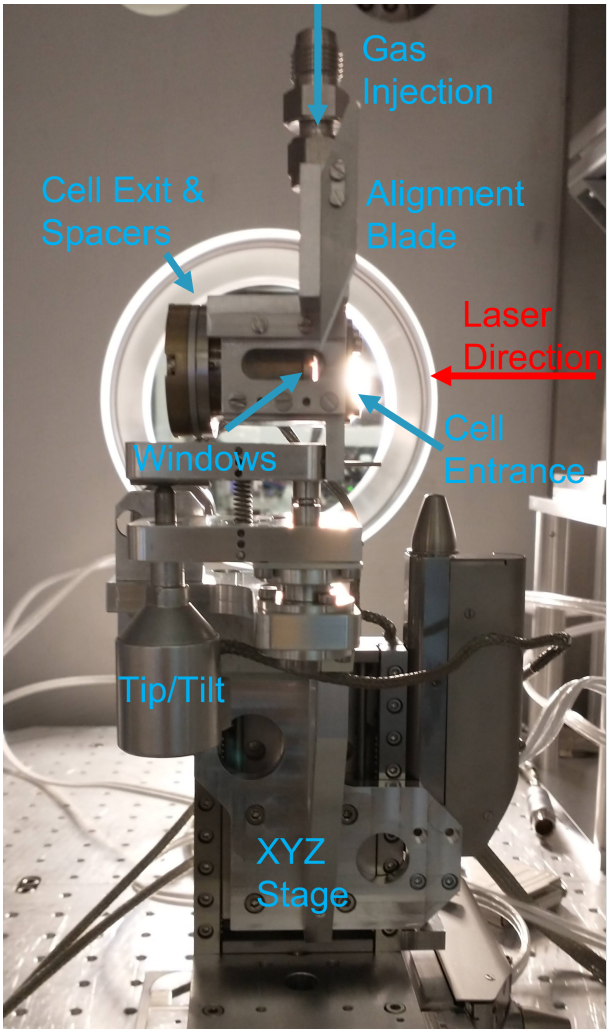

Figure 2.14 – ELISA gas cell mounted on an XYZ and tip/tilt positioning stage in the Apollon LFA experimental chamber. The laser travels from right to left. Gas injection piping is disconnected and enters above. The alignment blade is visible at the entrance (right side of the cell). A brass exit piece with spacers is displayed on the left of the cell. High-quality anti-reflection coated glass windows are mounted on the sides of the cell for transverse plasma diagnostics. The transmitted light inside the cell shows the plateau region between the entrance and exit faces.

A solenoid injection valve attached between the reservoir and the gas cell is opened through a home-built valve actuator which provides the necessary current for valve actuation when triggered by Transistor-Transistor Logic (TTL) signal.

The opening duration of the valve is controlled by the length of the TTL signal given to the signal converter allowing for the gas injection duration to be controlled. Shock-absorbing piping is placed between the solenoid valve and the internal vacuum piping to the gas cell to limit oscillations on the plasma source induced by gas injection and vibrations from triggering the solenoid. The full system

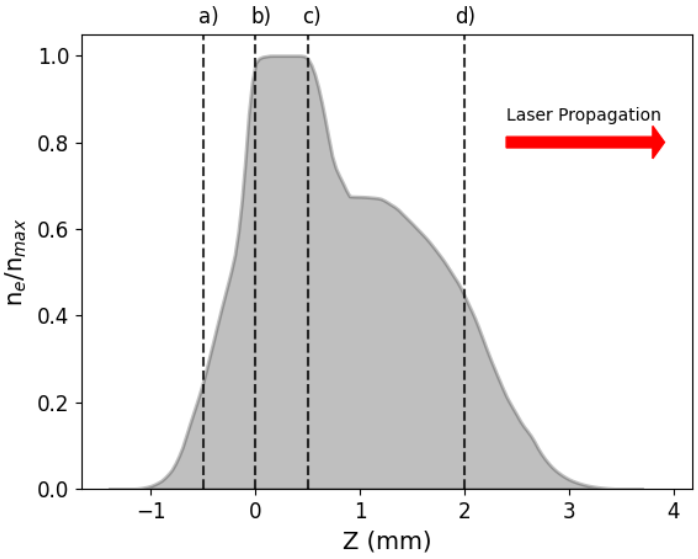

Figure 2.15 – Plasma electron density profile along laser axis in the gas cell from fluid simulations[121] normalised to the peak plateau density with asymmetric entrance ($500\,\mu\mathrm{m}$) and exit plate ($1500\,\mu\mathrm{m}$) lengths and a $500\,\mu\mathrm{m}$ plateau region. The entrance face begins at a), with the spacing between the two faces creating a plateau region between b) and c) and then the exit plate between c) and d). The laser travels from negative to positive z values as marked by the red arrow.

is fully remote controlled and can be automated to provide a closed-loop pressure regulation system allowing for the pressure regulator and gas venting system to work in unison to reach arbitrary backing pressures within the working range of the Bronkhorst of 0 to 1000 mbar and within 2 mbar accuracy.

From the equations of chapter 1 it is clear that the plasma density plays a defining role in the laser-plasma interaction. The measurement of the on-shot plasma density using reliable methods is a challenging task. During this thesis, an on-shot, self-referenced plasma density diagnostic using a wavefront sensor was developed. An offline Mach-Zehnder based interferometer using a rapid camera was also developed for measuring the temporal filling on the $\mu\mathrm{s}$-scale.

The plasma density probing is limited to the region within the ELISA gas cell, accessible from the glass windows on the sides of the cell. Therefore, the plasma measurement methods presented here apply to the plateau plasma density. The up and down-ramp regions of the gas cell are controlled within the aperture of the stainless steel cell faces and, therefore, cannot be transversely optically probed. Plasma density gradients within these regions of the gas cell are calculated using previous openFOAM[122] fluid simulation results by T.Audet *et al.*[121] and scaled to absolute values of density using the plateau density that is found between the entrance and exit faces of the gas cell using the methods described in the next sections.

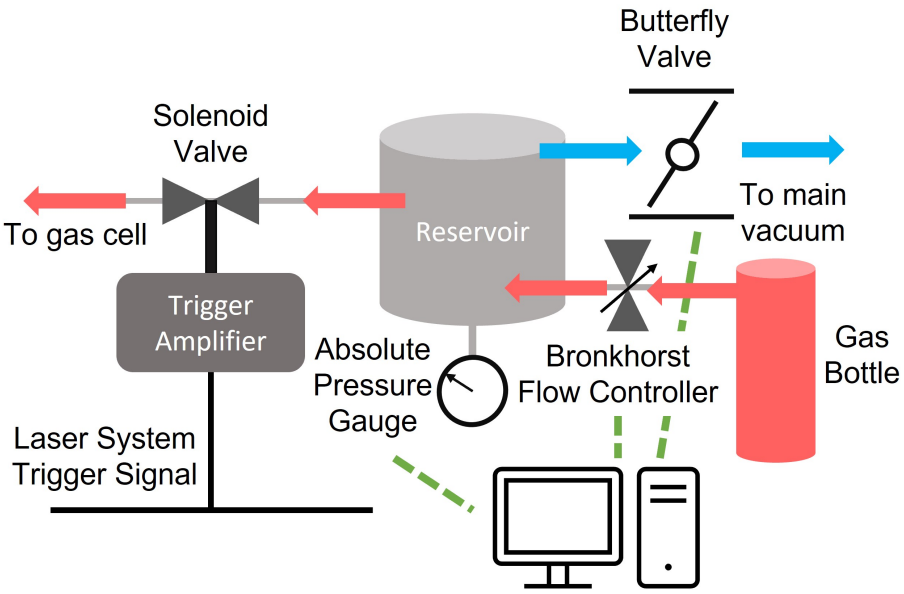

Figure 2.16 – Overview of the gas injection system for regulating the gas pressure inside the gas cell. Green dashed lines indicate the components connected to the gas pressure control script. Red and blue arrows indicate the direction of gas filling and emptying, respectively.

2.2.2 . Rapid Camera Mach-Zehnder Interferometer

To measure the temporal filling process of the ELISA gas cell and optimise the laser injection time with respect to the gas injection time, and act as an offline validation of the maximum on-axis plasma density, a Mach-Zehnder interferometer with a continuous wave (CW) $633\,\mathrm{nm}$ He-Ne laser, combined with a rapid camera (Phantom VEO 710) was set-up. This was completed using a replica of the experimental set-up used during the second low-energy LPI campaign (presented in Chapter 4) with the same piping, injection system and control of the filling and purging system to produce the same hydrodynamic behaviour of the gas, in this case, pure hydrogen. Whilst nitrogen-dopant was used during these experiments, the maximum dopant percentage was 5% leading to minimal differences in the hydrodynamic behaviour of the gas allowing the results of the rapid-MZ to simply be scaled from gas density to electron density of a doped gas by taking into account the extra electrons from the outer shells of nitrogen.

Fig. 2.17 shows the Mach-Zehnder experimental set-up used during these measurements. The CW He-Ne is first spatially filtered by focusing through a $25\,\mu\mathrm{m}$ aperture to homogenise the beam. The laser is then recollimated and passed into the vacuum chamber, where the beam is split using a 2-inch beam splitter into a reference and measurement arm. The gas cell is mounted transversely to the measurement arm of the interferometer, where the laser passes through the optical

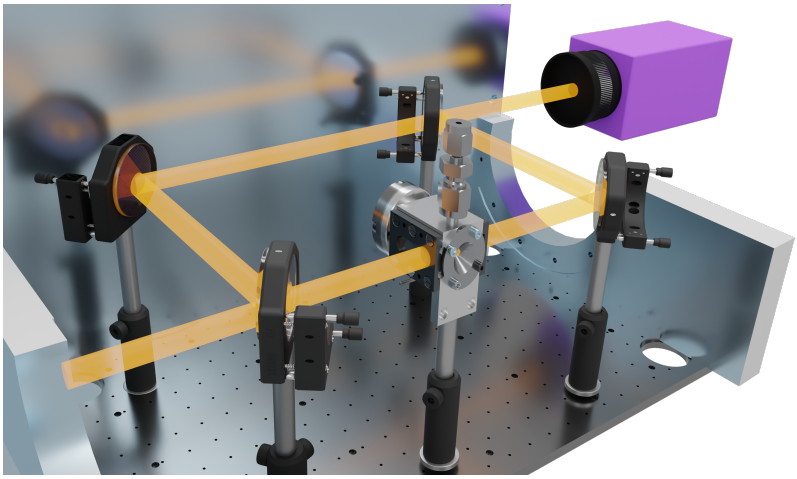

Figure 2.17 – The layout of the experimental replica used for offline characterisation of the gas cell filling dynamics using a Mach-Zehnder interferometer and a rapid camera to measure fringe shifts and extract gas density with time. The probe beam enters from the left before being split in two by a beam splitter. The measurement arm enters the cell transversely where the nominal entrance face of the gas cell is facing towards the reader. The beams are then recombined and the time-dependent interference pattern is measured on the rapid camera in purple. The camera records the interference pattern at different times; the area delimited by red dashed lines indicates the internal region of the gas cell in a typical interference image.

quality cell windows and the gas in the plateau region of the cell. The two arms are then superimposed in a second beam splitter and leave the vacuum chamber; the interference pattern is then measured by the rapid camera in air. A rapid camera with a repetition rate of 25KHz was used to give a temporal resolution of 40μs. The hydrodynamic timescale is on the order of μs when considering the gas cell length scales of centimetres and the sound speed of hydrogen at 1320m/s at atmospheric conditions, which we assume for this calculation.

The camera and gas injection system are temporally synchronised using a signal generator. During gas injection, the fringe shift due to the phase shift induced by the change in time of refractive index of the gas in the cell is measured on the rapid camera. Therefore, the rapid camera allows us to measure the filling dynamics of the gas cell and calculate the temporal and spatial gas density distribution. We can then calculate the plasma density profile for a given laser injection time. This measurement indicates the optimum temporal window for firing the laser pulse into the gas cell after it has reached the desired gas density.

The analysis method is demonstrated in Fig. 2.18. Figure 2.18 a) shows the interference pattern after automated rotation, which minimises the average distance between peak intensities which geometrically occurs at a normal angle to the fringes. A rotation angle of 49° with respect to the horizontal axis of the cell was found using this method. This step could be eliminated in future experiments by improving the alignment of the interference pattern to the gas cell but was not

completed due to time constraints. Regardless there will likely always be a small angle between the horizontal axis at the interference pattern, and so this automated rotation is helpful for the analysis. Figure 2.18 b) demonstrates the tracking of the peak signal as measured by a line out normal to the interference pattern. Higher gas densities lead to larger phase shifts, which can result in the initially tracked peak leaving the region of interest. The analysis, therefore always tracks the direction of phase shift and selects an appropriate next fringe which is then backpropagated to extract the pixel shifts from the previous frame. This results in a continuous phase shift which is inherently unwrapped in terms of 2π shifts. In Fig. 2.18 c) the fringe shift is converted to phase shift by dividing the pixel shift by the average spacing of the peaks in the interference pattern. Whilst the pixel size was calibrated in the imaging system to be $4.3\,\mu\mathrm{m}$/pixel, this value is not required to extract the phase shift with this method. Only the propagation distance of the laser through the gas is required. This was measured to be 2 cm within the gas cell. Finally in Fig. 2.18 d) the measurement of the phase shift at each time is combined to extract the time-dependent phase shift. Units on Fig. 2.18 c) and d) have been plotted in ms to display the long-term evolution.

Whilst the analysis method does not require that the plasma density is integrated spatially, no difference was found when measuring the plasma density at other spatial locations within the gas cell. This spatial homogeneity could have been caused by the rotated angle of the fringes with respect to the cell structure that was used during the measurement. This angle means that the phase shift measurement is spread across both the horizontal and vertical planes leading to a smoothing of any spatially dependent filling dynamics.

Work completed by Ovidiu Vasilovici at LPGP identified sources of vibration within the laboratory during interferometry measurements. Main sources of vibration came from a $29.4\,\mathrm{Hz}$ signal which was measured to be caused by the primary vacuum pump running at a nominal 1750 RPM, and an unknown source of higher frequency noise between 140 and 216 Hz. These frequencies were present under experimental conditions but without gas injection and have therefore been removed from the phase shift signal using two notch filters between 25 and 35 Hz and 140 and 216 Hz. Comparison of the low pass filter limited at 140 Hz and the two notch filters, supported by analysis in frequency space of the signal through FFT, indicate that the majority of signal noise comes from high frequencies. Signal analysis after removal of these frequencies leaves a strong frequency at 120 Hz for the example presented in Fig. 2.19.

The final phase shift is extracted as the average cumulative sum of the phase shifts as shown by the orange line in Fig. 2.19. The average cumulative sum is calculated after the initial injection period which is extracted by fitting a step-function to the signal and found to be approximately $25\,\mathrm{ms}$ after valve opening. Peak phase shift is therefore calculated after the injection point at the end of the fast increase to calculate the peak plasma density. Molecular density is then

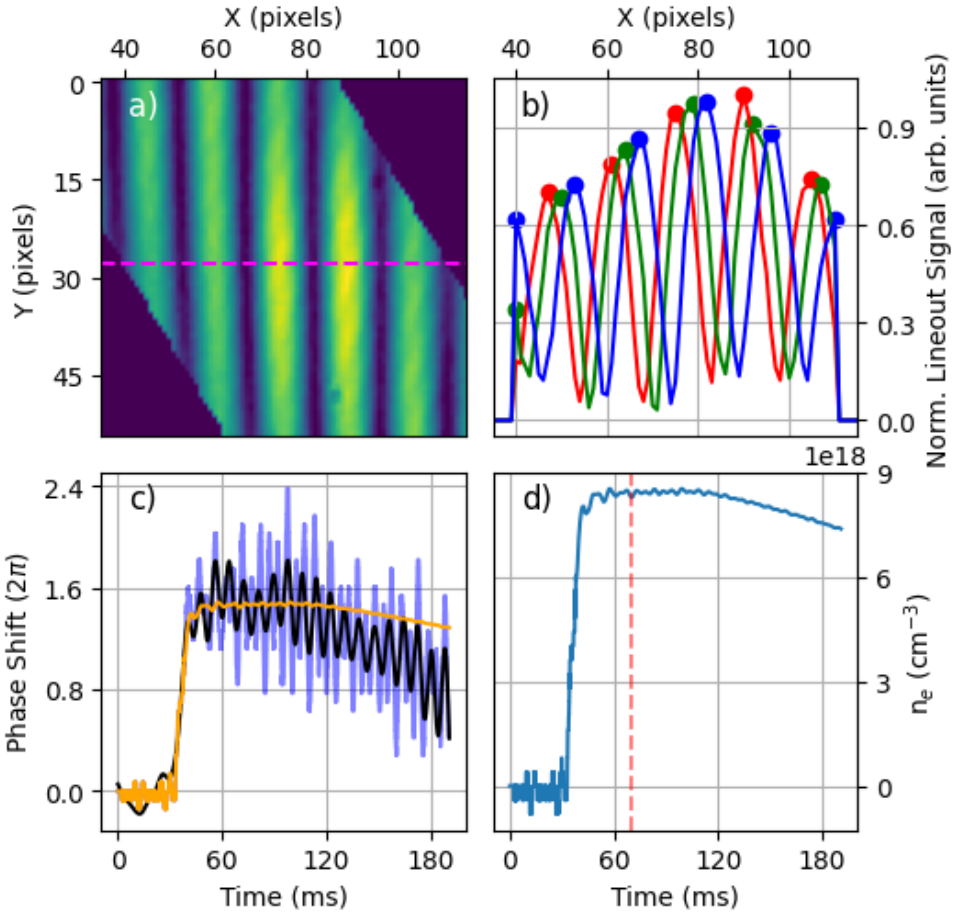

Figure 2.18 – Analysis method performed on the rapid camera Mach-Zehnder interferometer measurements. a) Interference pattern median filtered, cropped and rotated. b) Peak signal is tracked from magenta lineout of a) where $t_{red} < t_{green} < t_{blue}$. c) Fringe shift is converted to phase shift where the raw signal is in blue, the noise-suppressed signal is in black, and the running average of the cleaned signal is in orange. d) Plasma density at each time is extracted from the running average. Zero time is defined as the triggering of the solenoid valve with takes approximately $30\,\mathrm{ms}$ to open. The end of the trigger signal, and the start of the valve closing, begins at $70\,\mathrm{ms}$ as shown by the vertical red line.

calculated from the phase shift through:

$$\Delta\phi = \frac{3}{2} A_r m_g \frac{2\pi}{\lambda_0} n_{H_2} L\,, \tag{2.11}$$

where $\Delta\phi$ is the phase shift, A_r, m_g, n_{H_2} are the molar refractivity, gas atom mass and molecular gas density respectively, and $\lambda_0 = 633\,\mathrm{nm}$ is the laser wavelength.

Using known values for pure dihydrogen[123] we can reduce $\frac{3}{2} A_r m_g = 5.22 \times 10^{-24}\mathrm{cm}^3$. The plasma density is then calculated assuming full ionisation, by multiplying the molecular density by 2 for 2 electrons ionised from the H_2 molecule. We

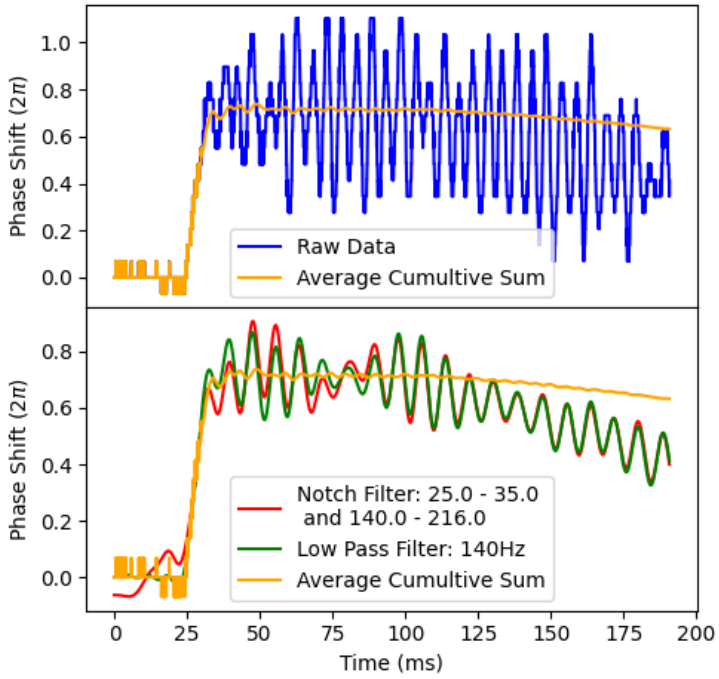

Figure 2.19 – Example of the phase shift output against time for a backing pressure of $400\,\mathrm{mbar}$. Zero time is defined as the triggering of the solenoid valve with takes approximately $30\,\mathrm{ms}$ to open.

can then calculate a scaling factor, S, for the plasma density to include the electrons from the nitrogen dopant using: $S = (N_e^{H_2} * (100 - D)/100) + (N_e^{N_2} * D/100)$ where $N_e^{H_2}$, $N_e^{N_2}$ are the number of electrons donated by dihydrogen (2) and dinitrogen (10) respectively and D is the dopant concentration.

This method allows for us to calibrate the plasma density versus backing gas density over the whole experimental range. In Fig. 2.20 we present the values for pure dihydrogen.

Rapid Mach-Zehnder interferometer measurements were completed using the method above, over the full range of backing pressures used during the second low-energy LPI campaign. Each measurement in Fig. 2.20 corresponds to the average of two measurements where the error is given by the standard deviation. Extracting the line of best fit we find $n_e = 3.05 \times 10^{16} P - 4.58 \times 10^{17}$, where P is the backing pressure in mbar, and the plasma density in electrons per cubic centimetres, giving zero density at a backing pressure of $15\,\mathrm{mbar}$. This is likely due to a different filling regime at very low backing pressures where the cell is not efficiently filled due to the low pressure throughout the injection piping. The theoretical plasma density for pure hydrogen gas is displayed in green. This is calculated assuming perfect

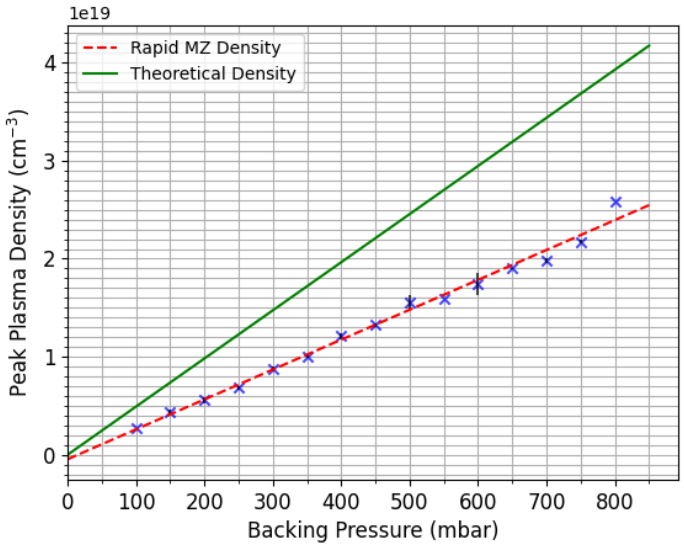

Figure 2.20 – Plasma density calculated from the rapid Mach-Zehnder interferometer measurements assuming pure hydrogen plasma at various backing pressures in the ELISA gas cell. Each measurement, blue crosses, is analysed using the method presented in Fig. 2.18 and averaged over two experimental data points then a linear fit is applied, shown by the red dashed line. Theoretical density assuming perfect filling from reservoir to internal gas cell is plotted as a green line.

filling between the gas cell and the gas reservoir and using the ideal gas law due to the low pressure:

$$n_e[\mathrm{cm}^{-3}] = \frac{n_{H_2} P \times 100}{k_b T 10^6}\,, \tag{2.12}$$

where the temperature T is assumed to be $295\,\mathrm{K}$, k_b is the Boltzmann constant, pressure P is in mbar, and the number of electrons from dihydrogen, $n_{H_2} = 2$. This indicates that, whilst the filling response of the gas cell as measured by the rapid Mach-Zehnder interferometer is linear, the gradient is significantly smaller. This infers that the density inside the gas cell is smaller than the backing pressure and that the difference is larger for the higher pressure range. The range of interest for gas cell experiments is for plasma density lower than 10^{19} cm^{-3}, where backing pressures are lower than 400 mbar.

The results of this gas fill measurement will be compared to direct electron density measurements in section 2.2.4.

2.2.3 . Wavefront Sensor as Plasma Density Diagnostics

2.2.3.1 . Principle

Wavefront sensors (WFS) are used to retrieve phase gradients of an input laser beam through shifts in reference images recorded through masks or arrays on a CCD. Arrays of spots are typically created by sending a beam through diffraction

masks or micro-lens arrays. During these measurements, a PHASICS SID4 WFS was used providing an imaging resolution of 160 x 120 pixels with $30\,\mu\mathrm{m}$ apparent pixel size after the phase retrieval algorithm. Phasics SID4 wavefront sensors use a "Quadriwave lateral shearing interferometry"[124, 125] technique which splits the incoming wave into four separate waves using a diffractive grating. These waves then overlap on the detector and interfere where the interference pattern encodes the phase gradients of the incoming beam.

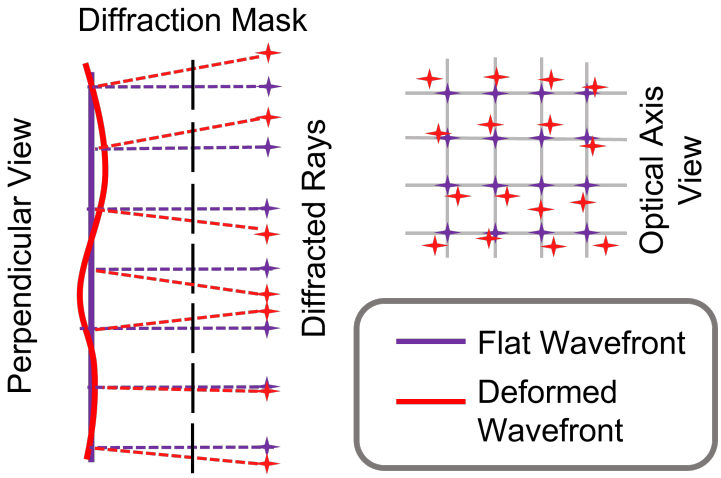

Figure 2.21 – Comparison of diffracted ray positions for flat (in purple) and deformed (in red) wavefronts propagating through a diffraction mask. Ray shift is proportional to phase curvature at each location and where the position of the ray is determined by the interference between the beamlets passing through the diffraction mask. The perpendicular view illustrates the 1D principle and the optical axis view demonstrates how the 2D gradients are extracted at each grid point. During a measurement with a WFS only one wavefront is used: two are shown here for comparative purposes only.

Figure 2.21 illustrates a simplified 1D overview of a wavefront sensor using a diffraction mask inspired by the description in reference[100]. Typically, imaging of the diffraction grating will be performed to produce an array of spots focused on the CCD. In the flat wavefront case, the focal spots are equally spaced on the reference positions of the wavefront sensor. Deviation from a flat phase profile leads to shifts in the focal spot position, which arise from the local wavefront curvature, leading to changes in beamlets' angle and position through the diffraction grating. Retrieval of the phase gradients from shifts in the beamlet images is a complex problem which has been tackled with correlation methods in the spatial and frequency domains[126]. In the case of the Phasics SID4 with the four-wave interference pattern, the phase gradients are calculated through a minimisation of the phase gradient map to be calculated and the input interference pattern in Fourier space[124]. This allows for the beam curvature to be calculated at discrete positions of the wavefront and interpolated between these positions and then inte-

grated to retrieve the phase map. Imaging of the focal spot position in x/y requires four pixels to map the gradients in 2D at each position.

2.2.3.2 . Wavefront Sensor Plasma Density Measurements: State-of-the-Art

Plasma density measurements are a key issue in LWFA experiments where accurately describing both the plasma density and distribution are required for modelling, for example, the evolution of the laser a_0 in the plasma from self-focusing or electron injection due to gradients in the plasma. Typical two-arm interferometric plasma density measurements such as Mach-Zehnder interferometry are extensively used to measure the phase shift acquired by a probe beam. However, they come with the disadvantage that they are challenging to align, require precise timing of the two beam paths when using short pulse probes, and the different paths of the two arms can be prone to vibrations which cause variability in the phase measurement[127]. Wavefront sensors, on the other hand, provide an incredibly simple alignment where the plasma is imaged onto the wavefront sensor, in a single-arm manner, meaning that the effect of vibrations is reduced.

Here we present the state-of-the-art of using wavefront sensors for plasma density measurements. Plateau compared the use of a wavefront sensor and a folded wave interferometer to measure plasma densities during an LWFA experiment[127] where they calculate the plasma density, in both cases, by averaging 50 phase maps. Wavefront sensors have also been applied to discharges in air where a background phase map[128] was used and have been averaged over many measurements[129]. In this work, we present a single-shot method where phase averaging is not required due to the lack of reliance on a background phase map. In this work, we present the development of a single-shot self-reference wavefront sensor-based plasma density measurement technique which removes the requirement of background images through a self-referenced background subtraction. This provides the benefit that shot-to-shot fluctuations in the probe wavefront are accounted for in the analysis method. Single-shot plasma density measurements are, therefore, more stable and do not require averaging over multiple shots.

2.2.3.3 . Abel Inversion for Density Retrieval

Abel transforms were applied to WFS measurements of plasma density in order to take into account the radial dependence of plasma density in the direction perpendicular to laser propagation.

An Abel transform allows for the conversion between 3D cylindrically symmetric distributions and their 2D projections. Calculation of the 3D volumetric phase shifts from 2D projections, which are measured with the WFS, can be performed using an Abel inversion which maps in the opposite sense to the Abel transform. The Abel inversion can be performed if the projection is smooth, axially symmetric and decays to zero within a finite distance. In our experimental case for the plasma density measurement, the plasma column is typically axis-symmetric, smoothly varies, and

is confined to a small region of the WFS, meaning that the Abel inversion integral, Eq. 2.14, is finite.

The Abel transform (3D $\rightarrow$ 2D) and inversion (2D $\rightarrow$ 3D) described by[130] are written in 1D coordinates as:

$$F(x) = 2\int_x^\infty \frac{f(r)r}{\sqrt{r^2 - x^2}} dr\,, \tag{2.13}$$

$$f(r) = \frac{-1}{\pi}\int_r^\infty \frac{dF}{dx}\frac{dx}{\sqrt{x^2 - r^2}}\,. \tag{2.14}$$

Applying the Abel inversion to an arbitrary 2D phase shift map F(x,y), allows us to calculate the radial phase shift f(r) resulting from the electron density of the plasma. We can then calculate this electron density with the following equation:

$$n_{e_{x,y}} = n_c\left[1 - \left(1 - \frac{\lambda f(r)}{2\pi L_{pix}}\right)^2\right] \tag{2.15}$$

where λ and L_{pix} are the probe laser central wavelength and the apparent pixel size for density scaling, respectively. During the analysis in this thesis, the python Pyabel package[131] was used to perform the Abel inversion.

We take the plasma column to have cylindrical symmetry around the central acceleration axis that must be assumed without a secondary orthogonal plasma diagnostic. The typical RASP values are on the order of 10^{-2} for the focal spots presented in this thesis (see Fig.2.12), meaning that the laser pulse deviates from a perfect rotational symmetry by 1%. As the plasma columns structure on the short time scales is directly linked to the intensity profile of the laser pulse through barrier suppression ionisation (presented in section 1.2.3), rotationally symmetric laser pulses will create rotationally symmetric plasma columns and therefore the assumption of cylindrical symmetry can be made.

2.2.3.4 . Self-Referenced Wavefront Sensors for Plasma Density Measurement

During this thesis, we apply a self-referenced technique for the background phase shift removal measured by the WFS. This technique assumes that the plasma region is surrounded by unionised gas (in the transverse and vertical direction with reference to the laser path.) This produces a phase shift which can be separated into the gas and plasma phase shifts.

Here we present the development of a self-referenced, single-shot, wavefront sensor-based plasma density measurement. In gas cells, the plasma is typically surrounded by unionised gas in regions where the electric field of the laser is too weak to perform barrier suppression ionisation ($I < 10^{14}\mathrm{W\,cm^{-2}}$ for H_2). In other wavefront plasma density measurements, a reference image is taken of the phase distribution of the probe pulse with gas but without the ionising main beam. This phase map can then be used as a reference to calculate the plasma-induced phase shift when the main beam is present. However, this method has an inherent flaw

in that it relies on the wavefront phase stability of the probe beam. Since probe beams used in most experimental setups are not phase stabilised and could change throughout the experiment with a shift in main beam properties if they are extracted as a small portion of the main beam, this introduces an unknown error into the density calculation, which would require a secondary phase map measurement to correct. Here we present the results for single-shot plasma density retrieval without a reference image, to reduce the reliance on phase-stability.

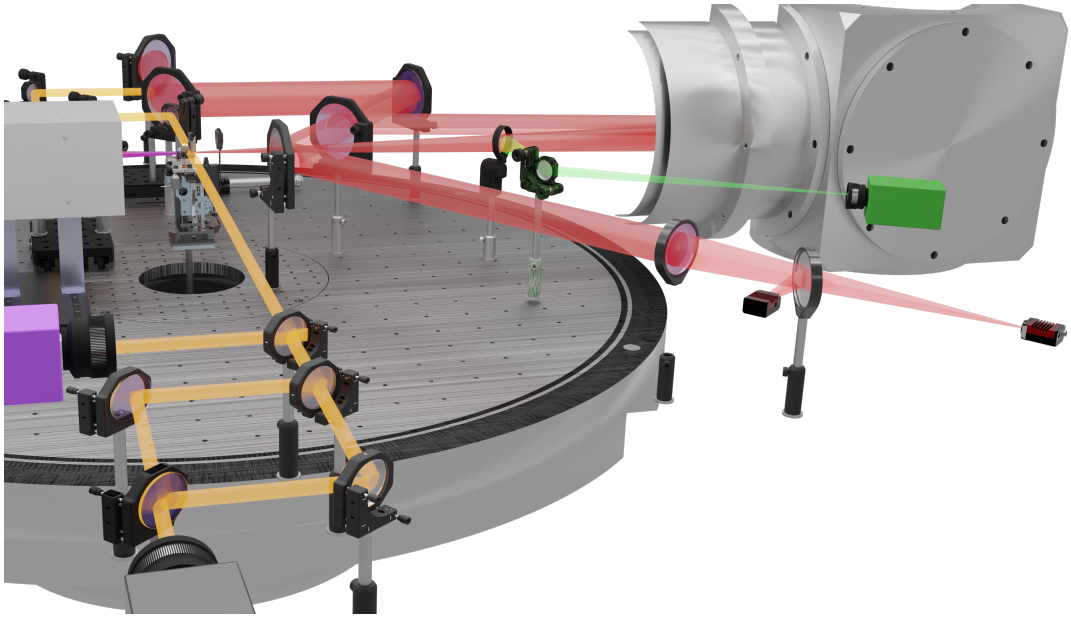

Figure 2.22 – Simplified experimental set-up of the wavefront-sensor and MZ interferometry measurements of the plasma density as part of the LWFA experiment. The off-axis parabola is contained within the cube on the right and focuses the main laser in red into the gas cell above the centre circle. The probe line, in orange, propagates transversely to the gas cell. The wavefront sensor takes the reflection from the first beam-splitter at the lower portion of the orange beam path. The Mach-Zehnder interferometer uses a delay stage to synchronise the two arms of the interferometer.

Figure 2.22 illustrates the experimental layout used during the LWFA experiment for plasma density retrieval. During the low-energy LPI experiments described in section 4, a probe beam is created from a small pickup mirror on a movable stage which could be inserted into the collimated main beam before focusing. At the Apollon facility used for the high-energy LPI experiments described in section 5, the central portion of the main collimated beam is extracted through a holed turning mirror. The probe beam is then temporally synchronised to the main pulse at the interaction point using mirrors mounted on a delay stage as shown in Fig. 2.23 and looking at the probe signal through the gas cell. Temporal synchronisation was achieved by imaging the plasma column with the shadowgraphy and interferometry CCDs whilst changing the position of the delay stage for the probe line. As shown in Fig. 2.23, the delay was lengthened until the entire plasma column was visible,

indicating that the probe beam arrived just after the plateau plasma column had been formed. We then define this delay time as the zero point, and as illustrated in Fig. 2.23, by changing the probe delay we can image a plasma column formed over a fraction of the gas cell length.

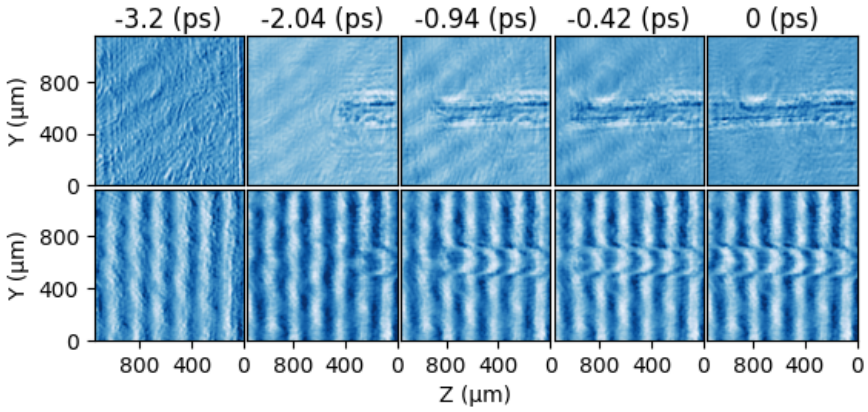

Figure 2.23 – Plasma column creation as a function of the probe beam delay as measured by shadowgraphy (top line) and interferometry (bottom line) in the plasma plateau region. Relative delays of the probe line are annotated above, where 0 delay is defined as the laser traversing the whole plasma plateau. Laser propagates from right to left.

WFSs calculate the phase gradients and intensity maps based on the relative shifts of an array of focal spots as described in section 2.2.3. In this analysis, the intensity map is used for localising the plasma column and creating a region of interest which is then applied to the phase map to calculate the plasma density. The different steps of the method are illustrated in Fig. 2.24. The intensity map retrieved by the WFS is displayed in a) where the laser travels in the negative Z direction. These images have been spatially calibrated at $30\,\mu\mathrm{m}$/pixel to allow for the number density of electrons to be calculated in the final result. The plasma column is visible across the gas cell between $Y = 1000$ and 1400 µm, while gas only is present for Y outside this interval. The dark areas are images of the cell's metallic walls blocking the probe beam. In Fig. 2.24 b) is displayed the result of a Sobel–Feldman operator (commonly Sobel filter[132]) applied to the image in a), to calculate a 2D map of the intensity gradients at each pixel location. This allows us to extract the 'edges' (regions of high-intensity gradients) in the image, which are characterised by strong amplitude gradients between adjacent pixels located at the cell walls and the plasma column edges. Ideally, these would represent only the edges of the cell and plasma, however, due to diffraction noise in the probe beam image b) contains 'edges' within the gas region of the plasma. These diffraction rings arise from the edges of the small pick-up mirror placed into the beam path of the collimated main beam to extract the probe line during these results. The image is then projected and averaged in the horizontal and vertical direction to give

the solid green and red lines, respectively. A peak-finding method is then applied to these projections, and the cell edges are extracted directly from the vertical projection displayed as the vertical dashed red lines. For the plasma column edges, we take the peaks in the horizontal direction and then shift the limits away from the plasma column by 10 pixels to ensure that the plasma signal is not included in the background phase map analysis. These final plasma column limits are shown by the horizontal dashed red lines.

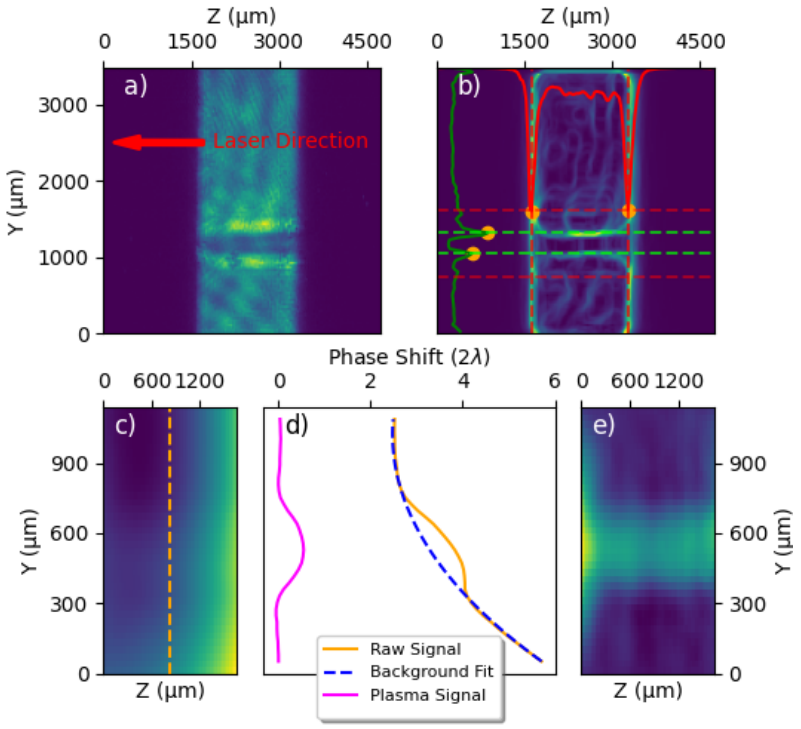

Figure 2.24 – Demonstration of the plasma finding algorithm and phase retrieval on experimental data from the second low-energy LPI campaign. a) Intensity map retrieved from the WFS. b) Plasma edge-finding through the integrated signal of intensity image after Sobel-filtering. Box enclosed by red dashed lines is used for plasma density analysis c) Phase map cropped to red dashed enclosed region calculated from in intensity image in b). d) Total, gas, and plasma-induced phase shift, for a single phase column corresponding to the column from the dashed orange line in c). e) Plasma phase map after completing the iterative phase extraction over each column.

As can be seen from Fig. 2.24 b) the edge-finding method resolves the plasma position which allows for the analysis to be highly flexible and the plasma column well retrieved even when moving the gas cell during focal position optimisation or drifts in the vertical direction from day-to-day. Figure 2.24 c) shows the phase map cropped to the region of interest enclosed by the horizontal and vertical dashed red lines in b). To illustrate the phase calculation, we have taken an example column

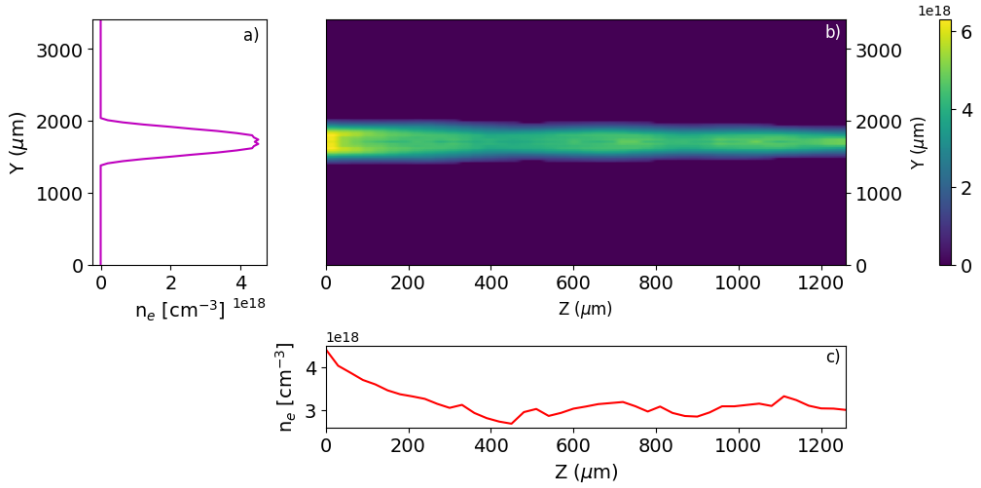

Figure 2.25 – Plasma density distribution across the plasma column. Average non-zero signal of the plasma column, displayed in b), is calculated through longitudinal and transverse projections in a) and c), respectively. The laser travels from right to left in b).

at the centre of the image. The following analysis is conducted for each column in the phase map to create a 2D plasma phase shift map. For each column in the phase map an interpolated spline fit is applied over the region outside of the plasma column from Fig. 2.24 b) to extract the phase shift induced by the background gas and inhomogeneous phase in the probe beam due to pick up extraction of a partial beam. This background fit is then interpolated across the plasma region within the red dashed region as demonstrated by the background fit dashed blue line in Fig. 2.24 d). Here we show only a cropped view to align the scales of the phase map and extracted fits, whereas during analysis this fit is performed across the full gas volume. The background fit is then subtracted from the raw phase shift signal, shown as the orange line, for each column which then retrieves the phase shift due only to the presence of the plasma, shown in d) in magenta. Applying this process over each column, each time extracting a new background fit, allows a 2D phase shift map to be created. This phase map is a 2D projection of the phase shifts induced by the 3D plasma volume, and therefore to estimate the phase shift per unit volume, which is a function of the plasma density, we perform an Abel inversion. These volumetric phase shifts are then scaled to plasma density through calibrated pixel size ($30\,\mu\mathrm{m}$) and critical plasma density as in Eq. 2.15. An inherent limitation of the Abel inversion technique is the assumption of axial symmetry leading to plasma columns which are rotationally symmetric around the laser axis.

Using the method presented above, the plasma density array displayed in Fig. 2.25 was retrieved demonstrating the single-shot capabilities of the plasma column. he horizontal axis is the same as the ones shown in Fig. 2.24 c) and e)

and the vertical axis has been resized to the detector range. As can be seen at the peak value in the longitudinal projection (left), density fluctuations close to the axis are due to the increased error close to the axis of the Abel inversion due to the error scaling inversely with the radial distance from the axis. It was therefore chosen to define the average plateau plasma density as the average of the average transverse projection (lower projection plot in Fig. 2.25 c)). Note that in this plot the values outside of the red dashed region of interest in Fig. 2.24 b) have been set to zero for the plasma phase shift ; an assumption which is confirmed with Fig. 2.24 d) plasma shift extraction, where the plasma shift already goes to zero within this region of interest.

This method was applied to each shot, however, the retrieval efficacy was approximately 53% indicating that further improvements in the phase retrieval algorithm are required. It should, however, be noted, this issue was mostly due to limitations in the imaging system when working with short cell setups, as sufficient phase curvature could only be calculated for a small number of pixels leading to a larger error in the retrieved density. Erroneous measurements were characterised by a zero on-axis density, multiple plasma columns, and thin repeated structures, all of which were seen to arise from a lack of signal being supplied to the Abel inversion algorithm.

WFS results are not well retrieved below $50\,\mathrm{mbar}$ backing pressure due to plasma-induced phase shift being on the order of the fitting noise and therefore all analysis and comparison were conducted above this backing pressure. Comparison of the efficacy of the plasma density retrieval using this self-referenced method are benchmarked against a Mach-Zehnder interferometer used during the second low-energy LPI experiment. Analysis of the Mach-Zehnder interferometer was performed by Francesco Filippi for each dopant percentage and cell length/exit face setting used during the experiment.

2.2.4 . Plasma Density Retrieval Method Comparison

As will be shown in chapter 4, a comparison of the simulated results of Fig. 4.10, small changes in the plasma density can lead to large effects in the resulting laser-plasma dynamics and the resulting electron spectra. To improve the determination accuracy of the plasma density we performed three measurements of the plasma density: a typical MZ set-up with a vertically split reference, where one image was used as an interferogram, and the second as a shadowgraphy measurement, a PHASICS SID4 wavefront sensor (WFS) used to extract the wavefront curvature as a single arm, self-referenced single-shot measurement of the plasma density, and finally, an offline measurement of the gas filling dynamics measured with a rapid camera through a MZ on a replica of the experiment to study the filling dynamics on the 10s µs-scale and also provides a measurement of the plasma density in the plateau region whose results are presented in section 2.2.2. Plasma density measurements were collected during the Bayesian optimisation experiment

presented in chapter 4.

Here we compare the results of these three types of measurements and validate the WFS and rapid camera based methods against the well-tested online MZ set-up. Figures 2.26, 2.27, and 2.28 show the evolution of the plasma density in the plateau region of the gas cell as a function of reservoir pressure obtained with the three different plasma density diagnostics. For this discussion, we refer to the self-referenced wavefront sensor as SRWFS, the rapid Mach Zehnder as RMZ and use the usual acronym for the Mach-Zehnder interferometer. These measurements were conducted in the ELISA gas cell, presented in section 2.2.1, with a $500\,\mu\mathrm{m}$ plateau length. The theoretical line is the maximum achievable plasma density assuming full conversion of the reservoir pressure into cell pressure for the given atomic species.

In general, the three Figs. 2.26, 2.27, and 2.28, show that the three measurements are comparable and provide measurements on different backing pressure scales. The combination of the electron plasma diagnostics with the gas-filling resolution of the RMZ allows for full characterisation of the gas cell plateau. In

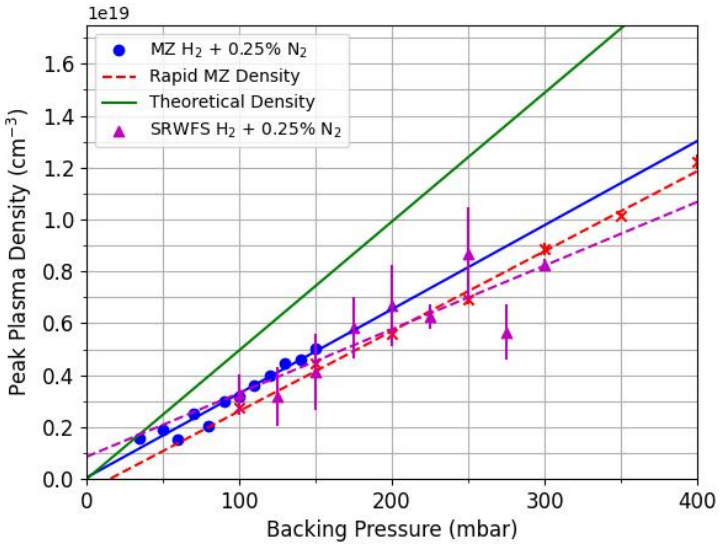

Figure 2.26 – Plasma density as a function of backing pressure for a 99.75% H 0.25% N gas mixture, for online self-referenced wavefront sensor (SRWFS - purple triangles), Mach-Zehnder (MZ - blue circles) directly measuring plasma density and offline temporally resolved Mach-Zehnder (Rapid MZ Red circles) measuring pure hydrogen. Solid and dashed lines represent the line of best fit to the data for the MZ and the novel plasma density diagnostics, respectively. Rapid MZ and theoretical maximum density (green) are scaled corresponding to extra electrons from the dopant percentages. Backing pressures were measured with the same injection system for all cases.

Fig. 2.26 we see that for backing pressures below 200 mbar, the three methods are in agreement. However, the lines of best fit deviate at higher pressures. One

measurement is significantly outside the line of best fit for the SRWFS around a backing pressure of 275 mbar. Shadowgraphy images for this shot indicate that the plasma column is well formed, the Abel inversion is completed correctly and then the density map is constructed well. As there are no MZ measurements at higher pressures for this sample set, it is unclear whether there was a plateauing of the filling rate in these gas pressures on this day or if the difference comes from incorrect plasma phase signal calculation, as the other points agree well with the MZ measurement. Comparison between the rapid MZ and the online MZ in Fig. 2.26, indicates that the two lines of best fit have only a 17% difference in their gradients (rapid MZ: 3.17×10^{16} vs MZ: 3.83×10^{16} cm^{-3}mbar-1) and approximately a 1×10^{17} cm^{-3} shift in their intercept. A systematic error in the MZ measurement of this degree would be below the measurement threshold and should be explored in further work.

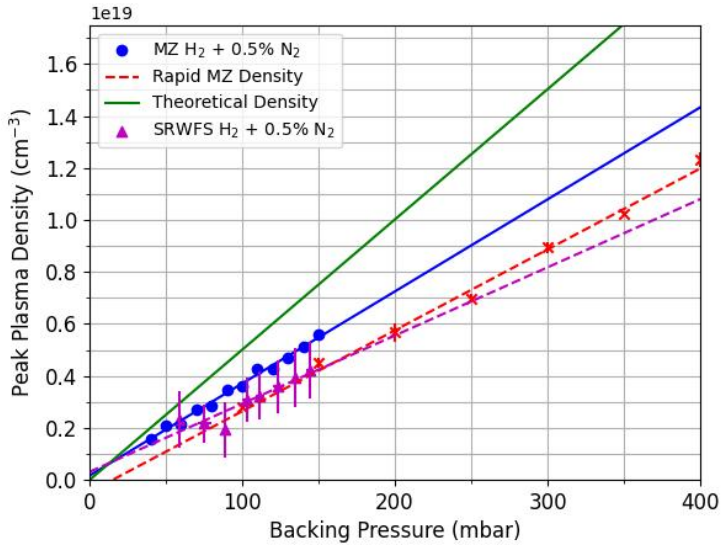

Figure 2.27 – Same description as Fig. 2.26 for 99.5% hydrogen and 0.5% nitrogen dopant.

Figure 2.27 shows a different example of electron density measurements using 0.5% nitrogen. In this case, the best agreement is achieved between the SRWFS and the RMZ where the SRWFS displays the same linear correlation with the MZ over the region 90 to 150 mbar. The measurements are also significantly more stable for the SRWFS as can be seen by the reduced error bars and a linear trend after 100 mbar. At low gas pressures, the limitations in extracting the plasma phase shift from the background noise become apparent for the SRWFS as the points increase in plasma density at lower pressures.

Larger fluctuations in the plasma density, calculated by the SRWFS, are seen in Fig. 2.28 in comparison to the previous examples.During this experimental run,

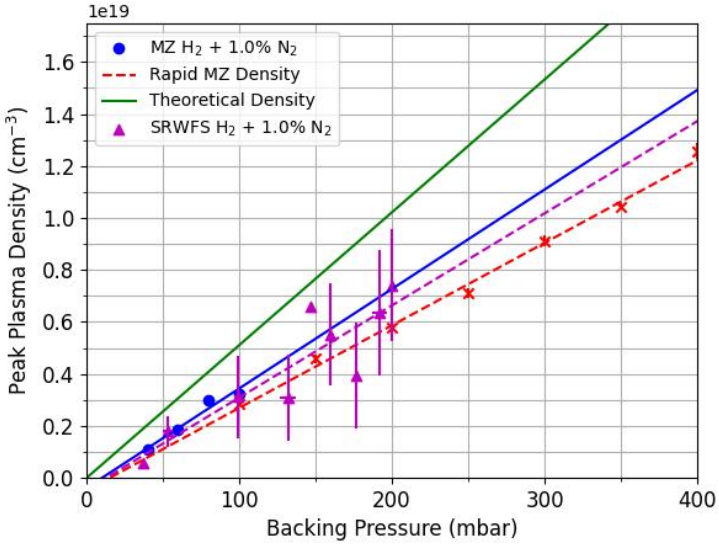

Figure 2.28 – Same description as 2.26 for 99% hydrogen and 1% nitrogen dopant.

measurements of the apparent cell size using the shadowgraphy indicate a line of sight through the cell of $190\,\mu\mathrm{m}$ which corresponds to only six pixels on the SRWFS. As the mean values are still between the MZ and RMZ densities, this indicates that the SRWFS method can work at short cell lengths, but an increase in the measurement uncertainty is seen. As the gas cell is set to plasma plateau length of $500\,\mu\mathrm{m}$, with cell width 40 times greater at 20mm, small angular misalignment of the probe line, or in the cell alignment, can reduce the viewing angle significantly as seen in this set of measurements.

In summary, both the SRWFS and RMZ have been shown to be in good agreement with the MZ interferometer, especially in the region 70-150 mbar where the majority of LWFA experiments were performed. Limitations in the phase retrieval at short cell lengths require higher magnification and more reliable transverse probe alignment.

For long plasma targets such as those presented in chapter 1.6.4, the 30 $\mu\mathrm{m}$ pixel size of the SRWFS limits the field of view whilst keeping adequate resolution on the plasma gradients. One method of tackling this problem is the use of cylindrical optics, which allow the light to be focused on one axis. A system of these lenses would allow for the plasma to be magnified in the vertical direction to provide resolution on the phase curvature and demagnify in the horizontal axis to expand the field of view.

2.3 . Electron Diagnostics

The development of high-quality laser-plasma injectors requires reliable methods to measure the properties of accelerated electrons. Measurements of the charge, energy distribution, and spatial properties of accelerated electrons for short relativistic electron bunches were used to understand the laser-plasma interaction during this thesis. In this section, we will present the theory of energy and charge measurements for the accelerated electrons alongside the parameter definitions of the electrons, which will be used throughout the rest of the results.

2.3.1 . Electron Spectrometer

Here we present the principle of an electron spectrometer consisting of a permanent dipole magnet, scintillator and imaging system and the corresponding energy and charge calibration for this system. The electron spectrometer allows for measurements of the charge, energy and spatial distribution, such as the divergence and average bunch displacement from the accelerator axis, of the electron spectra. Measurements of the accelerated spectra allow us to extract information on the accelerating dynamics produced during the laser-plasma interaction such as the charge injection process, beam loading, accelerating gradients of the wake, etc. Whilst the specifics of each design are different in each experiment presented in this thesis, the basic principle remains the same throughout: accelerated electrons beams are dispersed in terms of energy through interaction with the magnetic field of a permanent dipole magnet. The interaction between this energy-dispersed beam and a scintillating screen produces transient radiation in the visible spectrum which is then imaged by a high-dynamic range camera system. A counts-to-charge calibration is then performed - which is outlined below in sections 2.3.1.3 and 2.3.1.4 - on the imaging system, allowing the dQ/dE to be calculated for each spectrum which can be used for peak detection to calculate electron parameters. Spatial calibration is also performed to recover the pixel-to-energy scaling from the theoretical electron dispersion curves due to the magnetic field and geometric distances. The spatial properties of the electron bunch in the non-dispersive plane can then also be calculated from the geometric distances from the electron source to the scintillator and changes in path length due to the curved path in the magnetic field.

2.3.1.1 . Calculation of Electron Trajectories

Dispersion of an electron bunch in terms of energy allows us to measure the number of electrons at each energy within our measurement range (which is determined by the magnet strength and imaging system.) Electron paths between the LPI source and scintillator can be theoretically calculated to produce an energy-space calibration of the imaging set-up. We begin by assuming non-divergent electron bunches so we can neglect off-dispersive plane displacements. Before and after the magnetic field of the magnet the electrons are freely propagating where only

the drift velocity from the divergence of the electron bunch from the source alters the path of the electrons.

Once an electron enters the dipole magnet with constant magnetic field B_0 transverse to the motion of the incoming electron bunch, it will undergo a partial circular trajectory with a constant angular frequency, ω_c, which is defined as the relativistic cyclotron frequency:

$$\omega_c = \frac{eB_0}{m_e\gamma_e}\,, \tag{2.16}$$

where we have included γ_e for the relativistic mass corrections to the electron mass, m_e. Assuming relativistic electron motion, which is applicable to all electron spectrometer energy detection bounds used during this thesis, the radius can then be calculated as:

$$R_c = \frac{c}{\omega_c} = \frac{cm_e\gamma_e}{eB_0}\,. \tag{2.17}$$

The relativistic energy for a particle is given by

$$E_{rel}^2 = m_e^2c^4 + p^2c^2\,. \tag{2.18}$$

When the rest mass is much less than the particle momentum, i.e $m_ec \ll |\vec{p}|$, we can neglect the rest mass term and using the relativistic momentum where $v_e \approxeq c$ retrieve γ_e as:

$$\gamma_e \approx \frac{E_{rel}}{m_ec^2}\,. \tag{2.19}$$

Combining equations 2.17 and 2.19 gives us the Larmor radius in terms of the particle energy:

$$R_c = \frac{c}{\omega_c} = \frac{1}{eB_0}\frac{E_{rel}}{c}\,. \tag{2.20}$$

In our simple zero-divergence example, we take the origin of the circular portion of the electron's trajectory to be at the centre of the magnet gap. We can then define our coordinates as in Fig. 2.29 with y in the vertical axis, x transverse to the magnetic field and z longitudinally along the initial electron propagation direction.

For an arbitrary geometry, we can then calculate the time-dependent position of a particle interacting with the magnetic field before free propagation as:

$$\theta(t) = \omega_c t\,, \tag{2.21}$$

$$x(t) = R_c\left[1 - cos\left(\theta(t)\right)\right]\,, \tag{2.22}$$

$$y(t) = 0\,, \tag{2.23}$$

$$z_B(t) = z - z_{i\ magnet} = R_c \sin\left(\theta(t)\right)\,. \tag{2.24}$$

$$\tag{2.25}$$

where θ is the angle in the $x0z$ plane. We can then calculate the angle of exit as:

$$\theta_x = \arccos\left(1 - \frac{W_B}{R_c}\right) , \tag{2.26}$$

$$\theta_z = \arcsin\left(\frac{L_B}{R_c}\right) , \tag{2.27}$$

$$\theta_{exit} = min[\theta_y, \theta_z] . \tag{2.28}$$

where W_B and L_B are the half-width (in the x-direction) and full length (in the z-direction) of the magnet respectively. It is necessary to take these two conditions into account for electrons at different energies where they can exit at the side or end of the magnet.

Using the above equations we perform electron tracking for the f9 Apollon campaign presented in chapter 5, where the realistic magnetic field map (i.e using a 3D array of magnetic field strengths inside and outside of the bulk of the magnet) was used with a mean field of 1.73T, 250mm length, 100mm width and a 17mm gap. Measurements performed by LLR indicated that edge fields were minimal. Using the above equations of motion for the electrons in free drift and interaction

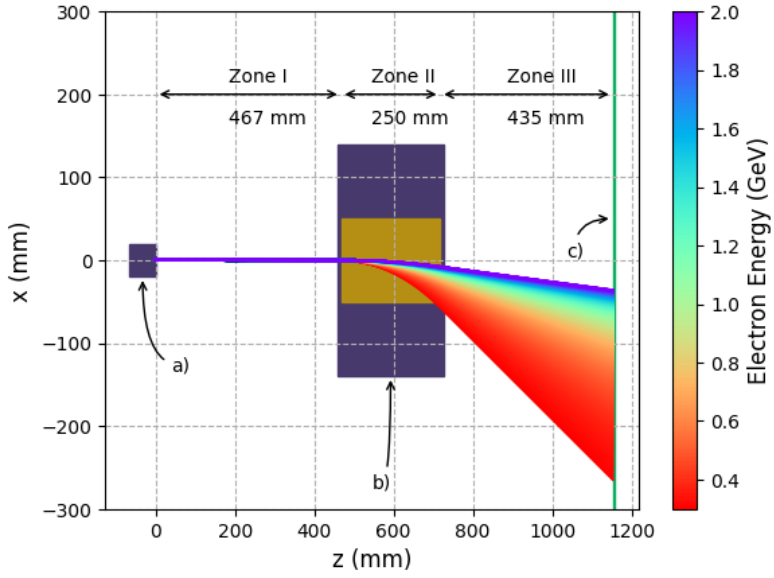

Figure 2.29 – Electron trajectory tracking for electron energies between 0.4 to $2.0\,\mathrm{GeV}$. a) electrons accelerated from the LWFA process exit the gas cell and freely propagate in zone I. In zone II the magnetic field of the dipole magnet, b), then deflects the electrons as a function of their energy. In zone III the electrons freely propagate again until they reach the diagnostic axis at c).

with the magnetic field of the dipole, we can produce Fig. 2.29 where the paths of the electrons with different energies are mapped throughout the electron spectrometer. From Fig. 2.29 we can see that as the electron energy increases, their deflection angle decreases placing them closer to the laser axis at x = 0.

A complication of the high-energy spectrometer was the inclusion of electrons which exit at the side and the end of the C-shaped magnet. This leads to a discontinuity in the electron tracking which corresponds to the corner of the magnet closest to the scintillator. The high field of the magnet is, however, required for having ample resolution of electrons at high energy and is, therefore, a design choice which must be considered.

From this analysis, it can be seen that the design of the spectrometer in terms of magnet strength, and geometric layout of the magnet and scintillant, will determine the energy measurement range and the resolution at each energy i.e the δE for each pixel along the energy dispersion axis.

2.3.1.2 . Calculation of Induced Energy Error due to Divergence

Electron bunches will have a finite divergence due to the injection and accelerating processes inside the wake occurring over finite volumes. Taking a non-zero initial divergence we can solve the equations of motion with the addition of an initial displacement term into the dipole with allows us to produce Fig. 2.30. Figure 2.30

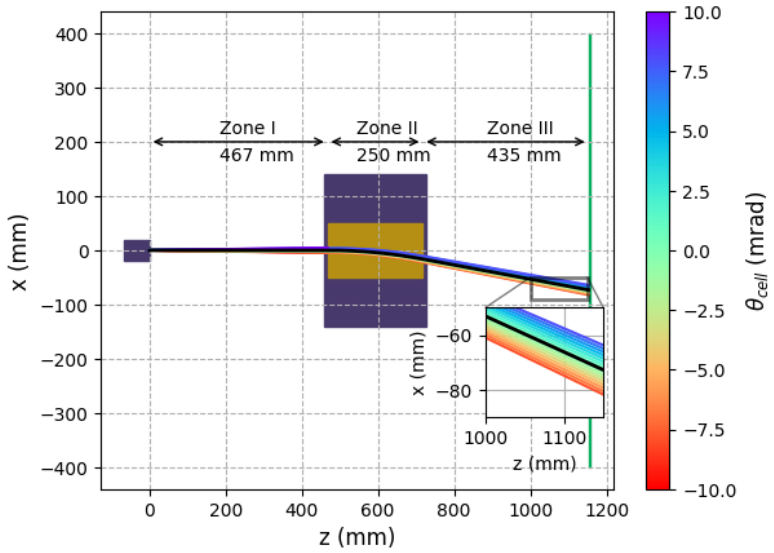

Figure 2.30 – Electron trajectory tracking for electron energy of $1\,\mathrm{GeV}$ and a range of laser-plasma exit angles, θ_{cell} between $\pm 10\,\mathrm{mrad}$. The black line indicates the position of the detector with zero initial angle.

shows electron trajectories with a non-zero initial angle at the exit from the gas cell for $1\,\mathrm{GeV}$ electrons. This finite divergence exists in both the spatial and energy-dispersion planes, leading to uncertainties in the energy measurement which must be taken into account. We can calculate the induced error for a known divergence in the energy plane, however, during experiments we do not have access to this information. So this requires that we assume that the divergence measured in the non-dispersive plane is on the same order as the divergence in the energy-dispersion

plane. This assumption is valid for symmetric accelerating cavities as they will lead to similar divergences in both transverse axes. One effect to be considered, however, is the laser polarisation plane which leads to electron bunches with larger divergences in this plane[133]. This effect arises from the ionised electrons gaining momentum in the laser polarisation direction[134]. In the case where the dispersive plane of the dipole magnet is aligned to the polarisation direction, literature values for expected increases in electron bunch divergence can be included in the energy errors.

2.3.1.3 . Charge Determination from Scintillator Based Diagnostics

Theoretical CCD count-to-charge calibration can be performed using the following method and using calculated constants for LANEX screen emission. An example of this calculation is given here for the electron spectrometer imaging system used during the low energy injector Bayesian optimisation experiment (section 4.2.) However, the processes is similar for other spectrometer geometries.

The charge calibration depends on:

— Scintillator used ;

— Collection efficiency of the imaging system ;

— Solid angle of the light collection ;

The type of scintillator determines the calibration factor of photon emission to impinging charge. During this thesis, most measurements used LANEX as the scintillating medium. However, a YAG-based crystal detector was also implemented during the second Apollon campaign outlined in section 5.2. This was however calibrated using the method described in section 2.3.1.4. The collection efficiency can be calculated using a power calibrated laser where the transmission ratio is calculated from the source position to the CCD position using a calorimeter. Finally, the solid collection angle can be calculated geometrically from the light collection and transport optics.

Using the geometric layout of the light collection optics in Fig. 2.31 resulting in a total distance of $54\,\mathrm{cm}$ and noting that the 50 mm/1.8 Nikon Nikkor camera objective used with the Princeton Instruments Pixis 400 has an aperture diameter of $3.5\,\mathrm{cm}$ we can calculate the CCD collection solid angle as:

$$\frac{A_{objective}}{r^2} = 3.30 \times 10^{-3}\mathrm{sr}\,. \tag{2.29}$$

Using the value for solid angle photon emission per pC charge given by Kurz *et al.*[135] for Carestream LANEX Regular as 3.1×10^9 ph/sr pC. and the geometric collection solid angle, we calculate the portion of photons that are collected, giving the photons per pC as 1.023×10^7ph pC^{-1}. Using a 520 nm, calibrated light source, set to 1.00 mW, directed at the camera, the approximate number of photons per count can be calculated using the energy per photon to find the number of photons

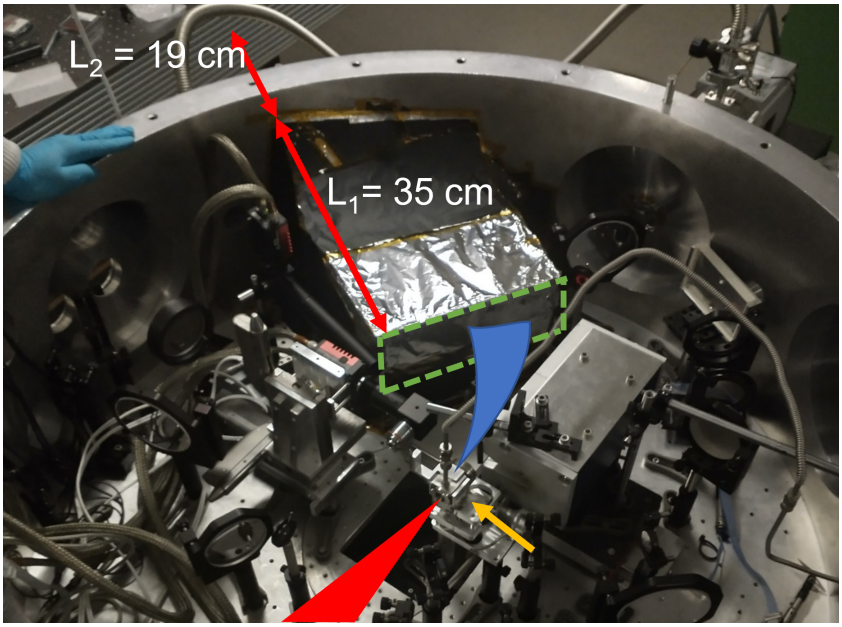

Figure 2.31 – Image of the experimental set-up of the dipole-LANEX electron spectrometer at the LLC. The electrons, shown in blue, which are accelerated by the laser, shown in red, from the gas cell, indicated with the yellow arrow, are dispersed in energy (even though the dipole magnet is off-axis in the displayed image.) The boundary of the LANEX screen, protected by a piece of aluminium foil, is shown with the dashed green line. Distance L_1 and L_2 are the distances between the LANEX screen and the vacuum window and the 16-bit CCD chip respectively. The view of the camera is obscured here by the vacuum chamber.

over a short period of 20 ms which was also used for the acquisition during the experiment:

$$P = \frac{\mathcal{E}}{\tau} = \frac{n_\gamma \hbar \omega}{\tau} \tag{2.30}$$

where $\mathcal{E}$ and n_γ are the total energy and the number of photons respectively. The acquisition time of the camera is optimised such that it opens just after the passage of the laser pulse to limit x-ray noise on the camera produced during the laser-plasma interaction from electron-ion recombination, laser-cell/dipole interaction, etc., and for a sufficiently short time to minimise thermal noise on the camera. Integrating the total counts on the camera from the continuous wave power calibrated laser for a short exposure time allows for the number of counts per photon to be calculated. We found $n_\gamma = 4.587 \times 10^8$ photons for 1.168×10^8 counts leading to approximately 3.927 photons/count. Finally, we can scale this value by the power-calibrated transmission ratios of the imaging objectives to retrieve the count to charge calibration and arrive at 5.1×10^{-4} fC/count.

Performing this calibration for other scintillating-based electron detectors requires calculating the collection angle, measuring the transmission of the imaging

system, and applying standard emission values for the scintillant. For the Apollon experiments presented in chapter 5, this process was performed for the LANEX-based electron spectrometer that used a periscope system to transport the emitted light above the experimental chamber to the radiation-protected CCD. The collection angle of these mirrors and the imaging objective on the camera were then taken into account providing a count-to-charge calibration of 4.1×10^{-2} fC/count.

2.3.1.4 . Integrating Current Transformer Charge Calibration

During two of the four experiments (low energy injector Bayesian optimisation - section 4.2 - and high-energy injector f9 - section 5.2) conducted during this thesis, an integrating current transformer (ICT), shown in Fig. 2.32, was implemented, and the results analysed by the LIDYL group. This device measures the total charge through an aperture allowing for the direct measurement of the bunch charge without the imaging system calibration defined above in section 2.3.1.4. However, it sacrifices information on the bunch's spatial properties and energy spectra.

The operating principle of an ICT can be understood from the Fourier transform of an arbitrary bunch current profile in time, $i(t)$, into frequency space[136]:

$$I(\omega) = \int_{-\infty}^{+\infty} i(t)\, e^{-i\,\omega\, t}\, dt, \quad I(0) = \int_{-\infty}^{+\infty} i(t)\, dt = Q \tag{2.31}$$

Disregarding the higher frequency terms and taking only the DC bias ($\omega = 0$) removes our knowledge of the bunch shape, but provides us with information on the total charge of the bunch.

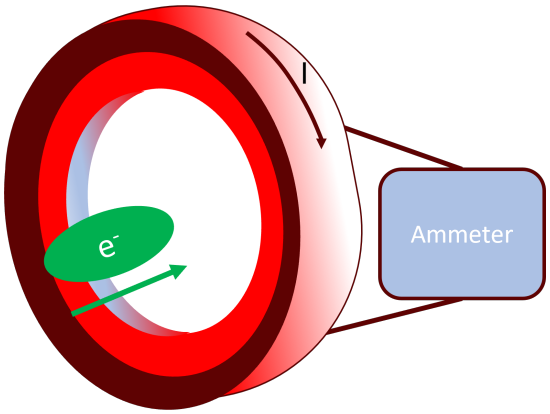

Figure 2.32 – Simplified principle of integrating current transformers. Current induced in a secondary conducting medium from the magnetic field from the current of a charged particle bunch (here electrons.) is used to calculate the total charge of the particle bunch.

Figure. 2.33 shows the method for charge calibration of the LANEX and YAG electron scintillating detectors used during the second Apollon high-energy LPI campaign in section 5.2. To calibrate the charge of the other destructive electron

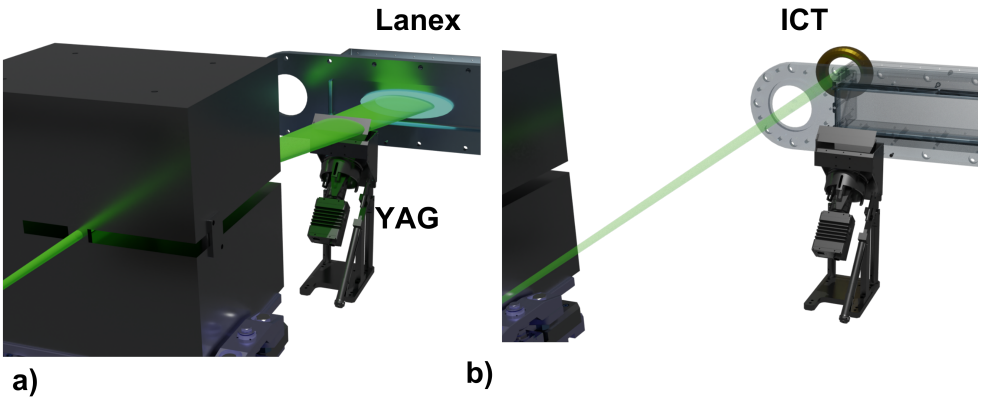

Figure 2.33 – a) Dipole magnet on the beamline dispersing the electrons (in green) in terms of their energy onto the YAG and LANEX scintillant detectors. b) Dipole magnet off beam line, electron bunches leave the vacuum through the flange and their charge is measured by an ICT. The LANEX screen has been made transparent for visibility.

diagnostics, experimental parameters were optimised to achieve spectra which were stable in terms of total charge from shot-to-shot. A sample set of data were then collected on the LANEX and YAG crystal detectors at different set pressures to vary the quantity of charge on the detectors. The dipole magnet was then removed from axis so that the electrons propagate through the aperture of the ICT and the same pressure settings were used. This was completed over several shots and the average charge calibration was calculated from the signal on the destructive and ICT electron diagnostics; this calculation was completed by Matthew Streeter.

2.3.2 . Electron Parameter Definitions and Calculation Methods

From the energy-dispersed electron spectra, many physical parameters of the electron bunch can be calculated. Here we will describe how the different parameters calculated during this thesis for the electron bunches are defined and calculated, including total and peak charge, bunch energy, maximum bunch energy, average displacement angle and bunch divergence.

Figure 2.34 shows an example of typical parameter extraction for a peaked electron spectrum achieved during the campaign described in section 4.2. The following section uses this figure to describe how electron parameters are defined.

2.3.2.1 . Charge Parameters

The total charge is defined as the integrated signal of $\mathrm{dQ/dE}$ over all energies:

$$Q_{tot} = \int_{E_{min}}^{E_{max}} \frac{dQ}{dE} dE \,, \tag{2.32}$$

where E_{min} is cropped in Fig. 2.34 to $30\,\mathrm{MeV}$ and E_{max} to $150\,\mathrm{MeV}$.

Peak charge was chosen to be calculated as the integral of the charges within the blue *and* red shaded regions of Fig. 2.34 as global analysis of the electron

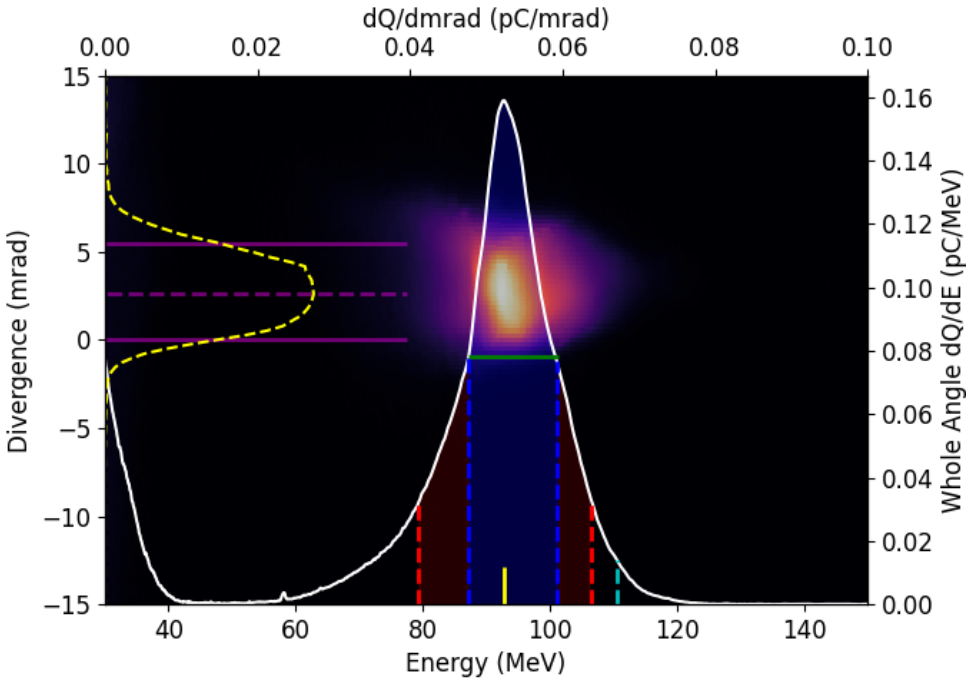

Figure 2.34 – Electron distribution in divergence-energy space. The whole angle dQ/dE (pC/MeV) is displayed with the solid white line. The energy at the peak dQ/dE is marked by the vertical yellow line. Full-width-half-maximum (FWHM) dQ/dE is shown by the horizontal green line. The FWHM region is shown by the blue-shaded region. 2×FWHM is shown by the red shaded region. The maximum energy is shown by the vertical cyan line. The yellow dashed line is the lineout in pC/mrad through the bunch at the peak energy corresponding to the column marked by the peak energy. Solid magenta horizontal lines indicate the FWHM limits on the bunch in the divergence axis. The dashed horizontal magenta line is the average angular displacement of the bunch over the energy FWHM in the divergence plane.

spectra was seen to be sensitive to the calculation of the FWHM. Using 2×FWHM, therefore, represents a higher value of charge, but better captures the charge within the peaked region for analysis and comparison to the simulated results. This is therefore defined as:

$$Q_{peak} = \int_{E_{-2FWHM}}^{E_{+2FWHM}} \frac{dQ}{dE} dE \,, \tag{2.33}$$

where $\pm 2FWHM$ corresponds to the upper and lower vertical red dashed lines respectively.

2.3.2.2 . Energy Parameters

Maximum energy is defined as the energy value in which the $\mathrm{dQ/dE}$ signal drops to 10% of its peak value in the positive energy direction. The choice of 10% allows for the signal to remain above background noise whilst still well describing the maximum achievable electron energy of the system.

The energy spread of the bunch is calculated as the FWHM width in energy, illustrated with the horizontal green line, divided by the peak energy value shown by the vertical yellow line as a percentage.

The total energy contained within the bunch can be extracted by calculating the number of electrons from the charge in each energy bin and then scaling by the absolute energy of each bin. This process is completed for both the total energy range and the energy range defining the peak of the spectra which gives the total and peak beam energy respectively. This parameter provides a measure of the transformer efficiency between the energy contained within the drive laser and the extracted energy converted into the electron momenta. It should be noted that the bunch energy in this case is in units of Joules rather than electron volts.

$$Q_i = dq_i \times dE_i \; \forall i \tag{2.34}$$

$$\mathcal{E}_{e^-} = \sum_{i=E_-}^{E_+} Q_i \times E_i \tag{2.35}$$

where E_+, E_- are the upper and lower energy limits which for the total and peak energies are defined as: $E_- = E_{min}$, $E_+ = E_{max}$, and $E_- = E_{-2FWHM}$, $E_+ = E_{+2FWHM}$, respectively. The energy of an electron in MeV is then converted to Joule for comparison to the laser driver energy by multiplying by 1.6×10^{-13} from the definition of the electron volt.

2.3.2.3 . Spatial Parameters

As the electron bunch is dispersed in energy along a single axis, we can extract information from spectrum measurement on the spatial quality of the beam in the transverse axis. We use this to calculate the bunch divergence and angular displacement from the accelerator or reference laser axis in vacuum (equivalently, the average divergence.) The accelerator axis was defined in the experiment by sending an attenuated laser onto the scintillator and measuring the average pixel position on the scintillating screen.

A lineout of the dQ/dmrad signal extracted at the peak energy is shown by the dashed yellow line in Fig. 2.34. The horizontal magenta lines display the FWHM for this lineout. The distance between these two lines is defined as the divergence of the electron bunch at a single energy. The FWHM is calculated for all lineouts within the blue region of Fig. 2.34 to calculate the average divergence of the bunch. Similarly, the average angular deviation of the bunch is calculated by finding the displacement of the peak in the spatial axis for each lineout and averaging over these values, as shown by Fig. 2.35.

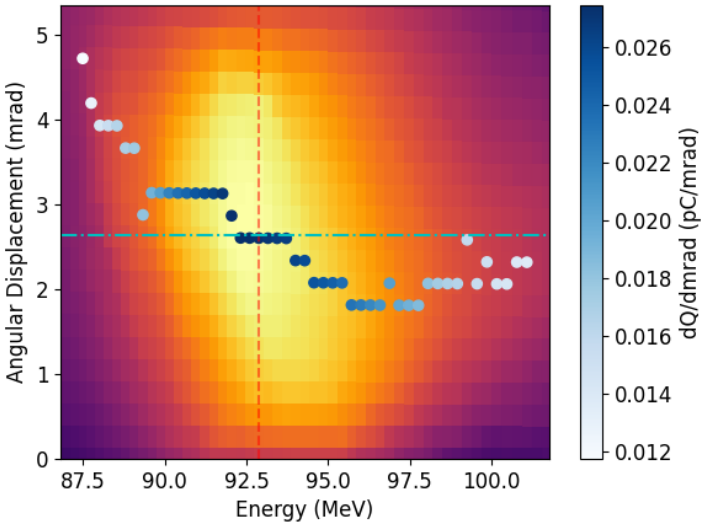

Figure 2.35 – Illustration of the angular displacement of the electron bunch calculated from the FWHM around the peak in dQ/dE shown by the vertical dashed red line. Divergence-energy spectrum is the same data as Fig. 2.34 cropped to the FWHM in energy. The average displacement is shown by the dash-dotted cyan line. The values have been charge-weighted (dQ/d mrad).

3 - Introduction to Numerical Tools: Machine Learning and Simulation

This chapter covers the theory and development of numerical tools applied during this thesis including machine learning techniques applied to laser wakefield acceleration experiments and particle-in-cell (PIC) simulations using realistic laser descriptions. The application of Bayesian optimisation for finding experimental optima is presented with an explanation on the theory of Bayesian optimisation and relevant terminology. Implementation of realistic laser descriptions in the simulations is shown to improve the accuracy of simulated results (results described in section 4.1.3.2). We therefore describe the method of calculating the modal description of the complex electric field of the laser via transverse fluence images around the focal plane which can then be introduced into simulation codes. In this chapter, the development of a generative adversarial model (GAN) which allows for the on-shot focal spot to be reconstructed will be presented. Particle-in-Cell simulations provide an invaluable tool for the study of underlying physical processes of the highly non-linear interaction between laser and plasma at the heart of laser wakefield acceleration. A general description of PIC simulations will therefore be provided, followed by the specifics of the Fourier-Bessel PIC code (FBPIC) used for simulation results and details on the inclusion of realistic laser profiles in these simulations.

3.1 . Machine Learning

The use of machine learning (ML) techniques in LWFA is an emerging field[137]. In this section we focus on signal prediction networks through the use of a trained neural network (NN) to predict on-shot focal spots, and on the problem of experiment optimisation, where we applied Bayesian Optimisation (BO) to perform high-dimensionality optimisation searches during an LWFA experiment.

3.1.1 . Artificial Neural Networks in Laser-Matter Interaction

Artificial neural networks have been applied to the prediction of experimental results, and automated analysis in laser-matter interaction experiments. Typically NNs are used to correlate complex relationships between input and output states which have difficult to characterise, or hidden, relationships[138]. The large quantity of data obtained from a large number of diagnostics during experiments, and the nonlinear interaction between the laser and plasma, make LWFA experiments prime candidates for the application of NNs.

To understand the cause, and predict the effect of electron parameter fluctuations from laser driver fluctuations in a laser wakefield accelerator, Kirchen *et al.*[70] trained a NN to estimate the beam charge, median and spread of energy from 15 laser parameters. During NN training they used the mean absolute error between the real and estimated electron parameters as the loss function. Including only the laser parameters, they were able to estimate the electron parameters to a coefficient of determination better than 0.73 meaning that at least 73% of the variance in the electron parameters can be explained by the variance of the input parameters using their NN. NNs have also been developed for ion acceleration to predict the ion energy and temperature using experimental inputs[139].

NNs have also been used for automated analysis where for example, Simpson *et al.* used a NN to perform rapid analysis of the x-ray spectra resulting from the betatron oscillations of electrons in an LWFA experiment[140]. This application of NNs to data processing allows for the speed-up of diagnostics necessary for future high-repetition-rate LPIs.

Calculation of wavefront distortion and Zernike polynomials (discussed in section 2.1.1.3) from intensity image distortion was performed by Wang *et al.*[141] where they created two encoder-decoder architecture for atmospheric turbulence correction for telescopes.

During this thesis, we trained a NN for image-to-image translation to reconstruct the focal spot of the drive beam using measurements of a fraction of the main beam, on a spatially separated camera. The reconstruction of the transverse fluence profile of the focal spot is possible due to the large degrees of freedom that can be encoded by the NN to describe the complex changes between the two focal spot images due to alterations in imaging set-up, the spectral transmission of the extraction and imaging optics, differences in the magnification, etc. that would be extremely difficult to map analytically. To the author's knowledge, this is

the first time that a machine-learning method has been applied to laser focal spot reconstruction.

3.1.2 . Generative Adversarial Networks : Neural Networks for Image-to-Image Transfer

During laser experiments, a portion of the focusing beam is typically sampled to track pointing fluctuations. It would be, however, beneficial to have knowledge of the fluence distribution alongside these measurements. We therefore applied neural networks to the problem of image-to-image translation where one input image is mapped to another. Here we will present the theory of the neural network architecture that was used to produce this model, and in section 3.2.2 describe the experimental implementation, training of the model, and the resulting efficacy of the focal spot retrieval.

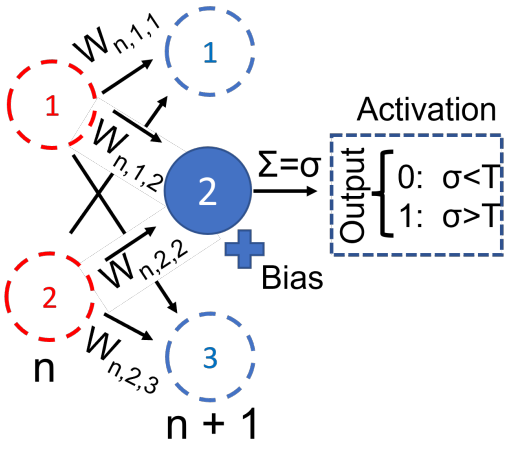

Figure 3.1 – Overview of a sub-network neuron with two input and three output connections as part of a larger network. We examine the output of neuron 2 in layer n+1. Signals from the input neurons are weighted and summed. If the output of the sum, σ, is greater than some threshold value, T, a 1 will be output and 0 otherwise. This simple type of threshold is referred to as threshold logic unit[142]. This output is generalised over all neurons. Weight notation for the first to third and second to first neurons of layers n to n+1 have been omitted for clarity.

Artificial neural networks are systems of neurons which take inspiration from biological neurons[142]. On a basic level, these act as signal processors, where an input signal passes through n-layers of m-neurons (where the number of layers, and neurons in each layer, changes depending on the application) resulting in a processed output signal. A simple overview of a small portion of an artificial neural network is depicted in Fig. 3.1. In red, we have the first layer which we will consider as the input in this example and where the input neurons, marked with 1 and 2 in red, are connected to every blue neuron in the second layer. The weighting on each

connection, which controls how the signal is processed by each neuron, is defined with $W_{n,m,i}$. Here i refers to the weight of the connection to the i^{th} neuron of the $n+1$ layer from the m^{th} of the n^{th} layer. We have excluded the weighting on the two longest connections (red 1 to blue 3 and red 2 to blue 1) for clarity. Each neuron also contains a bias, which is shown for the case of blue 2. This is a constant added to the summation of all the signals entering a neuron, which alters the level of signal required to activate the neuron and pass a 1 signal rather than a 0. This process is displayed for blue 2 where the input connections are multiplied by their weights, summed, a bias is added, and then this value is checked against a threshold value which determines whether the neuron sends a 1 or a 0 to the next layer. This weighting between the neurons and the biases of the neurons are typically what is "trained" when creating a neural network for a specific application.

Neural networks are useful for image processing tasks as they allow for complex relationships between the pixels of pre- and post-transformed images to be mapped. Classically, during image-to-image translation tasks, where an input image array is mapped to an output image array, a neural network model would be produced on a pixel-by-pixel basis to perform the translation. This results in each pixel's model being independent of the surrounding pixels. In the case of focal spot reconstruction from a spatially distinct camera - as targeted in this work - it was hypothesised that the relation between a single pixel in the reference and measurement images would likely not be strongly correlated, but the overall structure of the focal spot, in terms of both energy distribution and average position, would play a stronger role in focal spot prediction. This was hypothesised due to the different imaging systems used on the cameras where the apparent pixel size was significantly larger for the reference camera meaning that a one-to-one mapping of the pixels between the cameras could not be achieved. During the development of a focal spot prediction artificial neural network, we chose to use a Generative Adversarial Network (GAN) as the model. GANs were chosen as they provide a generalised approach to artificial neural network building which trains on the structure of sub-regions of the input and target data[143], and have had success in other image prediction and translation applications[144]. They are fully unsupervised in their training where the user needs only to supply grouped sets of input and output images. Specifically the "pix2pix" method, developed by Isola *et al.*[143], was chosen due to its flexibility and efficacy in image translation.

A further advantage of GAN models arises from their architecture, displayed in Fig. 3.2, where the generator and discriminator are shown. A difficult task in image-to-image translation is describing a loss function which can be minimised during the training of the transfer neural network. Rather than directly training on a predefined loss function, the model is trained on a loss that tries to classify whether an image is real (from the input sample set) or fake (generated by the generator model)[145]. It is this method of training that provides GANs with flexibility as the loss function adapts to the data type.

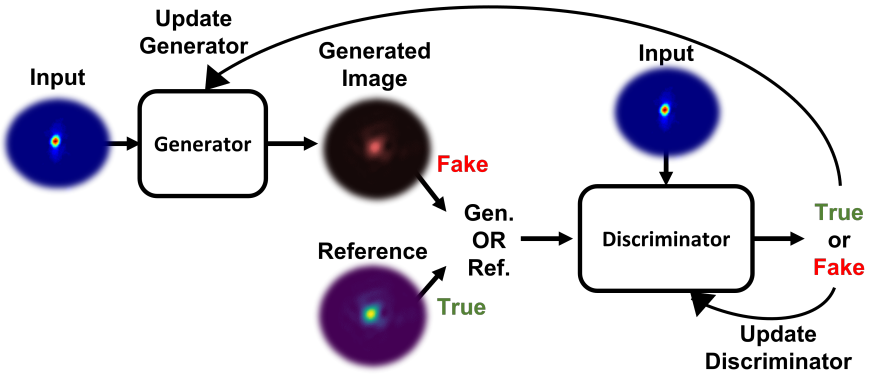

Figure 3.2 – Simplified process of generative adversarial model training. We use here the example of laser focal spots, however, the process is generalised for all types of images. The generator is given an input image, which it then uses to create a generated "fake" image. Either the fake image or the matching reference image for the input image, are then given to the discriminator. The discriminator then attempts to determine if the image is fake or not by comparison to the input image. If the discriminator chooses correctly it is positively rewarded and the generator is negatively rewarded as it has not been able to fool the discriminator. If the discriminator chooses incorrectly it is negatively rewarded as it has been fooled by the generator which is then positively rewarded. This competition continues, with the generator and discriminator improving at their respective tasks.

This specific type of GAN model employed in this work is classified as a conditional generative adversarial network (cGAN)[146]. This means that the discriminator in Fig. 3.2 has knowledge of the input image. To train a neural network we need something to describe how well it is performing ; this is the role of the loss function[147]. The loss function of the cGAN is described by[143]:

$$\mathcal{L}_{cGAN}(G,D) = \mathbb{E}_{x,y}\left[\log D(x,y)\right] + \mathbb{E}_{x,y}\left[\log(1 - D(x,G(x)))\right] , \tag{3.1}$$

where G, D are the generator and discriminator respectively, $\mathbb{E}$ is the expected value, and x, is the input image, y the reference image.The first term on the right-hand side refers to the discriminator being able to correctly distinguish that an image is real given the input and reference image, and the second term refers to the discriminator being fooled by the generator. The generator, G, acts to minimise equation 3.1 whilst the discriminator, D, attempts to maximise it. The usefulness of this type of neural network architecture is that the loss function, $\mathcal{L}_{cGAN}$, in Eq. 3.1, is defined by the discriminator and so we do not have to define a specific loss function for training the generator that could bias the type image transformations that are produced.

3.1.3 . Bayesian Optimisation

Black-box functions are those in which we observe only the input and output values without knowledge of the functional form. Performing a maximisation of

this black box function can be described as:

$$x^{\star} = \arg\max_{x \in \mathcal{X}} f(x) \tag{3.2}$$

where f is our black-box function, x is a choice of input parameters that is a subset of all possible input parameters $\mathcal{X}$, and the arg function extracts the argument of the function. Bayesian optimisation (BO) is a machine learning algorithm for optima finding of expensive to evaluate black-box functions. In our examples, the black-box functions are the merit functions that we try to optimise. These are based on the underlying physical processes during the laser-plasma interaction and are characterised in terms of measurable parameters such as total charge, average electron energy, average angular deviation from the accelerator axis, etc. The advantage of Bayesian optimisation arises from the optimisation process as it uses a surrogate model to optimise the merit function rather than direct optimisation of the function itself.

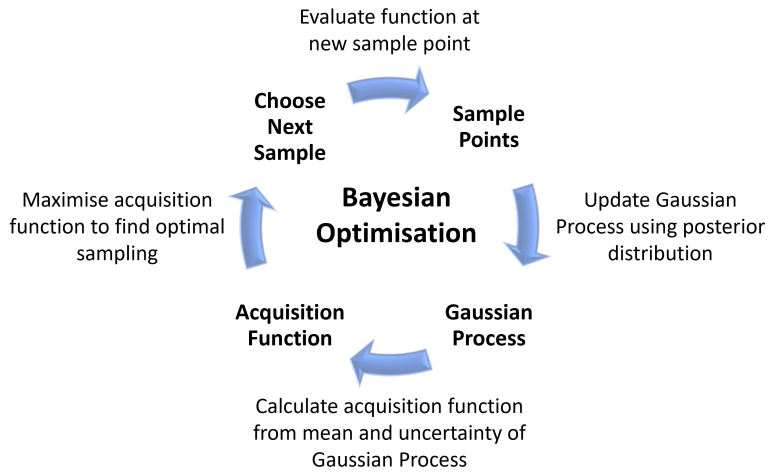

Figure 3.3 – Overview of the Bayesian optimisation process.

The BO process can be dissected into four main steps as shown in Fig. 3.3. We will describe the process here before defining in more detail the specific terms below.

First, data points are observed and a merit function is evaluated on these points to produce an initial data set. Secondly, a surrogate model is built to describe these sampled points in terms of a posterior distribution which is typically a Gaussian Process. Next, an acquisition function is created from the posterior distribution, which is then maximised, dictating the next optimal point for sampling. Finally, this new data point is sampled and added to the list of sampled points to update the posterior distribution. This process is then repeated allowing the black-box function to be maximised until a target value or number of iterations is achieved. A detailed discussion of each of these processes follows.

3.1.3.1 . Sampling and Merit Functions

Initial data sampling to provide a basis for the surrogate model is provided by random sampling or known data points. In the case of laser wakefield experiments, this would correspond to data point sampling within physically reasonable parameters in terms of focal position, plasma density etc. corresponding to previous facility or literature results. An example starting sample set, if not randomly sampled, could include, for example, plasma densities far from resonant conditions, which for a given laser system, will likely lead to no electrons being trapped and accelerated, and plasma densities close to resonant condition, such that the model quickly learns the merit function scaling with the plasma density.

3.1.3.2 . Gaussian Processes and Kernels

After the initial sampling, the surrogate model then fits the observed data points and attempts to quantify the mean value and uncertainty of the parameter space which is yet to be sampled. This process is completed by a Gaussian process that makes assumptions on the behaviour of the black-box function without assumptions on the functional form[148]. For example, a Gaussian process assumes that the function is smoothly varying and that points close together in the input parameter space will result in points close together in the output parameter space[149]. The Gaussian processes are described in terms of their predicted mean and uncertainty as a function of each point in the input parameter space.

Given a distribution of sample measurements, there are many functions that will fit these samples. Gaussian processes calculate the mean from the probability distribution of all these possible functions providing the most likely function which describes the sample data[150]. The Gaussian process produces a posterior distribution which describes the uncertainty in the model of the function from the set of sampled points. Fig. 3.4 illustrates fitting by the Gaussian process applied to randomly selected sample points with no optimised sample selection.

The code to produce this figure was adapted from the example code provided with scikit-learn[151]. Figure 3.4 a) illustrates the prior distribution of functions $Y = f(x)$, where no data points have been sampled. In this case, the average of the sampled functions will form a Gaussian distribution around the mean value at zero. After sampling in Fig. 3.4 b) the standard deviation close to the sampled points decreases, which can be understood from the constrained functions in this region producing a Gaussian distribution with a smaller standard deviation. Continued sampling in Fig. 3.4 c) - f) reduces the standard deviation throughout the space and provides a Gaussian process where the posterior distribution is a good approximation of the toy model displayed with the red line in Fig. 3.4 f).

The chosen kernel calculates the uncertainty for the unsampled points in the parameter space. The kernel, or covariance function, encodes the assumptions on how similar (equally correlated) two points in input parameter space are, allowing for uncertainty on this space to be approximated[148]. This is where the above

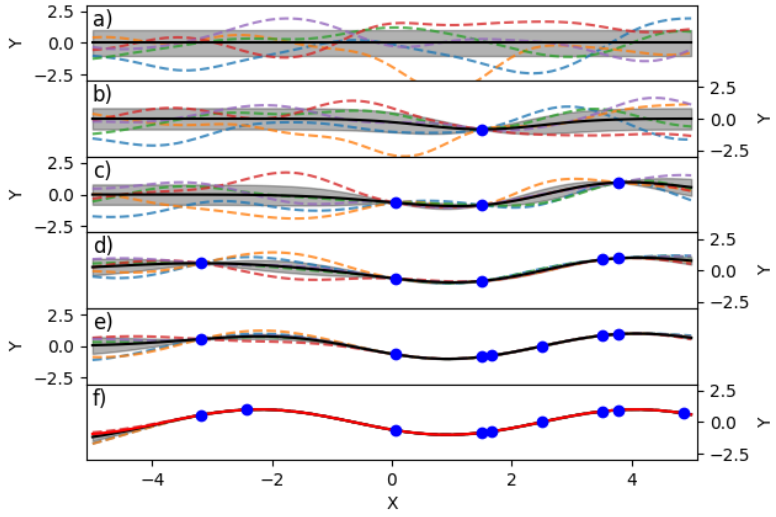

Figure 3.4 – The Gaussian process is applied to randomly sampled points from a 1D toy function. Dashed lines are a sample of possible functions from the Gaussian process distribution. The solid black line indicates the mean value calculated from all possible functions. The shaded region indicates the standard deviation around the mean value. Blue circles are randomly sampled points. a) is the prior distribution before any samples are taken, and b) - f) displays the posterior distribution of the Gaussian process after data sampling. The red line in f) indicates the toy function values.

assumption, that points close together in the input parameter space will result in points close together in the output parameter space, is required. In Fig. 3.4, the radial basis function kernel was used which is described by:

$$\mathcal{K}(x, x') = \exp\left(-\frac{||x - x'||}{\Sigma}\right) \tag{3.3}$$

where, x and x' represent two points in the input parameter space and Σ is a free parameter. It can be seen from this equation that the closer the points are together, the closer $\mathcal{K}$ is to one. The kernel describes how the correlated input parameter space. Fig. 3.5 a) shows a visual representation of the radial basis function kernel.

The form of the correlation between the input parameters can be altered by choosing different kernels for the Gaussian process. The correlation matrices for various kernel choices on toy input parameters are shown in Fig. 3.5, where the correlation between input parameter values for x_i and $x_i^{'}$ are indicated by the normalised heat map.

It can be seen, for example, that in the case of Fig. 3.5 a), for the radial basis function kernel, that numerically similar x_i and $x_i^{'}$ are highly correlated, and this correlation quickly decreases for larger separations. The effect of choosing different kernel functions on the optimisation efficacy are presented in section 4.2.4.2.

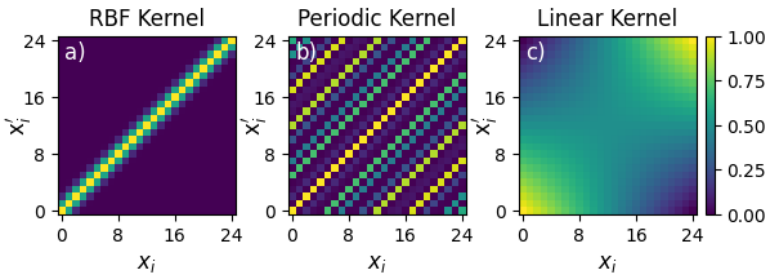

Figure 3.5 – Examples of normalised covariance matrices in 2D produced from the a) radial basis function kernel, b) period kernel, and c) linear kernel. x_i and $x_i^{'}$ are arbitrary parameter space inputs used to calculate their covariance where one is high and zero is low covariance.

3.1.3.3 . Acquisition Functions

In the previous section (section 3.1.3.2) in Fig. 3.4 we sampled the 1D parameter space at random. During Bayesian optimisation, however, the following sample point is chosen by maximising the acquisition function.

The acquisition function examines the Gaussian processes and characterises the points by a combination of their mean and uncertainty. Whilst the form of the chosen acquisition function can change, and the weighting of the exploration vs exploitation (preference for a reduction in uncertainty vs increase in mean value, respectively) can be altered, this function always acts as the middle process between the Gaussian process of the black-box function and the subsequent measurement choice.

As shown in Fig. 3.6, the parameter set that maximises the chosen acquisition function is selected for the following sampling. To clarify, the optimisation is performed on the acquisition function rather than the Gaussian process model of the black box function itself. This proves advantageous since the acquisition function is not costly to evaluate as it is defined in terms of only the mean and uncertainty at each point[149]. After this new parameter set is chosen, measurements are taken at these settings, and the Gaussian process model is updated as shown in the top row of Fig. 3.6. The acquisition function then chooses the next best position, and the process continues until a threshold value or maximum number of iterations is met.

3.1.3.4 . Bayesian Optimisation in LWFA: State of the Art

As BO provides a means of optimising expensive to evaluate black box functions, such as that of the parameter space in LWFA schemes, applying BO techniques to LPIs and their associated secondary radiation is a developing field. Further, BO allows for the inclusion of measurement error into the acquisition function[149], which is critical in an LPI due to shot-to-shot variability. As BO in LWFAs is an emerging field of study, we will examine the work completed by other groups

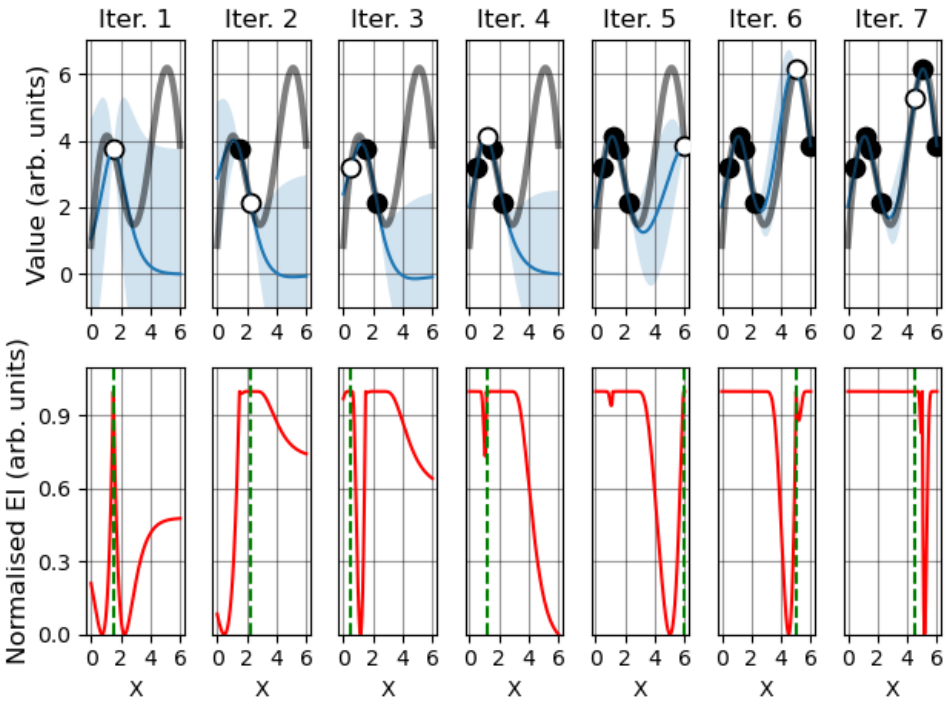

Figure 3.6 – Fitting of Gaussian process to arbitrary function using expected improvement (EI) acquisition function. The top row shows the sampling per iteration where the real function (grey line) is sampled (black circles), and the next point to be sampled (white circles) are selected by the acquisition function in the bottom row. The mean and standard deviation of the Gaussian process are shown by the blue line and shaded area, respectively. In the bottom row, the acquisition function (red line) is maximised (green dashed line) to select the next X value for sampling.

and the relevance of the work completed during this thesis.

The first work applying BO to LWFAs was completed by Shalloo *et al.*[81] in 2020. Their results demonstrated the use of BO models for improving, separately, the electron charge, total bunch energy and divergence, and the x-ray flux through the 6D optimisation of laser focal position, plasma density and length, and 2^{nd}, 3^{rd}, and 4^{th} order spectral phase terms. During 6D optimisations of the electron bunch charge, they demonstrated a threefold increase in charge from 5.6 to $17\,\mathrm{pC}$ between the previous day's best experimental settings and the optimum retrieved by the BO process. An increase in the x-ray yield was noted with a five times increase during a separate 6D scan optimising the counts on an x-ray camera, demonstrating that the laser that would typically be considered too low energy to produce a usable betatron induced x-ray flux in the keV range[14] could be obtained through high-dimensional parameter tuning with BO.

Recent work by Ye *et al.*[152] also focused on optimising betatron X-ray production, where they performed a 2D optimisation of the plasma density and laser

focal position within a gas cell. Optimised settings found through BO produced a maximum photon count of 2×10^7 photons in their experiment. In comparison to the work by Shalloo *et al.*[81], the photon count was increased by a factor of approximately ten by using a laser system with three times greater a_0 ; however, photon energies are not stated in the work of Ye *et al.* This indicates that lower-power laser systems can produce comparable results when a higher dimensional optimisation is performed. We explore in this thesis higher dimensional searches where focal position, plasma density, and the GDD, TOD, and FOD of the spectral phase are altered.

Work completed by Jalas et al.[153], and Kirchen *et al.*[70] in 2021 combined BO of PIC simulations with experimental validation for the flattening of electron bunch phase-space and a secondary optimisation on the stability of the electron spectra. Their simulations indicate that the electron energy spread could be reduced by flattening the phase space through LPI parameter tuning.

They performed 4D BO of the focal position and energy of the laser, the plasma density and dopant concentration of the first gas mixture in a two-compartment cell to optimise electron spectral density defined using the merit function $\frac{\sqrt{Q}E}{\Delta E_{MAD}}$, where E, ΔE_{MAD}, and $\sqrt{Q}$ are the median and median absolute deviation of the bunch energy and the scaled charge, respectively. They showed using simulations that the main improvements in the energy spread come from optimising the effects of the initial phase space of the injected electrons, the correlated energy spread produced by the strong acceleration gradients that are non-constant over the longitudinal axis of the bunch, and the beam loading of the bunch that causes flattening of the accelerating gradient due to the space-charge field of the electron bunch.

Work by Irshad et al., in 2022, applied the BO method to simulations with the multi-objective method for the first time to explore the Pareto front, which describes the region, in this case of an LPA, where an objective cannot be improved further without detriment to another[154]. Future facilities will likely wish to optimise multiple parameters of the electron source, such as the charge and bunch energy. Inherent physical limitations, such as an increase of injected charge leading to an overloading of the wakefield that will induce a positive energy chirp on the bunch leading to increased energy spread, leads to trade-offs when optimising multiple bunch parameters simultaneously. Multi-objective optimisation allows for the Pareto front to be extracted, which can then define the constraints on how parameters can be optimised concurrently. This not only defines the limitations of an LPI arising from the experimental set-up (such as laser energy, focal spot size, and laser temporal duration) but also on optimum working points, which can be chosen based on these results. They further examine the effect of merit function choice on the final optimised electron spectra in simulations through different scaling and combinations of the total and bunch charge, median energy, energy spread and the difference between the median energy and target energy.

These results suggest that the ability of LPIs to produce electrons with a broad range of spectral properties allows them to be highly adaptable systems capable of producing user-defined bunch properties. However, this flexibility requires optimisation methods that are flexible and carefully chosen merit functions to produce desired particle bunch and radiation properties. Whilst BO currently provides the optimiser flexibility, further work on the choice of merit functions and their resulting spectra is required to use this technique fully. In chapter 4 we will present the effect of merit function selection performed online during the experimental campaign on the resulting electron spectra and their properties.

3.2 . Focal Spot Analysis Methods

Knowledge of the on-shot experimental focal spot allows for the input of realistic laser parameters into simulations and analysis of the spatial effects of the laser on the electron spectra. The improved accuracy of simulations using realistic laser profiles (in both time and space) will be shown in sections 4.1.3.2 and 4.1.3.3. In this section, we will present the methods of on-shot focal spot retrieval using conditional generative adversarial networks and the calculation of the complex electric field of the laser from transverse fluence focal volume images. Gilles Maynard completed the development of the complex electric field retrieval.

3.2.1 . Retrieval of Laser Electric Field: Modified GSA Algorithm

Here we present a method to produce a Hermite-Gauss (Cartesian) / Laguerre-Gauss (Cylindrical) mode-based description of an arbitrary laser pulse from fluence images recorded experimentally throughout the focal volume. This modal description can then be used to input realistic laser profiles into PIC codes. In this thesis, the FBPIC simulation code (see section 3.3.2) was used. It is based on quasi-cylindrical geometry, and therefore the discussion here will be tailored to the Laguerre-Gauss modal description.

We present a method to extract a modal description of the laser electric field from fluence images throughout the focal volume based on a modified Gerchberg-Saxton algorithm[79]. By neglecting spatiotemporal coupling (STC), the fluence distribution can be directly transformed into an intensity distribution using the experimentally measured pulse duration. To obtain the complex amplitude of the laser electric field (CAL) from the intensity, it is necessary to determine the distribution of the CAL phase. As shown in chapter 4, experimental electron parameters can be well retrieved from the simulation using only the transverse energy distribution and neglecting STC. This indicates that the effect of STC, in this case, can indeed be assumed negligible. This was done using the following procedure that takes into account shot-to-shot pointing fluctuations of the laser beam.

The complex amplitude of the laser electric field (CAL) is required for realis-

tic laser description. In the paraxial approximation, the vacuum CAL of the laser transverse electric field (the dominant component) is described by:

$$\mathrm{E(x,y,z,t)} = \mathrm{A(x,y,z)} \times \exp\left[-\left(\frac{t - z/c}{\tau_L}\right)^2\right] \times \exp\left[-i\omega_0(t - z/c)\right] \qquad (3.4)$$

where ω_0 is the central laser frequency, τ_L is the laser $1/e^2$ pulse duration, and x0y and z are the transverse planes and laser propagation axis, respectively. We can describe the laser intensity from the transverse component of the vector potential $A(x, y, z)$ as $I_0(x, y, z) = \kappa|A(x, t, z)|^2$ where κ is a constant. Retrieval of the CAL, however, requires that we have both the phase and the intensity. The CAL must satisfy Maxwell equations providing a relation between the electric field amplitudes at two spatially separated values of z. Therefore we can use multiple measurements of the fluence distribution in the transverse plane (as measured experimentally by a CCD) to calculate the intensity from the pulse duration, and then use these measurements to calculate the intensity and phase map of the laser pulse.

The CAL is first projected over a large number of Hermite-Gauss (HG) functions, with a fixed origin given by the maximum intensity in the focal plane. Initially, we assume a uniform phase for the CAL in the focal plane. The images before the focal plane are then included in a generalised Gerchberg-Saxton iteration[79] to determine the phase corresponding to initially fixed origins of the HG functions at these image positions. The error associated with this procedure also depends on the position of the HG mode's origins, which are optimized separately. Minimizing the reconstruction error directly, varying together the coefficients of the HG modes and the origins of the modes would yield a computationally expensive procedure. Thus, the positions of these origins are separately determined - allowing the reconstruction to be performed more quickly - by minimising the error between the reconstructed and the experimental intensity distributions at the pre-focus longitudinal positions ($z \leq 0$ where $z = 0$ denotes the nominal focal position).

The FBPIC simulations using the reconstructed laser field are performed on a cylindrical grid, meaning an expansion in Laguerre-Gauss (LG) modes for the reconstructed field is necessary. However, the minimisation of the error on the origin position is performed on the HG functions rather than their LG projections, as the polynomial coefficients are less sensitive to alterations of the function origin. During this iterative procedure, the HG modes are propagated to the following position, where their coefficients are mixed with the previous iteration results, along with a weighting factor, until convergence. Finally, the reconstructed intensity distributions for the positions $z > 0$ are compared to the experimental ones to validate that the CAL has been well retrieved.

From the reconstructed expression of the obtained CAL, one can then determine the dependency of the laser energy on the azimuthal angle by writing the CAL in

cylindrical coordinates:

$$\mathcal{A}_{\mathrm{HG}}(x,y,z,t) = \sum_{\ell=0}^{N_{\mathrm{C}}-1} \mathcal{A}_{\mathrm{LG},\ell}(r,z,t)e^{j\ell\theta}, \tag{3.5}$$

where $j^2 = -1$, $\mathcal{A}_{\mathrm{HG}}$ is the CAL in Cartesian coordinates projected on HG functions while $\mathcal{A}_{\mathrm{LG},\ell}$ is the CAL corresponding to the ℓ angular mode, written as a sum of Laguerre-Gauss (LG) functions. N_{C} is the total number of complex angular modes taken into account, and the total number of angular modes in real space is $N = 2N_{\mathrm{C}} - 1$. The fundamental angular mode $\ell = 0$ has a perfect cylindrical symmetry, while the contribution of the excited angular modes $\ell \neq 0$ reflects a departure from this symmetry. Once the projection has been completed, the CAL in cylindrical geometry can inject a realistic, complex electric field of the laser pulse into PIC simulations with a cylindrical grid like those performed with FBPIC.

3.2.2 . Retrieval of On-Shot Focal Spot: GAN Modelling

The use of realistic laser parameters shown in section 4.1.3.2 in PIC simulations have been shown to improve the accuracy of simulation results. High-power laser systems have fluctuations in the spatial energy distribution and pointing of the laser beam due to heating, turbulent air effects, changes in humidity, day-night cycle, etc.[2, 87, 155]. Accounting for these fluctuations in simulations requires estimating the focal spot size on each shot. It is, however, not possible to measure the focal spot size directly due to the laser being focused into the plasma.

The introduction of realistic laser parameters into simulations has classically been completed using parameters measured from the focal spot in vacuum at discrete moments throughout an experimental campaign. However, the evolution of the laser profile can occur over the course of an experiment leading to the initially measured parameters being invalid or at least a worse approximation of the laser profile. Further, it has been demonstrated by Maier *et al.*[87] that fluctuations in the laser focus position, pointing, and energy result in fluctuations of the electron bunch energy. It can therefore be extrapolated that alterations in the transverse energy distribution of the laser would likely modify the spatial properties of the resulting electrons. Alterations of the transverse laser energy profile are amplified during self-focusing of the laser pulse. In turn, the wakefield generation and evolution, and therefore the accelerating fields, are modified as they occur in the most intense regions during laser propagation. As demonstrated later in this thesis in section 4.1.3.2, we will see that this in fact the case, and that alterations in the transverse energy distribution of the laser do alter the spatial properties of the accelerated electrons. In order to develop more accurate single-shot laser diagnostics we therefore present a method for calculating an approximate transverse intensity distribution for the focal spot on each shot.

3.2.2.1 . On-Shot Focal Spot Reconstruction Method Overview

Using an externally calibrated CCD and a conditional generative adversarial network model trained on correlated data between the external camera and a camera at focus, one can generate an approximate focal spot transverse energy distribution with high accuracy. An on-shot energy-calibrated CCD is then used to re-scale these retrieved focal spots in terms of energy, allowing for a fluence map to be calculated on each shot. The fluence map can finally be converted to intensity through the measured pulse duration (assuming negligible spatiotemporal coupling). As the focal camera must be displaced to allow the laser pulse to impinge on the gas cell during the experiment, without this calibration, there is no direct way of measuring the focal spot, and its intensity, on each shot.

To overcome this intrinsic obstacle during specific measurements, a portion of the laser leaking through a dielectric mirror was extracted, focused, and correlated with the "real" focal spot, at the interaction point.

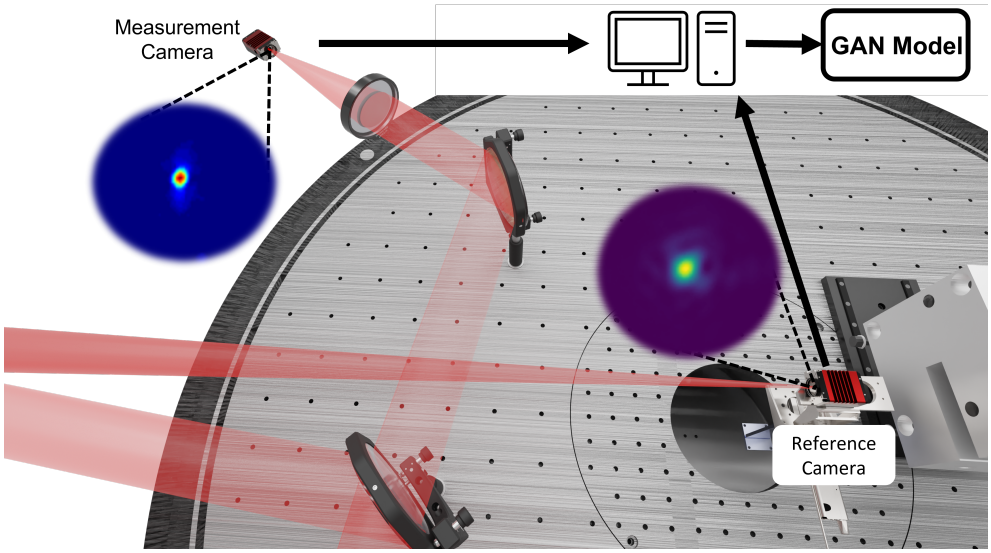

Figure 3.7 – Experimental set-up during the 2021 Lund campaign for creating the data set of trainable focal spot and reference images. The laser is focused by an off-axis parabola after full amplification and attenuation before compression into a CCD at focus. The leak through a dielectric mirror is used to extract a portion of the beam and focus this onto a secondary reference CCD. These data sets are used to train a GAN model. Typical focal spot images on the two cameras are shown in the insets.

To apply this reconstruction to experimental data, we must first prepare a data set for training a neural network to perform the transform between the measurement and “real” focal spot measurement. As can be seen in Fig. 3.7 the reference camera is placed at focus in vacuum with the laser fully amplified and attenuated before compression to allow for the direct measurement of the focal spot with parameters closely resembling those that will be used during the LWFA experiment. The

measurement camera collects a leakage through the final dielectric mirror before focusing and is imaged outside of the experimental chamber such that this data is available on each shot throughout the campaign. 1000 images were then taken, background subtracted and cropped, sorted and paired into a data set where the correlated images can be used to train the neural network. The reference camera is then removed from the beamline during the experiment.

Due to the saving rate for the two cameras running at 10Hz being close to the maximum writing speed of the PC, the images were first temporally aligned to ensure that matching data were used for the model training. Images are then processed to remove the background signal and cropped to the size required for the training model at 256×256 pixels.

In Fig. 3.8 we use the models saved throughout the training process to demonstrate the improving efficacy and eventual saturation of the transfer function between the two images.

Using the terminology from section 3.1.2, the reference camera provides the "real" images for the discriminator to train from the measured images. This data set was used to train the adversarial model where two models are produced: the generator that attempts to create increasingly accurate fabricated images resembling the measured focal spot and a secondary model, the discriminator, which attempts to ascertain whether the images are from the measurement camera or fabricated by the generator. The training is completed by rewarding the discriminator for correctly choosing the origin of the image, and rewarding the generator when it successfully fools the discriminator by creating images that are indistinguishable for the discriminator from the reference sample set.

This method applies the general pix2pix algorithm based on the generative adversarial network (GAN) method described in detail in section 3.1.2, which is typically used for image-to-image transfer tasks. After this model has been trained the weights of the neural network are stored and can be used to rapidly convert any measurement camera image into an image of the reconstructed focal spot.

The training was performed on an Nvidia 1070 in approximately 10 minutes for a data set of 1000 images. GAN models typically find an equilibrium between the generator and discriminator models as they do not necessarily converge. Therefore tracking the accuracy of the conversion between the reference and reconstructed images is completed periodically throughout the training. The most efficient model, in terms of minimising the average error between a randomly selected sample of the reconstructed and target images, is then chosen. This model is then used for the focal spot reconstruction for the remainder of the images taken throughout the experimental campaign.

3.2.2.2 . Training Results and Model Validation

To demonstrate the progress of model training, we show the pre-interaction laser measured by the reference camera with the generated and actual focal spot against training iterations. As illustrated in Fig. 3.8 the initially noisy generated

image begins to contain the general features of the focal spot after 110 iterations when the majority of the signal is contained within a central spot. Between iterations 110 and 250 the fine structures of the focal spot begin to be retrieved such as the slight astigmatism of the focal spot due to a probe beam pick-up mirror. By iteration 650 we see that the signal between the generated and reference image begins to match, and for the next approximately 10,000 iterations there are diminishing returns on the training of the model.

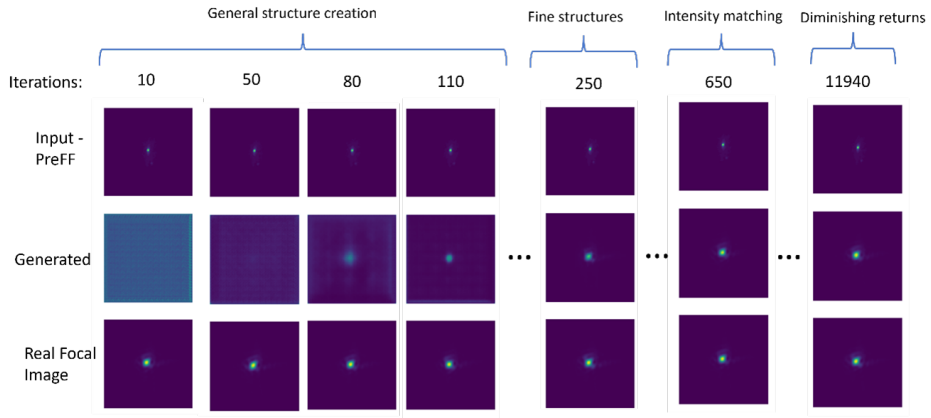

Figure 3.8 – Measurement, generated and reference focal spot images extracted during the GAN training to evaluate the effect of iterations on the efficacy of the model.

To examine the fine structure retrieval we artificially saturated the reference and generated images in Fig. 3.9. The small structures of the focal spot are well retrieved where we see an effectively smoothed version of the reference focal spot in the case of the generated image created from the reference input.

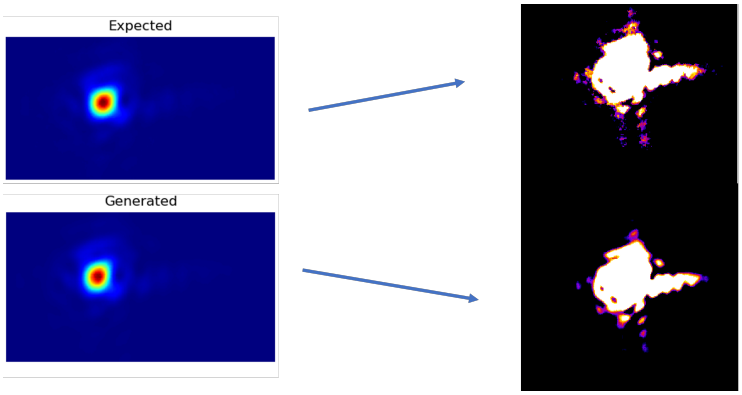

Figure 3.9 – Cropped and saturated images of the expected and generated focal spots.

Figure 3.10 demonstrates the result of the focal spot retrieval method for a single randomly chosen focal spot reconstruction. The measurement camera input,

displayed in a), is transformed into the generated focal spot, b), using the GAN neural network. The difference between the generated image and the reference focal spot, c), for the 16-bit re-scaled images is plotted in d). The maximum and minimum count differences are 6892 and -4090 respectively. For the 16-bit image format, where the images range between 0 and $2^{16} = 65536$, this corresponds to a maximum deviation of 10.5%.

Panel e) demonstrates that the average radial profiles for the generated and reference focal spots, when rotated around their peak signal, produce almost identical radial projections. Results of Fig. 3.10 f) demonstrate that this method provides sub-µm centroid reconstruction accuracy and almost identical radial projection retrieval. Comparing the results of e) and f) of Fig. 3.10 we can see that the difference in the generation accuracy shown in Fig. 3.10 d) is mostly due to the shift in the predicted focal spot centre which was extracted with a Gaussian fit to the reference and generated focal spots. In this measurement, the spatial calibration of the CCD was $1.13\,\mu\mathrm{m}$/pixel indicating that the peak focal spot position is also limited by the imaging accuracy.

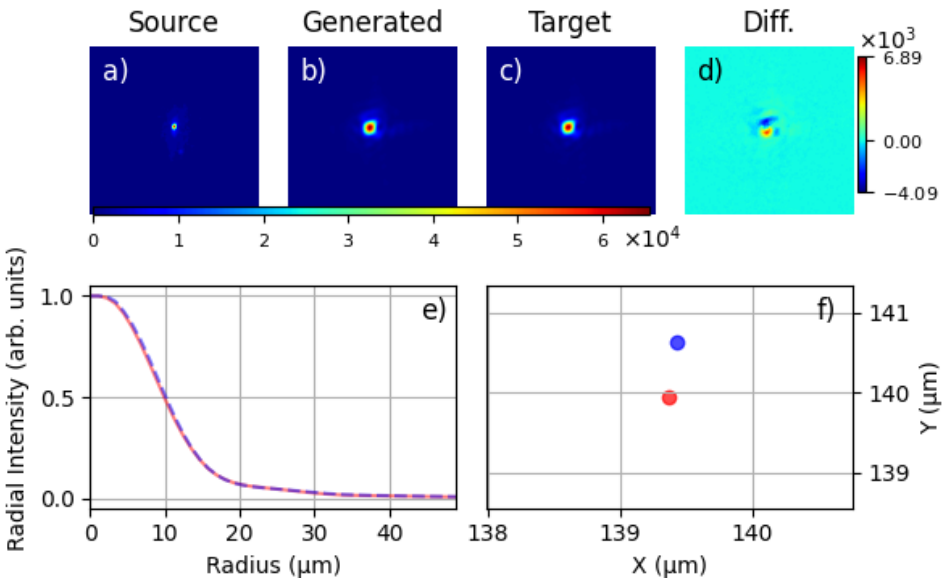

Figure 3.10 – Randomly selected focal spot generation using trained GAN model. a) Input focal spot image, b) Generated focal spot image, c) Reference focal spot image, d) Difference between generated and target image e) Radial average of reference focal spot shown as red solid line and generated as dashed blue line f) Centre of reference and generated focal spot in red and blue respectively extracted from Gaussian fit.

Analysis of a larger sample set of measurement input images indicates that the average deviation between the radial projection of the generated and reference focal spots, cropped to $50\,\mu\mathrm{m}$ in the radial direction to limit bias by areas far away from the focal spot, results in a percentage difference of 5.7%.

3.2.2.3 . Comparison of Retrieval to Typical Laser Stability

To illustrate the efficacy of focal spot retrieval we compare a sample of experimental data used to train the GAN against the resulting generated focal spot images. The efficacy of the focal spot reconstruction is characterised by fitting a 2D Gaussian to the transverse fluence images and generated focal spots, then extracting the origin of the Gaussian fit and $\sigma_{x/y}$ for comparison.

Fig. 3.11 compares the relative shifts in the real focal spot origins (red) and the generated focal spot origins (blue). If pointing was generally well retrieved by the model, we would expect the blue and red distributions to have the same distribution and centroid. As can be seen in Fig. 3.11, the centroid of the generated distribution is shifted in the negative y direction with respect to the real focal spot images. This result indicates, that in its current state, the model does not reconstruct well the pointing jitter of the real focal spot in comparison to the transverse energy distribution. Numerically, the average angular pointing fluctuations in the case of the real and generated focal spots in this data set are $1.017\mu\mathrm{rad}$ and $0.269\mu\mathrm{rad}$ in rescaled units due to re-centring of images during training. This indicates that the model underestimates the pointing fluctuations by a factor of almost four. The reduction in the pointing retrieval efficacy could be due to image preparation for training, where cropping to the region of interest for the reference and measurement focal spot images input training laser images were centred on the peak intensity. This leads to a reduction in the shot-to-shot fluctuations in both the reference and measurement focal spots. Discussion on the stability of the laser system in an absolute case is presented in section 4.2.2.2.

3.2.2.4 . Conclusions, Limitations, and Future Improvements

The ability to reconstruct on-shot focal spots is useful for experimental and simulation analysis. We have shown that the model reconstructs well the average radial profile and spatial energy distribution of the real focal spot. For simulations, a major benefit of producing this type of calibration is the ability to accurately input realistic laser parameters into simulation codes for shots of interest rather than relying on spare measurements during the experimental campaign. Whilst the pointing retrieval is currently inadequate for describing the jitter in the focal spot position, simulations typically initiate the laser on-axis and will therefore still benefit from this calibration method.

As the calibration images are taken for a single experimental set-up, care has to be taken to avoid altering the alignment and components of the optical system. Whilst the laser and CCD systems were capable of data taking at 10Hz, at higher power laser systems these repetition rates are not possible leading to long calibration times if experimental layouts are altered. From a predictive perspective, as the NNs are generative, the exact conversion between the input and output images is seeded with random noise leading to variations when recalculating a single shot. This leads to a randomly seeded error in the focal spot reconstruction which, al-

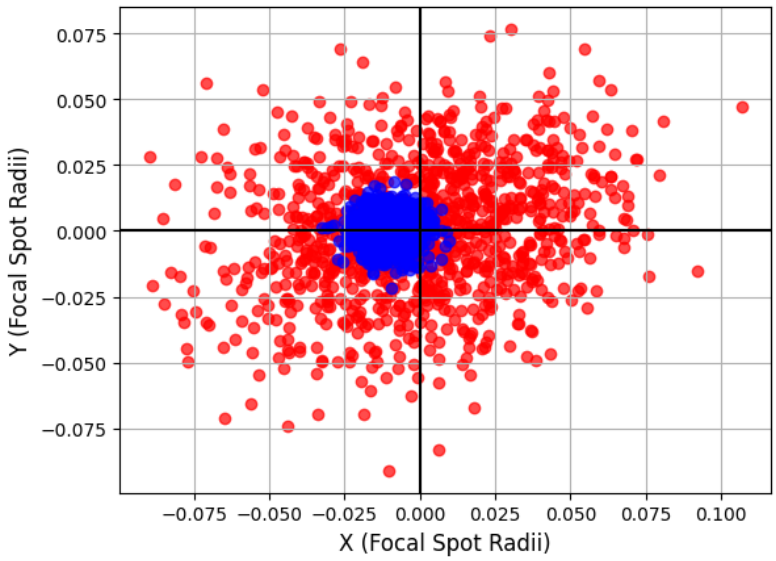

Figure 3.11 – Comparison of pointing fluctuations for real focal spot data and generated focal spots in red and blue, respectively, in units of average focal spot radius for the real focal images. The origin of both sets of focal spots was centred onto the average focal spot position for the real data.

though small, will need to be accounted for in future work which uses these focal spots for simulations.

As we show in chapter 4, the inclusion of realistic laser parameters improves the agreement between simulated and experimental results. Including the laser transverse energy distribution at focus for a single corresponding shot would likely improve the agreement further.

During a Bayesian optimisation procedure, the focal spot may be significantly altered through the implementation of laser spatial phase control by adaptive optics. As focal spot reconstruction is fast once the GAN model has been created, on-shot retrieval of the focal spot and its fluctuations could be included in the Bayesian optimisation model errors. This would likely increase the efficacy of the optima finding by including more experimental errors and removing their fluctuations from the effects of changing the experimental parameters.

This current method is limited by the stability of the LLC laser being exceptionally stable with an average pointing fluctuation of $6\,\mu\mathrm{rad}$ and a stable radial profile. This induces limitations in the type of focal spot that can be reconstructed by the cGAN as it is trained on a sample set where the images are close in both pointing and energy distribution. Purposefully inducing aberrations in the beam through alterations in the adaptive optic or creating instabilities in the laser chain would provide a more diverse training set and a more adaptable final reconstruction model.

The GSA algorithm presented in section 3.2.1 requires at least two transverse

laser images for calculating the intensity and phase map of the laser pulse and a further image for validating the propagation of the laser modes. Since this method returns solely the focal plane measurement of the laser it limits the implementation of this method to assume that the near-field images of the laser before and after focus are static and only changing at focus, which is an unphysical assumption. To improve this method in future implementations two additional cameras could be added to the reference and measurement arms of the experiment (six cameras in total) to measure the laser pre, at and post-focus to enable the retrieval of the phase and intensity maps of the laser on each shot with a verification position. This would allow the GSA algorithm to provide a modal description of the laser pulse after projection on HG-modes (Cartesian simulations) or LG-modes (cylindrical simulations) which could then be used in PIC codes to provide realistic laser input for every shot effectively decoupling laser intensity and pointing fluctuations from comparisons between experimental and simulated results. This would require training three separate transfer models for each camera pair.

3.3 . Particle In Cell Simulations

Due to the non-linear interaction between the laser and plasma, and the many coupled effects, it is not possible to find analytical expressions to accurately describe laser-plasma interaction regime $a_0 \gtrapprox 1$ in the general 3D case[3]. Since this is the regime of interest for a laser-plasma injector, we therefore rely on simulations to uncover the physical influence of different parameters in experiments and to validate experimental results. Here an overview of the Particle-In-Cell (PIC) method[51] is provided, which is the most common numerical technique to simulate LWFA and the method that has been used during this thesis for validating experimental results.

3.3.1 . Principle

Solving the Maxwell-Vlasov equations for the laser-plasma system numerically, typically written in terms of $\vec{E}$ and $\vec{B}$ contrary to the description in terms of potentials provided in section 1.1, allows for the laser-plasma interaction to be simulated. The goal of a PIC code is therefore to simulate the self-consistent interaction between particles and electromagnetic fields[156]. A fully kinetic simulation, however, involving the evolution of all plasma particles, with their corresponding 6D momenta-position space and all corresponding self-consistent electromagnetic fields would require a prohibitively high computing cost. PIC codes therefore group real particles in a small volume of phase-space into macro-particles by making some assumptions about their distribution in this phase-space subset. Formally, the macro-particles sample the plasma distribution function in the Vlasov equation, whose characteristic lines have the form of particle trajectories in the phase space. Therefore, the evolution of positions and momenta of the macro-particles can be obtained by solving their "equations of motion". While the macro-particles

can move continuously in space, the electromagnetic fields and their sources are defined on a numerical grid made of many cells, hence the name of the PIC method.

In addition, the different scales of the laser-plasma interaction and electron dynamics in time and space pose problems for the required resolution of the simulations. For example, the ionisation injection of electrons requires sufficient resolution on the laser oscillations to describe the injection process as it is dependent on the fast oscillations of the laser's electric field on the order of λ_{laser}, whilst the acceleration length of a typical LPI will be on the order of mm to cm. Several methods have been proposed to tackle this issue such as the envelope model which approximates the laser to the modulus of its complex amplitude[47] increasing the minimum spatial scale to be resolved by a factor $\lambda_p/\lambda_{laser} \approx 10 - 100$ for typical pulse duration on the order of 10s of fs[157, 158].

A typical time step in a PIC simulation code involves the steps outlined in Fig. 3.12.

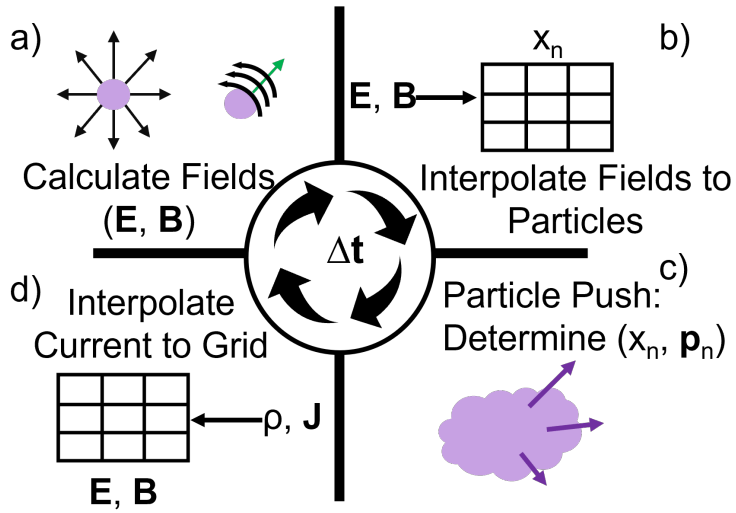

Figure 3.12 – The PIC cycle over one time step is illustrated. a) Electric and magnetic fields defined on the numerical grid are updated using the fields on the grid at the previous time step and the current density on the grid as source terms of Maxwell's equations. b) The fields are interpolated from the grid to the macro-particles' positions. c) A macro-particle pusher performs the change of position and momentum of the macro-particles by solving its equations of motion. d) The updated positions and velocities of the macro-particles are used to project their current and charge density on the grid, to be used as source term in Maxwell's equations to perform the next time step.

In step a) of Fig. 3.12 the electric and magnetic fields are calculated from:

$$\begin{aligned} \frac{\partial \vec{B}}{\partial t} &= -\nabla \times \vec{E} \\ \frac{\partial \vec{E}}{\partial t} &= c^2 \nabla \times \vec{B} - \mu_0 c^2 \vec{J} \end{aligned} \tag{3.6}$$

These fields are then interpolated onto the n macro-particles positions in step b). In step c) the position and momentum of the macro-particles are then updated using their equations of motion, with the fields interpolated at step b) acting as source terms. For the macro-particle n, the evolution of its position and momentum will be thus found by solving the following equations:

$$\frac{d\vec{x}_n}{dt} = \vec{v}_n \tag{3.7}$$

$$\frac{d\vec{p}_n}{dt} = q(\vec{E}_n + \vec{v}_n \times \vec{B}_n), \tag{3.8}$$

where q, $\vec{x}_n$, $\vec{v}_n$ and $\vec{p}_n$ are the macro-particle charge, position, velocity and momentum, $\vec{E}_n$ and $\vec{B}_n$ are the electromagnetic fields interpolated at the macro-particle position. In step d) the charge density and current of each macro-particle of index n is then calculated from its $\vec{x}_n$ and $\vec{v}_n$ and then added to the global charge and current density on the grid. After the contribution of each macro-particle to these densities is added, the current density on the grid can be used as the source term of Eq. 3.6 to calculate update the electric and magnetic fields. The charge density on the grid is typically used as a diagnostic. This process repeats until the desired number of time steps have been completed.

3.3.2 . FBPIC

The PIC code used during this thesis is Fourier-Bessel Particle-In-Cell (FBPIC)[159]. The code uses quasi-cylindrical geometry to simulate the laser-plasma interaction using 2D-radial grids[160]. Laser-plasma interactions tend to have approximate cylindrical symmetry due to Gaussian focal spots having the highest laser intensity at focus. Deviations from cylindrical symmetry can be included in FBPIC through the azimuthal mode decomposition[161], which allows for each radial grid to describe higher-order asymmetry. This allows for the injection of realistic laser profiles into the simulation code. Note that it is the inclusion of the azimuthal mode decomposition that renders the geometry as quasi-cylindrical. Here we will denote the azimuthal mode number as ℓ where we have N_M total azimuthal mode. We can therefore write the complex amplitude of the laser pulse (whose method of calculation is presented in section 3.2.1) as:

$$A(r,z,\theta) = A_{\ell=0}(r,z) + \sum_{\ell=1}^{N_M} [A_\ell(r,z)\cos(\ell\theta) + A_{-\ell}(r,z)\sin(\ell\theta)] \tag{3.9}$$

From this description, we can see that the initial term with $\ell = 0$ is independent of θ. It should be noted that $N_M = 1$ is required for any polarised laser pulse to take into account the polarisation direction.

A major issue with PIC codes is the numerical dispersion due to the finite difference method typically used for the solver of the Maxwell equations for field propagation. This numerical error artificially slows down the propagating electromagnetic fields, which interact with relativistic macro-particles and generates the

numerical artefact referred to as numerical Cherenkov radiation[162]. To mitigate this effect FBPIC uses a spectral solver where the electric and magnetic fields are calculated in the spectral space[160] which correctly calculates the dispersion of the electromagnetic wave[163] thus removing the numerical Cherenkov radiation.

The code allows for the input of arbitrary laser pulses through a Laguerre-Gauss polynomials description that is calculated via the method described in section 3.2.1. The inclusion of the plasma density functions can also be described in terms of splines allowing for the inclusion of realistic density profiles.

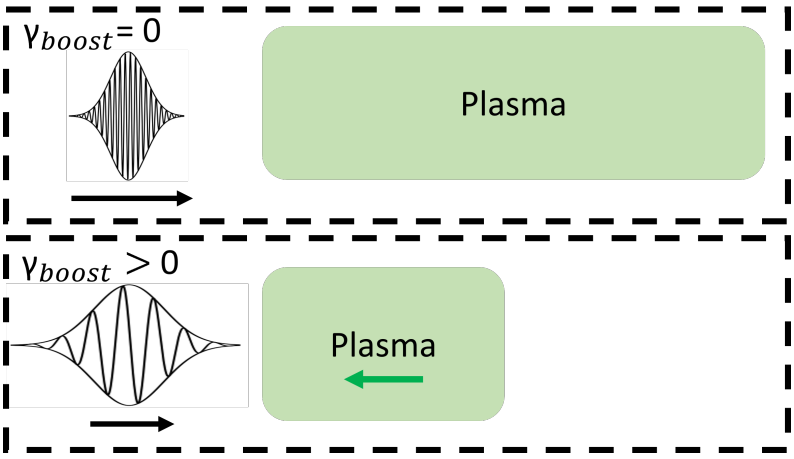

Figure 3.13 – Principle of the boosted frame technique where the simulation is performed in a Lorentz boosted frame with a relativistic factor γ_{boost}. In the boosted frame the frequency of the laser is reduced, thus increasing the minimum grid cell size that can be used to sample the laser oscillations. Besides, the length of the plasma is reduced, thus reducing the total propagation length to simulate. These two effects yield a considerable speed-up for PIC simulations in the boosted frame compared to PIC simulations performed in the laboratory frame.

Reduction of the ratio between the longest scales to be simulated and the smallest scales to be resolved in a PIC simulation of LWFA can be achieved through performing the FBPIC simulation in a Lorentz-boosted frame[164]. This allows for a speed-up of the simulation time by one order of magnitude[165]. The principle of the boosted frame method is that the spatial and temporal scales of the interaction can be found to result in few required time-steps with larger spatial scaling in a Lorentz boosted frame[165]. Figure 3.13 demonstrates qualitatively the effect of using a boosted, rather than laboratory reference frame, when simulating the laser-plasma interaction. In a Lorentz-boosted frame following the laser propagation, the laser frequency is reduced. This increases the minimum spatial step size that can be used in the simulation. The length of the plasma also decreases due to length contraction from the relativistic drift velocity in the frame following the laser pulse.

The Lorentz factor used for the boosted frame can be chosen based on the Lorentz factor of the plasma wake (i.e $\gamma_{boost} \approx \gamma_{wake}$). As the velocity of the wake

is approximately the group velocity of the laser pulse, one can calculate γ_{boost} in terms of the plasma density using Eq. 1.48 and 1.29. For boosted-frame simulations in FBPIC, it is recommended to use $\gamma_{boost} < \gamma_{wake}/2$ to avoid discrepancies in the temporal and spatial scaling of the results when transformed back into the laboratory frame. Using γ_{boost}, the plasma macro-particles initially at rest in the laboratory frame are instead initialized with relativistic velocities in the boosted frame. With a finite difference solver for Maxwell's equations, the Numerical Cherenkov radiation and Numerical Cherenkov instability generated by many relativistic macro-particles would have detrimental effects on such a boosted frame simulation. Instead, the use of a spectral solver in FBPIC can considerably reduce these artefacts arising when using the boosted frame[164].

4 - Low-Energy Laser-Plasma Injector

During two experiments in 2019 and 2021 at the Lund Laser Centre (LLC), the optimisation of a $150\,\mathrm{MeV}$ LPI was targeted through control of plasma plateau density and profile, focal position, laser wavefront, and spectral phase control through an acousto-optic crystal. The aim was to understand the impact of these mechanisms to approach the set of parameters, bunch energy ($150\,\mathrm{MeV}$), energy spread ($<$5%) and charge ($30\,\mathrm{pC}$) outlined in the EuPRAXIA Conceptual Design Report[2]. During the first experiment, the effect of these parameters on the accelerated electron spectra was studied and the physical origins of these effects were explored through the comparison of experimental and simulated results.

Extension of the plasma density downramp by $1000\,\mu\mathrm{m}$ was seen to increase the electron energy by $100\,\mathrm{MeV}$ and increase the range of focal positions that could trap electrons allowing for improved tuning. The electron total charge and average angular displacement of the bunches were then optimised through alterations in the focal position of the laser within the plasma. These results were compared to realistic simulations where a good agreement is achieved when including realistic laser intensity and temporal profiles. Spatially-Gaussian laser drivers are shown to strongly overestimate the accelerated charge in comparison to the realistic case. The underlying process for the average angular displacement was explored through PIC simulations that cannot be explained when using symmetric Gaussian laser drivers. Finally, the effect of the laser wavefront on the injection and acceleration dynamics of electrons is explored by alterations of an adaptive optic.

Investigation of the effect of pre-focal plane laser symmetry on ionisation injection uncovered a novel injection regime, where the laser is focused far before the plasma target, with improved pre-focal symmetry, resulting in electron spectra with reduced energy spread and divergence. These results can be understood from the a_0 injection threshold of the inner shell nitrogen electrons which are strongly localised due to the realistic laser evolution in the plasma.

The second experiment develops an optimisation procedure by the implementation of machine learning (ML) methods - namely Bayesian optimisation and the automation of the experimental control. The Bayesian optimisation process was shown to successfully improve the electron properties from an initially far from

optimum configuration resulting in strongly peaked spectra with high peak charge percentage. The effect of group delay dispersion (GDD) of the laser pulse on the electron's total charge was investigated. The optimum GDD was seen to change with the plasma density in terms of accelerated charge and higher plasma densities allowed for a wider range of GDD to inject comparable total charge.

The Bayesian optimisation process was then explored using offline optimisation where the Bayesian optimiser searched over a parameter space corresponding to the one explored during the experiment. We use this search to justify the use of Bayesian optimisation alongside qualifying the use of different figures of merit, kernel choices, and acquisition functions used during the optimisation procedure. This technique allows for improved selection of the Bayesian optimisation processes hyper-parameters for given experimental data as preparation for, or post-analysis of, laser wakefield experiments.

Machine learning using conditional generative adversarial networks was applied for the retrieval of focal spot images using a spatially separated camera and a neural network trained to convert between these images using data taken during the second experiment. This produces a reconstruction of the on-shot focal spot, allowing for alterations in the pointing and energy distribution of the focal spot to be tracked for each experimental data point thus decoupling the effects of laser fluctuations from those of the electrons.

These two experiments are used to qualify the progress on producing a $150\,\mathrm{MeV}$ injector and understanding the physical processes that can be used to further improve the quality and stability of the accelerated electrons. It is shown that whilst the bunch energy and energy spread of the electrons can be achieved in line with the EuPRAXIA guidelines for an injector, the bunch charge needs augmentation to reach the required value.

4.1 . Laser-Plasma Coupling for Injector Control: 1st Experiment at LLC

4.1.1 . Introduction

An experiment was performed using the TW laser at the Lund Laser Centre (LLC) to explore laser-plasma coupling through density downramp length, focal position and laser wavefront, as means of controlling electron bunch parameters. We present an overview of the LWFA experiment followed by an in-depth analysis of the achieved experimental results, which, when compared to simulations using realistic laser parameters, allow us to extract the underlying physical effects responsible for the recorded electron dynamics. As the laser pulse quality is a key component for the mechanism of ionisation injection, particular care was taken to analyse the characteristics of the laser pulse in the experiment and implement these properties in the simulation code. Working at intermediate laser energy ($\approx 0.7\,\mathrm{J}$) and low dopant concentration (0.25 - 1%) we examine the effect of laser wavefront controlled by an adaptive optic (AO) on resulting electron spectra. This work provides information on the physical mechanisms to control accelerated electrons' energy spectra and alignment of the accelerated bunches with the laser axis. The axial alignment of the accelerated electrons is an important consideration for accelerator applications, and experiments requiring fine alignment between the accelerated bunch and the accelerator axis is the average displacement of the electron bunch from the central axis (defined in LWFA experiments as the laser axis.) Experimental results are compared to particle-in-cell (PIC) simulations, and difficult-to-model parameters such as charge are reliably reproduced using realistic laser and plasma parameters. We first present the numerical and experimental methods, followed by a discussion of results, which highlight the main effects on bunch quality through comparison of experimental and simulation results.

4.1.2 . Experimental Arrangement and Methods

An overview of the experimental arrangement is shown in Fig. 4.1. The different aspects of the set-up are described in chapter 2. For the reader's reference (in order of laser path) adaptive optic (section 2.1.1.3), wavefront sensor (section 2.2.3 & 2.1.1.3), ELISA gas cell (section 2.2.1), and electron spectrometer (section 2.3.1).

4.1.2.1 . Laser Pulse Characterisation and Modelling

The LLC 20 terawatt laser (described in detail in section 2.1.2), measured during this experimental campaign to have an average pulse energy of $736\,\mathrm{mJ}$ and $0.8\,\mu\mathrm{m}$ central wavelength, was focused with a $f = 775\,\mathrm{mm}$ off-axis parabola to a focal spot size FWHM of $12\,\mu\mathrm{m}$, achieving a peak intensity of $9.8 \times 10^{18}\,\mathrm{W\,cm^{-2}}$, corresponding to a peak normalised vector potential of $a_0 = 2.15$.

The temporal envelope was determined from measurements using frequency-

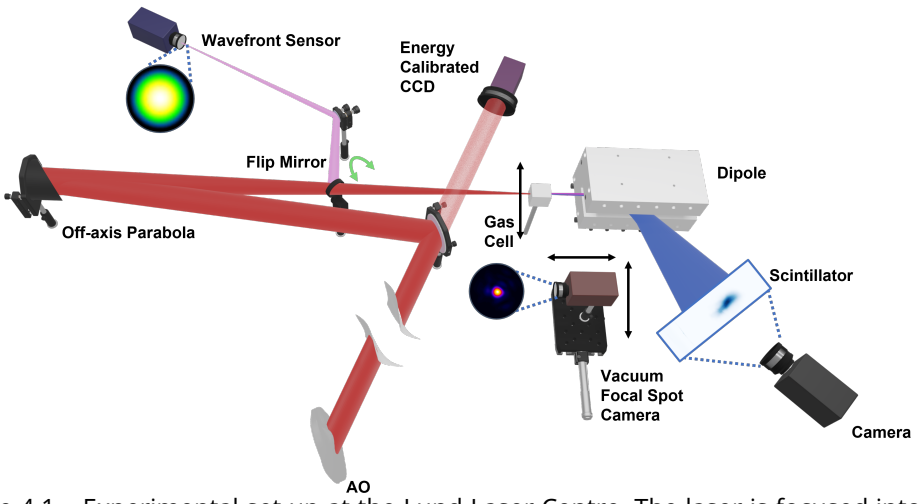

Figure 4.1 – Experimental set up at the Lund Laser Centre. The laser is focused into the gas cell by the off-axis parabola. The interaction between the laser and the plasma produces an accelerating cavity and electron bunch from ionisation injection. Accelerated electrons exiting the gas cell are then dispersed with the permanent dipole magnet and produce scintillating radiation on a LANEX screen which is then imaged onto a 16-bit CCD. An Adaptive optic, set after the compressor, is used to tune the beam wavefront. Laser diagnostics are performed in vacuum using attenuators before the compressor: using the flip mirror, the beam (in pink) can be extracted to measure wavefront curvature using a Phasics wavefront sensor; the energy distribution in the focal volume is recorded in vacuum using a camera movable on axis in place of the gas cell. The adaptive optic settings are altered to produce the three laser setting cases displayed in Fig. 4.4 as measured by the focal spot camera under vacuum. Energy measurements are taken using the leak beam (shown in light red) through a dielectric mirror and a calorimeter-calibrated camera.

resolved optical gating (FROG)[166] for various compressor grating separations. The optimum value of this separation (in terms of LWFA efficiency) was at the shortest pulse duration, with an FWHM pulse duration of 42 fs shown in Fig 4.2. These measurements also show an asymmetry between the front and back of the pulse gradients as illustrated in Fig. 4.2. Note that in these measurements the negative direction is earlier in time meaning that the rising edge of the laser is located in the $t < 0$ portion of the plot. In order to take into account this asymmetry, the pulse temporal profile was expressed using a bi-Gaussian function. The bi-Gaussian function is described by the function:

$$y = \begin{cases} y_0 + Aexp\left(\frac{-1}{2}\frac{(x-x_0)^2}{\sigma_b^2}\right) & \text{if } x < x_0 \\ y_0 + Aexp\left(\frac{-1}{2}\frac{(x-x_0)^2}{\sigma_a^2}\right) & \text{if } x \geq x_0 \end{cases} \tag{4.1}$$

FWHM in intensity pulse duration was extracted as $\sigma_{b/a} \times 2.3548$ for the pulse for the σ value of the bi-Gaussian before (b) and after (a) the peak in intensity. The $42\,\mathrm{fs}$ full-width half-maximum (FWHM) pulse duration was measured to have a bi-Gaussian pulse profile with $25\,\mathrm{fs}$ half-width at half-maximum (HWHM) after

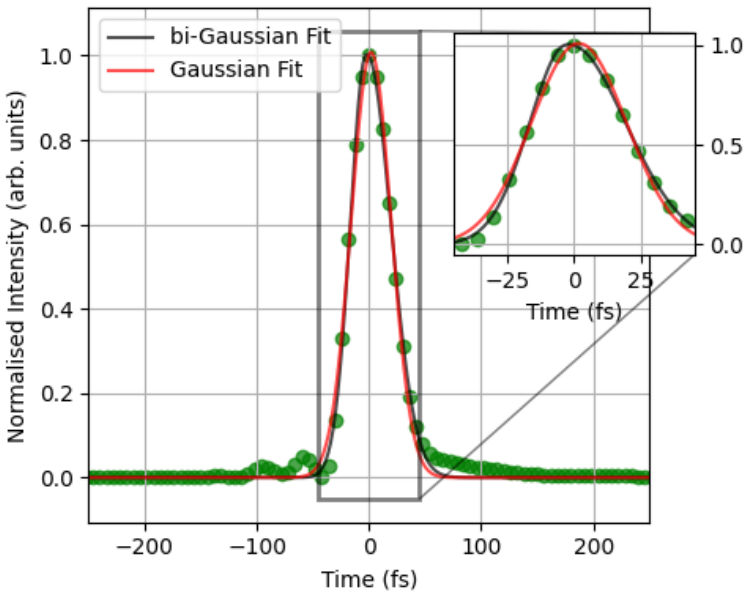

Figure 4.2 – Measured normalised intensity of the laser pulse from the LLC at optimal compression as a function of time over a $500\,\mathrm{fs}$ window. Gaussian and bi-Gaussian fits are shown in red and black lines respectively for the pulse duration measurements shown by the green circles. The zoomed inset shows the pulse between $\pm 45\,\mathrm{fs}$ and indicates that the bi-Gaussian fit provides a closer representation of the temporal profile than a single Gaussian function.

the peak intensity and $17\,\mathrm{fs}$ HWHM before, using frequency-resolved optical gating (FROG) described in section 2.1.5.1. Comparison of the Gaussian and bi-Gaussian fits demonstrates that the pulse shape is better described by the bi-Gaussian profile, which better fits the sharper rising edge and shallower gradient of the falling edge. This asymmetric pulse duration has been included in the simulations. The spectral chirp was also extracted from this measurement and included in the simulation for completeness, although it was found to have minimal effect on the electron dynamics.

A laser energy measurement was taken at the output of the final amplifier before compression. The energy was also measured on every shot using an energy-calibrated laser leak through the final mirror before focusing as shown in Fig. 4.1, and an energy stability of $1.95\,\%$ (std) fluctuations was measured as shown in Fig. 4.3.

Finally, the calibration of the system transmission was performed at multiple points throughout the experimental campaign to globally validate the energy measurements between the amplifier and the energy-calibrated CCD. Tuning and control of the laser were performed in vacuum using the fully amplified laser beam, attenuated before compression to allow direct diagnostics at focus.

Images of the transverse fluence distribution, taken at different positions using

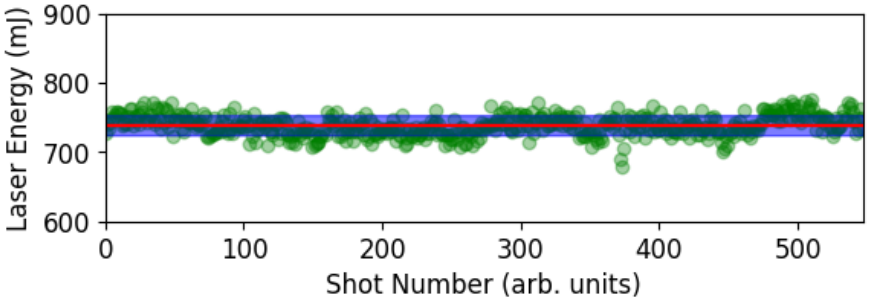

Figure 4.3 – Laser energy as measured by the energy-calibrated CCD over 500 consecutive shots shown by green circles. RMS energy and standard deviation around this value are shown by the horizontal red line and blue-shaded region respectively.

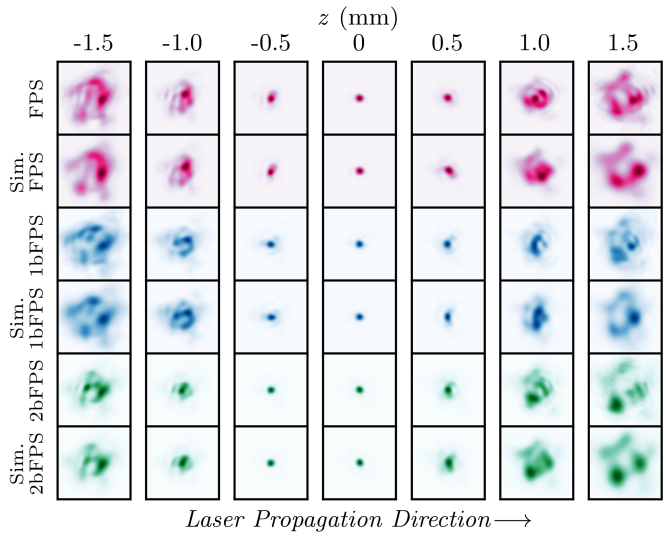

Figure 4.4 – Laser energy distribution in the transverse plane around the focal position - relative position marked above - for three different settings of the AO and their corresponding energy profiles displayed from their modal description used in the simulation (denoted by *Sim.*). Flat phase setting (FPS) and two manually altered AO setting fluence profiles, 1bFPS and 2bFPS, are displayed in pink, blue and green respectively. Each image is normalised to its maximum value for visibility.

the vacuum focal spot camera in Fig. 4.1, $\pm 1.5, \pm 1, \pm 0.5, 0$ mm from the focal plane along the laser axis and for three different AO settings, are shown in Fig. 4.4. Each image was cropped to a $130\,\mu$m box around their centre of mass. These fluence distributions have been obtained for three AO configurations: the wavefront sensor feedback loop provides a nearly flat phase profile at focus, FPS (flat phase settings). Next, to improve the laser pulse quality at the beginning of the laser-plasma interaction when focusing inside the plasma, we have manually altered the AO settings to improve the pre-focal plane cylindrical symmetry at

$z = -1\,\mathrm{mm}$, leading to configurations 1bFPS and 2bFPS, obtained during two different experimental days. Fig. 4.4 shows that the three AO settings provide similar fluence distributions, particularly at the focal plane where the size of the central spot yields a Rayleigh length $z_R \simeq 400\,\mu$m. A significant variation of the laser spot shape is observed qualitatively between the AO settings at each consecutive position.

Angular asymmetries can have detrimental effects on LWFA by inducing large transverse fields that can deflect the trapped electron bunch. We therefore analyse in more detail the rotational symmetry of the laser spot in a transverse plane for the three AO settings at the same longitudinal positions as in Fig. 4.4. As described in section 2.1.5.2, we can calculate the rotational asymmetry parameter (RASP), $\mathcal{R}$, using transverse fluence images of the laser. We calculate the RASP at each fluence image position through the focal volume to compare the evolution of the three laser settings as shown in Fig. 4.5 a).

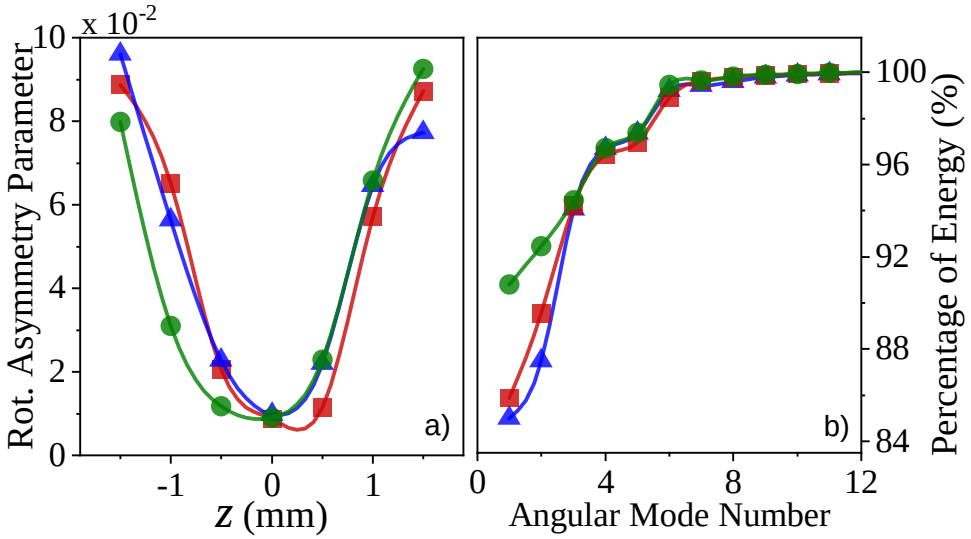

Figure 4.5 – a) Rotational asymmetry parameter through focus for the three experimental laser energy distributions shown in Fig. 4.4; b) Cumulative fraction of energy contained in successive angular modes in the simulated laser distributions. For both a), b) FPS, 1bFPS and 2bFPS are displayed in red squares, blue triangles and green circles respectively.

In Fig. 4.5a) the calculated values of $\mathcal{R}$ are plotted for the longitudinal positions and AO configurations corresponding to those in Fig. 4.4. It shows that the three AO settings yield the same small minimum value of $\mathcal{R} \simeq 1\%$, obtained at the focal plane position. $\mathcal{R}$ remains close to its minimal value over a distance of $\simeq 0.5\,\mathrm{mm}$, then rapidly increases by more than a factor of six at $\pm\,1\,\mathrm{mm}$ from the focal position. These images have a factor of 2 higher RASP (higher asymmetry) at focus than in the example case shown in section 2.1.5.2, Fig. 2.12 a), as the

pick-up mirror used to extract a part of the main pulse as a probe beam has been inserted into the laser path.

The experimental results for the fluence distribution shown in Fig. 4.4, were used to derive an analytical form of the complex amplitude of the laser electric field (CAL) using the modified Gerchberg-Saxton method presented in section 3.2.1 using images at $z = -1.5$, -1.0, and -0.5 mm and at/post focus for result validation. As seen from Fig. 4.4, the obtained analytical intensity distributions are in very good agreement with the experimental ones at all positions for the three AO settings, validating this procedure. This agreement also demonstrates the good shot-to-shot stability of the laser beam at the LLC since the phase retrieval method has converged accurately on input data ($z \leq 0$) and predicts well future positions ($z > 0$), whilst using data from different laser shots.

In Fig. 4.5b), the percentage of modal laser energy, calculated from the CAL given by equation. 3.5, is plotted versus the angular mode number N for the three AO settings of Fig. 4.4. This plot indicates the fundamental mode contains more than 85% of the laser energy for all the AO settings, with the 2bFPS configuration having the best cylindrical symmetry with more than 90% of energy in the fundamental mode. The laser energy rapidly increases with N, where 99 % of the pulse energy is contained when $N = 7$ angular modes are included. This indicates that the main part of the asymmetric contributions come from low-order excited modes ; justifying the description in quasi-cylindrical geometry which is implemented in the FBPIC (described in section 3.3.2) simulations used during this work. Importantly, this asymmetry is generated mainly in a transverse space approximately $30\,\mu\mathrm{m}$ from the propagation axis, in comparison to a plasma wavelength of $\lambda_p \approx 13\,\mu\mathrm{m}$. It therefore contributes little to the plasma wave that can trap and accelerate plasma electrons. The contribution of high-order excited modes is reduced when considering only the domain close to the central laser spot, in which the use of modes up to $N = 5$ already accounts for 99% of the total laser flux. Therefore, this value of $N = 5$ was used in the simulations of laser-plasma interaction presented in this section.

4.1.2.2 . Gas Cell Characteristics

To achieve localised injection in this experiment, the evolution of the laser intensity is controlled through non-linear self-focusing[3] via a tailored plasma density implemented in the custom-built ELISA (ELectron Injector for compact Staged high energy Accelerator) gas cell used in this experiment, through variation of the aperture and length of the entrance and exit cell facings[134, 167]. The gas cell was set in two configurations, short exit (SE) and long exit (LE), providing two different density profiles by changing the cell exit face, previously calibrated[167], and shown in Fig. 4.6.

Gas mixture values of 99.75% hydrogen doped with 0.25% nitrogen were chosen according to previous simulations results[134] and following optimisation of the dopant concentration during the experimental campaign between values of 1, 0.5

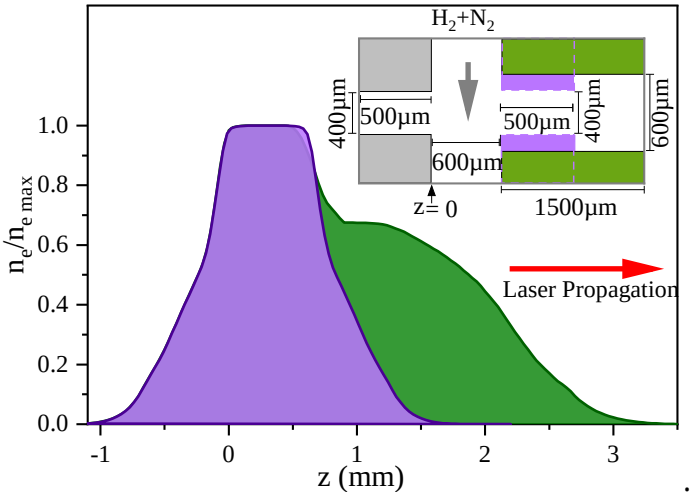

Figure 4.6 – Normalised electron density profile along laser axis in the gas cell from fluid simulations. Short and long exit configurations are indicated by purple and green plasma densities and inset dimensions, respectively. The laser travels from negative to positive z values as marked by the red arrow.

and 0.25% nitrogen. Results presented in this section were obtained at a plasma density of $n_e \simeq 7 \times 10^{18}$ cm^{-3}. The gas density was calibrated offline using a Mach–Zehnder interferometer whose principle is described in section 2.2.2.

4.1.2.3 . Electron Diagnostics

Measurement of the accelerated electron energy distribution was performed using an electron spectrometer composed of a $20\,\mathrm{cm}$, $0.83\,\mathrm{T}$ permanent dipole magnet, and LANEX scintillating screen imaged with a 16-bit Andor camera, providing an energy detection range of $11.3\,\mathrm{to}\,300\,\mathrm{MeV}$ as illustrated in Fig. 4.1. The CCD signal-to-charge calibration was performed using known intensity light sources, calibrated optical density filters, and the values by Kurz *et al.*[135] for the count-to-charge calibration of the scintillating screen[168] using the method presented in section 2.3.1.3.

A spatially moving mask of $\pm 4\,\mathrm{mrad}$ around the electron peak $\mathrm{dQ/dE}$ value in the non-dispersive axis (vertical direction on all spectra plots) was used for both the experimental measurement and analysis of simulated results. The divergence of the moving mask was chosen to include the accelerated electron peak whilst minimising the effects of highly diffuse electrons over the measured parameters. This analysis technique was applied because, in simulations, all accelerated charge can be tracked and accounted for, whereas highly diffuse electrons can be lost during the interaction with the magnetic field of the dipole in the electron spectrometer. Electron spectra are displayed within windows of $\pm 7.5\,\mathrm{mrad}$ angular width symmetrical around the laser axis ; analysis of all spectra was conducted between $\pm 4\,\mathrm{mrad}$ symmetrically around the electron peak axis in the angular plane for each

spectrum. This dynamic cropping is illustrated in Fig. 4.7 within a larger angular window.

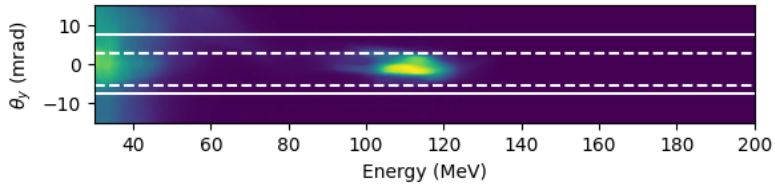

Figure 4.7 – Illustration of the moving divergence cut applied to an arbitrary electron spectrometer measurement. Solid white lines indicate $\pm 7.5\,\mathrm{mrad}$ around the laser axis used for the angular cropping for all spectra visualisation and dashed white lines the moving angular cut at $\pm 4\,\mathrm{mrad}$ around the electron peak axis in the angular plane for all electron bunch parameter calculations.

Using the method presented in section 2.3.1.2 we can estimate the divergence-induced error in the energy measurement of the electron spectra. Using the approximation that divergence in the non-dispersive and dispersive axis are of similar values, divergence-induced energy errors of 0.5, 1.2, and 1.6% per milliradian divergence at 11, 150, and 300 MeV, respectively, were calculated. In this experiment, the laser polarisation is along the energy dispersion plane likely leading to larger divergences and therefore larger induced energy errors. Previous simulation results[134] for a similar cell configuration, nitrogen dopant percentage, and lower $a_0 = 1.6$, indicate there is a factor 1.4 between the electron divergence in the non-dispersive and dispersive axis which validates this assumption.

4.1.2.4 . Simulation Method

Numerical simulations were performed with the spectral quasi-cylindrical PIC code FBPIC[160] presented in section 3.3.2. The complex laser amplitude at the plasma entrance was introduced through an analytical form, as described in section 3.2.1, corresponding either to a given AO setting shown in Fig. 4.4, or to a Gaussian transverse profile. In the former case, the laser complex amplitude is described with $N_\mathrm{C} = 3$ complex angular modes ($N = 5$), while the simulations are performed with $N_\mathrm{C} + 1$ complex angular modes to take into account the linear polarisation along the x-axis of the laser electric field (corresponding to the energy-plane of the experimental spectra.) For a Gaussian profile, only two complex angular modes are required. In all cases, the temporal profile of the laser pulse has the bi-Gaussian form extracted from the FROG measurement above from Fig. 4.2. The simulations used a moving window, together with the boosted-frame technique[169], described in section 3.3.2, with $\gamma_\mathrm{boost} = 4$. The Lorentz factor for the wake, calculated at a plasma density of $7 \times 10^{18}\mathrm{cm}^{-3}$, gives $\gamma_\mathrm{wake} \approx 15$, therefore comfortably satisfying the back-transform requirements of $\gamma_\mathrm{boost} < \gamma_\mathrm{wake}/2$. The simulation box has a dimension of $70\,\mu\mathrm{m}$ along the propagation axis and $200\,\mu\mathrm{m}$ in the radial direction with 2800 and 1500 cells respectively and 48 macro-particles

per cell. The initial ionisation state of plasma atoms was 1+ for hydrogen and 5+ for nitrogen. Calculations were performed at the Mesolum cluster of Université Paris-Saclay. Typical running time was 10^4 core-hours per simulation with four complex angular modes. Simulations took three times less in the Gaussian laser case.

4.1.3 . Results and Discussion

Here we analyse the relative importance of three main parameters: plasma density profile, laser focus position and laser wavefront quality on the control of the accelerated electrons as evaluated through their energy, charge and bunch angular deviation. In the following section, we demonstrate that, in this configuration, extension of the plasma density downramp provides an increase in the electron energy and peak charge ; change of the focal position of the laser within the plasma has a large effect on the total trapped charge and displacement from the laser axis for the accelerated bunches ; and finally, change of the laser symmetry can be used to improve the accelerated electrons in terms of divergence and energy spread, down to the mrad and per cent level, respectively, whilst minimising the amount of charge in the low energy part of the spectra.

4.1.3.1 . Plasma Downramp Length

Simulations of ionisation-induced injection in a laser-driven plasma wakefield[134, 170] show that high-quality electron injectors in the 50–200 MeV range can be achieved in a gas cell with a tailored density profile. Extending the plasma exit downramp was shown numerically to provide an increase in the peak and maximum electron energy of the accelerated bunches. This effect was observed experimentally and is illustrated in Fig. 4.8 and 4.9. AO settings correspond to the FPS case with laser focus in the up-ramp at $z = -0.35\,\mathrm{mm}$ for Fig. 4.8 and at the beginning of the density plateau, $z = 0\,\mathrm{mm}$, for Fig. 4.9. For each case of focus position, experimental electron spectral density images in the angular-energy plane illustrate a) short exit (SE) and b) long exit (LE) configurations. For all $\mathrm{dQ/dE}$ plots the solid line corresponds to the spectral density images displayed to their left with the standard deviation of multiple consecutive shots. The spectrum in Fig. 4.9 were selected by choosing the spectra that minimised the difference between their $\mathrm{dQ/dE}$ and the average $\mathrm{dQ/dE}$ of the sample set for both cases. For both laser focus positions, measured electron spectra show an increase of almost an order of magnitude in spatial integrated charge density and approximately $100\,\mathrm{MeV}$ in maximum energy in the LE case, compared to the SE case. Extending the density downramp from $500\,\mu\mathrm{m}$ to $1500\,\mu\mathrm{m}$, corresponding to the change in plasma structure illustrated in Fig. 4.6, increased the peak energy from $(51 \pm 2)\,\mathrm{MeV}$ to $(158 \pm 11)\,\mathrm{MeV}$, as illustrated in Fig. 4.8. This corresponds to an average accelerating gradient greater than $100\,\mathrm{GeV\,m^{-1}}$ throughout the density downramp.

Comparing peak $\mathrm{dQ/dE}$ values from Fig. 4.8a) and Fig. 4.8b) demonstrates an increase in the accelerated charge-energy density of 1.9 times for the LE case,

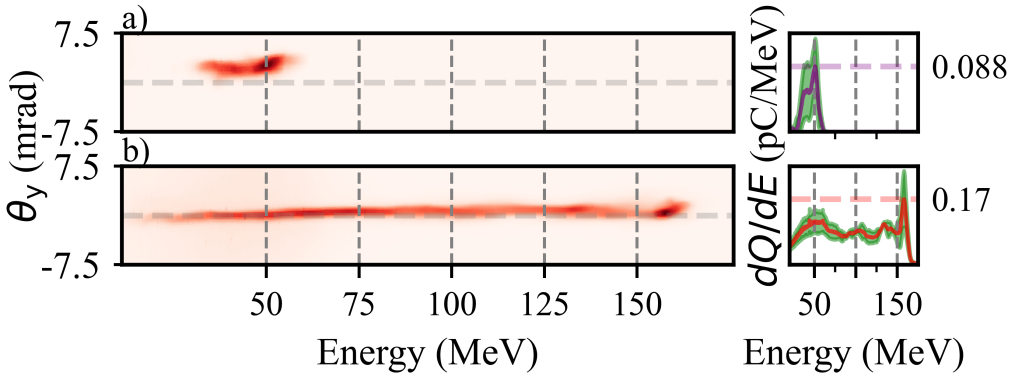

Figure 4.8 – Experimental electron charge density in divergence-energy space and their corresponding spatially-integrated $\mathrm{dQ/dE}$ ($\mathrm{pC\,MeV^{-1}}$) within a $\pm 7.5\,\mathrm{mrad}$ window around the laser axis indicated by the dashed horizontal grey line with the laser focus at $z = -0.35\,\mathrm{mm}$ for the two exit plate configurations illustrated in Fig. 4.6: a) short exit configuration (SE) case, and b) long exit configuration (LE). Standard deviation of four and three consecutive shots for a) and b) respectively are illustrated by the shaded green region. All $\mathrm{dQ/dE}$ plots are plotted from zero ($\mathrm{pC\,MeV^{-1}}$) in linear scaling. The purple and red dashed lines indicate the maximum value of $\mathrm{dQ/dE}$ for the displayed spectra.

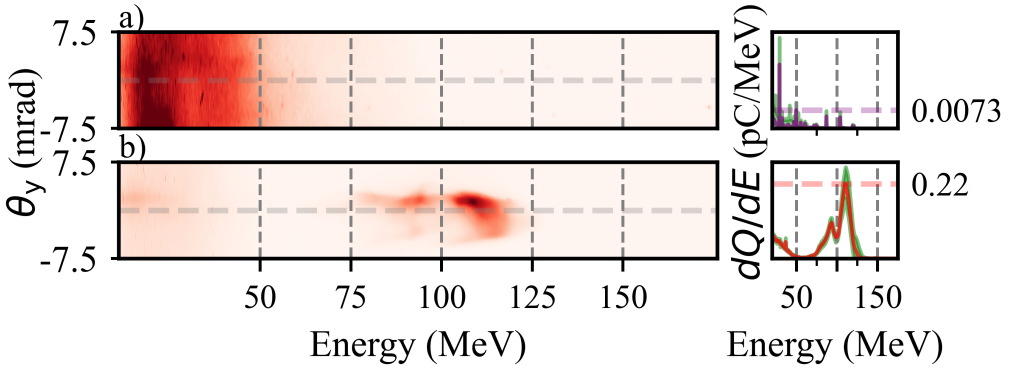

Figure 4.9 – Same as Fig. 4.8 for laser focus at $z = 0\,\mathrm{mm}$ with three consecutive shots included in the standard deviation.

indicating that trapping continues to occur in the plasma downramp region, leading to a broad energy spectrum. Reduction in energy spread of the electron bunches is achieved for the LE case by moving the focus position of the laser to the beginning of the plasma density plateau, as illustrated in Fig. 4.9b). A broad, low-energy spectrum is produced when the same settings are used in the SE case (Fig. 4.9a)). This indicates that the laser does not undergo sufficient self-focusing when focused at the start of the plasma density plateau with the short ramp to both inject and accelerate the electrons. The extension of the downramp allows for the electrons

which are injected deeper into the cell to be accelerated through the downramp, reaching energies over $100\,\mathrm{MeV}$. The large increase in peak dQ/dE The LE configuration was used for all results shown in the following sections.

4.1.3.2 . Optimisation of Laser-Plasma Coupling Through Focus Position

In addition to the density downramp increase of the LE case, further control and improvements of the electron spectra were achieved by exploring the focal position of the laser with respect to the plasma density profile. The position of laser focus relative to the density profile is one of the main input parameters that can be used to tune the electron bunch properties. The focal position defines the initial conditions for laser-plasma coupling through self-focusing which alters the resulting accelerating fields and electron bunch dynamics. Guiding simulations for this campaign predicted improvements in accelerated electron parameters by focusing close to $z = 0$.

Fig. 4.10 a) to c) show representative experimental electron spectral density images (again chosen through the minimisation of their $\mathrm{dQ/dE}$ versus the average) in the angular dispersion-energy plane at three laser focal positions, a) pre-plateau: $z = -0.8\,\mathrm{mm}$, b) peri-plateau: $z = 0\,\mathrm{mm}$, and c) post-plateau: $z = 0.8\,\mathrm{mm}$ for the LE case and 1bFPS AO settings. The average total charge and vertical angular displacement of the electron spectra over multiple shots are plotted at different laser focus positions relative to the plasma density distribution (indicated by the grey line in Fig. 4.10d)). Total charge for the spectra are calculated inside a mask of $\pm 4\,\mathrm{mrad}$ of the electron bunch peak spatial location which is calculated from the laser axis using the method presented in section 2.3.2.3. The light blue shaded area indicates the amplitude of shot-to-shot fluctuations.

Ionisation-induced injection of the innermost nitrogen electrons ($N^{6/7+}$ states) is the main electron trapping mechanism at the laser intensity and plasma density used in this experiment. This has been confirmed experimentally and in the simulations, indicating minimal electron self-injection. For the value of density used ($n_\mathrm{e} \simeq 7 \times 10^{18}$ cm^{-3}) self-injection requires $a_0 \geq 4.3$[52]. In this experimental configuration, simulations show that a_0 remains below this value, even for cases leading to the highest accelerated charges.

Figure 4.10d) shows that the accelerated charge is strongly dependent on the focal position of the laser with a characteristic length $\simeq 0.5\,\mathrm{mm}$ close to the value of the Rayleigh length z_R. This result is in accordance with the variation of the laser fluence profiles with the focal position shown in Fig. 4.4. As relativistic self-focusing becomes efficient slightly before the density plateau, when the focal plane is too far from this position the laser intensity cannot reach high enough values for trapping a significant amount of charge (as seen in Fig. 4.10d)) and the large deformation of the laser radial profile leads to a large bunch angular deviation (as seen in Fig. 4.10e)).

Focusing at $z = -0.8\,\mathrm{mm}$ produces a spectrum peaked at $(118 \pm 5)\,\mathrm{MeV}$ with

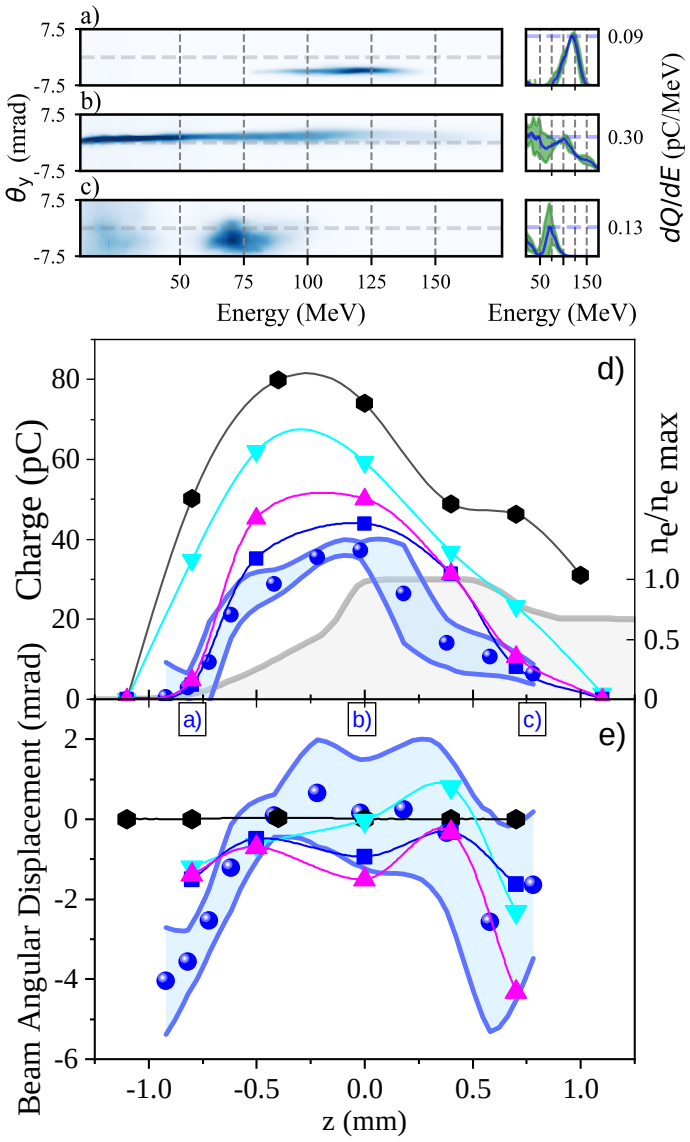

Figure 4.10 – Representative experimental electron spectra within $\pm 7.5\,\mathrm{mrad}$ window around the laser axis between 11 and $175\,\mathrm{MeV}$, corresponding to laser focal positions along the longitudinal spatial axis, z, a) pre-plateau: $z = -0.8\,\mathrm{mm}$, b) peri-plateau: $z = 0\,\mathrm{mm}$, and c) post-plateau: $z = 0.8\,\mathrm{mm}$ for the LE case and 1bFPS AO settings. d) total charge within a $\pm 4\,\mathrm{mrad}$ of the electron bunch peak spatial location, and e) electron bunch peak displacement from laser axis, defined as zero angular deviation, are shown as blue circles as functions of position along the laser axis. Simulated results for $n_e = 6.7 \times 10^{18}$ cm^{-3} and $a_0 = 2.15$ are plotted as black hexagons for a Gaussian laser bunch and realistic 1bFPS sim laser as blue squares; for comparison $n_e = 7.5 \times 10^{18}$ cm^{-3} and $a_0 = 2.15$ are indicated by cyan down triangles ($a_0 = 2.0$ by magenta up triangles). Plasma density profile is illustrated by the grey line. Errors are given by the standard deviation of the values for both parameters and $\mathrm{dQ/dE}$ from consecutive shots.

an energy spread of $27\,\%$, a divergence of $(2.9 \pm 0.6)\,\mathrm{mrad}$ (full angle), and an average bunch deflection of $(-3.6 \pm 0.3)\,\mathrm{mrad}$. In this case, the accelerated charge is low at $(3.32 \pm 0.64)\,\mathrm{pC}$ due to the reduced effect of self-focusing because the laser starts diverging before self-focusing. However, the percentage of charge within $2\times$ FWHM of the peak reaches $94.8\,\%$ showing that the majority of accelerated electrons are within the peak, leading to an exceptionally clean signal.

Placing the focal position at $z = 0$ produces spectra with the highest charge (Fig. 4.10b) with peak $\mathrm{dQ/dE}$ of $(0.30 \pm 0.06)\,\mathrm{pC\,MeV^{-1}}$ at $(102 \pm 4)\,\mathrm{MeV}$ and charge of $(33.6 \pm 6.6)\,\mathrm{pC}$. These bunches have improved coaxiality with the laser axis with a reduced average displacement close to zero for these settings and a slightly increased divergence of $(4.4 \pm 0.6)\,\mathrm{mrad}$. The reduced value of the peak energy and the broad energy spectra that extend up to $(200 \pm 14)\,\mathrm{MeV}$ give a signature that a large plasma-wave accelerating field is generated, but it is significantly reduced for a large part of the trapped electrons by beam loading effects. As described in section 1.5.2.3, a non-optimal beam loading will lead to an increase in energy spread due to the inhomogeneous accelerating field over the particle bunch. The increased peak $\mathrm{dQ/dE}$ in this case indicates significant charge at higher energies capable of changing the wake structure, leading to the increased energy spread that we see in the electron spectra at this focal position setting. We find a difference in the energies of the lowest and highest energy electrons of approximately $200\,\mathrm{MeV}$. Further, from simulations we know that injection of electrons is unlikely to occur in the upramp due to the contracting wake structure during the increase in plasma density, so we can assume z = 0 to be the earliest injection point providing 2000$\mu\mathrm{m}$ of plasma for acceleration. Assuming that the charge was injected over a short distance (i.e. $L_{inj.} \ll L_{accel.}$), we find an alteration in the accelerating gradient of the wake structure of approximately 3 GV/m/pC. Beam loading has been found to alter the wakefield structure longitudinal field by approximately 1 GV/m/pC[61] and so this toy model over-estimates the magnitude of the effect of the beam loading on the energy spread of the electrons.

Finally increasing the focal position to $z = 0.8\,\mathrm{mm}$ decreases the trapped charge down to $(10.7 \pm 2.1)\,\mathrm{pC}$ with a peak energy of $(71 \pm 10)\,\mathrm{MeV}$ and an energy spread of $39\,\%$ (spectrum Fig. 4.10c)). The presence of low-energy electrons indicates two different zones of trapping. The bunch broadens with a $(13.0 \pm 0.6)\,\mathrm{mrad}$ full angle divergence. Focusing at $z = 0.8\,\mathrm{mm}$ further increases the fluctuations in the electron bunch pointing as seen by the increases in the errors due to the increased sensitivity to the laser energy distribution pre-focus. More generally, comparing 4.10d) with 4.10e), larger fluctuations in the bunch angular deviation than in the total charge is observed.

Simulations were performed for different settings of the input laser pulse ; the resulting electron charge and bunch angular deviation are plotted in Fig. 4.10d) and e) for comparison with experimental data. Gaussian pulse case (black hexagons) is compared to a realistic transverse distribution using 1bFPS settings (plotted as

blue squares), for $a_0 = 2.15$ at $n_e = 6.7 \times 10^{18}$ cm^{-3}, which are the estimated experimental values. In order to show the influence of the plasma density and the laser intensity, we have also plotted simulation results for $n_e = 7.5 \times 10^{18}$ cm^{-3} with either $a_0 = 2.15$ (cyan down triangles) or $a_0 = 2.0$ (magenta up triangles).

The overall dependence of charge against the focal position is adequately described in the four simulation cases. However, the Gaussian calculation results in an overestimated charge, with an error of more than a factor of two close to the maximum charge, and significantly higher simulated charges for early and late values of focal position. The higher accelerated charge is due to the increased laser energy partition within the bubble which produces a larger proportion of the laser above the threshold intensity for ionisation of the inner shell electrons of nitrogen. Further, as the laser energy is more concentrated, the efficiency of self-focusing increases which then drives the laser intensity to higher values. On the contrary, simulated results using realistic laser parameters provide good agreement to experimental results: the fast decrease of the charge at late focal positions is well reproduced. Further, the overestimation of the maximum charge is only 17% in the realistic case. Increasing the density in the simulation by 12 % leads to an additional increase of 41% for the value of the maximum of charge and a broadening of the corresponding charge curve in Fig. 4.10d) (cyan down-triangles), which approaches the Gaussian case. Finally, as seen in Fig. 4.10d) (magenta up-triangles), a decrease of 14 % of the laser energy compensates for the effect of the density increase at early and late focal positions.

As expected, the electron bunch remains aligned with the laser axis for all focus positions when the axis-symmetric Gaussian pulse is used (see Fig. 4.10e) black hexagons) as there is no radial asymmetry to drive asymmetric wakes. Experimental data for the angular deviation of the bunches are well reproduced by the simulation when including the realistic laser complex amplitude. In particular, the counter-intuitive fact that the sign of the displacement is unchanged when going from large negative z values to large positive ones. In the former case, laser-plasma interaction occurs mainly with the laser profile in front of the focal plane, whereas in the latter case, it is behind. Between these two positions, there is a change of sign of the laser phase in vacuum, but not for the electron displacement inside the plasma, indicating that large non-linear effects determine the final direction of the electron bunch. Fig. 4.10e) shows that the bunch angular deviation exhibits similar trends as the charge along the laser axis for variations of 12 % in plasma density or 14 % in laser power.

In order to analyse more closely the correlation between the laser propagation and the transverse displacement of the electrons accelerated up to the peak energy, we have plotted in Fig. 4.11 the evolution of corresponding average values inside the plasma with the same spatial units as Fig. 4.6. Here three cases are presented: a pre- and post-plateau focal position corresponding to positions a) and c) of Fig. 4.10, and a peri-plateau focal position corresponding to the simulated case with the

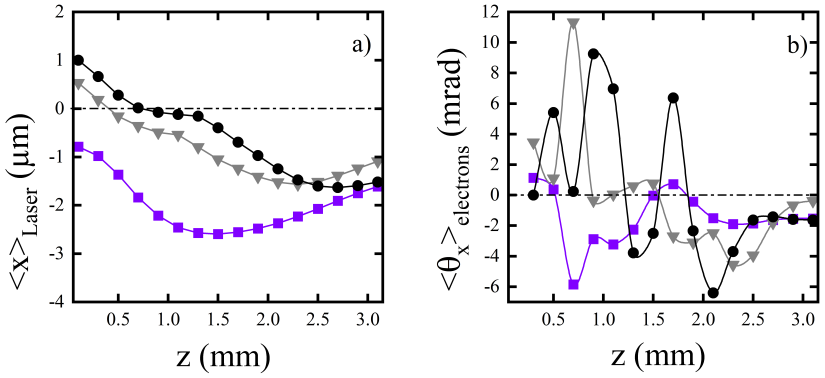

Figure 4.11 – Simulation results for a) the evolution of the centre of mass of the laser fluence inside a disk of $20\,\mu$m radius, and b) of the average angle of the electrons accelerated to the energy peak, as a function of position on the laser axis, for three focal positions: $-0.8\,\mathrm{mm}$ (purple square symbols), $0.4\,\mathrm{mm}$ (grey triangles) and $0.7\,\mathrm{mm}$ (black circles).

lowest electron bunch axial deflection. Simulation results for the evolution of the x positions of the centre of mass of the laser fluence $< x >_{\mathrm{Laser}}$ during propagation, calculated over a transverse disk of $20\,\mu\mathrm{m}$ radius centred on the z-axis, for three focal positions $z_{\mathrm{foc}} = -0.8\,\mathrm{mm}$, $0.4\,\mathrm{mm}$ and $0.7\,\mathrm{mm}$ as parameters, are plotted in Fig. 4.11a), corresponding to the case of 1bFPS AO settings, $n_e = 6.7\times10^{18}$ cm^{-3} and $a_0 = 2.15$ (blue squares in Fig. 6). Here we use z_{foc} to distinguish between the vacuum focal positions and the longitudinal position (z) dependent behaviour of the laser and electrons. During the first stage of propagation, $< x >_{\mathrm{Laser}}$ is decreasing for all focal positions, with an angular direction of the order of $-1\,\mathrm{mrad}$, reflecting the asymmetry of the injected laser intensity profile. This decrease of $< x >_{\mathrm{Laser}}$ continues during self-focusing. This variation of $< x >_{\mathrm{Laser}}$ induces a displacement of the centre of mass of the accelerated electrons toward negative values of x. After z =1.5 mm for z_{foc} =$-0.8\,\mathrm{mm}$, z =2.5 mm for z_{foc} =0.4 mm and $z_{\mathrm{foc}} = 0.7\,\mathrm{mm}$, the value of $< x >_{\mathrm{Laser}}$ either stabilises or increases as transverse diffraction of the laser becomes dominant with the decrease of plasma density.

Between z =0.5 mm and z =2 mm, the plasma wakefield has the highest amplitude, not only accelerating electrons but also producing transverse betatron oscillations of the accelerated electrons as can be seen from the average electron angle evolution, plotted in Fig. 4.11b). After z=2 mm, electrons can perform only a fraction of the betatron oscillation period, determining the final average angle at the exit. For $z_{\mathrm{foc}} = 0.4\,\mathrm{mm}$, there is a nearly perfect final focusing, leading to a very small exit angle. At the same time, for the other two focal positions, the coupling between the laser intensity and density gradient have non-optimal values close to the plasma exit, resulting in larger final angles. [171]

It has already been reported that the exit gradient can be optimised to reduce the final RMS divergence of the electron bunch[172-174]. The interaction between

the wake and electron bunch has been studied extensively in these references in terms of RMS bunch parameters. In addition to the above references, we show that the asymmetry in the laser fluence profile can influence the electron bunch axial displacement due to the final average bunch divergence, as demonstrated in Fig 4.11b) after $z = -0.8\,\mathrm{mm}$. The magnitude of this effect can be controlled by modifying the laser-plasma coupling through a shift in the focal position.

In summary, the final angular deviation of the electron bunch is determined by three main factors. First, the initial symmetry of the focusing laser. Second the position of the focal plane relative to the plasma density profile at which self-focusing becomes dominant. Third, laser amplitude and plasma density gradient at the exit region of the plasma. These results show that for optimal focal positions, the plasma density profile originating from the ELISA gas cell design can efficiently reduce the angular deviation leading to better coaxiality of the electron bunch with the laser axis. Simulations show that this reduction of the angular deviation is efficient for both transverse directions, y as well as x.

4.1.3.3 . Influence of Laser Wavefront on Electron Bunches

A third control mechanism was explored using the AO settings to study the influence of the laser wavefront on the injection process. This influence is analysed in more detail for the focal position $z_{\mathrm{foc}} = -0.8\,\mathrm{mm}$ because, as seen in Fig. 4.10a), it can produce electron bunches with single peak spectra and was not previously studied. In most previous works, either experimental or theoretical, the laser focal plane was set deep inside the plasma to optimise the position where the primary trapping process occurs[17, 70, 134].

Results obtained at focal position $z = -0.8\,\mathrm{mm}$ are compared in Fig. 4.12 for the three AO settings described in section I, FPS, 1bFPS and 2bFPS. These three AO configurations (FPS, 1bFPS, 2bFPS) yield similar values for the total charge in the peak (1.6 ± 0.3, 2.3 ± 0.4, 3.7 ± 0.7) pC and for the peak energy (126 ± 8, 114 ± 7, 125 ± 3) MeV. However, the corresponding experimental electron spectra differ significantly for the FPS case, as seen from Fig. 4.12 a) to c).

Whereas FPS settings yield a broad spectrum in energy and a larger dispersion in angle, the 1bFPS and 2bFPS configurations generate single peaks with a lower dispersion both in energy (18% and 8.7% FWHM) and angles (4.4 ± 0.6, 1.8 ± 0.6) mrad full angle, a maximum $\mathrm{dQ/dE}$ of (0.09 ± 0.02, 0.22 ± 0.04) $\mathrm{pC\,MeV^{-1}}$ and a bunch angular deviation of (-3.3 ± 0.3, -4.3 ± 0.3) mrad; it contains (93, 60)% of the total charge in $\pm 1\times$ FWHM leading to a total energy of (0.2, 0.4) mJ. These values indicate that the 2bFPS configuration provides better quality electron bunches, with two times more energy in the peak (see Eq. 2.35 for definition), together with a reduced dispersion in energy and angle. Simulation results are in good agreement with the experimental data. The maximum value of the power of the laser during the experiment was $P_0 = 16.5$ TW, and for $n_e \simeq 7 \times 10^{18}$ $\mathrm{cm^{-3}}$, the critical power P_C for relativistic self-focusing is 4.2 TW. The ratio $P_0/P_C \simeq 4$ corresponds to the intermediate non-linear regime[3, 175]. Laser-plasma coupling

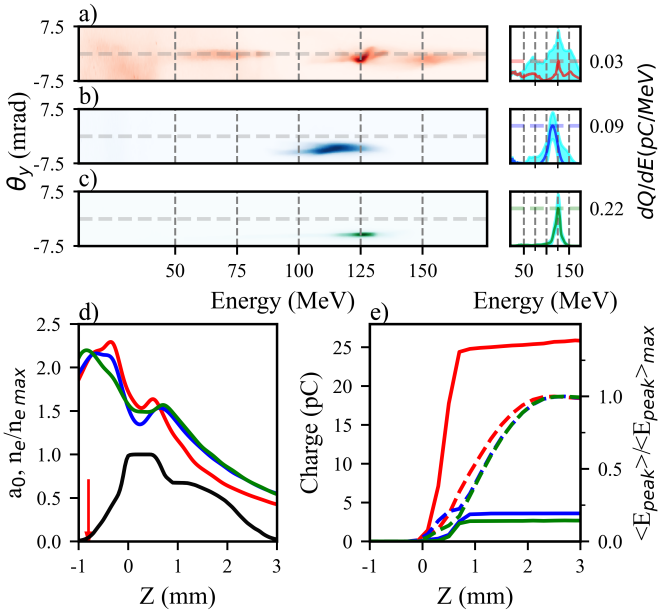

Figure 4.12 – Experimental spectra a)-c) illustrating the effect of phase front optimisation on accelerated electron bunches at laser focus z_{foc} = $-0.8\,\mathrm{mm}$ for wavefront configurations a) FPS, b) 1bFPS and c) 2bFPS. Electron charge density in divergence-energy space ($\mathrm{pC\,MeV^{-1}\,mrad^{-1}}$ and their corresponding spatially-integrated $\mathrm{dQ/dE}$ ($\mathrm{pC\,MeV^{-1}}$) within a $\pm 7.5\,\mathrm{mrad}$ window around the laser axis indicated by the dashed horizontal line and in an energy window $11.3\,\mathrm{MeV}$ and $175\,\mathrm{MeV}$. Standard deviation was calculated over five shots and plotted here in cyan. d) simulation results for the evolution along the propagation distance z of the normalised vector potential a_0 of the laser pulse: the black curve represents the normalised plasma density profile, while the focus position, z_{foc}, is marked by the red arrow; e) evolution with z of the charge of the electrons having final energy above 10 MeV (solid lines) and average energy of the electrons contributing to the peak in energy normalised by its maximum values (dashed lines). For figures d-e, the red curves correspond to FPS, blue curves to 1bFPS, and green to 2bFPS.

during propagation, which strongly impacts electron injection and acceleration, has a strong dependency on the laser wavefront shape at the plasma entrance in this regime as the laser is self-focused but does not strongly collapse. It thus provides additional means to control the number of trapped electrons and the output bunch parameters.

The simulated result plotted in Fig. 4.13 shows the electron density map and laser amplitude in the xz plane (transverse to the laser polarisation plane) corresponding to the best case of this study (Fig. 4.12 c)) at $z = 1\,\mathrm{mm}$. This illustrates the asymmetry of the laser shape acquired during propagation and highlights the importance of analysing the impact of the input laser mode distribution.

To better understand the physics involved, we have plotted simulation results for the laser a_0 in Fig. 4.12d), and the evolution of the charge of the accelerated

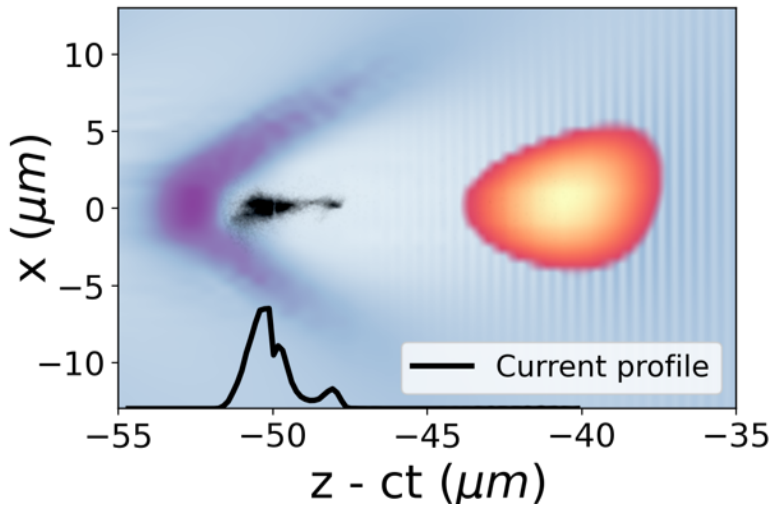

Figure 4.13 – Snapshot of electron density and laser amplitude in the xz plane from FBPIC simulation after $2\,\mathrm{mm}$ of laser propagation in the plasma. Accelerated electrons are shown in black along with their current profile in arbitrary units and the background plasma in blues where darker blue is a more dense region of the plasma. This simulation was performed by Gilles Maynard and Ioaquin Moulanier.

electrons and the average energy of the electrons contributing to the peak of energy in Fig. 4.12e). The three AO settings provide similar curves with two maxima for the evolution of a_0. The first maximum is due to the focusing of the incoming beam being slightly increased by relativistic self-focusing of the front of the laser pulse. In contrast, the second maximum comes from the ponderomotive focusing of the rear of the pulse.

Injection through ionisation occurs only if the laser field is high enough to tunnel ionise the ion N^{5+}, which occurs for $a_0 > 1.5$. Fig. 4.12d) shows this corresponds to the zone around the first ($z \approx -0.5$ mm) and second maxima ($z \approx 1$ mm). Once generated through N^{5+} ionisation, an electron needs also to be trapped by the plasma-wave field. Trapping requires a sufficiently high plasma density such that the wake potential is large, moreover, it is greatly favoured by a rapid increase of the longitudinal length of the positively charged bubble just behind the laser pulse. This increase occurs either in a density downramp or by a rapid increase of the laser intensity. Figure 4.12e) shows that trapping occurs at the position of the second maximum for cases 1bFPS and 2bFPS. The slight increase in the value of a_0 for FPS causes trapping for $0 < z < 0.5$ mm, and a small amount of trapping throughout the downramp, as shown by the increase in total charge leading to the stronger low energy electron signal of Fig. 4.12a). For 1bFPS and 2bFPS, no trapping occurs around the first maximum of a_0 because either the density is increasing or the intensity is decreasing. However, the zone $0.5 < z < 1.0$ mm around the second maximum is optimised for trapping: the density is decreasing and the intensity is increasing. Comparison of a_0 curves for

FPS and 1bFPS configurations shows that in the FPS case, the second maximum is slightly higher and at a slightly smaller value of z. As a_0 values are close to the threshold $a_0 = 1.5$, small variations of a_0 result in a large difference in the trapped charge and in the energy spectra. In particular, the higher value of a_0 observed for the FPS results in a larger trapping zone, thus producing a broader energy spectrum. This high sensitivity at z_{foc}=$-0.8\,\mathrm{mm}$ also explains the fact that the total charge obtained in simulation for FPS can be higher than the experimental value.

The average energy of the peak electrons has a similar behaviour for the three AO settings, increasing up to the plasma exit and showing that the acceleration distance is smaller than the dephasing length. For $z_{\mathrm{foc}} = -0.8\,\mathrm{mm}$, trapping occurs at low densities, putting the electrons at a large distance behind the laser pulse, therefore increasing the length of acceleration compared to trapping at positions close to $z_{\mathrm{foc}} = 0$.

1bFPS and 2bFPS settings lead to very similar results, particularly concerning the evolution of the laser amplitude a_0 in Fig. 4.12d). In terms of electron trapping, the main difference is that the second 2bFPS peak is localised at a slightly larger z than the 1bFPS one. As a consequence of this small shift, the trapping of electrons starts slightly later for 2bFPS (at a lower density) and has a smaller duration, leading to a reduction of the energy spread and a small increase in the peak energy, because, in 2bFPS, the electrons are localised at a slightly longer distance from the laser pulse. As pointed out previously, close to the ionisation threshold of N^{5+} in the trapping zone, the total charge is strongly dependent on the exact position of the focal plane. Nevertheless, the acceleration process depends only weakly on the total charge in the regime achieved here, where beam-loading does not contribute significantly.

These electron bunches are deflected from the laser axis by approximately $4\,\mathrm{mrad}$ and additional mechanisms must be introduced to keep accelerated bunches on-axis whilst retaining high bunch quality. In comparison to the results presented in Fig. 4.10 it could be assumed that the target beam parameters ($150\,\mathrm{MeV}$, 5% energy spread, $30\,\mathrm{pC}$) could be achieved through improving the laser quality closer to that of a Gaussian beam as at $z_{\mathrm{foc}} = -0.8\,\mathrm{mm}$ this provides $50\,\mathrm{pC}$. However, in this configuration the injection volume is increased due to the longer distance over which a_0 exceeds the injection threshold, leading to larger energy spread of the resulting spectra. This effect is seen in Fig. 4.12a) where FPS, the most symmetric setting (Fig. 4.5a)), produces the broadest spectra in energy and stronger fluctuations in consecutive electron spectra as illustrated by the standard deviation in the $\mathrm{dQ/dE}$ plot. Optimisation of the LPI therefore requires the simultaneous tuning of a larger number of experimental parameters. The rotational symmetry of the laser pulse, as discussed in section 4.1.2.1, could be used as an input parameter for an optimisation scheme using, for example, a Bayesian optimisation model[81, 153] to produce electron bunches with the target parameters using the large ex-

perimental parameter space. Further, the use of pulse rotational symmetry would provide a simple input parameter in an optimisation model allowing for a reduction in the complexity usually associated with controlling individual AO pistons, or their corresponding Zernike polynomials. Whilst it was not applied during this thesis it is a topic of future work.

4.1.4 . Conclusions

Previously predicted improvements in injector electrons with an elongated plasma density downramp are realised for the ELISA gas cell[134, 170]. Advances in the understanding of LPI are achieved through experimental and simulated studies of the laser-plasma coupling with alterations in plasma density structure, focal position, and laser pre-focal symmetry.

To optimise the injector, we have selected three main parameters for their significant impact on the resulting electron spectra in the regime studied: the length of the plasma density downramp to control the acceleration and focusing fields which the trapped electrons experience, the focal position to control the non-linear coupling between the laser and the plasma, and the laser wavefront to alter the transverse energy distribution of the laser through focus to control the dynamics of the wakefield through the effect of self-focusing. Through careful optimisation of the density downramp, focal position, and shaping of laser symmetry, electron bunches with energy in the 100 MeV range, less than 10 per cent energy spread, multi-pC charge and sub $2\,\mathrm{mrad}$ divergence are produced as illustrated in Fig. 4.12c). Comparison to realistic simulations uncovers the physical mechanisms controlling the electron dynamics which produce these desirable bunches. Bunch energy ($125\,\mathrm{MeV}$) and energy spread (8.7%) approach the desired values ($150\,\mathrm{MeV}$, 5%), however, the level of charge must be augmented significantly by a factor of 8 from $3.7\,\mathrm{pC}$ to $30\,\mathrm{pC}$, to reach the desired value for an LPI within the EuPRAXIA framework. Future optimisation work should explore larger parameter spaces to improve the results of this novel injection mechanism using rotational symmetry as an input parameter.

Changing the pre-focal symmetry whilst retaining a similar focal spot is shown to have a measurable effect on the accelerated electron bunches and suggests that this could be another control mechanism to utilise when optimising LPIs. Simulations using realistic laser parameters produced accurate descriptions of the accelerated bunch dynamics whilst Gaussian models failed to achieve this. This work expands on the physics of injectors and provides a simulation method using realistic laser parameters for improving the accuracy of predictions for laser wakefield acceleration schemes in a computationally inexpensive way.

4.2 . Bayesian Optimisation for Low-Energy Injectors: 2^{nd} Experiment at LLC

From the results of the 2019 campaign presented in section 4.1.3.3 it was hypothesised that the high-quality electron spectra that were achieved during the previous campaign could be further improved through the use of ML-based optimisation. During the previous experiment, multiple parameter scans were performed sequentially but, as demonstrated in reference[81] by Shalloo, it is not always possible to find a global optimum of two coupled parameters using this method. We therefore used Bayesian Optimisation to search the parameter space and optimise various merit functions of desired variables such as total charge and total beam energy, energy spread, etc. and scaled products of these variables.

4.2.1 . Bayesian Optimisation Experiment Overview

A second experiment was conducted at the LLC in 2021 to investigate the implementation of automation and optimisation within LWFA experiments. The aim of the campaign was to produce a fully automated experiment that could then be controlled by a Bayesian optimisation (BO) process to achieve electron spectra with desired characteristics. This was achieved through the automated control of the focal position of the laser pulse controlled by shifting the gas cell, the plasma density within the cell controlled by changing the pressure of the gas injection system and the dazzler 2^{nd}, 3^{rd}, and 4^{th} order settings to alter the spectral phase of the laser pulse. Once the control of these experimental parameters - that form core variables in any LWFA experiment - was automated, they could then be varied by an optimisation script that chose the next experimental settings based on the output of the electron spectra as measured by the electron spectrometer and analysed in real-time.

Real-time analysis required all electron spectrometer calibrations to be completed before performing online measurements. Orders of magnitude increase in charge between the initial testing and BO runs required the addition of extra optical filters on the imaging system of the electron spectrometer that were taken into account in post-processing. Due to the availability of the automated control, automated N-dimensional scans were also completed to explore the parameter space in a grid-like fashion for the validation of results in a more classical manner, and to provide a larger data set for the offline optimiser method presented below in section 4.2.4. In addition, this automated control lead to a speed-up of data acquisition due to the absence of user control where the shot repetition rate was limited solely by the evacuation time of the pumping system to keep vacuum pressure under $10^{-5}\mathrm{mbar}$ for compressor longevity.

This experiment investigated the implementation of BO optimisation in LWFA experiments through the variation of the optimiser settings and the inter-communication between experimental settings and an automated optimiser. Machine-learning neural-

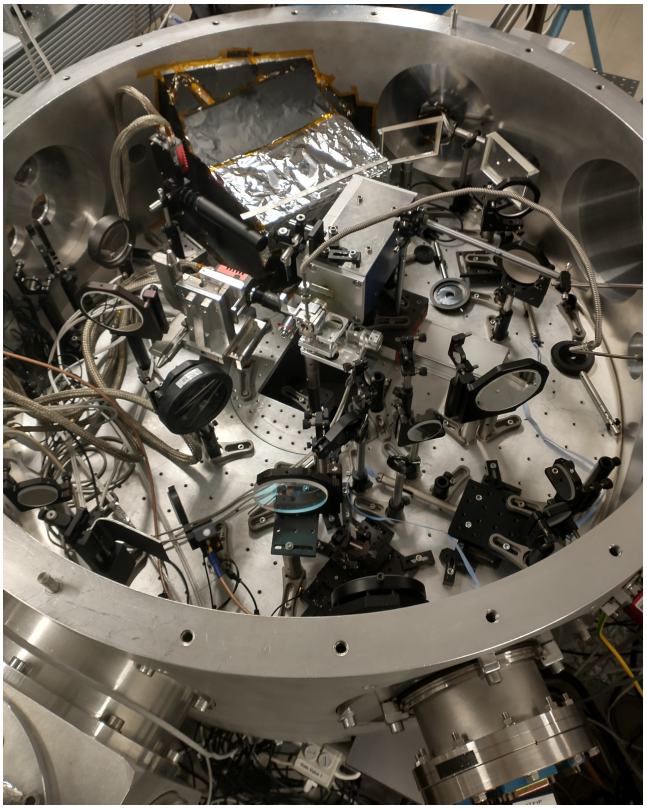

Figure 4.14 – Image of the interaction chamber taken during the second campaign, corresponding to the drawing shown in fig. 4.15.

network-based approaches for laser focus retrieval were also developed and are detailed in section 3.2.2. In addition, we used the results obtained by the Bayesian optimisation to explore interesting physical phenomena on the group delay dispersion induced in the laser pulse by the Dazzler.

In the remainder of this section, we first give an overview of the experimental implementation used during this campaign and the process of automation and optimisation. We then examine the use of optimiser models, their results during this experiment and the implementation of an offline BO procedure for improving optimisation efficacy (how well an optimum is achieved) and efficiency (number of iterations required to reach the optimum configuration) in future experiments.

4.2.2 . Overview of Experiment

During this campaign, a fixed-length version of the ELISA gas cell was implemented where plateau plasma length was controlled using metal spacers placed on the gas cell to control the separation of the cell's two faces in steps of $0.5\,\mathrm{mm}$. Whilst this excluded the option of altering the plasma length during the optimisation, this set-up was chosen as it enabled a more robust configuration lowering errors on the determination of plasma density, and sensitivity to electromagnetic

pulse hazard. Typical plasma plateau lengths in this fixed configuration ranged between 100 and 800 $\mu\mathrm{m}$. Otherwise, the mechanical components of the gas cell were identical to the previous experiment described in section 2.2.1.

An upgraded laser system was used during the second campaign, delivering a maximum energy in the focal plane increased from 0.7 to $1.0\,\mathrm{J}$. The calibration of the system transmission was completed by measuring the pulse energy at the end of amplification (located between the final multi-pass amplifier and the beam spatial expansion stage in Fig. 2.6) and at Interaction Chamber Center (ICC, located at the crossing point of the main laser in red and the probe line in yellow in Fig. 4.15). A compressor-to-interaction region transmission of 62% was measured at the beginning of the experimental campaign. Due to compressor degradation and optical damage during the 4000 experimental shots the transmission was reduced to 23% at the end of the campaign. The laser pulse energy was again tracked throughout the experiment using an energy-calibrated CCD which measured the fluence of a leak through the final dielectric mirror before focusing thus allowing the effects of laser energy reduction to be decoupled from changes in the electron spectra. Pulse duration during this experiment was slightly shorter at $38\,\mathrm{fs}$ FWHM (from $42\,\mathrm{fs}$ during the previous experiment) at optimal compression whilst the pulse contrast remained the same as the previous campaign at 1×10^{-8} in intensity up to $150\,\mathrm{ps}$ before the main pulse. The focal spot during this experimental campaign was slightly larger at $16\,\mu\mathrm{m}$ FWHM. Coupled with the reduction in pulse duration and the increase in on-shot energy the resulting a_0 changes only to 2.02 from 2.15 in the previous campaign.

4.2.2.1 . Implementation of Automated Experimental Control

Typically experiments at the LLC are conducted as fully user-controlled where each experimental setting is set by hand between each shot. To increase the efficiency of data taking and to allow the BO algorithm to control directly the experimental parameters an automated control script was created to change the settings for the focal position, the backing gas pressure for the injection system and therefore the plasma density and the three spectral phase terms controlled by the DAZZLER AO-PDF. The focal position of the laser within the gas cell was controlled through a vacuum-compatible motor aligned in the longitudinal direction allowing the cell to be rapidly shifted with respect to the ICC between shots within $10\mu\mathrm{m}$ accuracy. The backing pressure of the injection system was controlled by a negative feed-back loop where input was controlled by a Bronkhorst flow metre calibrated for hydrogen providing an increase in pressure in the reservoir, and a butterfly valve connected to the main vacuum system could reduce it. The solenoid injection valve connected to the reservoir was triggered for injection $50\,\mathrm{ms}$ before the laser pulse as described in section 2.2.1. The AO-PDF spectral phase terms were controlled directly by the DAZZLER where spectral phase terms were requested by writing directly to a request file inspected by the DAZZLER control box. Shot timing was automated and limited by the completion of all experimental

parameters being altered and the vacuum chamber pressure that was constantly monitored for compressor longevity. All laser and electron diagnostics were temporally synchronised to the main pulse timing. Electron spectrometer data were analysed online to allow for realistic electron parameters to be used for merit function evaluation.

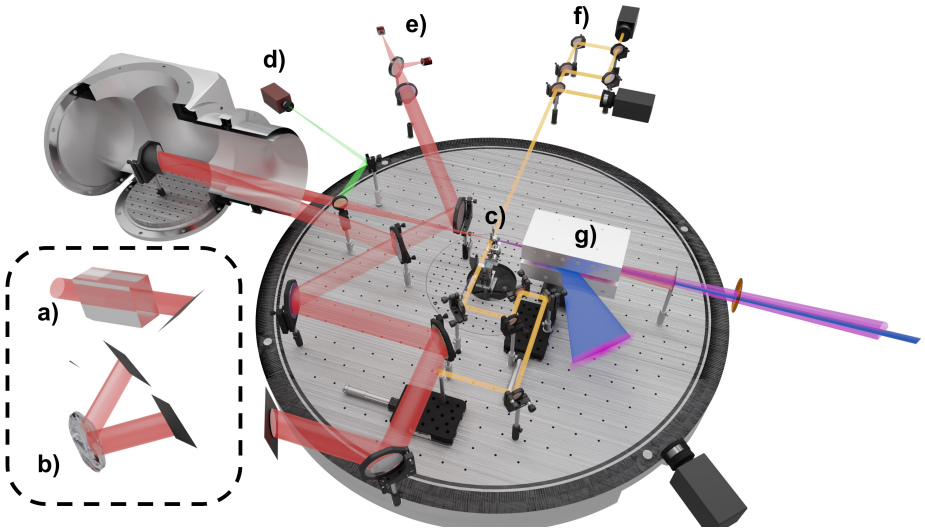

Figure 4.15 – Overview of the experimental set-up for the Bayesian optimisation LPI campaign. The AOPDF a) is used to control the spectral phase before the final amplification stage, and adaptive optic b) is placed after the compressor in the same vacuum chamber. The laser enters the interaction chamber from the transport line at the bottom. It is then transported to the off-axis parabola where it is focused into the ELISA gas cell c). d) A wavefront sensor can be used to measure the attenuated laser beam (green) to determine the wavefront curvature at focus. e) A portion of the laser is extracted via the final dielectric mirror before the parabola to track the energy and image of the laser in the far field. A small portion of the main beam is extracted using a small mobile pick-up mirror. This beam then enters a delay line to probe the plasma just after the main pulse has interacted with it. f) The probe line then propagates to the plasma diagnostics section at the top where the plasma density is measured by a Mach-Zehnder interferometer and a wavefront sensor. g) The electrons (blue) and depleted laser then exit the gas cell and electrons are dispersed in energy by the dipole magnet. The electrons then interact with a scintillating LANEX screen which produces visible light that can be imaged by the electron spectrometer camera in the bottom right.

	Laser Spatial Control		
Parameter	Laser Energy (J)	Focal Position (mm)	Adaptive Optic
Exploration Range	1	-2 $\leftrightarrow$ 2	N/A
on-shot monitoring	Yes	Yes	Yes
Automated	No	Yes	No

Table 4.1 – Explored parameter ranges, state of on-shot monitoring of resulting experimental parameters and if their control was automated. Adaptive optic provides 32 actuators with different voltage control and so is given the value N/A.

Allowed parameter regions for the optimiser to explore are displayed in tables 4.1, 4.2, and 4.3 for the spatial and spectral properties of the laser and the plasma profile, respectively. The laser energy(table 4.1) was not varied during the optimisation as there was no automated way of achieving this in the current laser system set-up. The laser energy was monitored on each shot using the energy-calibrated CCD discussed above in section 4.2.2. The focal position range was limited to $\pm 2\,\mathrm{mm}$ around the start of the plasma plateau due to the beam waist of the laser, causing significant ablation to the cell faces when focused before and after this position, which limited the number of shots. The vacuum stage responsible for controlling the relative position between the gas cell and the focal position provided $\mu\mathrm{m}$-scale monitoring of the motor position. The adaptive optic used a membrane with 32 actuators for wavefront correction. The wavefront was monitored periodically using the wavefront sensor and the attenuated green beam in Fig. 4.15 d) is extracted using the flip mirror. It was not possible to automate the adaptive optic during the time frame of the experiment.

	Laser Spectral Control		
Parameter	GDD (fs^2)	TOD (fs^3)	FOD (fs^4)
Exploration Range	8000 $\leftrightarrow$ 14000	-7000 $\leftrightarrow$ 40000	-100000 $\leftrightarrow$ 100000
on-shot monitoring	Yes	Yes	Yes
Automated	Yes	Yes	Yes

Table 4.2 – Explored parameter ranges, state of on shot monitoring of resulting experimental parameters and if automated for the spectral parameters of the laser.

Limitations on the spectral distortion of the laser pulse, listed in table 4.2, were defined and set by the laser team at the LLC to avoid damage of the compressor grating or strong spectral clipping due to the acoustic waveform of the AO-PDF being outside the allowed bandwidth.

The backing gas pressure was chosen from the minimum pressure required for electron injection and an upper limit from a large electron signal at low energy for the majority of focal position configurations.

	Plasma Control	
Parameter	Gas Injection (mbar)	Cell Configuration
Exploration Range	50 $\leftrightarrow$ 400	(see gas cell sec.)
on-shot monitoring	Yes	N/A
Automated	Yes	No

Table 4.3 – Explored parameter ranges, state of monitoring of resulting experimental parameters and if automated for the plasma density parameters. Cell configurations are mechanically set and so given the value N/A

4.2.2.2 . Focal Spot Quality During Bayesian Optimisation Experiment

The large sample set of focal spot images collected for the training of the cGAN described in section 3.2.2 allows us to accurately describe the typical focal spot pointing and radial profile stability of the LLC laser at focus.

Figure 4.16 shows the exceptional spatial stability of the focal spot at the LLC. The average radial profile in Fig. 4.16 b) over 1000 shots is indistinguishable from the mean value indicating a very stable transverse energy distribution of the focal spot. A Gaussian fit is used and applied to the transverse focal plane images, such as the example case in Fig. 4.16 a), to retrieve the centroid pointing fluctuations in Fig. 4.16 c). Using the focal length of the off-axis parabola as $775\mathrm{mm}$ and the average absolute pointing fluctuation of $4.6\,\mu\mathrm{m}$, the average fluctuation angle over 1000 shots is $6\,\mu\mathrm{rad}$ with a maximum pointing fluctuation of $19\,\mu\mathrm{rad}$. Pointing fluctuations are typically along the diagonal axis where they are clustered in two regions as can be seen from Fig. 4.16 d). The source of these oscillations along this diagonal have not currently been identified but could be due to vibrations on the focusing optic, or small alterations from the automated beam pointing piezo motorised mirrors.

4.2.3 . Experimental Results

During this experiment, a BO combined with automated control for improvements in the spectral density of the resulting electron spectra was implemented. Results achieved through the BO indicate the important role of spectral phase terms in reducing the energy spread of the resulting spectra. Further the implementation of the optimiser on offline data allowed for the exploration of merit function choice and tuning of hyperparameters such as the kernels and acquisition functions, which will be presented in future publications but are not included in this work due to time constraints. The plasma density data that was used to validate the self-referenced single-shot wavefront sensor plasma density measurements are shown in section 2.2.4. We performed analysis on the BO process and the resulting electron spectra.

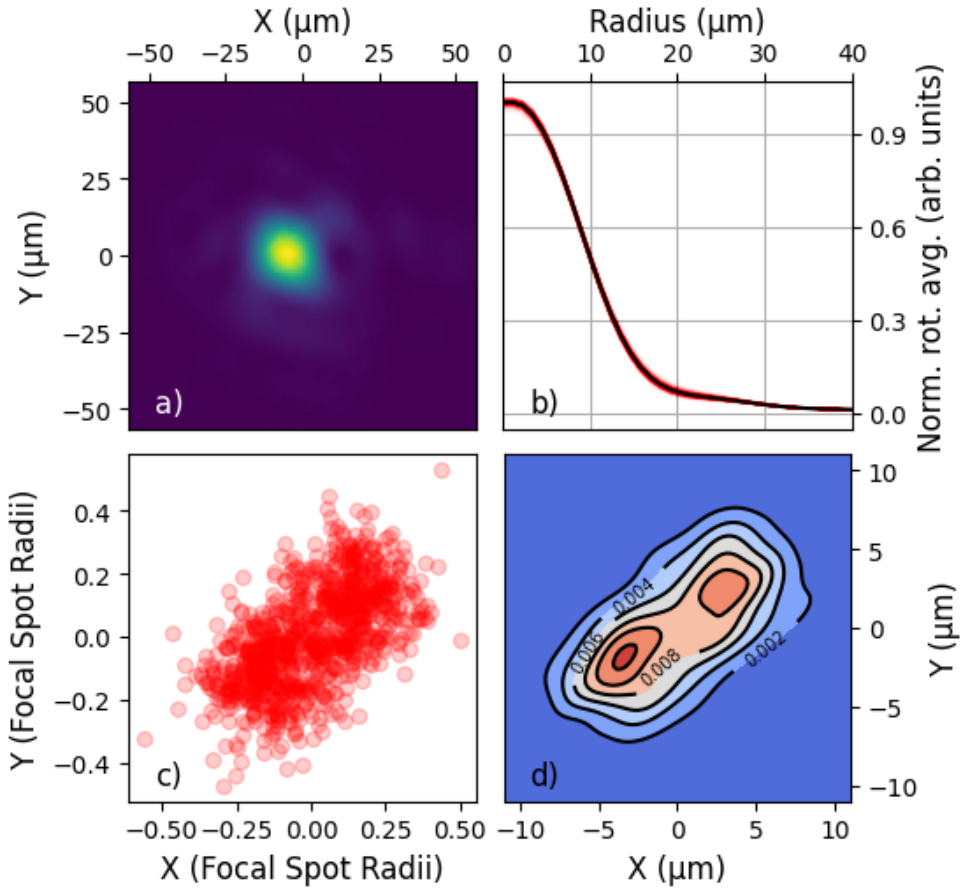

Figure 4.16 – Illustration of the stability of the focal spot at the LLC. a) demonstrates a typical focal spot chosen at random cropped to the centre of mass in an approximately $100 \times 100 \mu m$ box. b) Illustrates the average normalised radial profile, plotted here for 1000 shots in red, with the average profile in black. c) demonstrates the pointing fluctuations of the focal spot extracted from the origins of a Gaussian fit in units of the average focal spot radius. d) Gaussian kernel density estimation distribution of focal spot pointing fluctuations using the same spatial scaling as c). Both c) and d) are centred on the average focal spot position.

4.2.3.1 . Bayesian Optimisation Results During Experiment

A 4D spectral density BO was completed using the focal position of the laser and dazzler 2nd, 3rd, and 4th order spectral phase terms using 5% nitrogen 95% hydrogen gas mixture. Table 4.4 displays the experimental boundaries that were set during the optimisation.

Parameter	Focal Position (mm)	GDD ($\phi^{(2)}$)	TOD ($\phi^{(3)}$)	FOD ($\phi^{(4)}$)
Min. Setting	-1.6	-3000	-7000	-100000
Max. Setting	1.4	3000	40000	100000

Table 4.4 – Parameter Boundaries of Bayesian Optimisation run in Fig. 4.17

We took inspiration from the merit function, $M_{Mad} = \frac{\sqrt{Q}E}{\Delta E_{MAD}}$, in the BO work from Jalas[153], due to the exceptional results presented in their work in terms of electron stability and energy spread, to optimise the electron parameters starting from a region far from optimum. In this work we have modified their description and scaling of the bunch parameters in the merit function based on the experimental spectra achieved during the BO optimisation experiment.

Here we apply a quadratic scaling to the median energy, E, and use a generalised method for finding the energy spread of both peaked and broad spectra rather than the median absolute derivation of the energy distribution used in reference[153]. This results in the merit function $M_{peak} = \frac{\sqrt{Q}E^2}{\Delta E}$ where Q, E and ΔE are the total charge, median energy and the energy spread of the accelerated bunch, respectively. We chose to scale with the square of the median energy to reduce the effect of high charge, low energy bunches when beginning the optimisation far from optimum settings.

Initially, five random points are sampled before the BO begins, as marked by the grey dashed line in Fig. 4.17. The merit function of the initial five randomly sampled points is improved to the optimum value by a factor of 4.9, from 331 to 1631 ($pC^{1/2}MeV$) over the course of 28 consecutive BO iterations taking 14 minutes. Individual blue circles in Fig.4.17 represent the merit function that is measured from each sampling. It can be seen that whilst there is variability between iterations there is an increasing trend of the merit function with iterations. The variability between iterations arises from the exploration-exploitation parameter that is given to the BO process with a weighting parameter ϵ. During this optimisation, an upper confidence bound (UCB) acquisition function (defined previously in section 3.1.3.3) was used for the selection of the next parameter value to measure. As a reminder for the reader, we define the UCB acquisition function, a_{UCB}, as $a_{UCB}(x) = \mu(x) + \epsilon\sigma(x)$, where μ and σ are the means and variance of points x in the multi-dimensional parameter space and ϵ is a scaling parameter for the exploration and exploitation preference. Large ϵ favours a next sample point with high uncertainty, leading to wider exploration due to greater weight of the predicted variance into the acquisition function[176]. Conversely, a small ϵ favours optimising around the best-known result. Scaling of ϵ is a known challenge within machine learning due to the optimum value for each optimisation experiment being different or even varying over the course of an experiment. Work has been completed on producing a general method for the exploration-exploitation trade-off and methods of adaptive ϵ have been proposed[176], where ϵ is dynamically set throughout the optimisation procedure. In the optimisation example shown in this section, a value of $\epsilon = 0.01$ was used.

To illustrate the improvements in the electron bunch parameters with the BO process we show in Fig. 4.18 a waterfall graph of spatially integrated electron spectra for the BO process corresponding to Fig. 4.17. The spectrum corresponding to iteration 31 that optimises the defined merit function is indicated with the red

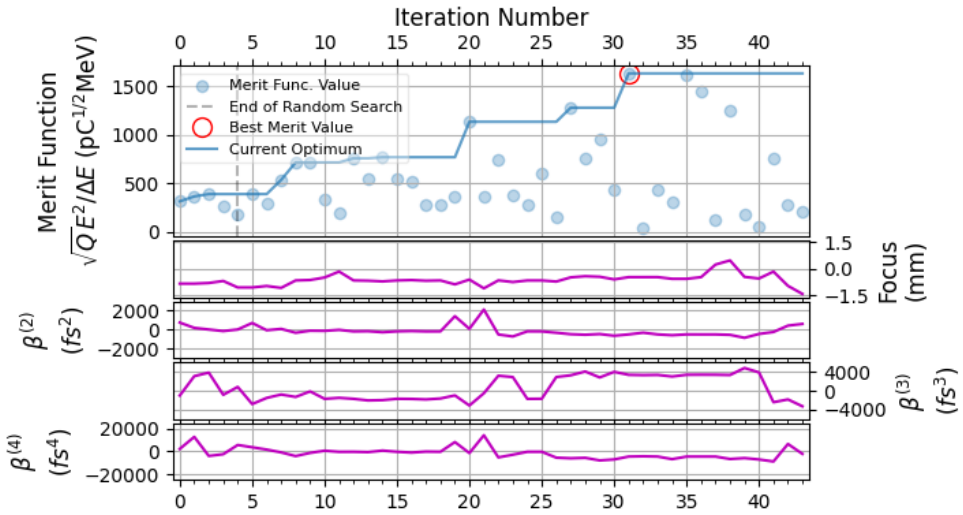

Figure 4.17 – Value of merit function, $\frac{\sqrt{Q}E^2}{\Delta E}$, as a function of iteration number in BO process. Random search finishes after 5$^{\text{th}}$ iteration. The best evaluation is tracked by the solid blue line. Individual evaluations are displayed in blue circles with the best evaluation circled in red. Explicit values for the 4D parameter scan are displayed below for the focus position within the gas cell and the three spectral phase terms.

tick label and corresponds to the red circled point in Fig. 4.17. Figure 4.18 indicates that peaked electron spectra with reduced energy spread, higher mean energy, and improved peak charge percentage were produced during the BO process from initially broad spectra.

The improvements in the electron spectra are illustrated in Fig. 4.19 where initial random positions are shown in the left column and the top contenders in terms of merit function are displayed in the right-hand column.

The spectrum that optimised the merit function during this optimisation routine is presented in Fig. 4.20 where the charge is plotted in divergence-energy space. Peak and total charge for this spectrum are 3.77 and $4.84\,\mathrm{pC}$ respectively providing a peak to total charge percentage of 78%. Median energy and energy spread were calculated at $96.9\,\mathrm{MeV}$ and 12.7% respectively. Parameter comparison between this spectrum with the highest bunch energy, lowest divergence and lowest energy spread, achieved during the previous campaign from Fig. 4.12 c) is shown in table 4.5. Comparison of the experimental parameters indicates that in the previous by-hand optimisation the electron bunch had a higher total charge whilst the peak charge values are comparable. This is explained however by the larger energy spread in our BO case indicating that the charge is more diffuse in energy. The peak energy value is also almost $30\,\mathrm{MeV}$ higher in the previously optimised case. The values are, however, close, and were achieved here in a 14 minutes optimisation in comparison to by-hand optimisation of the spectra where optimum focal position, plasma density and wavefront were all optimised consecutively ta-

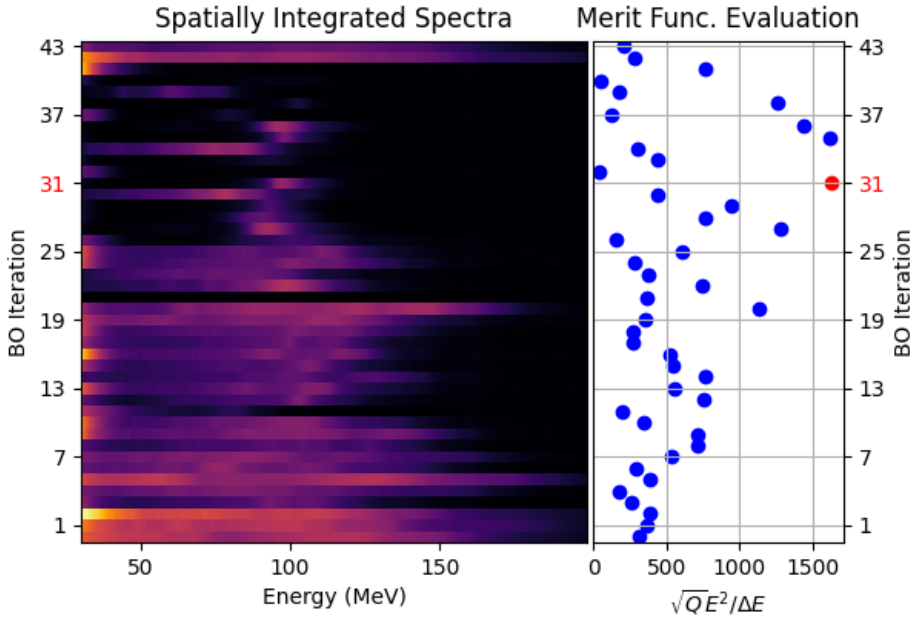

Figure 4.18 – Spatially integrated spectra over the course of the BO process displayed as a waterfall plot. Each spectrum is labelled with its interaction number indicated on the vertical left axis. Merit function evaluations are shown on the right-hand side plot where blue circles are evaluations of the merit function for a given spectrum which is optimised for iteration 31 with the red circle.

king significantly more time. This demonstrates the power of the BO process when applied with well-chosen merit functions. The inclusion of laser wavefront control via adaptive optic into the BO routine would likely further improve, or allow the modification of, the electron properties as only flat laser wavefront was used in this BO experiment. This alteration of the wavefront could provide the necessary transverse focusing to reduce the peak angular displacement of the electron bunch.

To measure the electron bunch stability at the optimum configuration found by the BO process, nine consecutive measurements were taken without changing input parameters. Stacked spectral measurements cropped within an energy range of 60 to $125\,\mathrm{MeV}$ and divergence mask of -20 to $20\,\mathrm{mrad}$ are presented in Fig. 4.21. The laser axis in vacuum defines the zero divergence position. All spectra within this stability scan are above the laser axis with an average deviation angle of $(6.3 \pm 2.5)\,\mathrm{mrad}$. This indicates that at these experimental settings, a consistent asymmetry in the accelerating dynamics forces the electrons off-axis. Whilst further simulations are required to clarify the underlying physical process, this effect could come from the spectral deformation of the pulse induced by the third and fourth-order dispersion terms inducing off-axis injection of the electron bunches

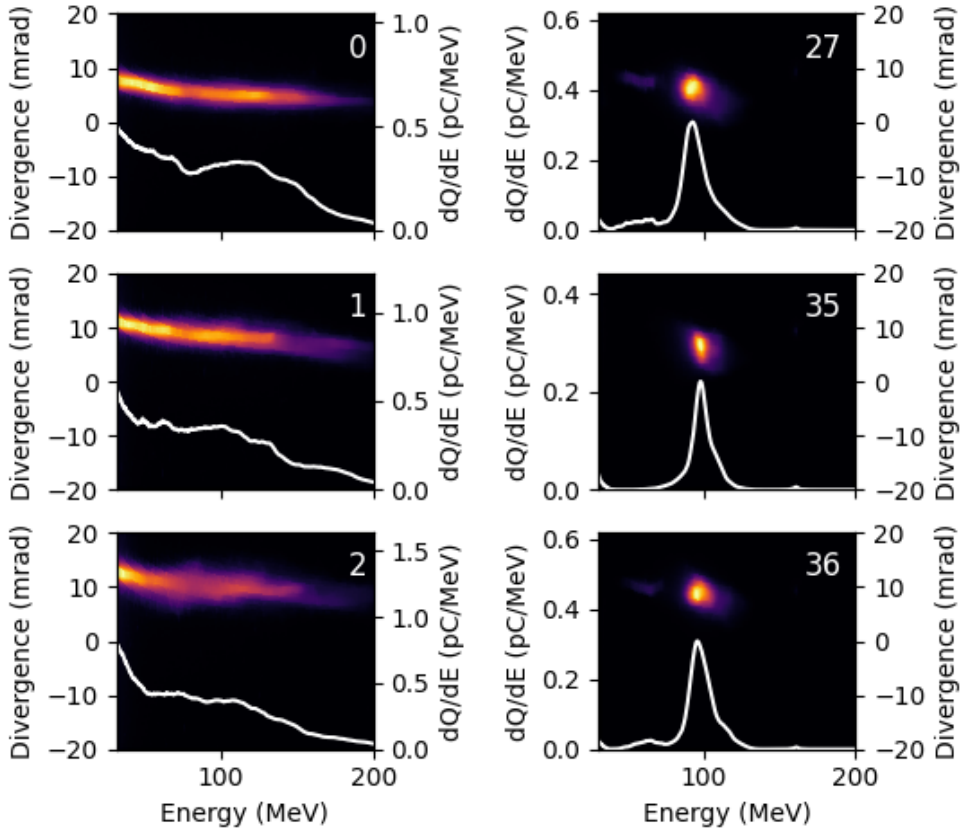

Figure 4.19 – Electron spectra in energy-divergence space with their spatially integrated $\mathrm{dQ/dE}$ with optimisation index number inset. The first three from random selection are shown in the left column and high merit function spectra are shown in the right column cropped to an energy window of 30 to 200 MeV

Spectrum	Total Charge (pC)	Peak Charge (pC)	Peak Energy (MeV)	Energy Spread (%)	Avg. Div. (mrad)
2bFPS	6.1	3.7	125	8.7	-4.3
Iteration 31	4.8	3.8	96.9	12.7	9.3

Table 4.5 – Comparison of electron bunch parameters for optimised settings in a manually optimised (2bFPS) settings and for the Bayesian Optimisation case (Iteration 31).

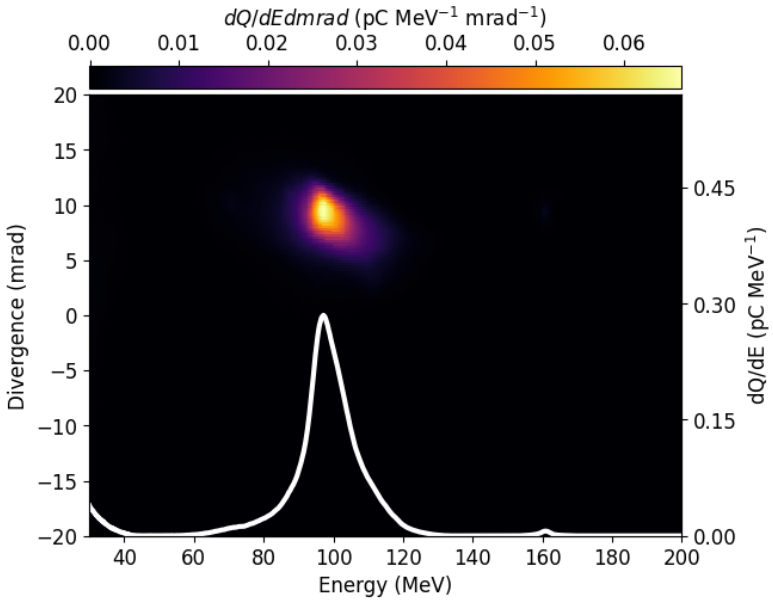

Figure 4.20 – Electron spectrum retrieved from optimisation of the spectral density projected into energy-divergence space with spatially integrated $\mathrm{dQ/dE}$.

and leading to a non-ideal phase space trajectory of the accelerated particles.

Figure 4.21 illustrates the stability of the bunch parameters: peak charge, median energy, the divergence of the bunch at peak $\mathrm{dQ/dE}$ and angular deviation from the laser axis in vacuum. The RMS deviation error percentage (in order of decreasing stability) is 5.6% for the median energy, 14.3% for divergence, 40.5% for the peak angular displacement, and 54.5% for the peak charge. Comparison of the relative fluctuations of these parameters indicates that whilst the energy and divergence of the electron bunches are stable, the amount of charge injected into the peak and the average displacement angle of this charge, strongly fluctuates during this stability measurement. Whilst not plotted here, the maximum energy of the electron bunches had an RMS deviation error percentage of 4.4%. From these values, we can see that the longitudinal position of the electron injection within the plasma, and the accelerating gradients, must be consistent between each shot to provide consistent electron energy at the end of the accelerating process. From the simulations of Fig. 4.11, we can see that the evolution of the laser pulse and the resulting transverse fields of the wake were the cause of the off-axis electrons. In this experiment, however, we use a flattened phase at focus, optimised with an adaptive optic loop, which should produce quasi-on-axis electrons as shown in Fig. 4.12 a).

Assuming that the plasma wave retains a similar structure on each shot, the phase of injection of electrons can be altered due to the spectral phase components. For ionisation injection, the local instantaneous electric field of the laser is responsible for freeing the inner electrons of the dopant ion. Fluctuations of the

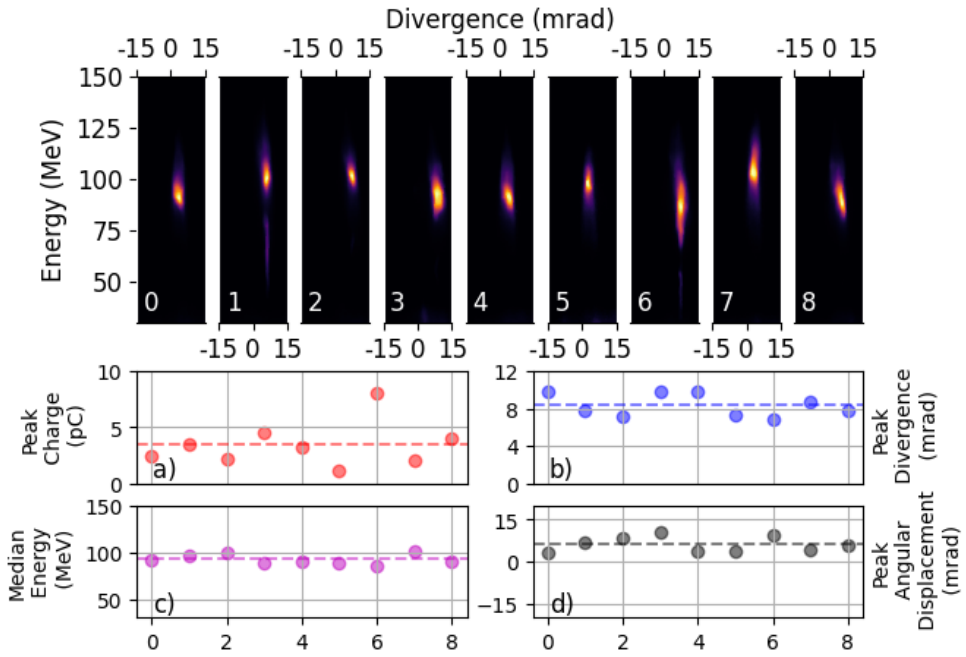

Figure 4.21 – Nine consecutive electron spectra measured using optimised BO settings. Spectra are cropped to an energy window of 30 to $150\,\mathrm{MeV}$ and a divergence window of $\pm 15\mathrm{mrad}$. Laser axis in vacuum is at zero divergence. Electron parameters calculated from the stability run with a) Charge within $2\times$FWHM of the peak, b) FWHM divergence of the peak, c) median energy of the electron bunch, and d) angular deviation of the electron bunch from the laser axis.

temporal envelope of the laser pulse through higher-order spectral phase dispersion could therefore lead to fluctuations in the phase of the electron ionisation and electron injection. We explore this effect in the following section.

4.2.3.2 . Effect of Spectral Dispersion on Electron Spectra

Fluctuations in the angular deviation and amount of injected charge, whilst using a laser pulse with a flat wavefront profile, suggests that the fluctuations in the electron spectra are due to the spectral phase dispersion terms. From the experimental parameters of Fig. 4.17 we can see that the focal position is in the centre of the exploration range whilst the spectral phase terms are strongly altered for the optimum case that was then examined as a stability measurement in Fig. 4.21. We therefore explore in more detail the effect of spectral phase terms on the electron acceleration process. Figure 4.22 b) illustrates that whilst the third order dispersion does not have a strong influence on the average value of the angular displacement of the electron bunch across all explored values, fluctuations increase at values of the TOD far from the zero position, which is especially true for negative values of TOD. From the experimental parameters of Fig. 4.17 it can be seen that, for the selection of high merit value spectra, displayed in the right column of Fig. 4.19,

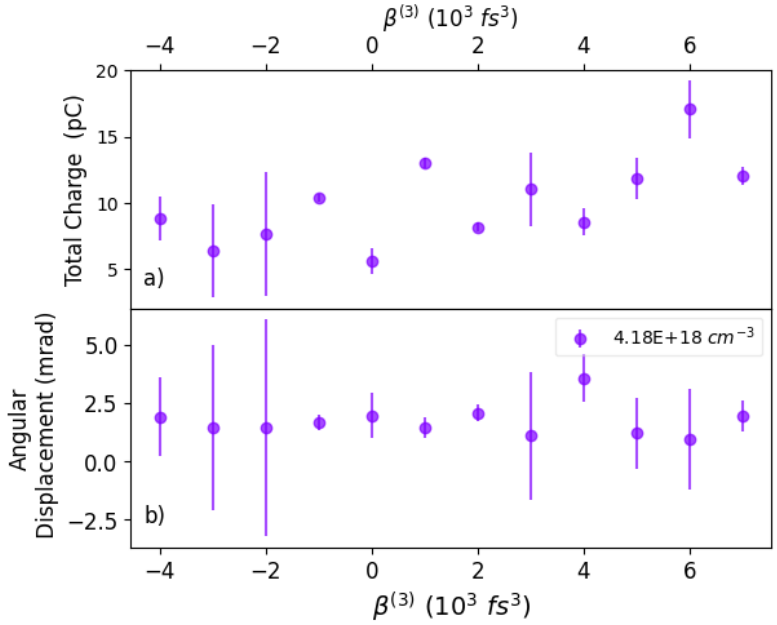

Figure 4.22 – Effect of third order spectral dispersion of the laser against the a) total accelerated charge and, b) angular displacement, both averaged over multiple shots. Error bars are given by standard deviation.

third order dispersion adds an oscillating modulation to the laser temporal envelope. However, the exact form must be solved numerically for each case. These oscillations of the laser temporal envelope alter the local electric field of the laser in the plasma and therefore the injection phase of the electrons. The frequency of these oscillations is likely sensitive to the nonlinear temporal pulse evolution due to pulse etching and modulation from the wavefront. It is therefore hypothesised that this is the main source of fluctuation in the angular deviation of the BO spectra in Fig. 4.21. However, further simulation work is required to fully understand the effects of the TOD on the injection process in the intermediate ionisation injection regime and will be included in future publications.

To investigate the effect of second order phase on electron bunch properties we performed scans of $\beta^{(2)}$ for different plasma densities. Laser focus was set at $100\,\mu\mathrm{m}$ before start of plasma density plateau, a typical position for the best quality electron spectra achieved during this experiment due to the enhanced laser-plasma coupling and increase in a_0 through self-focusing. $\beta^{(2)} = 0$ is defined as the position of the second order phase distortion term that produces an optimally compressed pulse at the output of the compressor as measured through frequency resolved optical gating (FROG).

The laser pulse duration is minimised for zero chirp pulses when the GDD is zero. Addition of non-zero chirp, positive or negative, leads to an extended pulse duration due to the relative phases of the spectra in the pulse imparted by the

frequency dependent delay. We use equation 2.7 for calculating the theoretical pulse duration from the linear chirp imparted by the GDD. Using a FROG measurement conducted at the beginning of the experiment for the laser spectra and duration at optimum compression gives an un-chirped pulse duration of $\tau_0 = 38\,\mathrm{fs}$ (FWHM). The FROG was used during the experiment in the post-plasma laser temporal measurements and so was not available for pulse duration measurements during the experimental campaign. Using this parameter we can define the pulse duration scaling and resulting pulse duration approximation for each GDD setting that is shown in Fig. 4.23. We then compare these theoretical values against the FWHM pulse duration measured by an autocorrelator in air with the low power seed on the laser diagnostics table after compression. Comparison to auto-correlator results are found to agree well with the theoretical pulse duration from equation 2.7. From

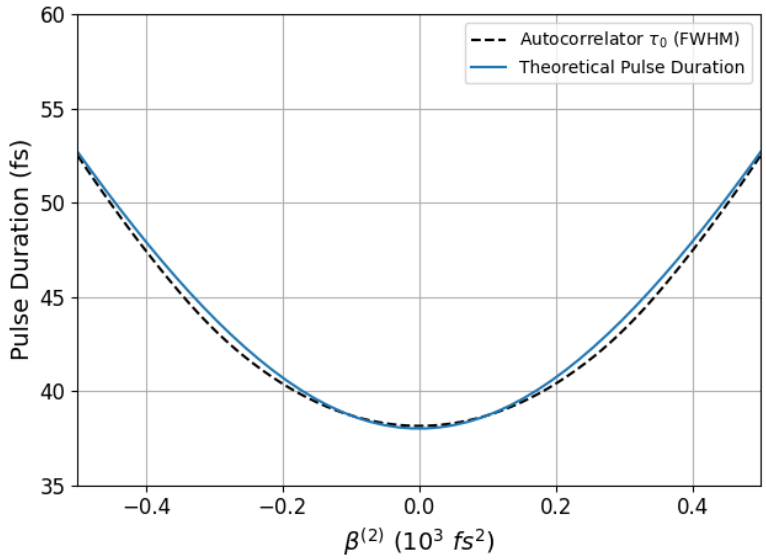

Figure 4.23 – Theoretical and experimentally retrieved pulse duration with GDD over range of GDD settings used during the experiment.

Fig. 4.23, the autocorrelated temporal duration and theoretical value agree well for small values of GDD around the optimum compression there is a deviation at $\beta^{(2)}$ values lower and higher than -0.15 and 0.15 respectively. This effect is explained by a crack in the doubling crystal used in the autocorrelator measurement where large values of $\beta^{(2)}$ induce a broader spectrum in time which is cropped by this damage, resulting in a decrease in the light signal and an apparently shorter pulse duration than expected. Nevertheless, the autocorrelator measurements at the maximum range measured provide a pulse duration within 7% of the theoretical value. The theoretical pulse duration was calculated from the optimum spectral phase terms of iteration 31 using the relations presented in [26] creating the laser pulse envelope shown in Fig. 4.24. In this optimised case, the pulse is stretched asymmetrically

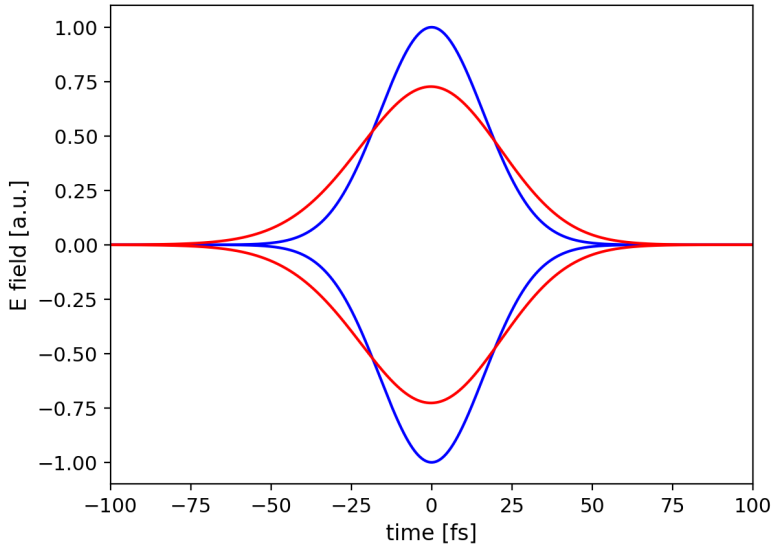

Figure 4.24 – Gaussian intensity temporal profile (blue) with a pulse duration of 38fs and the corresponding theoretical temporal envelope (red) after the inclusion of the GDD, TOD, and FOD spectral phase terms for the optimised electron spectra.

from the Gaussian intensity temporal profile of 38fs FWHM to a front HWHM of 25 and a back HWHM of 27fs. In this case, the peak intensity is correspondingly reduced by 28% due to the increased temporal duration.

Fig. 4.25 demonstrates the resulting charge on the LANEX within a $\pm 5\,\mathrm{mrad}$ window around the average divergence angle of the electron signal. Measurements are averaged over multiple experimental shots and errors are given as the RMS error of these values. As illustrated in Fig. 4.25, the total number of accelerated electrons depends on the value of $\beta^{(2)}$ and on the plasma density ; however, increased plasma density reduces the effect of the $\beta^{(2)}$ on the resulting charge value and extends the range of GDD values where a large number of electrons is measured. Comparison of measurements at 3.30×10^{18} and $4.18 \times 10^{18} cm^{-3}$ indicates that the increase of $\beta^{(2)}$ from 0.3 to $0.5 \times 10^3\,\mathrm{fs}^2$ results in a decrease of the total charge by a factor of 2.5 from 15.1 to $6.1\,\mathrm{pC}$ but only a factor of 1.03 from 27.1 to $26.3\,\mathrm{pC}$ at the higher density.

Due to the increased nonlinear effects at higher density, the effect of the spectral chirp on the plasma is likely radially compensated at higher plasma densities through photon deceleration and through relativistic self-phase modulation leading to a frequency-broadened pulse and therefore a shorter wavelength. This would reduce the magnitude of the chirp and return the pulse duration closer to the one of optimum compression.

A line of best fit is applied to the sample of each plasma density's maximum total charge value. This result indicates that increasing the plasma density shifts the optimum $\beta^{(2)}$ to lower values. As the $\beta^{(2)}$ defines the group delay dispersion

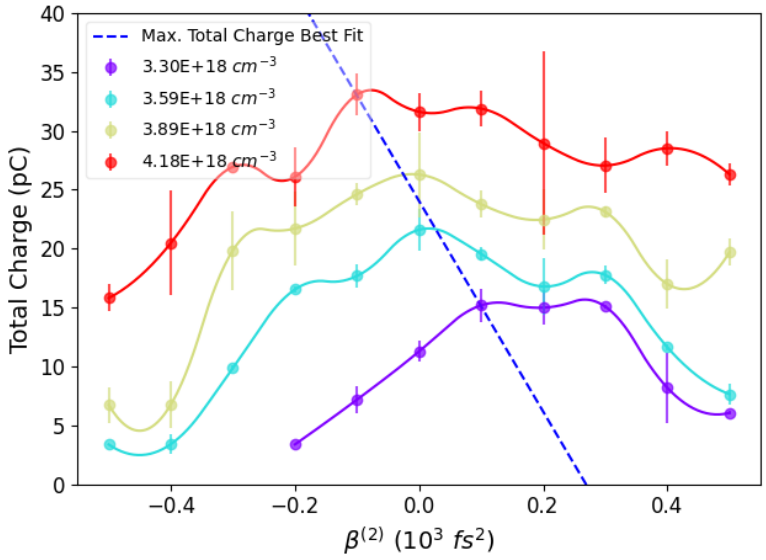

Figure 4.25 – Total charge measured on the lanex as a function of the GDD value controlled by the DAZZLER for different values ofplasma density. Linear regression fitted to the maximum total charge for each pressure and GDD setting scan is plotted with a dashed line.

(GDD) of the laser pulse, and equivalently the linear chirp[101], this indicates the optimum chirp passes from positive to negative for these experimental parameters with a transition around $3.75 \times 10^{18} cm^{-3}$. We must also take into account the sign of the chirp as it has been shown in previous work that the chirp plays a key role in the resulting electron parameters[177]. From a qualitative view this can be explained through the evolution of the laser pulse within the plasma. Just as the AO-PDF is used to offset the spectral dispersion of the amplification chain, the GDD can also be used to control the evolution of the spectral phase of the laser in the plasma through pre-compensating the pulse compression and evolution of different frequencies within the plasma.

These results indicate that the TOD can induce fluctuations in the angular deviation of the electron spectra at $\beta^{(3)}$ far from optimum however further simulation work is required to uncover the physical description of the effect of the temporal envelope and phase of the laser. These results also demonstrate that the GDD can provide a means of altering the electron parameters through the evolution of the laser pulse in the plasma and the resulting wakefield dynamics. Further, the effect of GDD on the plasma is shown to be density-dependent due to the nonlinear interaction between the laser and plasma which scales strongly with the plasma density. To optimise electron spectra it is therefore necessary that a multi-dimensional optimisation of the GDD and plasma density are included in the experimental parameters.

4.2.4 . Offline Bayesian Optimisation

Whilst the example presented in section 4.2.3.1 indicates that the BO process is capable of finding desirable electron spectra with parameters that are reproducible, time constraints during the experiment limited the number of BO scans that could be conducted. We therefore present here a general method that was used to validate its efficacy on optima finding on LWFA electrons and improve the BO procedure and its hyperparameters, by using the collected data set and all known experimental parameters to rerun the optimisation procedure on offline data post-experiment. This method could be used by any group wishing to implement BO in their experiments and provides a pre- and post-experiment tool for tuning the parameters and merit functions to produce desired electron spectra.

4.2.4.1 . Motivation

As the use of optimisers for LWFA is a new field of study with a limited literature, especially regarding the technical implementation of the optimisation parameters, we explored various parameters of the optimiser to produce more consistent results. A further issue experienced during the experiment was the optimiser searching at the boundary limits of the experimental parameters. Improvements in the scaling parameters chosen for the anisotropic parameter space (i.e different scale lengths associated with the focal position and plasma density effects) would likely resolve this issue and lead to more efficient search. The offline version of the code has allowed for autoscaling of the input parameter space which has removed this issue. This makes exploration of the different underlying choices of the Bayesian optimisation process, simpler using the offline optimiser. During the time scale of this work, only the presentation of the kernel optimisation will be shown. However, as the kernel effectively provides our assumptions on the input parameter space, it is imperative that an optimum choice is made for Bayesian optimisation processes for a specific input parameter space.

More concretely, we use a version of the optimiser implemented during the experimental campaign (referred to as online optimisation) and an offline version in which the optimiser is allowed to explore the parameter space, but it is discretised into the experimental parameter space that was searched during the experiment. This requires altering the Gaussian process to take into account that the input parameter space is no longer continuous. For example, if the optimiser requests a cell position of -0.2 mm and a backing pressure of 130 mbar but the closest data to this is -0.25 mm and 135 mbar then this shot is selected, the previously calibrated and calculated electron parameters are loaded, the merit function is calculated and the true (i.e loaded) experimental parameters are then given to the optimiser to correct for the shift between the requested parameter space and the available one. Using this method we can allow the optimiser to run over the data space that we have obtained for the experiment (approximately 4000 shots including optimiser and automated scans) allowing us to explore the effect of scaling parameters and

kernel choice on the ability of the optimiser to find global maxima for a given merit function. This also allowed the inclusion of the discrete variables of plasma plateau and exit face length to be included in the optimisation, as these were manually changed between data acquisition during the experiment.

The aim of this study is to demonstrate that with a sample set of data, future optimisation experiments can be improved by optimising scaling factors, kernel choice, the dimensionality of the search and choice of merit function using this offline method allowing for a simple method for experimental preparation and improving the next set of data taking/optima finding. A further advantage of this approach, and one that was used to test the optimiser functioning before this optimisation experiment, is that data which are acquired through classical experimental scans can be used as the input parameter space for the optimiser. This means that facilities that have access to large quantities of data can prepare better for initial optimisation studies simply using the data that are already available to them. Then, by tweaking the optimiser parameters based on the inherent scaling laws of the underlying physics, a more efficient implementation of the BO process can be used for the beginning of the experimental campaign.

4.2.4.2 . Effect of Kernel Choice on Optima Retrieval

A challenging aspect of applying optima finding to LWFA experiments is the existence of discontinuities in the merit function space due to electron injection thresholds existing in the underlying physics. As the kernel choice will affect the prior distribution used to model the black-box function, it is important to use the correct choice when performing Bayesian optimisation during an LWFA experiment. It has previously been shown that dynamically altering the choice of kernel for the Gaussian process can reduce the number of required iterations to optimise a function[178] however implementation of this algorithm is outside the scope of this thesis. Here we present the results of applying different static kernel choices to the same merit function and examining the average number of iterations required to reach a known optimum in the data set. The most common kernel choices when specifying the hyperparameters for an unknown optimisation problem are explored.

As the kernel is a description of our assumptions on the input parameter space, alterations of the kernel selection can provide more rapid optimisation by making accurate choices on the input parameter space distrobution. This will increase the efficacy of the successive measurements as the uncertainty will be more accurately calculated. Fig. 4.26 demonstrates the effect of altering the Gaussian process kernel during 2D optimisation of the focal spot position within the interaction region and the backing pressure of the injection system during offline optimisation. The merit function was defined as the total charge multiplied by the total electron energy. A known maximum merit function value of 15.675 is plotted as the horizontal dot-dashed line to compare the progress of the various kernels. 10 epochs of 200 iteration optimisations were performed for each kernel. The average maximum value for the 10 epochs for each kernel is illustrated with the solid black line. If this

line reaches the maximum known value it means that all epochs were successful in finding the optimum value.

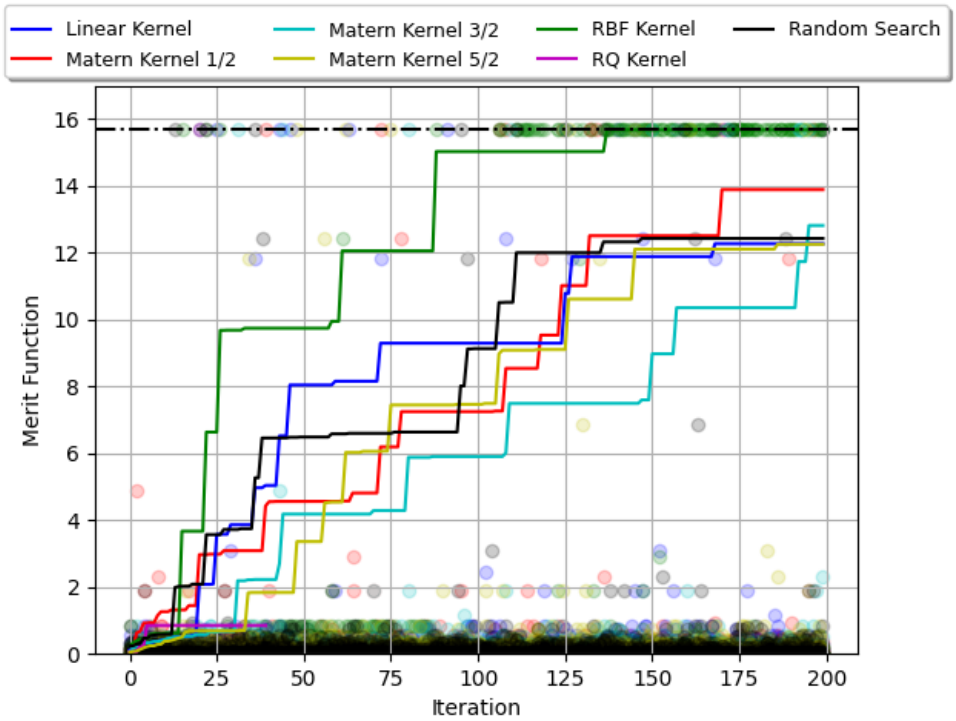

Figure 4.26 – Average maximum value found by each Gaussian processes kernel choice during 2D optimisation of the focal position within the gas cell and the backing gas density. The merit function in this case was the total charge multiplied by total beam energy. Maximum measured merit function of this experimental dataset was 15.675 shown by the black horizontal dot-dashed line. Individual merit function evaluations from requested input parameters are displayed as circles with their colour corresponding to the solid line for each kernel.

From fig. 4.26 we can see that that the radial basis function (RBF) kernel is successful, on average, at locating the optima after approximately 140 iterations and performs significantly better than the other kernels and random selection. In fig. 4.26 we see that only Matern $1/2$, $3/2$, and the RBF kernels performed better than the random search at the end of the 200 iterations. Comparison of the random selection to the other Bayesian optimisation results indicates that the statistical likelihood of selecting the optimum parameters through random selection in 2D is very close to the efficacy of the Bayesian optimisation. Whilst the use of random selection is comparable to some kernel selections in the small discrete sample set used in the offline optimiser study, random sampling does not provide a probabilistic prediction of unsampled regions meaning that the likelihood of selecting a local optimum is increased.

4.2.5 . Conclusions

The optimisation of the electron spectra through Bayesian Optimisation was shown to function well and improve the spectral characteristics in 10s of iterations.

Due to time and shot rate limitations, multiple measurements were not performed at each sampling. The results indicate, however, that even without multiple-shot sampling it was still possible to optimise the electron spectra and achieve an order of magnitude improvement on the beam parameters with comparison to random search through the BO process in an acceptable number of iterations.

Comparison of the best results from the previous campaign exploring laser-plasma coupling and electron parameters achieved through BO presented in table 4.5, indicate that the BO method, in this case, does produces worse quality electron spectra. In the BO case no optimisation of the wavefront of the laser was performed which was shown in the previous campaign to localise the charge injection resulting in a reduced energy spread. The lower peak energy also suggests a later injection position which could be caused by the injection process being delayed until the pulse was sufficiently shortened in the plasma to ionise the inner shell electrons of the nitrogen dopant.

In the BO method we also see that the optimum search doesn't settle to the optimum value. This is due to the continued exploration of the BO to avoid trapping in a local optima but results in a significant portion of the optimum searching producing undesirable electron spectra. This trade-off between exploration and exploitation can be dynamically set and future work, which aims to fully optimise the capabilities of a given laser-plasma system, should perform dynamic balancing of these two goals of BO.

4.3 . Discussion of 150MeV Injector Results

The analysis of the two experimental campaigns at the LLC have demonstrated improvements in our understanding of laser plasma coupling through density downramp, focal spot and laser wavefront control. Further, we have developed multiple tools for improving future experiments, including optimisation of BO hyperparameters, merit function choice and neural-network based focal spot retrieval. Comparisons between experimental and simulated results have been improved through the use of carefully measured realistic laser parameters allowing the underlying physical mechanisms for the changes in electron parameters such as charge and angular displacement to be uncovered. Development of a two-compartment gas cell is underway to reduce the injection volume theoretically resulting in lower energy spread. Bayesian optimisation was applied online during a laser-plasma injector development experiment. The automated experimental set-up allowed for an increase in data taking due to the absence of user intervention increasing the total shot count by 25% in comparison to the initial experiment at Lund during the same time frame.

Offline application of Bayesian optimisation was shown to provide information of the type of spectra that were chosen based on the selected merit function.

The optimisation of kernel choice, describing how the uncertainty on the measurements is calculated based on the input parameter space, was explored. From this initial analysis, we find that whilst the RBF kernel reduces the number of iterations required on average to locate the optima, the failure rate of the code, alongside the increased time step per iteration, limited the application. The effect of dimensionality of the input parameter space on the kernel choice was also explored indicating that as the dimensionality increases, the benefits of Bayesian optimisation over random search improve.

5 - High-Energy Laser-Plasma Injector: Apollon Experiments

Producing GeV-class electron bunches requires higher peak laser powers to sustain sufficient a_0 for wakefield creation over the longer distances required to achieve high energies. The advantage of producing an injector at these energies is that a single stage can provide ultra-relativistic electrons which can be accelerated in further stages, as envisioned in a multi-stage LWFA experiment, or be used as a seed beam for secondary radiation production such as in a free-electron laser[179] or positron creation through pair-production mechanism produced during the interaction of the high energy electrons with high atomic number nuclei[180]. The Apollon laser facility was used to investigate the development of a high-energy laser-plasma injector due to the long focal lengths for the laser focusing and the high peak power.

Two experimental campaigns at Apollon were conducted during this thesis. They will be presented here: the first commissioning experiment using a gas cell in 2021 and the first external user experiment in 2022 in collaboration with Queen's University Belfast.

The commissioning experiment aimed to characterise the facility's electron acceleration capabilities and stability. Strong instabilities in the laser system made a detailed analysis of the LWFA physics difficult. However, we present an overview of the experimental electron spectra and demonstrate that using a realistic laser profile retrieved through the method presented in 3.2.1, allowed us to make accurate predictions on the electron spectra even with these strong fluctuations. Results on the retrieval of the electron spectra at Apollon during the commissioning experiment are extracted from a publication currently under review in Physics of Plasmas: *Realistic driver modelling of laser wakefield electrons acceleration at APOLLON Research Facility*, I. Moulanier, L. T. Dickson, *et al.* which can be viewed in the Appendix.

The external user experiment in 2022 was completed to explore the production of a GeV-class electron source with high charge and low energy spread, which could then be used for positron production by targeting a high-Z material with this electron beam and measuring the positrons produced from the resulting radiation cascade. Whilst the positron production was successful, it is outwith the scope

of this thesis which focuses on electron parameters. Large improvements in the stability of the focal spot parameters during the second experiment allowed us to explore the physics with large F-number focusing optics in LWFA experiments and produce electron spectra with high energy, low energy spread and intermediate charge.

A significant difference between the two experimental layouts was the focal length of the spherical mirror: $f = 3\,\mathrm{m}$ in 2021 and $f = 9\,\mathrm{m}$ in 2022. We therefore refer to the 2021 commissioning experiment as the f3 and 2022 as the f9 experiment throughout.

For reader reference, an overview of the Apollon laser facility is given in section 2.1.3, the electron spectrometer charge calibration method for the f3 experiment is presented in section 2.3.1.3 and 2.3.1.4 for f9.

Laser characterisation in terms of RASP, radial projection and focal spot fluctuations (see chapter 2) are presented. Finally, the achieved electron parameters of the two experiments, and their stability, are presented, with their correlations to the improvements in the laser system stability and on-shot measured energy demonstrated. The capabilities of the facility and the progress towards the development of a high energy, GeV-class electron injector will then be summarised.

5.1 . Commissioning Experiment: Apollon 2021

A commissioning experiment was conducted in the long focal area at Apollon in 2021 to explore the LWFA capabilities of the facility and develop a high-energy electron injector. Several diagnostics of the laser, plasma and electrons were implemented to characterise laser-plasma interaction and to understand the origin of the electron fluctuations that were seen during this experiment.

As this was a commissioning experiment, the Apollon facility was used before it was open to external users, and therefore the laser system was not in its final state. This experiment, and the analysis of the laser and electron parameters, were used to benchmark the initial capabilities of the Apollon laser system and to aid in the development of the facility for users.

5.1.1 . Experimental characteristics

5.1.1.1 . Experiment Layout

The commissioning experiment was performed in the long focal area of Apollon using the F2 laser in the experimental vacuum chamber shown in section 2.1.3. The set-up of the experiment is shown in Fig. 5.1: the collimated F2 beam enters through the beam transport line from the compressor from the back. The beam is reflected to the left from the holed-turning mirror a), before propagating through vacuum piping to the spherical mirror. The main beam is then focused by the $f = 3\,\mathrm{m}$ spherical mirror, set at a distance of $3\,\mathrm{m}$ from ICC, and returns down the vacuum piping before passing through the hole in the turning mirror and into the main interaction area. The main pulse ionised the gas within the cell b), which was placed at focus and drives plasma waves within the plasma.

The electrons which were trapped through the ionisation injection mechanism are then accelerated (shown in green) and leave the ELISA cell with the depleted laser pulse. The electrons are dispersed in terms of energy using a permanent dipole magnet c), designed and implemented by LLR. A thin $4\,\mathrm{mm}$ aluminium window is placed on the vacuum flange with a LANEX scintillating sheet d), placed directly at the exterior of the experimental chamber. The CCD to image this radiation is placed above the experimental chamber after an optical transport line, which minimises the laser-plasma interaction radiation signature on the camera. The laser pulse exits through a flange into a final vacuum chamber, where a multi-plate glass beam dump attenuates the laser energy.

As described in section 2.1.3, a $32\,\mathrm{mm}$ probe beam was created by using a small portion of the F2 beam that passed through the hole in the turning mirror. The probe beam then entered a temporal delay line, allowing for the relative delay between the main pulse and probe beam to be controlled within $\pm 1\,\mathrm{ns}$. The probe beam was set to within $10\,\mathrm{ps}$ of the main pulse using a photodiode connected to a rapid oscilloscope to measure the delay between the two beams, controlled by a motorized vacuum stage. The delay was then finely tuned using the vacuum delay

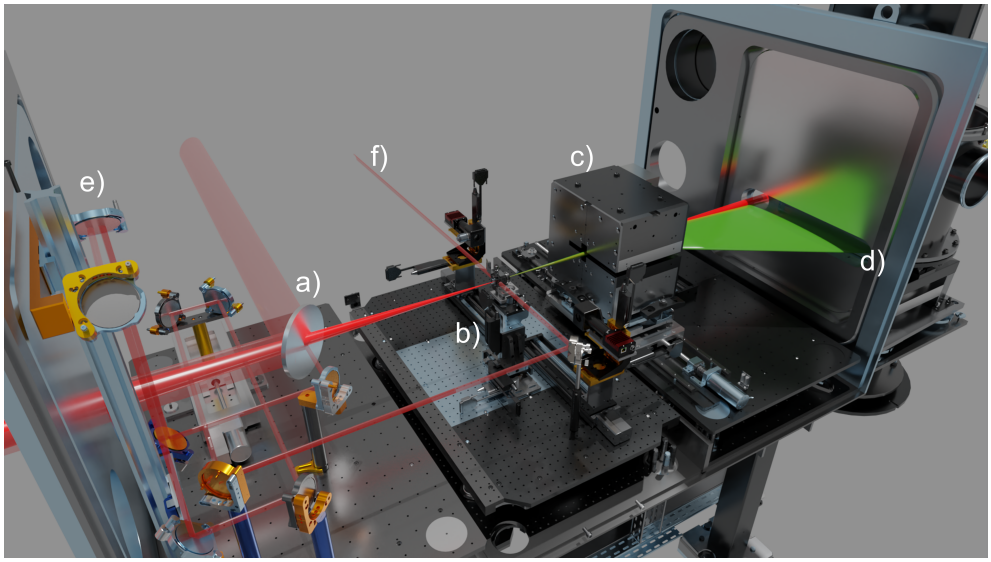

Figure 5.1 – Experimental setup of the 2021 commissioning experiment at Apollon demonstrating LWFA of electrons using a $f = 3\,\mathrm{m}$ focusing optic. The collimated F2 beam enters from the back after the transport line and is turned with a holed mirror, a). The beam then propagates to the left where it is focused on-axis by an $f = 3\,\mathrm{m}$ spherical mirror. The beam passes through the hole in the mirror and interacts with the gas cell at b). The electrons are trapped and accelerated and leave the gas cell with the laser. The electrons are then dispersed at c) in terms of energy in the horizontal axis with a permanent dipole magnet. The dispersed electron spectra then interact with a LANEX screen at d), and the interaction radiation imaged by a CCD above the experimental chamber. A small portion of the centre of the F2 beam, which passes through the holed mirror on the first turn, is sent to a delay line e), where it is temporally synchronised with the main pulse at the gas cell. The probe beam then propagates transversely to the main beam axis as used to probe the plasma density at f) outside the experimental chamber.

stage and imaging on the plasma diagnostic line. This relative delay of the probe line was then used throughout the experiment.

The probe beam propagated transversely to the main laser axis at focus. It arrived just after the plasma formation, set through alteration of the delay stage after approximate synchronisation, allowing for the plasma density to be measured on each shot using a wavefront sensor, set as described in section 2.2.3.4 in air on an adjacent optical table.

A focal spot camera was placed under vacuum on an XYZ stage, as can be seen in burgundy on the left-hand side of Fig. 5.2. This allowed for the alignment of the gas cell and for measurement of the laser focal volume in vacuum. These images through the focal volume were used alongside the modified GSA algorithm described in section 3.2.1, allowing for an intensity-phase map to be created and projected onto cylindrical Laguerre-Gauss modes for simulations using realistic laser parameters assuming a negligible spatiotemporal correlation of the laser pulse.

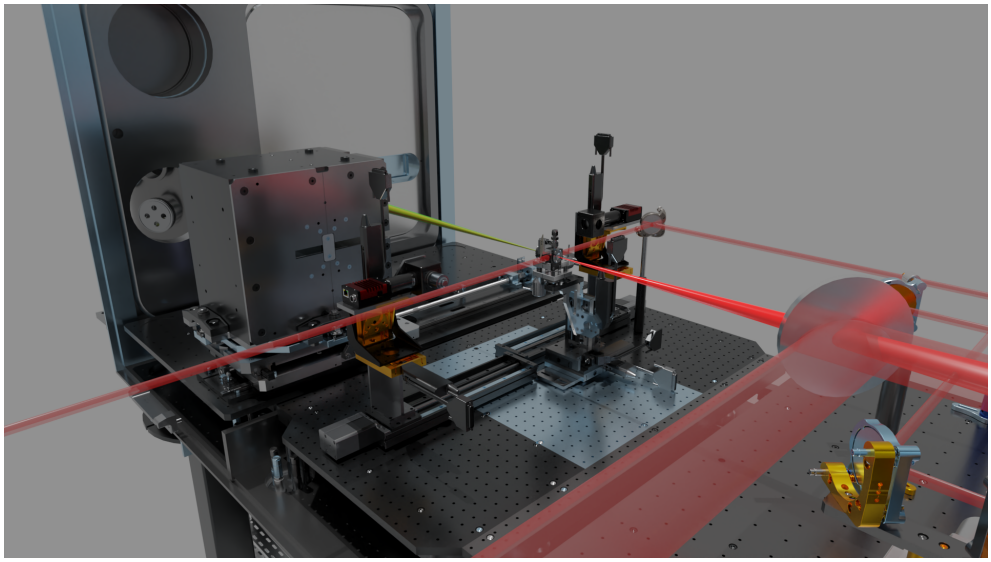

Figure 5.2 – Experimental setup of the 2021 commissioning experiment at Apollon showing the alignment cameras and the dipole magnet off-axis.

These measurements of the focal spot, which were conducted each day, further allow for a measurement of the laser stability during the experiment. A second axis-camera is shown on the right in Fig. 5.2. This CCD allowed for the tip-tilt alignment of the gas cell to be conducted under vacuum to optimise the gas cell axis to that of the incoming laser. This imaging system also allowed for tracking of cell face ablation during the experiment to minimise the amount of downtime.

The LFA uses an orange alignment beam to reference the acceleration axis for the entire experimental room. This provided the initial axis of alignment in which the plasma target, alignment system, magnet and laser beam dump were set to. After the initial alignment of this beam, the focal spot camera was used as it provided a more accurate reference of the day-to-day focal spot fluctuations and alignment of the 10Hz and attenuated full-power F2 laser.

A calorimeter was placed on a vacuum-compatible stage behind the magnet at the edge of the experimental chamber for measurement of the pulse energy in the target area of the full laser. These periodic calorimetry measurements were used to calibrate the energy on target for each shot allowing for fluctuations in the energy to be taken into account in electron bunch fluctuations.

5.1.1.2 . Plasma Diagnostics

Probing the plasma density transverse to the acceleration axis allows for measurements of the longitudinally dependent electron plasma density, which strongly affects the laser evolution and resulting injection and acceleration dynamics. Plasma density measurements were performed using the wavefront sensor (WFS) self-referenced technique introduced in section 2.2.3.4, where the relative curvature

of the laser wavefront is measured as a carrier of the phase information imparted by the plasma column. The WFS imaging system provided a resolution of $7.5\,\mu\mathrm{m}$/pixel to image a 0.9 by $1.2\,\mathrm{mm}$ region of the plasma column where the magnification of 1 was chosen to have ample resolution on the wavefront curvature.

As this is a small region of the total plasma length, imaging of the full plasma column was completed using a secondary shadowgraphy measurement, to measure the full length of the plasma column inside the gas cell, much longer than the Rayleigh length as the laser pulse undergoes self-focusing during propagation in the plasma as described in section 1.3.3. Shadowgraphy images are shown in Fig. 5.3 for a) strongly diffracted and b) regularly self-focussed laser pulse. The plasma density in these images was $2.3\times10^{18}\mathrm{cm}^{-3}$ and $1.5\times10^{18}\mathrm{cm}^{-3}$ for a) and b) respectively, with a focal position located in the plasma up-ramp and all other experimental parameters equivalent. This illustrates, visually, the coupling between the laser and the plasma parameters and how they affect the laser guiding. The change of refraction index due to the presence of plasma refracts the probe beam and provides qualitative information on the shape of the plasma along the direction of propagation of the driving beam and in the vertical perpendicular direction. As the plasma is created for laser intensities above the ionization threshold (10^{14} Wcm^{-2} for hydrogen), these images also reflect the higher laser pulse intensity distribution.

In Fig. 5.3 a), the plasma density is higher leading to stronger nonlinear self-focusing of the laser which diffracts the pulse over a shorter propagation distance. As the effect of diffraction and self-focusing are not well balanced in this case, the smaller focal spot increases the rate of diffraction leading to an expansion of the laser pulse resulting in the wide, conical, plasma structure that can be seen towards the right-hand side of a) after the initial strong focusing. In the case of b), diffraction and self-focusing are well-matched leading to the laser pulse propagating through the plasma with an approximately constant radius and creating a smooth plasma column.

5.1.1.3 . Gas Cell Characteristics

The ELISA gas cell, described in section 2.2.1, was used during the commissioning experiment. This was the first experiment to use a gas cell at the Apollon facility. The cell was used in the fixed length configuration where the cell length is controlled using stainless steel spacers to separate the entrance and exit faces in increments of $0.5\,\mathrm{mm}$. Cell lengths were typically in the 10s of mm with 400$\mu\mathrm{m}$/800$\mu\mathrm{m}$ diameter entrance and exit faces respectively where both were 500$\mu\mathrm{m}$ thick.

Figure 5.4 displays the entrance face a) and exit inner face b) for the gas cell after 108 shots during a day of the experiment with the cell length set to $20\mathrm{mm}$. Hole diameters were seen to increase by approximately 40-60% indicating that the laser was unstable during this campaign. The instability came from turbulent air during laser pulse propagation, a non-optimal deformable mirror (in both focal spot optimisation and piston operation), and issues with the pump lasers for the

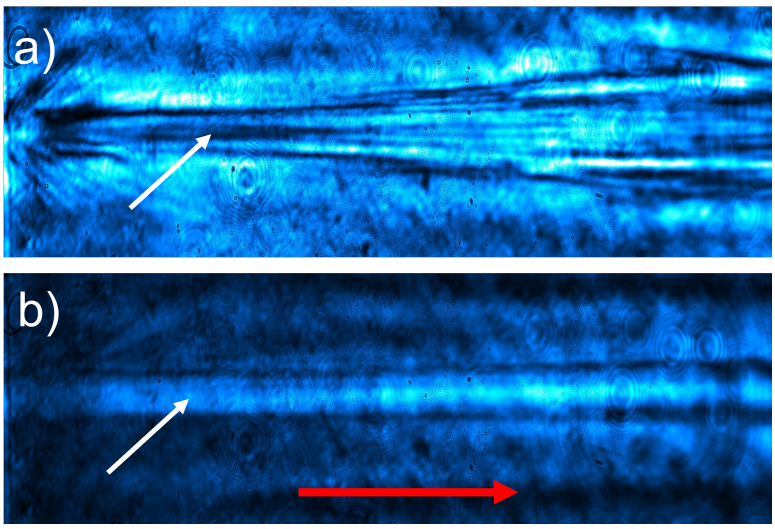

Figure 5.3 – Transverse shadowgraphy images of the formed plasma within the ELISA gas cell for a) strongly diffracted laser, b) smooth plasma column from well-balanced self-focusing laser propagation. The red arrow indicates the direction of laser propagation and the white arrows point to the plasma columns for clarity.

amplifiers.

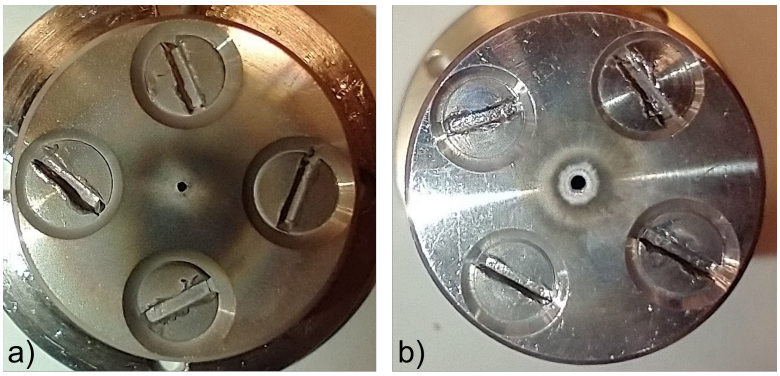

Figure 5.4 – Gas cell a) entrance and b) exit face minimal ablation after 108 shots with a $20\,\mathrm{mm}$ plasma plateau length. Diameters of the cell hole for a) were 400 and 560µm and b) 800 and $1310\,\mu\mathrm{m}$ for before and after laser shots respectively.

The average plasma density used during this experiment was $1.8 \times 10^{18}\mathrm{cm}^{-3}$ with a minimum and maximum plasma density of $9.0 \times 10^{17}\mathrm{cm}^{-3}$ and $5.0 \times 10^{18}\mathrm{cm}^{-3}$ respectively.

The plasma plateau lengths were calibrated offline using electronic micrometre callipers alongside transverse shadowgraphy images of the gas cell during the experiment. The gas cell was mounted on an XYZ translation stage, with two separate vacuum-compatible motors responsible for tip-tilt corrections to the gas cell.

The gas injection system was used as described in section 2.2.1 with 99% hydrogen 1% nitrogen. Pure hydrogen was also used as a null test, to verify that the main injection process was ionisation injection in the case of gas mixture. Reduction in reservoir pressure could be achieved through a butterfly valve attached to the main vacuum backing system allowing for careful control of the gas pressure. A secondary MKS absolute gauge was mounted onto the reservoir for monitoring the gas density separately from the downstream Bronkhorst regulator. All gas systems were controlled remotely from the control room.

5.1.1.4 . Electron Diagnostics

The permanent dipole with a mean field of $1.70\mathrm{T}$ was implemented by LLR during the experiment with a LANEX screen placed outside the chamber. The magnet was motorised allowing the electron bunch to freely propagate to measure the bunch pointing, and also to perform calorimetry measurements of the full unapertured laser beam. This also allowed for full laser axis alignment by shifting the magnet centre to the acceleration axis as aligned by the orange alignment beam. Tracking simulations using the realistic magnetic field map of the magnet was used for calibration between energy and position on the LANEX.

An optical transport consisting of a periscope formed by two rectangular mirrors and a Nikon F/1.8 camera objective attached to an ANDOR iDUS420 BU was then used to image the electron-LANEX interaction radiation. The method described in section 2.3.1.3 was used with a geometrically calculated collection angle of 5.5×10^{-4}sr limited by the transport mirrors, a transmission factor which took into account all optical components, and the theoretical emission of the LANEX "regular" at 6.96×10^{9}ph/pC/sr[135] to provide a count to charge calibration of $0.042\mathrm{fC}$ per camera count. Calculated charges for the spectra were compared to simulated results using the realistic profiles of the Apollon laser leading to an agreement between the results indicating the count-to-charge calibration provides a realistic description of the electron-LANEX interaction and the following collection of the emission radiation. Spatial calibration of the LANEX was performed using known distance points on the LANEX and verified against the imaging set-up providing a means of measuring the divergence on the electron spectra from the LANEX using the geometric distances between the magnet and the energy-dependent path length of the electron spectra.

5.1.2 . Apollon 2021: Results

5.1.2.1 . Laser Parameters

In Fig. 5.5 measurements of the laser fluence are shown in the transverse plane around the focal spot at a) (-1.8mm), c) ($0\mathrm{mm}$), and e) (+1.2mm) to illustrate the typical laser profile when the laser is functioning in a stable state. These fluence images are then processed using the method presented in section 3.2.1 to retrieve the complex amplitude of the electric field of the laser in terms of Hermite-Gauss

modes which are displayed in the second row of Fig. 5.5. Each column in Fig. 5.5 corresponds to the same longitudinal position.

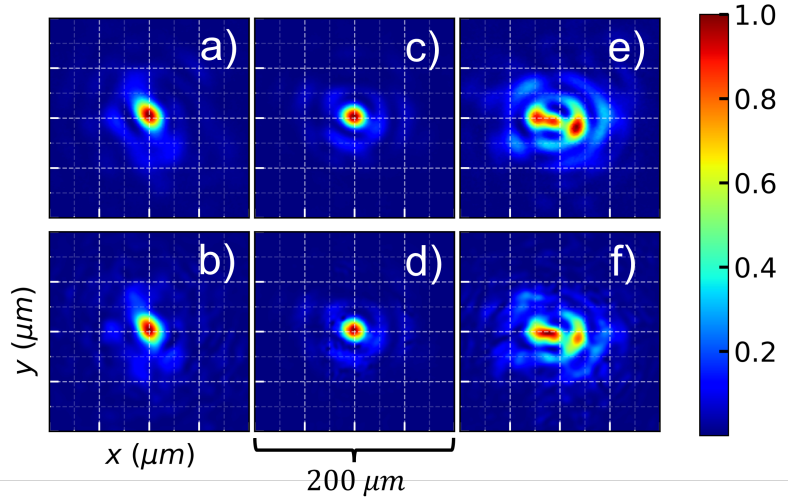

Figure 5.5 – Normalised transverse fluence image of the Apollon focal volume for the most stable case for CCD measurements in the first row and fitted Hermite-Gauss modes in the second row. Images corresponding to relative distances around the focus position as a)/b) -1.8mm, c)/d) 0mm and e)/f) +1.2mm. From Moulanier *et al.*.

Using the extracted Gaussian waist from the fluence images of $w_0 = 16.6 \pm 0.3\mu\mathrm{m}$, the pulse duration measurement from the WIZZLER[181] of $25\,\mathrm{fs}$ FWHM, and the fully amplified vacuum pulse energy calorimetry measurement of $11.7\,\mathrm{J}$ we find a peak intensity of $(2 \pm 0.2) \times 10^{19}\mathrm{W\,cm^{-2}}$ and a Rayleigh length of $1.6\,\mathrm{mm}$.

Whilst the nominal energy of the F2 beam is $15\,\mathrm{J}$, measurements of the laser energy during the experimental campaign indicated that the majority of shots were taken at approximately $5\,\mathrm{J}$ and pulse duration around $25\,\mathrm{fs}$ FWHM, as measured by a WIZZLER, significantly reducing the peak laser power from the PW-level to the $200\mathrm{TW}$-level.

The energy on each shot during the experiment is shown in Fig. 5.6 as measured via calorimetry at the exit of the compressor. The experiment was conducted at a nominal energy of 5 and 10J due to issues with a pump laser in the amplification chain. It was only possible to have a maximum energy of 10J, which is already 50% below the nominal operational energy, on 42% of the 1011 shots. The mean values for the laser energy in the two operational cases are plotted as a function of the shot index in Fig. 5.6 were the mean value is $10.8 \pm 0.91\mathrm{J}$, for the green sample set, and $5.2 \pm 0.65\mathrm{J}$ for the blue. The energy stability from shot-to-shot was found to be 8.6%.

5.1.2.2 . Electron Properties

Electron spectra were analysed using the calibration methods presented in section 5.1.1.4.

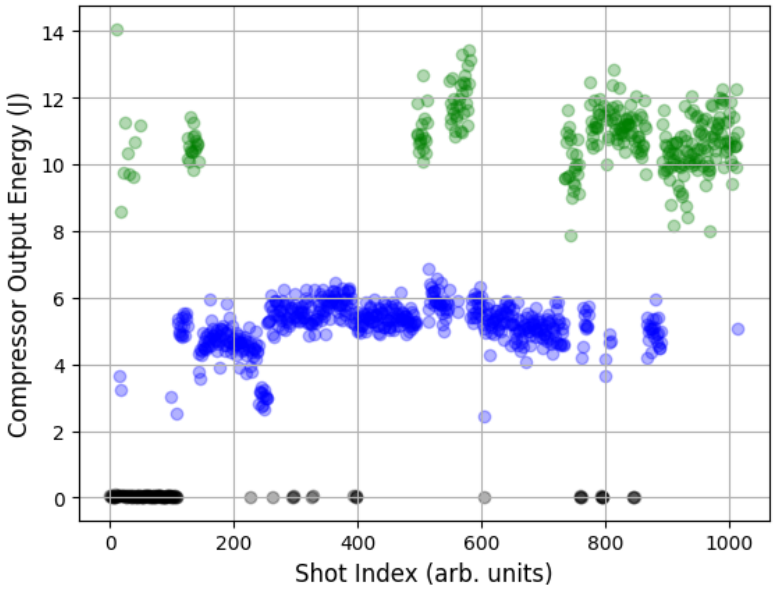

Figure 5.6 – Laser energy was measured by calorimetry at the output of the compressor for the F2 beam at Apollon during the f3 experimental campaign over 1011 laser shots. Energy values are colour coded with black < 1J, blue > 1J and < 6J, green > 6J.

In Fig. 5.7 and 5.8 selected electron spectra achieved during the campaign are presented. Strong fluctuations in the laser, which will be discussed in section 5.3, made exploration on the effect of experimental parameters in high-energy LWFA difficult. Here we present the best case spectra for peak energy, energy spread, maximum electron energy, and total charge to demonstrate that, electron beams with desirable qualities can be achieved with this facility, providing an incentive to improve the properties of the laser beam.

For all presented spectra the gas dopant composition was 99% hydrogen 1% nitrogen. Figure 5.7 a) shows the electron spectra with the highest peak energy at $754\,\mathrm{MeV}$ with an energy spread of 22% and a total charge of $48\,\mathrm{pC}$. This was achieved by focusing the laser $150\,\mu\mathrm{m}$ inside the density plateau with a plateau plasma density of $n_0 = 1.5\times10^{18}$ cm^{-3} and a plateau length of $13\,\mathrm{mm}$. Decreasing the plasma length to $10\,\mathrm{mm}$ in this case with a similar plasma density, $n_0 = 1.4\times10^{18}$ cm^{-3}, the sepctrum of Fig. 5.7 a) evolved towards the spectrum shown in Fig. 5.7 b), which exhibits the lowest energy spread of 13% at a peak electron energy of $547\,\mathrm{MeV}$. The total charge is also higher at $124\,\mathrm{pC}$, which was produced by focusing the laser at the start of the density plateau. This indicates that whilst the cell length is likely shorter than the depletion and dephasing lengths in the case of b) since the energy is lower, the large energy spread in a) could be due to several mechanisms that would need more systematic measurements to identify, such as laser driver fluctuations, beam loading effects, etc. Figure 5.8 a) shows the

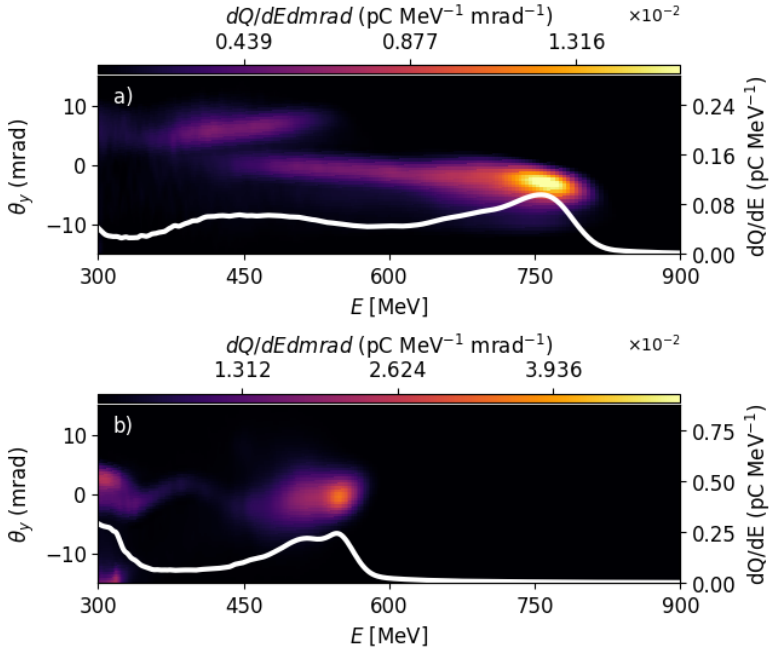

Figure 5.7 – Electron spectra in divergence-energy space representative of the spectrum variability in the f3 campaign, corresponding to the cases with a) highest energy peak, and b) lowest energy spread. All spectra are displayed in an energy window of 300 to $900\,\mathrm{MeV}$ and an angular window of $\pm 15\,\mathrm{mrad}$. The white line indicates the angularly integrated $\mathrm{dQ/dE}$.

electron spectrum with the largest maximum electron energy at $895\,\mathrm{MeV}$ where the spectrum reaches the end of the detection range of the LANEX screen. The total charge, in this case, was lower at $57\,\mathrm{pC}$. The plasma configuration is comparable with Fig. 5.7 a) where a plasma plateau length of $13\,\mathrm{mm}$ and a plasma density of $n_0 = 1.8 \times 10^{18}$ cm^{-3} were used, with the laser-focused at the beginning of the plasma density plateau. The total charges are close between Fig. 5.8 a) and 5.7 a) indicating that injection and acceleration processes of electrons reaching energies above 300MeV are similar, leading to widely spread energy spectra. In this case the maximum electron energy is increased slightly from 825 to $895\,\mathrm{MeV}$ with a $150\,\mu\mathrm{m}$ earlier focus. If we assume that this extra energy gain came from the earlier focus position, this would only be possible through a local accelerating gradient of $470\mathrm{GeV\,m^{-1}}$. However, for a plasma density of, $1.8{\times}10^{18}\mathrm{cm^{-3}}$, the theoretical nonlinear longitudinal electric field is $130\mathrm{GeV\,m^{-1}}$[58] suggesting that this increase in electron energy could come from a larger partition of laser pulse energy within the central region of the laser pulse which drives the plasma wave, or perhaps a more symmetric laser pulse to increase the proportion of laser energy which drives the longitudinal electric fields. Finally, in Fig. 5.8 b), the plasma density was significantly increased to $n_0 = 8.9 \times 10^{18}$ cm^{-3} resulting in the highest charge spectra, with a total charge of $750\,\mathrm{pC}$ was measured with peak energy at $546\,\mathrm{MeV}$.

This drastic increase in charge, by a factor of almost 10 in comparison to the other shots, demonstrates that the experimental set-up is capable of producing nC-class charges.

The production of the presented electron spectra comes with the caveat, however, that the laser energy was sufficiently high. In the presented cases the on-target laser energy was 9.7, 9.8, 9.7, and 8.9J for Fig. 5.7 a), b) and Fig. 5.8 a), b), respectively. As shown above in Fig. 5.6 this was the case for less than half of the experimental measurements.

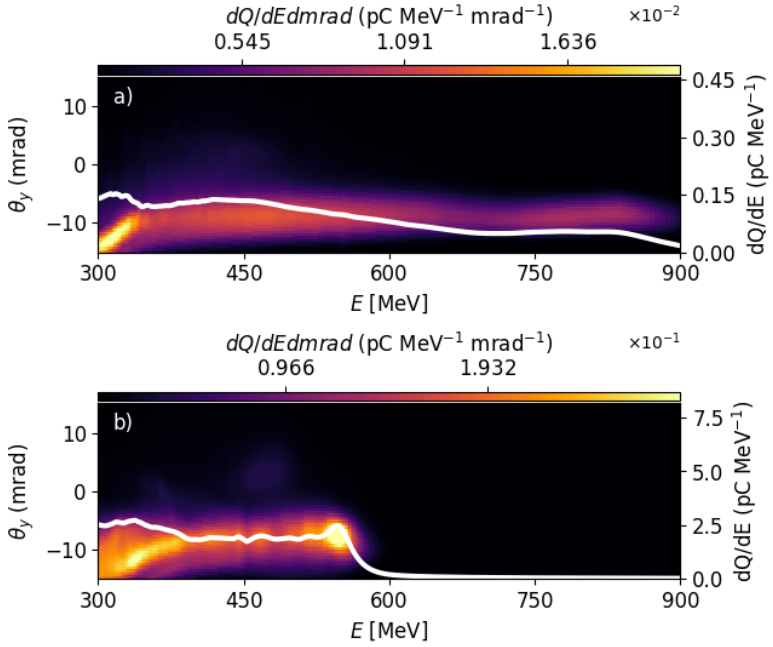

Figure 5.8 – Electron spectra in divergence-energy space from the f3 campaign corresponding to the a) maximum electron energy, and b) highest total charge. All spectra are displayed in an energy window of 300 to $900\,\mathrm{MeV}$ and an angular window of $\pm 15\,\mathrm{mrad}$. The white line indicates the spatially integrated $\mathrm{dQ/dE}$.

5.1.2.3 . Analysis of the Most Stable Electron Data Set

Laser parameters were monitored during the campaign. Here, we analyse in more detail, the most stable data set where the stability of the laser lead to electron spectra with consistent properties over several shots.

Figure 5.9 illustrates the characterisation of the laser driver in vacuum around the focal plane for two different days to illustrate the day-to-day differences in laser position and energy stability. Set 1, the most stable case, is compared to a typical data set obtained during the experimental campaign in Set 2. Set 1 in this case corresponds to images taken in the same sample set as 5.5. The four images taken at focus for both sample sets provide the reference centroid to which the other positions are compared. Comparison of Fig. 5.9 c) and d) indicates the

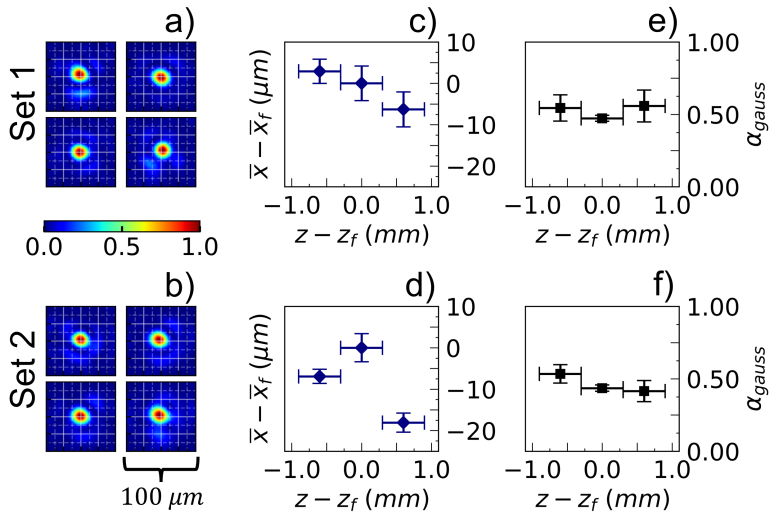

Figure 5.9 – Two sets of vacuum laser focal volume fluence measurements for stability comparison between stable, Set 1, and unstable, Set 2, sample sets. a) and b) show images of four consecutive images of the laser at focus corresponding focal data set 1 and 2 respectively. c) and d) illustrate the relative transverse shifts of the laser centroid around the laser focal position at three longitudinal positions. The zero position is defined as the centroid of the laser at focus. e) and f) illustrate the energy fraction, α_{gauss}, contained within a Gaussian fit of the focal spot which is propagated using Eq. 1.12 for each longitudinal position using the average beam waist from the $Z - Z_f = 0$ position.

instabilities in the pointing of the laser. In c) the laser centroid position decreases linearly over the focal volume from a maximum displacement of $3\,\mu\mathrm{m}$ to a minimum displacement of $-6\,\mu\mathrm{m}$. Images measured with the same imaging system on sample set 2, show that the pointing is shifted in the negative direction to both sides of the focal position indicating that strong pointing fluctuations in this case where the magnitude of the shifts also increases to $-7\,\mu\mathrm{m}$ and $-18\,\mu\mathrm{m}$ for the pre and post focus positions respectively. Figure 5.9 e) and f) illustrate the energy partition of the laser through the focal volume, defined as the energy contained within a 2D-Gaussian function with a waist defined at laser focus, and propagated using the definition of the Gaussian beam waist as a function of the longitudinal position defined in Eq. 1.12. The focal positions energy partition in set 1, e), and 2 f), are 46% and 40% respectively indicating that the 2D-Gaussian function does not well describe the laser transverse energy distribution. The errors can be seen to be significantly smaller at focus, however, indicating that the energy contained within the central lobe of the laser fluctuates less at focus than at the pre- and post-focal positions. This can be understood from the increased asymmetry of the laser profile before and after focus, as shown in Fig. 5.5, where the increased asymmetry will reduce the validity of the Gaussian description further, leading to increased errors from alterations in the transverse energy distribution.

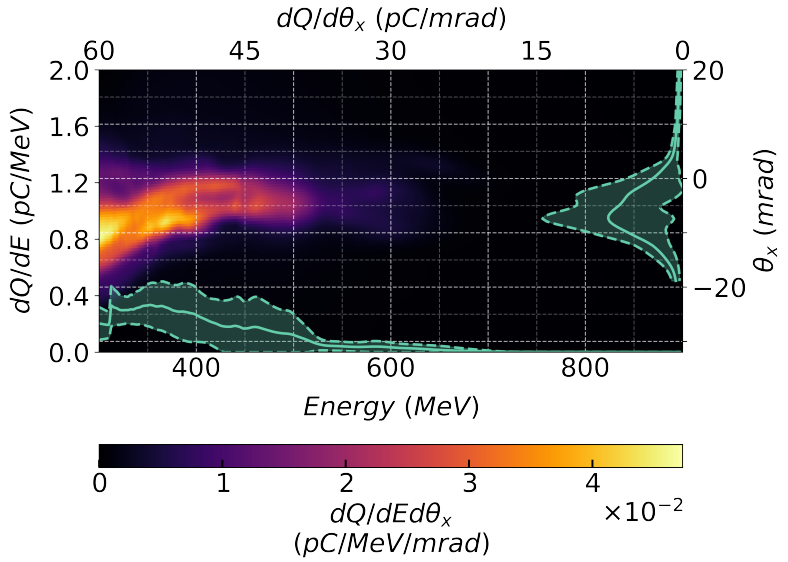

Figure 5.10 – Average electron spectrum of 10 consecutive shots taken using the laser profile shown in Fig. 5.9 Set 1 cropped to an energy window of 300 to $900\mathrm{MeV}$ and an angular window of -30 to $20\,\mathrm{mrad}$. Plasma density measurements using the wavefront sensor method retrieve an average density of $\overline{n}_0 = 2.2 \times 10^{18}$ cm^{-3}. Average spectral charge density $\mathrm{dQ/dE}$, and $\mathrm{dQ}/d\theta_x$ profile, and their corresponding $\pm$standard deviation over the ten measurements (shaded area), are shown by the horizontal and vertical green lines, respectively. Spectral charge density is calculated within $\pm 3\,\mathrm{mrad}$ around θ_x of the peak for each spectrum before averaging. $\theta_x = 0$ corresponds to the laser axis.

The laser profile in set 1, whose pre- and post-focus transverse energy distributions can be seen in Fig. 5.5, was focused into the ELISA gas cell at the beginning of the plasma density plateau with a plateau length of $6\,\mathrm{mm}$ and a gas composition of 99% hydrogen 1% nitrogen. Average plasma density over the 10 shots was found to be $\overline{n}_0 = 2.2 \pm 0.2 \times 10^{18}$ cm^{-3} as measured by the self-referenced wavefront sensor. The laser in this case had an average energy of $4.2 \pm 0.2\mathrm{J}$. The average of ten electron spectrometer measurements taken in this configuration are shown in Fig. 5.10.

The average total charge measured in the energy and the angularly cropped window was found to be $\overline{Q}_{tot} = 95 \pm 46$ pC leading to a 47% fluctuation in the charge. The average $\mathrm{dQ/dE}$ of the electron spectra, shown on the x-axis of Fig. 5.10, shows that the distribution of injected charge was stable for the central region of the electron spectra used for the $\mathrm{dQ/dE}$ calculation and that maximum electron energies up to $550\,\mathrm{MeV}$ were obtainable with $4.2 \pm 0.2\mathrm{J}$ of laser energy. Simulations performed with measured fluence distributions show that the spectrum shape, and detailed electron parameters close to experimental measurements can be achieved. Taking into account small fluctuations either on the gas density value or on the calculated energy distribution of the driving laser beam leads to

significant charge fluctuations, of the same order of magnitude as the one measured experimentally. For more details on the application of the GSA method to the laser focal volume, and the resulting comparison between realistic laser profile simulations and experimental spectra, see the pre-print article in Appendix .

5.2 . High Energy Injector Optimisation Experiment: Apollon 2022

The first external user campaign was conducted in the Apollon LFA during spring 2022. This experiment aimed to use a spherical mirror of f $= 9\,\mathrm{m}$ to increase the energy of LWFA accelerated electrons and then use these ultra-relativistic electrons to create relativistic positrons through the electromagnetic cascade produced during the interaction of the electron bunch with the nuclei of a high atomic number converter target[182]. The collimated F2 beam prior to focusing is on the order of $120\,\mathrm{mm}$ making this an f/60 focusing system. The large f-number allows for the investigation into the benefits of very long focal lengths for electron acceleration. Further, the increased laser stability, and energy reliability of the Apollon laser system, during this second experiment allowed for the investigation of electron bunch parameter control using a PW-class laser system.

Increasing the final focusing optic's focal length allows for a theoretical increase in the maximum achievable energy of the electron bunches by limiting the diffraction of the laser pulse. However, the dephasing length must be increased such that the laser-plasma interaction length is the limiting factor to benefit from this configuration. This requires working at lower plasma densities from the scaling presented in Eq. 1.78. Conversely, a decrease in the plasma density reduces the magnitude of nonlinear self-focusing and pulse compression of the laser which would normally act to increase the a_0 during propagation. In addition, increased focal spot size originating from a shallower focusing angle, causes the transverse energy profile of the laser to be more diffuse for a given pulse energy. Finally, ionisation injection of electrons requires, at minimum, the nonlinear regime where $a_0 \approx 1$ to ionise the inner shell electrons of the dopant. Considering the above points, ultra-high power laser systems in the PW-class are therefore required to achieve injection and acceleration of electrons to ultra-relativistic energies in this focusing regime. This placed more stringent requirements on the on-shot energy of the laser system, and its stability, during the second campaign.

Comparison of laser parameters between the two experiments shows major improvements in the available pulse energy and stability of the focal spot that was implemented by the Apollon team between the two campaigns. We show that the increase in focal length, energy and pointing stability, allow for the development of an ultra-relativistic electrons source, with good stability, electron energies up to $1.8\,\mathrm{GeV}$, per cent energy spreads, tens of pC in the peak, and sub-mrad divergences of the electron bunch.

5.2.1 . Experimental Characteristics

The first external user experiment was conducted in the LFA at Apollon in collaboration with LPGP, Queen's University Belfast, LIDYL, and LLR, to investigate the effects of extremely long focal length on electron acceleration and the creation of positrons through pair-production during the interaction of LWFA electron bunches and a high Z-material. Here we will present the alterations that were made in comparison to the above experiment in section 5.1.

Figure 5.11 illustrates the experimental set-up that was used during the f9 experiment. As the experimental set-up is similar to that presented above in section 5.1, only the major differences between the experiments will be presented.

Production of positrons from ultra-relativistic electron bunch requires interaction between the electron bunch and a high-z material. The addition of a metal target into the beam line adds additional complexity in comparison to the f3 experiment due to the requirement of laser extraction that was completed by using a Kapton tape drive inserted just after the gas cell. The surface of the tape drive becomes an over-dense plasma due to the rapid electron heating of the laser on the plastic. This then acts like a plasma mirror where the laser is reflected into a beam dump. The surface is destroyed in the process requiring a new region of tape to be fed with the drive between each laser shot. To limit noise on the probe line, it was chosen to place the beam dump in the opposite direction to the collection optics for the plasma density measurement.

A wedged high-z material converter can be moved into the beam to provide various thicknesses of the converter target for controlling the positron flux. Due to the radiation cascade created during the interaction of the electron bunch with the converter target, a lead wall was implemented with a small hole, leading to $\pm 8\,\mathrm{mrad}$ acceptance angle for the accelerated electrons and positrons. This shielding limited the radiation on the downstream diagnostics such as the CCD used for the electron spectrometer measurements.

The electrons propagate freely until the permanent dipole magnet which was the same as the one used during the previous campaign. As it was hypothesised that higher electron energies would be reached with the increased focal length, a complex dual spectrometer set-up was used during this experiment to provide laser-axis proximity detection of the very high energy electrons using a YAG crystal detector and imaging down to the 100sMeV level with the LANEX detector which was implemented by the LLR. The custom YAG electron diagnostic implemented by the LLR features a retractable YAG crystal and an in-vacuum camera placed below the electron bunch path to image the screen on each shot. Calibration of charge for the YAG and LANEX imaging systems was completed using two consecutive runs with the same experimental parameters whilst scanning the plasma density by altering the backing pressure of the gas injection system. During the first run, the electron bunch signal on the YAG and LANEX screens was measured with the magnet in the beam path to provide an energy-dispersed electron

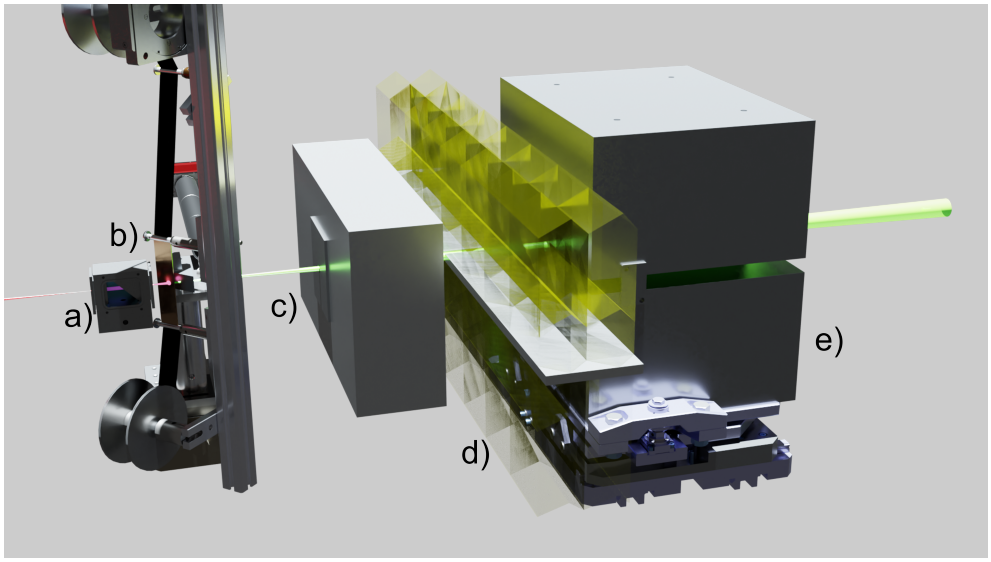

Figure 5.11 – Experimental setup of the 2022 f9 experiment at Apollon demonstrating LWFA of electrons using a $f = 9\,\mathrm{m}$ focusing optic. The laser enters from the left and interacts with the plasma inside the custom-made gas cell from QUB at a). Electrons are accelerated over cm-scales to GeV energies before exiting the plasma and into the vacuum. The depleted laser is then extracted using a Kapton tape drive at b) to avoid ablation of the insertable high-Z converter target. The Kapton tape drive is sufficiently thin to minimise the deviation of the electron bunch. c) The electrons then propagate through the first apertured lead target which produces a mask of $\pm 8\,\mathrm{mrad}$ on the LANEX imaging providing ample angular range for the electron measurements. d) The second lead shielding wall is then which is transparent for visibility of the beam path. e) Finally the electrons are dispersed in energy by the permanent dipole magnet before being imaged by either the YAG and/or LANEX detectors which are not visible in this figure.

beam on the detectors. With a second run, the magnet was removed to have an undispersed electron bunch in the forward direction where a calibrated integrating current transformer (ICT) magnetic sensor[183, 184], presented in section 2.3.1.4, was used to measure the total beam charge. The results were then mapped and a charge calibration was produced for the YAG and LANEX detectors. Spatial calibration of the two electron detectors was completed using geometric measurements of the experimental set-up and a measured magnetic field map of the dipole magnet. At the time of writing the angular calibration of the YAG detector has not been completed.

This experiment was completed in two stages: the primary stage consisted of producing high-quality electron bunches by altering the focal position, plasma density and plateau length, and laser spectral phase through the control of GDD and TDD using an AOPDF. The second consisted of using these electron bunches for the production of positrons. The analysis presented here focuses on the primary stage of electron injector optimisation.

5.2.2 . Preliminary Results

Optimisation of the LPI using the $f = 9\,\mathrm{m}$ spherical mirror led to increased electron bunch energies, lower transverse bunch divergence and increased stability of the resulting spectra. The experimental capabilities of the facility were greatly improved between the two campaigns leading to an increase in the quality of the obtainable electron spectra. The increase in laser stability will be presented here and is demonstrated to be the primary reason for the improvements in electron stability. The increase in the focal length has led to an improvement in the achievable electron parameters.

5.2.2.1 . Laser Performance

As the trapping, acceleration and resulting electron parameters are heavily dependent on the laser parameters, we examine here the laser energy, pointing and radial profile of the laser during the f9 experiment.

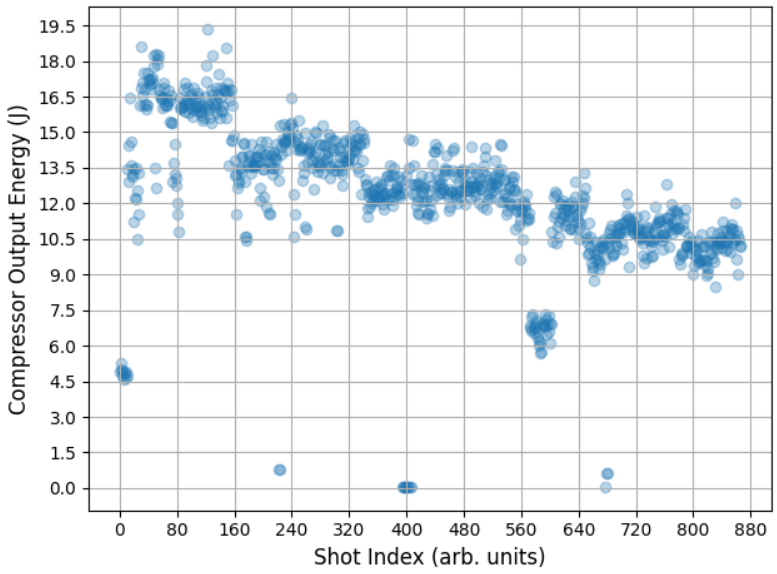

Figure 5.12 – Laser energy was measured by calorimetry at the output of the compressor for the F2 beam at Apollon during the f9 experimental campaign over 867 laser shots.

Figure 5.12 shows the laser energy measured at the output of the compressor over the f9 experimental campaign. Whilst the output energy decreases during the course of the campaign, likely due to compressor grating and optical system deposition, the mean energy has increased from 5.0 ± 0.7 to $12.3 \pm 0.1\mathrm{J}$ for the f3 and f9 campaigns respectively where errors are given as the standard deviation. The improved average energy provides a peak power of $490\,\mathrm{TW}$, allowing for the long focal length to be used. Due to this significantly improved mean energy and stability of the energy, over the f3 campaign, the electron acceleration process was

seen to be greatly stabilised and repeatable electron spectra could be produced as seen in Fig. 5.16.

Using successive images of the focal spot in vacuum - taken at full amplification and then attenuated - we can measure the stability of the focal spot over multiple consecutive shots. The results of this laser spatial stability study are displayed in Fig. 5.13.

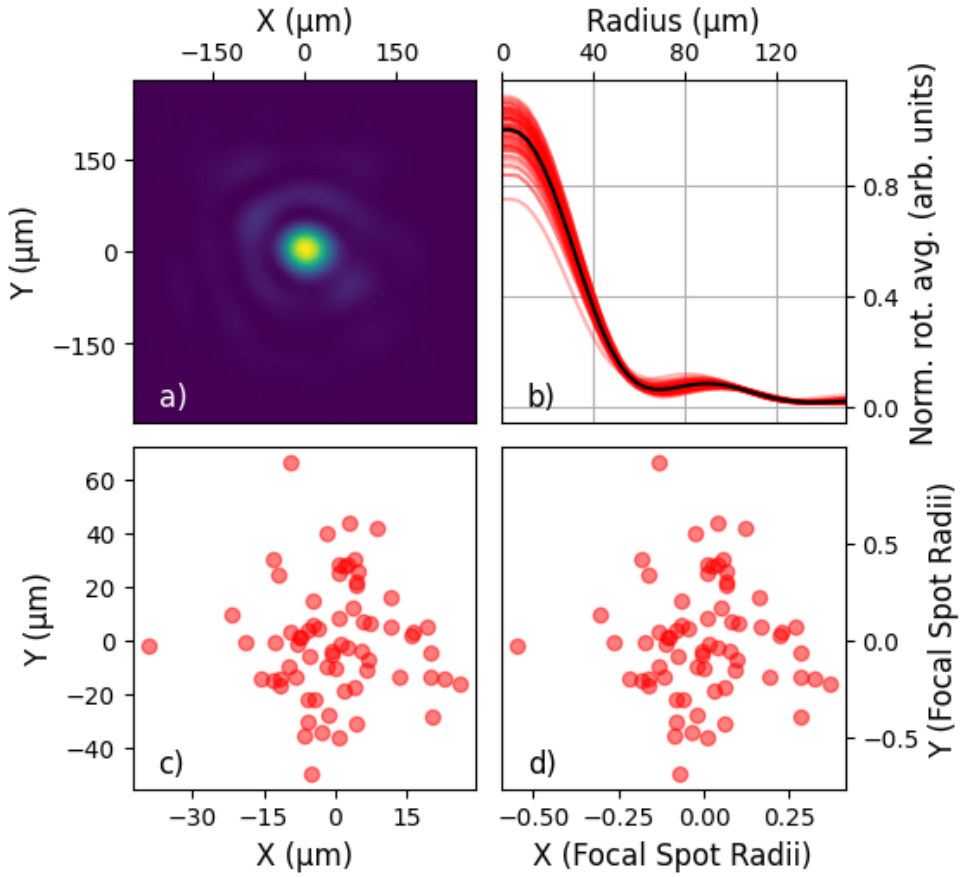

Figure 5.13 – Summary of laser spatial stability over a sample of 68 fully amplified ($\approx$15 J on-target) shots. a) A randomly selected example of the spatially scaled laser transverse fluence profile at focus. b) Rotationally averaged fluence images in red, normalised to the mean rotation average profile in black. Pointing fluctuations centred on the mean pointing value in absolute and focal spot radius units for c) and d), respectively.

Qualitatively in Fig. 5.13 a) we see that the focal spot is well defined by an Airy distribution. This can also be seen in b) where the rotation average provides the first zero of the Airy function at $68 \pm 3.7\mu\mathrm{m}$. For comparison to the data presented on the f3 campaign, we find the average Gaussian radius from the 68 laser shots to be $72.1 \pm 3.7\mu\mathrm{m}$. Comparison of the radial distribution indicates that the energy within the central lobe fluctuates leading to the vertical spread in the normalised

signal, however, the profile of the beam in the radial direction is stable over the 68 measurements. From the absolute and focal spot scaled pointing fluctuations in c) and d), we find average fluctuations, defined as the Pythagorean distance between the origin and the laser pointing value, of $20.9 \pm 3.7\mu\mathrm{m}$ and 0.29 ± 0.05 focal radii respectively corresponding to an angular fluctuation of $2.3 \pm 0.4\mu\mathrm{rad}$. The pointing fluctuations are seen to be dominated in the y-direction by a factor of 1.9. The maximum pointing fluctuation angle was found to be $7.4 \pm 0.4\mu\mathrm{rad}$.

Using the above values for the energy and Gaussian focal spot size, and with a temporal duration of $25\,\mathrm{fs}$, we find a peak intensity of $7 \times 10^{18}\mathrm{W\,cm^{-2}}$, a Rayleigh length of $22.1\,\mathrm{mm}$ and shot-to-shot energy stability of 4.3%.

A comparison of the relative stability between the f3 and f9 experimental campaigns indicates that the laser system was significantly more stable in terms of pointing, energy partition within the focal spot, and average radial form. Fig. 5.14 illustrates the improvement in the averaged radial profile of the f9 campaign over the f3. Fluctuations in the radial form from shot-to-shot in the f3 campaign led to difficulties in the production of stable electron parameters. Absolute variation around the mean of the normalised peak values was improved from 0.22 during the f3 campaign to 0.09 in f9 indicating a factor of two improvement.

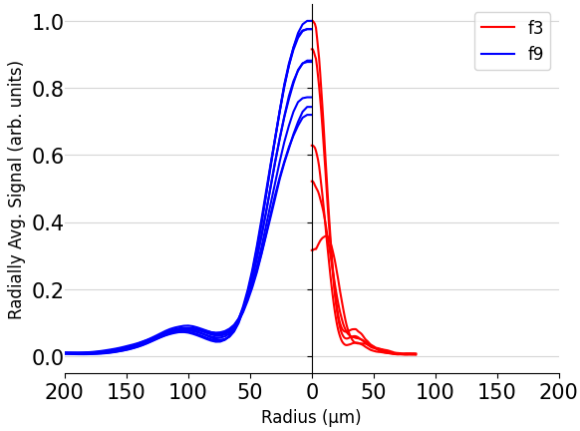

Figure 5.14 – Comparison of 5 consecutive averaged radial profiles of laser in vacuum at focus between the f3 (red) and f9 (blue) experimental campaigns normalised to the maximum value for each data set separately.

The improvement in laser stability has been a result of the hard work of the Apollon laser team to improve the laser system. Laser beam paths were covered with plastic piping when traversing air to reduce the effect of turbulent airflow on the laser profile. Several heat sources throughout the laser chain were found with IR imaging and moved or removed from the beam path to further reduce the effect of heat-induced air flux. Due to the required custom design of the deformable mirror, work was completed to increase the efficacy of the automated routine that was used for the focal spot optimisation and issues with actuators were resolved, resulting in

an improved wavefront correction routine. Finally, the energy stability was improved through the replacement of pump lasers used throughout the amplification chain.

5.2.2.2 . Electron Spectra: Lanex Detector

Measurements of the accelerated electrons in divergence-energy space were performed using the LANEX-based electron detector. Focusing $6\,\mathrm{mm}$ in the QUB gas cell with a $29.2\,\mathrm{mm}$ plasma length and a gas backing pressure of $140\,\mathrm{mbar}$, produced a high-energy, peaked spectra shown in Fig. 5.15 as part of a stability scan shown in Fig. 5.16.

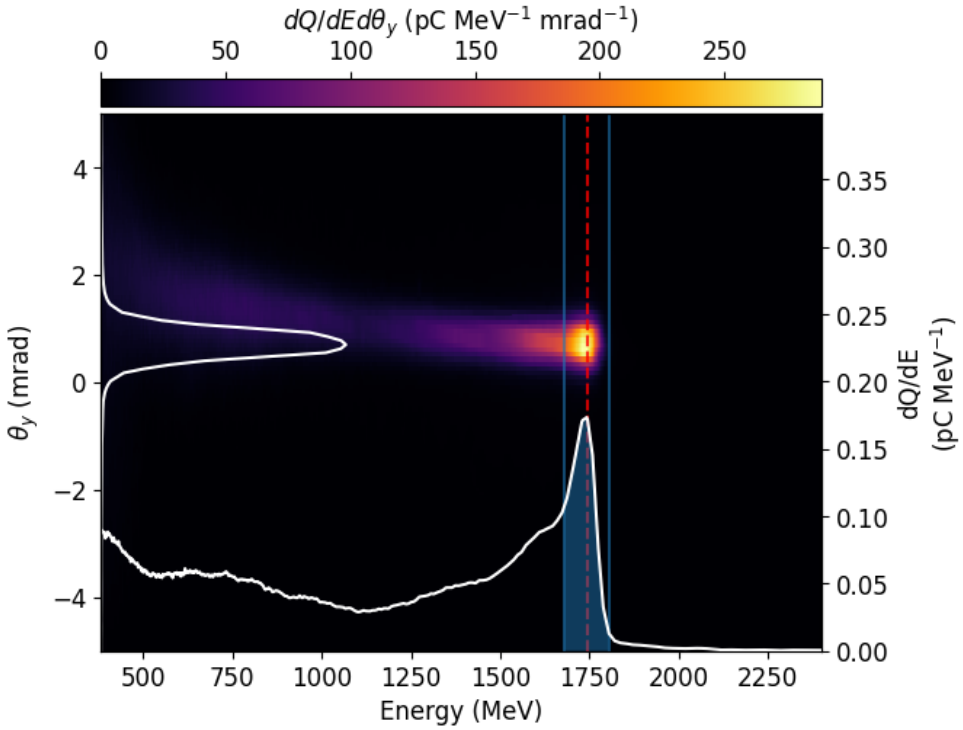

Figure 5.15 – High energy electron spectrum displayed in divergence-energy space. $\mathrm{dQ/dE}$ is displayed by the horizontal white line. Peak $\mathrm{dQ/dE}$ is displayed with the dashed red line. The filled blue volume corresponds to the region of charge selected to calculate the peak properties of the electrons defined as ±FWHM around the peak in $\mathrm{dQ/dE}$. The vertical white line corresponds to the average divergence projection of the electron bunch within ±HWHM around the peak in the energy axis.

Fig. 5.15 illustrates this electron measurement alongside the selection of charge within the peak defined as ±FWHM around the peak in $\mathrm{dQ/dE}$. Projection into divergence-energy space in Fig. 5.15 allows us to calculate a full set of quantities for the electron spectrum. The electron spectrum is of high quality in terms of both spatial and energy parameters. The average divergence of the electrons contained within ± half-width half-maximum (HWHM) of the peak in energy is $0.7\,\mathrm{mrad}$ with an average bunch deflection, over the same volume, of $0.6\,\mathrm{mrad}$. The peak energy

is $1740\,\mathrm{MeV}$ with a maximum energy reaching up to $1837\,\mathrm{MeV}$. The FWHM in energy of $62\,\mathrm{MeV}$ provides an energy spread of 3.6%. The total charge of the spectrum is adequate at $101\,\mathrm{pC}$ however the charge contained within the peak is only $15\,\mathrm{pC}$, leading to a peak charge percentage of 14.4%.

5.2.2.3 . Electron spectra: YAG Detector

The highest energy electrons were measured on the YAG electron detector close to the laser axis. Here we present the electron spectra measured by this detector and demonstrate that the spectra are stable in terms of energy and that their parameters can be tuned using the focal position, backing gas pressure, and group delay dispersion of the laser. Due to time constraints, the YAG detector has been calibrated in terms of absolute distance, but not divergence, at the time of writing.

Figure 5.16 illustrates the stability of the peak electron energy during 8 consecutive measurements using the experimental parameters from Fig. 5.15. The average peak energy of the stability scan was $1.68 \pm 0.06\mathrm{GeV}$ with stability of 3.5% and an average energy spread of 4.61 ± 0.74%. The total charge was more variable during this scan where the mean total charge was found to be $83.0 \pm 25.9\mathrm{pC}$. Larger relative variations in the peak charge were found with the mean value of $12.9 \pm 5.64\mathrm{pC}$ whereas the mean percentage of charge in the peak was 15.4 ± 3.5% which is slightly higher than for the single spectra of this run presented above in Fig. 5.15.

5.3 . Conclusion

The development of a high-energy laser-plasma injector was targeted during two experimental campaigns at the Apollon laser facility. Comparison of global electron spectra collected over the two presented campaigns demonstrates the improvements in the LWFA efficiency and stability between the two campaigns. Using the LANEX electron spectrometer, we compare the average electron spectra over the whole f3 and f9 campaigns in Figs. 5.17 and 5.18, respectively.

Averaged spectra measured on the LANEX detector are displayed in the same angular of $\pm 15\,\mathrm{mrad}$, but different energy windows, 300-900MeV and 300-2000MeV for the f3 and f9 results, respectively. In the case of f3 campaign, energies up to 900MeV were reached, but there is a large dispersion in the divergence of the electrons due to laser pulse parameter fluctuations. The additional acceleration distance offered by the longer focus optics allowed us to reach almost 1.8 GeV within a much smaller divergence region. Considering the $\pm 8\,\mathrm{mrad}$ angular mask from the lead shielding, the divergence of the spectra is still far within these bounds at energies greater than $500\,\mathrm{MeV}$, indicating that the high energy peaks are truly low divergence and not an effect of masking. The long focal length increases the energy and quality of the electron beams Comparing the maximum electron energy in Fig. 5.17 for the f3 and Fig. 5.18 f9 campaigns, we find an increase of over

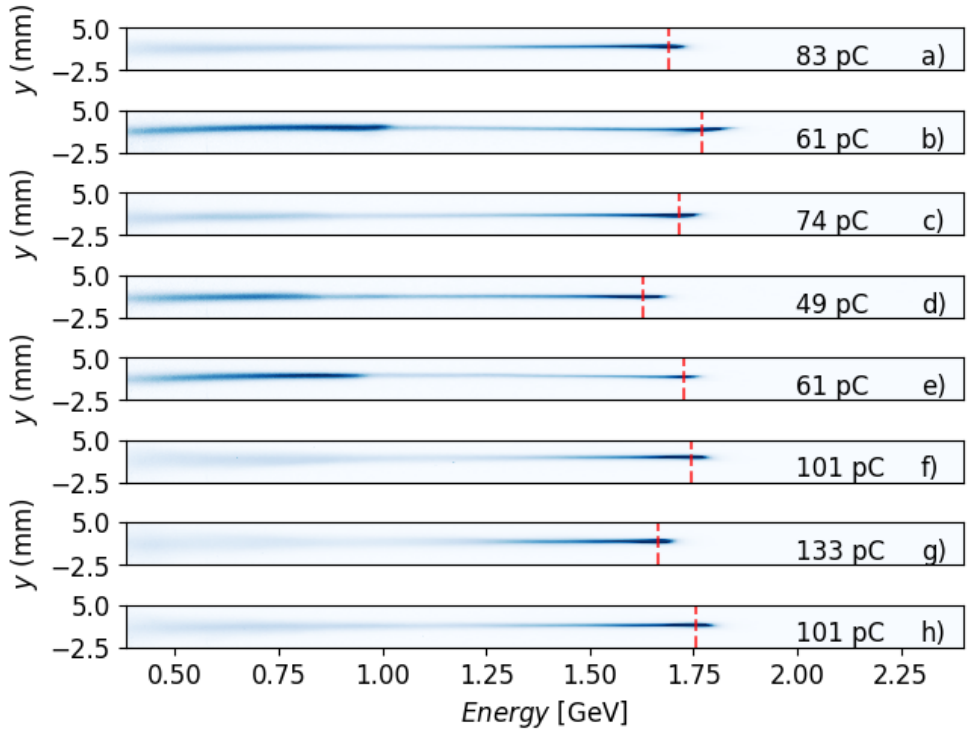

Figure 5.16 – 8 Consecutive electron spectra in the same experimental configuration in distance-energy space from the YAG-based electron detector cropped to an energy window of 0.38 to $2.4\,\mathrm{GeV}$ and spatially on the detector between -2.5 and $5\,\mathrm{mm}$. Inset values are total charge in pC integrated over the energy and space window. Images are scaled to their respective maximum charge density for visibility. The Red dashed line indicates the peak energy value.

$1\,\mathrm{GeV}$ in the peak energy of the electron spectra.

The commissioning experiment indicated that, although the laser was initially unstable, spectra with desirable properties could be produced. We were able to obtain nC-scale charges (over a large energy window between 300-600MeV) on certain shots, Fig 5.8 b) for example, and energies reaching the GeV-scale as demonstrated by the average spectra shown in Fig 5.8 a). Whilst these measurements were taken at approximately 9J laser pulse energy like approximately half of the measurements during the f3 campaign, the fluctuations in the form of the laser energy distribution from shot-to-shot reduced the number of measurements with desirable electron properties. Due to the absence of on-shot interaction chamber focal spot diagnostics, the exact form of the focal spots on these shots is unknown.

Although the fluctuations between spectra are large, this demonstrates that when working well, the laser during the f3 campaign was capable of producing desirable electron spectra. The stability scan demonstrated that during the f3 campaign electron spectra with stable properties could also be produced with the f $= 3\mathrm{m}$ focal length spherical mirror. One point to note is that all of the spectra

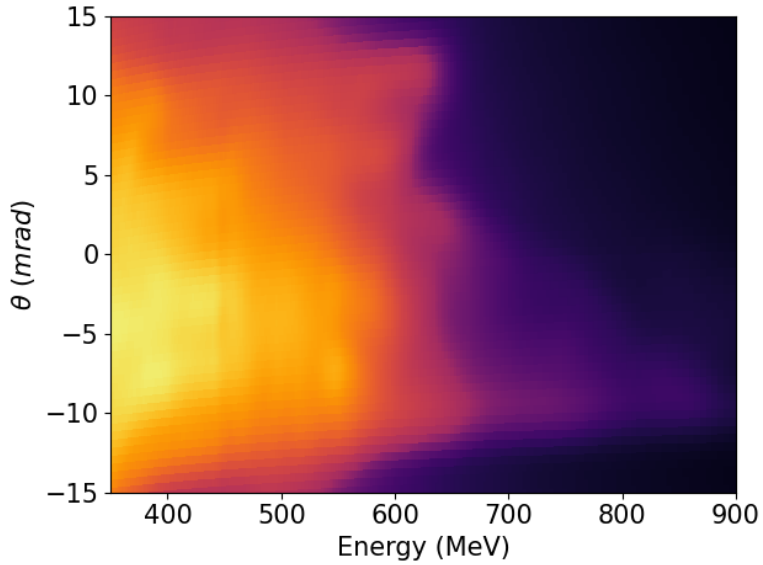

Figure 5.17 – Average electron spectra over the short focal length experimental campaign within a $\pm 15\,\mathrm{mrad}$ window around the laser axis and an energy range of 300 to 900MeV.

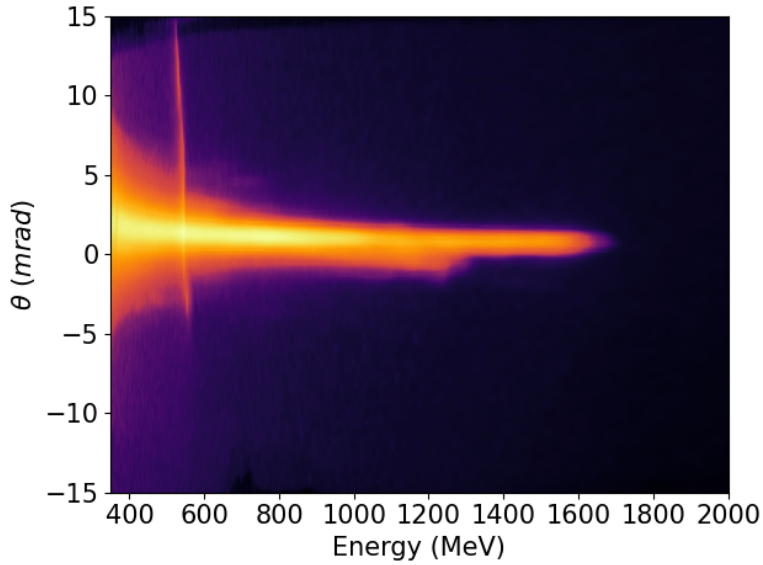

Figure 5.18 – Average electron spectra over the long focal length experimental campaign within a $\pm 15\,\mathrm{mrad}$ window around the laser axis and an energy range of 300 to 2000MeV.

with the best electron parameters, excluding the stability scan, were obtained with approximately 10J on-target energy. The number of shots at this energy was limited to 45% of the shots during the f3 campaign due to pump laser and amplifier

issues further limiting the data acquisition due to laser instabilities.

The availability of at least $10\,\mathrm{J}$ on the target for each shot during the f9 campaign allowed the use of an f = $9\mathrm{m}$ focusing optic, which allowed for longer acceleration distances and thus higher electron energies. The results of the f9 experiment indicate that a stable multi-GeV laser-plasma injector can be achieved using the f = 9m focal length spherical mirror at the Apollon laser centre. The peak energy and energy spread of the spectra demonstrate that, without external guiding, it is possible to achieve peak energies around $1.8\mathrm{GeV}$.

In summary, the use of PW laser systems allows for the stable acceleration of charge to multi-GeV energies with desirable bunch parameters. These preliminary results need to be analysed in detail and compared to simulation results.

6 - Conclusions and Future Perspectives

During this thesis the development of low and high-energy laser-plasma injectors at $150\,\mathrm{MeV}$ and $1\,\mathrm{GeV}$, respectively, were investigated along with their associated diagnostics.

Advances in our understanding of the physical processes of laser-plasma coupling were demonstrated with alteration to the density downramp, focal position within the plasma to control total charge and angular displacement of the bunch from the accelerator axis, and the effect of laser wavefront controlled by adaptive optics. Through careful tuning of these experimental parameters, and performing injection in a novel regime where the laser pulse with improved pre-focal symmetry was focused very early in the plasma upramp, it was possible to create stable electron spectra with $125\mathrm{MeV}$ peak energy, 8.7% energy spread, $1.8\mathrm{mrad}$ divergence, although the peak charge was low at $3.7\,\mathrm{pC}$. We investigated the physical processes creating these electron properties by employing realistic laser profiles in simulation PIC codes, which improved the agreement with experiments in comparison with the Gaussian driver case. For example, we have seen that this small charge value was due to the evolution of a_0 in the plasma being controlled by the density ramps and the laser wavefront causing the ionisation threshold to be very localised on the density downramp when the laser intensity was also increasing.

Application of Bayesian optimisation to LWFA experiments was presented illustrating that rapid optimisation can be performed which produces spectra with desirable and stable qualities. The effect of group delay dispersion and third-order dispersion on the electron spectra were then examined as these were shown experimentally to play a large role in determining the accelerated electron energy spread and fluctuations in the stability of the electrons. Inclusion of the adaptive optic into the optimisation routine would likely improve the spectra further as seen by the effect of the laser wavefront on the electron spectra in the initial low-energy injector campaign. An offline method was then presented that aimed to improve our understanding of how best to implement Bayesian optimisation in LWFA experiments through analysis of merit function, kernel and acquisition function choice for the Bayesian optimisation process.

The application of optimisation routines in the LWFA community will likely prove valuable due to the complex and non-linear parameter space involved in the production of high-energy electrons. However, much work remains to be completed. Investigations into general merit function design for LWFA and the inclusion of output parameter stability in the merit function must be completed. The interesting injection regimes that will likely be uncovered due to the complex relationships between the spatial and temporal evolution of the laser-plasma-electron system must

then be explored through realistic simulations to uncover the physical processes involved. Demonstration of the flexibility of LPIs could also be shown in future work by consecutively tuning merit functions to optimise the electron bunches for different parameters such as energy spread, charge, energy-separated bunches for driver-witness studies, etc.

The development of a focal spot reconstruction method using generative adversarial networks was shown to provide near-perfect radial profile retrieval and of approximately 5% error on the energy profile reconstruction. The pointing reconstruction, however, needs to be improved. This could be achieved by purposefully inducing vibrations into the laser system to bias training of the absolute position of the focal spot, as well as its energy distribution.

Development of a self-reference single-shot wavefront sensor-based plasma density diagnostic and a temporally resolved Mach-Zehnder interferometer were presented and retrieved plasma densities in agreement with the classical Mach-Zehnder interferometer method.

High-energy electron injectors were investigated at the Apollon laser facility where analysis of the laser stability allowed for the qualification of the LWFA capabilities of the laser system. Improvements in the quality of the accelerated electrons were seen through elongation of the focal length of the spherical mirror and energies reaching multi-GeV with low energy spread was achieved.

In addition to the peak energy, the small energy spread makes these electron bunches promising for further acceleration in secondary stages. The sub-mrad divergence of the spectra presented in section 5.2.2.2 also makes the electron spectra simpler to transport to a second stage as it reduces the requirements on magnetic focusing optics. At Apollon, it is envisioned to use the F1 $10\mathrm{PW}$ beamline currently under construction as the laser driver in a secondary stage to perform further acceleration in the linear regime to limit further electron injection. This would be completed using an equal, or longer, focusing optic and a low-density plasma. The length of the focusing optic is only limited by the room size and cost, allowing focal lengths of up to 20m. Implementation of a structured density downramp in the gas cell, as demonstrated in section 4.1.3.1 for the low-energy injector case, could further reduce the energy spread of the electrons making them immediately suitable for free-electron laser experiments at Apollon.

The peak charge of the electron bunches should be targeted for improvement as it is currently a factor of two below the requested peak bunch charge for a future laser-plasma injector within the EuPRAXIA framework. Increasing the dopant percentage would likely increase the amount of injected charge, however, the ionisation of the dopant gas induces diffraction of the laser pulse which would be problematic, especially for the approximately $30\,\mathrm{mm}$ plasma length used in this experiment. Therefore, a structured gas cell, where an increased dopant percentage is spatially constrained in a first compartment, could allow for the augmentation of charge, whilst continuing to not require external guiding.

Comparison to the EuPRAXIA framework request for the high energy injector of $1\,\mathrm{GeV}$ bunch energy, 5% energy spread, and $30\,\mathrm{pC}$, the energy and energy spread have been achieved in this experimental configuration and the charge must be augmented by a factor of two. For the low-energy injector case parameters presented above, the energy, energy spread and charge must all be improved. However, the charge is the most significant and requires to be increased by a factor of eight. To achieve this, we are currently performing simulations in an attempt to find optimum parameters for working points at intermediate laser energies between the Lund Laser Centre and Apollon.

Bibliographie

[1] T. Tajima et J. M. Dawson, “Laser Electron Accelerator”, *Phys. Rev. Lett.*, t. 43, p. 267-270, 4 juill. 1979. doi : 10.1103/PhysRevLett.43.267.

[2] R. Assmann et al., “EuPRAXIA conceptual design report”, *The European Physical Journal Special Topics*, t. 229, n° 24, p. 3675-4284, 2020.

[3] E. Esarey, C. Schroeder et W. Leemans, “Physics of laser-driven plasma-based electron accelerators”, *Reviews of modern physics*, t. 81, n° 3, p. 1229, 2009.

[4] A. Buck et al., “Real-time observation of laser-driven electron acceleration”, en, *Nature Physics*, t. 7, n° 7, p. 543-548, juill. 2011, issn : 1745-2473, 1745-2481. doi : 10.1038/nphys1942. adresse : http://www.nature.com/articles/nphys1942 (visité le 12/01/2023).

[5] A. Debus et al., “Electron bunch length measurements from laser-accelerated electrons using single-shot THz time-domain interferometry”, *Physical review letters*, t. 104, n° 8, p. 084 802, 2010.

[6] F. Grüner et al., “Design considerations for table-top, laser-based VUV and X-ray free electron lasers”, *Applied Physics B*, t. 86, n° 3, p. 431-435, 2007.

[7] J. Cole et al., “Experimental evidence of radiation reaction in the collision of a high-intensity laser pulse with a laser-wakefield accelerated electron beam”, *Physical Review X*, t. 8, n° 1, p. 011 020, 2018.

[8] K. Poder et al., “Experimental signatures of the quantum nature of radiation reaction in the field of an ultraintense laser”, *Physical Review X*, t. 8, n° 3, p. 031 004, 2018.

[9] B. Paroli et M. Potenza, “Radiation emission processes and properties: synchrotron, undulator and betatron radiation”, *Advances in Physics: X*, t. 2, n° 3, p. 978-1004, 2017.

[10] K. Huang, Z. Jin, N. Nakanii, T. Hosokai et M. Kando, “Experimental demonstration of 7-femtosecond electron timing fluctuation in laser wakefield acceleration”, *Applied Physics Express*, t. 15, n° 3, p. 036 001, mars 2022, issn : 1882-0778, 1882-0786. doi : 10.35848/1882-0786/ac5237. adresse : https://iopscience.iop.org/article/10.35848/1882-0786/ac5237 (visité le 12/01/2023).

[11] K. Behm et al., “Demonstration of femtosecond broadband X-rays from laser wakefield acceleration as a source for pump-probe X-ray absorption studies”, en, *High Energy Density Physics*, t. 35, p. 100 729, juin 2020, issn : 15741818. doi : 10.1016/j.hedp.2019.100729. adresse : https://linkinghub.elsevier.com/retrieve/pii/S1574181819300011 (visité le 12/01/2023).

[12] A. Döpp et al., “A bremsstrahlung gamma-ray source based on stable ionization injection of electrons into a laser wakefield accelerator”, *Nuclear Instruments and Methods in Physics Research Section A: Accelerators, Spectrometers, Detectors and Associated Equipment*, t. 830, p. 515-519, 2016.

[13] G. Sarri et al., “Table-Top Laser-Based Source of Femtosecond, Collimated, Ultrarelativistic Positron Beams”, *Phys. Rev. Lett.*, t. 110, p. 255 002, 25 juin 2013. doi : 10.1103/PhysRevLett.110.255002. adresse : https://link.aps.org/doi/10.1103/PhysRevLett.110.255002.

[14] F. Albert et A. G. Thomas, “Applications of laser wakefield accelerator-based light sources”, *Plasma Physics and Controlled Fusion*, t. 58, n° 10, p. 103 001, 2016.

[15] A. Alejo, R. Walczak et G. Sarri, “Laser-driven high-quality positron sources as possible injectors for plasma-based accelerators”, en, *Scientific Reports*, t. 9, n° 1, p. 5279, mars 2019, issn : 2045-2322. doi : 10.1038/s41598-019-41650-y. adresse : https://www.nature.com/articles/s41598-019-41650-y (visité le 12/01/2023).

[16] A. Gonsalves et al., “Petawatt laser guiding and electron beam acceleration to 8 GeV in a laser-heated capillary discharge waveguide”, *Physical review letters*, t. 122, n° 8, p. 084 801, 2019.

[17] J. Couperus et al., “Demonstration of a beam loaded nanocoulomb-class laser wakefield accelerator”, *Nature communications*, t. 8, n° 1, p. 1-7, 2017.

[18] J. Götzfried et al., “Physics of high-charge electron beams in laser-plasma wakefields”, *Physical Review X*, t. 10, n° 4, p. 041 015, 2020.

[19] L. Ke et al., “Near-GeV Electron Beams at a Few Per-Mille Level from a Laser Wakefield Accelerator via Density-Tailored Plasma”, *Physical Review Letters*, t. 126, n° 21, p. 214 801, 2021, Publisher: APS.

[20] P. A. Walker et al., “Facility Considerations for a European Plasma Accelerator Infrastructure (EuPRAXIA)”, in *10th Int. Particle Accelerator Conf.(IPAC’19), Melbourne, Australia, 19-24 May 2019*, JACOW Publishing, Geneva, Switzerland, 2019, p. 3635-3637.

[21] L. Gizzi et al., “Lasers for Novel Accelerators”, *Journal of Physics: Conference Series*, t. 1350, n° 1, p. 012 157, nov. 2019, issn : 1742-6588, 1742-6596. doi : 10.1088/1742-6596/1350/1/012157. adresse : https://iopscience.iop.org/article/10.1088/1742-6596/1350/1/012157 (visité le 21/04/2023).

[22] L. Dickson et al., “Mechanisms to control laser-plasma coupling in laser wakefield electron acceleration”, *Physical Review Accelerators and Beams*, t. 25, n° 10, p. 101 301, 2022.

[23] G.-Z. Sun, E. Ott, Y. Lee et P. Guzdar, “Self-focusing of short intense pulses in plasmas”, *The Physics of fluids*, t. 30, n° 2, p. 526-532, 1987, Publisher: American Institute of Physics.

[24] B. E. Saleh et M. C. Teich, *Fundamentals of photonics*. john Wiley & sons, 2019.

[25] A. Weiner, *Ultrafast optics*. John Wiley & Sons, 2011, t. 72.

[26] A. Borzsonyi, A. Kovacs et K. Osvay, “What We Can Learn about Ultrashort Pulses by Linear Optical Methods”, en, *Applied Sciences*, t. 3, n° 2, p. 515-544, avr. 2013, issn : 2076-3417. doi : 10.3390/app3020515. adresse : http://www.mdpi.com/2076-3417/3/2/515 (visité le 07/12/2022).

[27] J.-C. Diels et W. Rudolph, *Ultrashort laser pulse phenomena*. Elsevier, 2006.

[28] E. Huckel et P. Debye, “Zur theorie der elektrolyte. i. gefrierpunktserniedrigung und verwandte erscheinungen”, *Phys. Z*, t. 24, p. 185-206, 1923.

[29] L. Tonks et I. Langmuir, “Note on "Oscillations in Ionized Gases"”, en, *Physical Review*, t. 33, n° 6, p. 990-990, juin 1929, issn : 0031-899X. doi : 10.1103/PhysRev.33.990. adresse : https://link.aps.org/doi/10.1103/PhysRev.33.990 (visité le 09/12/2022).

[30] P. Gibbon, “Introduction to plasma physics”, *arXiv preprint arXiv:2007.04783*, 2020.

[31] S. Lautenbach et R. Grauer, “Multiphysics Simulations of Collisionless Plasmas”, *Frontiers in Physics*, t. 6, p. 113, oct. 2018, issn : 2296-424X. doi : 10.3389/fphy.2018.00113. adresse : https://www.frontiersin.org/article/10.3389/fphy.2018.00113/full (visité le 26/12/2022).

[32] A. Einstein, “Über einen die Erzeugung und Verwandlung des Lichtes betreffenden heuristischen Gesichtspunkt”, de, *Annalen der Physik*, t. 322, n° 6, p. 132-148, 1905, issn : 00033804, 15213889. doi : 10.1002/andp.19053220607. adresse : https://onlinelibrary.wiley.com/doi/10.1002/andp.19053220607 (visité le 09/12/2022).

[33] L. Keldysh et al., “Ionization in the field of a strong electromagnetic wave”, *Sov. Phys. JETP*, t. 20, n° 5, p. 1307-1314, 1965.

[34] C. Decker, W. Mori, K.-C. Tzeng et T. Katsouleas, “The evolution of ultra-intense, short-pulse lasers in underdense plasmas”, *Physics of Plasmas*, t. 3, n° 5, p. 2047-2056, 1996, Publisher: American Institute of Physics.

[35] G. Kentwell et D. A. Jones, “The time-dependent ponderomotive force”, *Physics Reports*, t. 145, n° 6, p. 319-403, 1987.

[36] B. Quesnel et P. Mora, “Theory and simulation of the interaction of ultraintense laser pulses with electrons in vacuum”, *Physical Review E*, t. 58, n° 3, p. 3719, 1998.

[37] R. Bingham et R. Trines, “Introduction to plasma accelerators: the basics”, *arXiv preprint arXiv:1705.10535*, 2017.

[38] R. W. Boyd, S. G. Lukishova et Y. R. Shen, *Self-focusing: Past and Present: Fundamentals and Prospects*. Springer, 2009.

[39] V. B. Pathak, J. Vieira, R. Fonseca et L. Silva, “Effect of the frequency chirp on laser wakefield acceleration”, *New Journal of Physics*, t. 14, n° 2, p. 023 057, 2012, Publisher: IOP Publishing.

[40] W. Lu et al., “Generating multi-GeV electron bunches using single stage laser wakefield acceleration in a 3D nonlinear regime”, *Physical Review Special Topics-Accelerators and Beams*, t. 10, n° 6, p. 061 301, 2007, Publisher: APS.

[41] M. Streeter et al., “Observation of laser power amplification in a self-injecting laser wakefield accelerator”, *Physical review letters*, t. 120, n° 25, p. 254 801, 2018.

[42] L. Gorbunov et V. Kirsanov, “Excitation of plasma waves by an electromagnetic wave packet”, *Zh. Eksp. Teor. Fiz*, t. 93, p. 509-518, 1987.

[43] E. Esarey et M. Pilloff, “Trapping and acceleration in nonlinear plasma waves”, *Physics of Plasmas*, t. 2, n° 5, p. 1432-1436, 1995. doi : 10.1063/1.871358. eprint : https://doi.org/10.1063/1.871358. adresse : https://doi.org/10.1063/1.871358.

[44] M. Chen, E. Esarey, C. B. Schroeder, C. G. R. Geddes et W. P. Leemans, “Theory of ionization-induced trapping in laser-plasma accelerators”, *Physics of Plasmas*, t. 19, n° 3, p. 033 101, 2012. doi : 10.1063/1.3689922. eprint : https://doi.org/10.1063/1.3689922. adresse : https://doi.org/10.1063/1.3689922.

[45] J. Faure, “Plasma Injection Schemes for Laser–Plasma Accelerators”, *CERN Yellow Reports*, t. 1, n° 0, p. 143, 2016. adresse : https://e-publishing.cern.ch/index.php/CYR/article/view/218.

[46] F. Massimo, A. Beck, J. Dérouillat, I. Zemzemi et A. Specka, “Numerical modeling of laser tunneling ionization in particle-in-cell codes with a laser envelope model”, *Physical Review E*, t. 102, n° 3, p. 033 204, 2020.

[47] P. Mora et T. M. Antonsen Jr., “Kinetic modeling of intense, short laser pulses propagating in tenuous plasmas”, en, *Physics of Plasmas*, t. 4, n° 1, p. 217-229, jan. 1997, issn : 1070-664X, 1089-7674. doi : 10.1063/1.872134. adresse : http://aip.scitation.org/doi/10.1063/1.872134 (visité le 13/01/2023).

[48] V. I. Berezhiani et I. G. Murusidze, “Interaction of highly relativistic short laser pulses with plasmas and nonlinear wake-field generation”, *Physica Scripta*, t. 45, n° 2, p. 87-90, fév. 1992. doi : 10.1088/0031-8949/45/2/007. adresse : https://doi.org/10.1088%2F0031-8949%2F45%2F2%2F007.

[49] E. Esarey, P. Sprangle, J. Krall, A. Ting et G. Joyce, “Optically guided laser wake-field acceleration*”, *Physics of Fluids B: Plasma Physics*, t. 5, n° 7, p. 2690-2697, 1993. doi : 10.1063/1.860707. eprint : https://doi.org/10.1063/1.860707. adresse : https://doi.org/10.1063/1.860707.

[50] D. Teychenné, G. Bonnaud et J.-L. Bobin, “Wave-breaking limit to the wake-field effect in an underdense plasma”, *Phys. Rev. E*, t. 48, R3248-R3251, 5 nov. 1993. doi : 10.1103/PhysRevE.48.R3248. adresse : https://link.aps.org/doi/10.1103/PhysRevE.48.R3248.

[51] C. K. Birdsall et A. B. Langdon, *Plasma Physics via Computer Simulation*. Taylor et Francis Group, 2004.

[52] F. S. Tsung, R. Narang, W. B. Mori, C. Joshi, R. Fonseca et L. O. Silva, “Near-GeV-energy laser-wakefield acceleration of self-injected electrons in a centimeter-scale plasma channel”, *Physical Review Letters*, t. 93, n° 18, p. 185 002, 2004.

[53] M. Chen, Z.-M. Sheng, Y.-Y. Ma et J. Zhang, “Electron injection and trapping in a laser wakefield by field ionization to high-charge states of gases”, *Journal of Applied Physics*, t. 99, n° 5, p. 056 109, 2006. doi : 10.1063/1.2179194. eprint : https://doi.org/10.1063/1.2179194. adresse : https://doi.org/10.1063/1.2179194.

[54] C. McGuffey et al., “Ionization induced trapping in a laser wakefield accelerator”, *Physical Review Letters*, t. 104, n° 2, p. 025 004, 2010.

[55] A. Pak, K. Marsh, S. Martins, W. Lu, W. Mori et C. Joshi, “Injection and trapping of tunnel-ionized electrons into laser-produced wakes”, *Physical Review Letters*, t. 104, n° 2, p. 025 003, 2010.

[56] B. Hidding et al., “Beyond injection: Trojan horse underdense photocathode plasma wakefield acceleration”, *AIP Conference Proceedings*, t. 1507, n° 1, p. 570-575, 2012. doi : 10.1063/1.4773760. eprint : https://aip.scitation.org/doi/pdf/10.1063/1.4773760. adresse : https://aip.scitation.org/doi/abs/10.1063/1.4773760.

[57] M. Zeng, M. Chen, Z.-M. Sheng, W. B. Mori et J. Zhang, “Self-truncated ionization injection and consequent monoenergetic electron bunches in laser wakefield acceleration”, *Physics of Plasmas*, t. 21, n° 3, p. 030 701, 2014.

[58] E. Esarey, P. Sprangle, J. Krall et A. Ting, “Overview of plasma-based accelerator concepts”, *IEEE Transactions on plasma science*, t. 24, n° 2, p. 252-288, 1996. adresse : http://pdfs.semanticscholar.org/727e/66d838cf607c6709264f73443c1d38fb2d0d.pdf.

[59] J. M. Dawson, “Nonlinear Electron Oscillations in a Cold Plasma”, en, *Physical Review*, t. 113, n° 2, p. 383-387, jan. 1959, issn : 0031-899X. doi : 10.1103/PhysRev.113.383. adresse : https://link.aps.org/doi/10.1103/PhysRev.113.383 (visité le 27/12/2022).

[60] S. W. T. Katsouleas et J. Su, “Beam loading efficiency in plasma accelerators”, *Part. Accel*, t. 22, p. 81-99, 1987.

[61] C. Rechatin et al., “Observation of Beam Loading in a Laser-Plasma Accelerator”, en, *Physical Review Letters*, t. 103, n° 19, p. 194 804, nov. 2009, issn : 0031-9007, 1079-7114. doi : 10.1103/PhysRevLett.103.194804. adresse : https://link.aps.org/doi/10.1103/PhysRevLett.103.194804 (visité le 28/12/2022).

[62] K. Ta Phuoc et al., “Demonstration of the ultrafast nature of laser produced betatron radiation”, *Physics of Plasmas*, t. 14, n° 8, p. 080 701, 2007.

[63] C. Geddes et al., “High-quality electron beams from a laser wakefield accelerator using plasma-channel guiding”, *Nature*, t. 431, n° 7008, p. 538-541, 2004, Publisher: Nature Publishing Group.

[64] S. P. Mangles et al., “Monoenergetic beams of relativistic electrons from intense laser–plasma interactions”, *Nature*, t. 431, n° 7008, p. 535-538, 2004, Publisher: Nature Publishing Group. adresse : https://www.nature.com/articles/nature02939.pdf.

[65] J. Faure et al., “A laser–plasma accelerator producing monoenergetic electron beams”, *Nature*, t. 431, n° 7008, p. 541-544, 2004, Publisher: Nature Publishing Group.

[66] C. Aniculaesei et al., “High-charge 10 GeV electron acceleration in a 10 cm nanoparticle-assisted hybrid wakefield accelerator”, *arXiv preprint arXiv:2207.11492*, 2022.

[67] Z.-H. He et al., “High repetition-rate wakefield electron source generated by few-millijoule, 30 fs laser pulses on a density downramp”, *New Journal of Physics*, t. 15, n° 5, p. 053 016, mai 2013, issn : 1367-2630. doi : 10.1088/1367-2630/15/5/053016. adresse : https://iopscience.iop.org/article/10.1088/1367-2630/15/5/053016 (visité le 26/01/2023).

[68] B. Beaurepaire et al., “Effect of the Laser Wave Front in a Laser-Plasma Accelerator”, en, *Physical Review X*, t. 5, n° 3, p. 031 012, juill. 2015, issn : 2160-3308. doi : 10.1103/PhysRevX.5.031012. adresse : https://link.aps.org/doi/10.1103/PhysRevX.5.031012 (visité le 26/01/2023).

[69] O. Kononenko et al., “2D hydrodynamic simulations of a variable length gas target for density down-ramp injection of electrons into a laser wakefield accelerator”, en, *Nuclear Instruments and Methods in Physics Research Section A: Accelerators, Spectrometers, Detectors and Associated Equipment*, t. 829, p. 125-129, sept. 2016, issn : 01689002. doi : 10.1016/j.nima.2016.03.104. adresse : https://linkinghub.elsevier.com/retrieve/pii/S0168900216301498 (visité le 26/01/2023).

[70] M. Kirchen et al., “Optimal Beam Loading in a Laser-Plasma Accelerator”, *Phys. Rev. Lett.*, t. 126, p. 174 801, 17 avr. 2021. doi : 10.1103/PhysRevLett.126.174801.

[71] T. Kurz et al., “Demonstration of a compact plasma accelerator powered by laser-accelerated electron beams”, *Nature Communications*, t. 12, n° 1, p. 1-9, 2021, Publisher: Nature Publishing Group.

[72] F. Foerster et al., “Stable and High-Quality Electron Beams from Staged Laser and Plasma Wakefield Accelerators”, *Physical Review X*, t. 12, n° 4, p. 041 016, 2022, Publisher: APS.

[73] A. Knetsch et al., “High average gradient in a laser-gated multistage plasma wakefield accelerator”, *arXiv preprint arXiv:2210.02263*, 2022.

[74] C. A. Lindstrøm, “Staging of plasma-wakefield accelerators”, *Physical Review Accelerators and Beams*, t. 24, n° 1, p. 014 801, 2021.

[75] S. Steinke et al., “Multistage coupling of independent laser-plasma accelerators”, en, *Nature*, t. 530, n° 7589, p. 190-193, fév. 2016, issn : 0028-0836, 1476-4687. doi : 10.1038/nature16525. adresse : http://www.nature.com/articles/nature16525 (visité le 26/01/2023).

[76] A. Ferran Pousa, A. Martinez de la Ossa, R. Brinkmann et R. W. Assmann, “Compact Multistage Plasma-Based Accelerator Design for Correlated Energy Spread Compensation”, en, *Physical Review Letters*, t. 123, n° 5, p. 054 801, juill. 2019, issn : 0031-9007, 1079-7114. doi : 10.1103/PhysRevLett.123.054801. adresse : https://link.aps.org/doi/10.1103/PhysRevLett.123.054801 (visité le 26/01/2023).

[77] N. Nakanii et al., “Effect of halo on the stability of electron bunches in laser wakefield acceleration”, *EPL (Europhysics Letters)*, t. 113, n° 3, p. 34 002, 2016.

[78] J. Ferri et al., “Effect of experimental laser imperfections on laser wakefield acceleration and betatron source”, *Scientific reports*, t. 6, n° 1, p. 1-10, 2016.

[79] R. W. Gerchberg, “A practical algorithm for the determination of phase from image and diffraction plane pictures”, *Optik*, t. 35, p. 237-246, 1972.

[80] Z.-H. He, B. Hou, V. Lebailly, J. Nees, K. Krushelnick et A. Thomas, “Coherent control of plasma dynamics”, *Nature communications*, t. 6, n° 1, p. 1-7, 2015.

[81] R. Shalloo et al., “Automation and control of laser wakefield accelerators using Bayesian optimization”, *Nature communications*, t. 11, n° 1, p. 1-8, 2020.

[82] D. Guénot et al., “Distribution of liquid mass in transient sprays measured using laser-plasma-driven x-ray tomography”, *Physical Review Applied*, t. 17, n° 6, p. 064 056, 2022.

[83] K. Svendsen, D. Guénot, J. B. Svensson, K. Petersson, A. Persson et O. Lundh, “A focused very high energy electron beam for fractionated stereotactic radiotherapy”, *Scientific Reports*, t. 11, n° 1, p. 1-8, 2021.

[84] J. Cole et al., “Laser-wakefield accelerators as hard x-ray sources for 3D medical imaging of human bone”, *Scientific reports*, t. 5, n° 1, p. 1-7, 2015.

[85] G. Sarri et al., “Generation of neutral and high-density electron–positron pair plasmas in the laboratory”, *Nature communications*, t. 6, n° 1, p. 1-8, 2015, Publisher: Nature Publishing Group.

[86] M. Thévenet et al., “Emittance growth due to misalignment in multistage laser-plasma accelerators”, *Physical Review Accelerators and Beams*, t. 22, n° 5, p. 051 302, 2019.

[87] A. R. Maier et al., “Decoding sources of energy variability in a laser-plasma accelerator”, *Physical Review X*, t. 10, n° 3, p. 031 039, 2020.

[88] A. Laser, *Laser femto*, Accessed on 31.12.2022. adresse : https://amplitude-laser.com/products_category/femtosecond-lasers/.

[89] *TeraWatt Systems*, Accessed on 31.12.2022. adresse : https://www.thalesgroup.com/en/worldwide/group/market-specific-solutions-lasers-science-applications/terawatt-systems.

[90] D. Strickland et G. Mourou, “Compression of amplified chirped optical pulses”, *Optics communications*, t. 55, n° 6, p. 447-449, 1985.

[91] P. Maine, D. Strickland, P. Bado, M. Pessot et G. Mourou, “Generation of ultrahigh peak power pulses by chirped pulse amplification”, *IEEE Journal of Quantum electronics*, t. 24, n° 2, p. 398-403, 1988.

[92] S. L. Chin, *Femtosecond laser filamentation*. Springer, 2010, t. 55.

[93] M. D. Perry, T. Ditmire et B. C. Stuart, “Self-phase modulation in chirped-pulse amplification”, en, *Optics Letters*, t. 19, n° 24, p. 2149, déc. 1994, issn : 0146-9592, 1539-4794. doi : 10.1364/OL.19.002149. adresse : https://opg.optica.org/abstract.cfm?URI=ol-19-24-2149 (visité le 16/12/2022).

[94] D. Papadopoulos et al., “High-contrast 10 fs OPCPA-based front end for multi-PW laser chains”, *Optics letters*, t. 42, n° 18, p. 3530-3533, 2017, Publisher: Optica Publishing Group.

[95] F. Tavella, “Multiterawatt few-cycle pulse OPCPA for applications in high-field physics”, PhD Thesis, lmu, 2008.

[96] F. Wu et al., “Wavefront Correction in Vacuum of SULF-1PW Laser Beamline”, en, *Photonics*, t. 9, n° 11, p. 872, nov. 2022, issn : 2304-6732. doi : 10.3390/photonics9110872. adresse : https://www.mdpi.com/2304-6732/9/11/872 (visité le 13/01/2023).

[97] J. W. Yoon et al., “Realization of laser intensity over 10^{23} W/cm ^{2}”, en, *Optica*, t. 8, n° 5, p. 630, mai 2021, issn : 2334-2536. doi : 10.1364/OPTICA.420520. adresse : https://opg.optica.org/abstract.cfm?URI=optica-8-5-630 (visité le 13/01/2023).

[98] S. P. D. Mangles et al., “Self-injection threshold in self-guided laser wakefield accelerators”, en, *Physical Review Special Topics - Accelerators and Beams*, t. 15, n° 1, p. 011 302, jan. 2012, issn : 1098-4402. doi : 10.1103/PhysRevSTAB.15.011302. adresse : https://link.aps.org/doi/10.1103/PhysRevSTAB.15.011302 (visité le 14/12/2022).

[99] v. F. Zernike, “Beugungstheorie des schneidenver-fahrens und seiner verbesserten form, der phasenkontrastmethode”, de, *Physica*, t. 1, n° 7-12, p. 689-704, mai 1934, issn : 00318914. doi : 10.1016/S0031-8914(34)80259-5. adresse : https://linkinghub.elsevier.com/retrieve/pii/S0031891434802595 (visité le 09/12/2022).

[100] V. Lakshminarayanan et A. Fleck, “Zernike polynomials: a guide”, en, *Journal of Modern Optics*, t. 58, n° 7, p. 545-561, avr. 2011, issn : 0950-0340, 1362-3044. doi : 10.1080/09500340.2011.554896. adresse : http://www.tandfonline.com/doi/abs/10.1080/09500340.2011.554896 (visité le 19/12/2022).

[101] A. Jain et D. N. Gupta, “Optimization of electron bunch quality using a chirped laser pulse in laser wakefield acceleration”, *Physical Review Accelerators and Beams*, t. 24, n° 11, p. 111 302, 2021.

[102] S. Payeur, S. Fourmaux, J. C. Kieffer et S. Maclean, *Pulse compression in chirped pulse laser systems*, US Patent 10,396,522, août 2019.

[103] P. Tournois, “Acousto-optic programmable dispersive filter for adaptive compensation of group delay time dispersion in laser systems”, *Optics communications*, t. 140, n° 4-6, p. 245-249, 1997.

[104] B. Aurand et al., “A setup for studies of laser-driven proton acceleration at the Lund Laser Centre”, *Laser and Particle Beams*, t. 33, n° 1, p. 59-64, 2015.

[105] A. V. Kudryashov, V. V. Samarkin et A. Aleksandrov, “Adaptive optical elements for laser beam control”, in *Spatial Light Modulators: Technology and Applications*, International Society for Optics et Photonics, t. 4457, 2001, p. 170-178.

[106] Z. Liao, “Wavefront correction on high repetition rate, high energy laser system”, in *The Advanced Maui Opticalvand Space Surveillance Technologies Conference, Wailea*, 2006, E32.

[107] K. Svendsen, “Applications of Laser-Plasma Acceleration”, PhD Thesis, Lund University, 2022.

[108] *Explore IR-Apollon in 3D*. adresse : https://my.matterport.com/show/?m=WzYCqomWH4o.

[109] J. Zou et al., “Design and current progress of the Apollon 10 PW project”, *High Power Laser Science and Engineering*, t. 3, 2015, Publisher: Cambridge University Press.

[110] D. Papadopoulos et al., “The Apollon 10 PW laser: experimental and theoretical investigation of the temporal characteristics”, *High Power Laser Science and Engineering*, t. 4, 2016.

[111] L. P. Ramirez, “Few-cycle OPCPA laser chain”, thèse de doct., Université Paris Sud-Paris XI, 2013.

[112] J.-C. M. Diels, J. J. Fontaine, I. C. McMichael et F. Simoni, “Control and measurement of ultrashort pulse shapes (in amplitude and phase) with femtosecond accuracy”, en, *Applied Optics*, t. 24, n° 9, p. 1270, mai 1985, issn : 0003-6935, 1539-4522. doi : 10.1364/AO.24.001270. adresse : https://opg.optica.org/abstract.cfm?URI=ao-24-9-1270 (visité le 07/12/2022).

[113] D. J. Kane et R. Trebino, “Characterization of arbitrary femtosecond pulses using frequency-resolved optical gating”, *IEEE Journal of Quantum Electronics*, t. 29, n° 2, p. 571-579, 1993.

[114] S. P. D. Mangles et al., “Controlling the spectrum of x-rays generated in a laser-plasma accelerator by tailoring the laser wavefront”, en, *Applied Physics Letters*, t. 95, n° 18, p. 181 106, nov. 2009, issn : 0003-6951, 1077-3118. doi : 10.1063/1.3258022. adresse : http://aip.scitation.org/doi/10.1063/1.3258022 (visité le 14/12/2022).

[115] S. Mishra, B. S. Rao, A. Moorti et J. A. Chakera, “Enhanced betatron x-ray emission in a laser wakefield accelerator and wiggler due to collective oscillations of electrons”, en, *Physical Review Accelerators and Beams*, t. 25, n° 9, p. 090 703, sept. 2022, issn : 2469-9888. doi : 10.1103/PhysRevAccelBeams.25.090703. adresse : https://link.aps.org/doi/10.1103/PhysRevAccelBeams.25.090703 (visité le 16/12/2022).

[116] P. Virtanen et al., “SciPy 1.0: Fundamental Algorithms for Scientific Computing in Python”, *Nature Methods*, t. 17, p. 261-272, 2020. doi : 10.1038/s41592-019-0686-2.

[117] J. Osterhoff et al., “Generation of Stable, Low-Divergence Electron Beams by Laser-Wakefield Acceleration in a Steady-State-Flow Gas Cell”, *Phys. Rev. Lett.*, t. 101, p. 085 002, 8 août 2008. doi : 10.1103/PhysRevLett.101.085002. adresse : https://link.aps.org/doi/10.1103/PhysRevLett.101.085002.

[118] M. Vargas et al., “Improvements to laser wakefield accelerated electron beam stability, divergence, and energy spread using three-dimensional printed two-stage gas cell targets”, *Applied Physics Letters*, t. 104, n° 17, p. 174 103, 2014.

[119] R. Garland et al., “Optimisation of the pointing stability of laser-wakefield accelerated electron beams”, *arXiv preprint arXiv:1407.6979*, 2014.

[120] M. Mirzaie et al., “Demonstration of self-truncated ionization injection for GeV electron beams”, *Scientific reports*, t. 5, n° 1, p. 1-9, 2015.

[121] T. Audet et al., “Gas cell density characterization for laser wakefield acceleration”, *Nuclear Instruments and Methods in Physics Research Section A: Accelerators, Spectrometers, Detectors and Associated Equipment*, t. 909, p. 383-386, 2018.

[122] H. G. Weller, G. Tabor, H. Jasak et C. Fureby, “A tensorial approach to computational continuum mechanics using object-oriented techniques”, *Computers in physics*, t. 12, n° 6, p. 620-631, 1998.

[123] D. R. Lide, *CRC handbook of chemistry and physics*. CRC press, 2004, t. 85.

[124] S. Velghe, J. Primot, N. Guérineau, M. Cohen et B. Wattellier, “Wave-front reconstruction from multidirectional phase derivatives generated by multilateral shearing interferometers”, *Optics letters*, t. 30, n° 3, p. 245-247, 2005, Publisher: Optical Society of America.

[125] J.-C. Chanteloup, “Multiple-wave lateral shearing interferometry for wave-front sensing”, *Applied optics*, t. 44, n° 9, p. 1559-1571, 2005, Publisher: Optical Society of America.

[126] R. K. Tyson et B. W. Frazier, *Principles of adaptive optics*. CRC press, 2022.

[127] G. Plateau et al., “Wavefront-sensor-based electron density measurements for laser-plasma accelerators”, *Review of Scientific Instruments*, t. 81, n° 3, p. 033 108, 2010, Publisher: American Institute of Physics.

[128] T. Fukuchi, Y. Yamaguchi, T. Nayuki, K. Nemoto et K. Uchino, “Development of a laser wavefront sensor for measurement of discharges in air”, *Electrical Engineering in Japan*, t. 146, n° 4, p. 10-17, 2004, Publisher: Wiley Online Library.

[129] Y. Inada, H. Matsumoto, S. Matsuoka, A. Kumada, H. Ikeda et K. Hidaka, “A Shack–Hartmann laser wavefront sensor for measuring electron density in low-current arc”, *Electrical Engineering in Japan*, t. 181, n° 4, p. 1-8, 2012, _eprint: https://onlinelibrary.wiley.com/doi/pdf/10.1 doi : https://doi.org/10.1002/eej.22319. adresse : https://onlinelibrary.wiley.com/doi/abs/10.1002/eej.22319.

[130] S. R. Deans, *Radon and Abel transforms*. 2000, t. 2, Publisher: CRC Press Boca Raton, FL.

[131] S. Gibson, D. D. Hickstein, R. Yurchak, M. Ryazanov, D. Das et G. Shih, *PyAbel/PyAbel: v0.9.0*, déc. 2022. doi : 10.5281/ZENODO.7438595. adresse : https://zenodo.org/record/7438595 (visité le 04/01/2023).

[132] N. Kanopoulos, N. Vasanthavada et R. L. Baker, "Design of an image edge detection filter using the Sobel operator", *IEEE Journal of solid-state circuits*, t. 23, n° 2, p. 358-367, 1988.

[133] K. T. Phuoc et al., "Imaging Electron Trajectories in a Laser-Wakefield Cavity Using Betatron X-Ray Radiation", en, *Physical Review Letters*, t. 97, n° 22, p. 225 002, nov. 2006, issn : 0031-9007, 1079-7114. doi : 10.1103/PhysRevLett.97.225002. adresse : https://link.aps.org/doi/10.1103/PhysRevLett.97.225002 (visité le 16/12/2022).

[134] P. Lee, G. Maynard, T. Audet, B. Cros, R. Lehe et J.-L. Vay, "Optimization of laser-plasma injector via beam loading effects using ionization-induced injection", *Physical Review Accelerators and Beams*, t. 21, n° 5, p. 052 802, 2018.

[135] T. Kurz et al., "Calibration and cross-laboratory implementation of scintillating screens for electron bunch charge determination", *Review of Scientific Instruments*, t. 89, n° 9, p. 093 303, 2018.

[136] D. Belohrad, M. Krupa, L. Søby et al., "A New Integrating Current Transformer for the LHC", *IBIC14, Monterey, USA (2014-these proceedings)*, 2014.

[137] A. Döpp, C. Eberle, S. Howard, F. Irshad, J. Lin et M. Streeter, *Data-driven Science and Machine Learning Methods in Laser-Plasma Physics*, 2022. eprint : arXiv:2212.00026.

[138] G. Carleo et al., "Machine learning and the physical sciences", *Reviews of Modern Physics*, t. 91, n° 4, p. 045 002, 2019, Publisher: APS.

[139] B. Djordjević et al., "Modeling laser-driven ion acceleration with deep learning", *Physics of Plasmas*, t. 28, n° 4, p. 043 105, 2021.

[140] R. Simpson, D. Mariscal, G. Williams, G. Scott, E. Grace et T. Ma, "Development of a deep learning based automated data analysis for step-filter x-ray spectrometers in support of high-repetition rate short-pulse laser-driven acceleration experiments", *Review of Scientific Instruments*, t. 92, n° 7, p. 075 101, 2021, Publisher: AIP Publishing LLC.

[141] K. Wang et al., "Deep learning wavefront sensing and aberration correction in atmospheric turbulence", en, *PhotoniX*, t. 2, n° 1, p. 8, déc. 2021, issn : 2662-1991. doi : 10.1186/s43074-021-00030-4. adresse : https://photoniX.springeropen.com/articles/10.1186/s43074-021-00030-4 (visité le 17/01/2023).

[142] K. Gurney, *An introduction to neural networks*. CRC press, 2018.

[143] P. Isola, J.-Y. Zhu, T. Zhou et A. A. Efros, "Image-to-image translation with conditional adversarial networks", in *Proceedings of the IEEE conference on computer vision and pattern recognition*, 2017, p. 1125-1134.

[144] I. Goodfellow et al., “Generative adversarial networks”, *Communications of the ACM*, t. 63, n° 11, p. 139-144, 2020.

[145] K. Cheng, R. Tahir, L. K. Eric et M. Li, “An analysis of generative adversarial networks and variants for image synthesis on MNIST dataset”, en, *Multimedia Tools and Applications*, t. 79, n° 19-20, p. 13 725-13 752, mai 2020, issn : 1380-7501, 1573-7721. doi : 10.1007/s11042-019-08600-2. adresse : http://link.springer.com/10.1007/s11042-019-08600-2 (visité le 13/01/2023).

[146] M. Mirza et S. Osindero, “Conditional Generative Adversarial Nets”, 2014, Publisher: arXiv Version Number: 1. doi : 10.48550/ARXIV.1411.1784. adresse : https://arxiv.org/abs/1411.1784 (visité le 17/01/2023).

[147] V. Vapnik, “An overview of statistical learning theory”, *IEEE Transactions on Neural Networks*, t. 10, n° 5, p. 988-999, sept. 1999, issn : 10459227. doi : 10.1109/72.788640. adresse : http://ieeexplore.ieee.org/document/788640/ (visité le 17/01/2023).

[148] C. K. Williams et C. E. Rasmussen, *Gaussian processes for machine learning*. MIT press Cambridge, MA, 2006, t. 2.

[149] S. Greenhill, S. Rana, S. Gupta, P. Vellanki et S. Venkatesh, “Bayesian Optimization for Adaptive Experimental Design: A Review”, *IEEE Access*, t. 8, p. 13 937-13 948, 2020, issn : 2169-3536. doi : 10.1109/ACCESS.2020.2966228. adresse : https://ieeexplore.ieee.org/document/8957442/ (visité le 06/01/2023).

[150] J. Görtler, R. Kehlbeck et O. Deussen, “A Visual Exploration of Gaussian Processes”, *Distill*, 2019. doi : 10.23915/distill.00017.

[151] *Illustration of prior and posterior Gaussian process for different kernels*, en. adresse : https://scikit-learn/stable/auto_examples/gaussian_process/plot_gpr_prior_posterior.html (visité le 18/01/2023).

[152] H. Ye et al., “Fast optimization for betatron radiation from laser wakefield acceleration based on Bayesian optimization”, *Results in Physics*, p. 106 116, 2022.

[153] S. Jalas et al., “Bayesian optimization of a laser-plasma accelerator”, *Physical review letters*, t. 126, n° 10, p. 104 801, 2021.

[154] F. Irshad, S. Karsch et A. Döpp, “Multi-objective and multi-fidelity Bayesian optimization of laser-plasma acceleration”, *arXiv preprint arXiv:2210.03484*, 2022.

[155] Z. Lv et al., “Photonic crystal rod-based high-performance ultrafast fiber laser system”, *High Power Laser Science and Engineering*, t. 8, 2020.

[156] J. M. Dawson, “Particle simulation of plasmas”, en, *Reviews of Modern Physics*, t. 55, n° 2, p. 403-447, avr. 1983, issn : 0034-6861. doi : 10.1103/RevModPhys.55.403. adresse : https://link.aps.org/doi/10.1103/RevModPhys.55.403 (visité le 27/12/2022).

[157] F. Massimo et al., “Efficient start-to-end 3D envelope modeling for two-stage laser wakefield acceleration experiments”, *Plasma Physics and Controlled Fusion*, t. 61, n° 12, p. 124 001, déc. 2019, issn : 0741-3335, 1361-6587. doi : 10.1088/1361-6587/ab49cf. adresse : https://iopscience.iop.org/article/10.1088/1361-6587/ab49cf (visité le 13/01/2023).

[158] F. Massimo, A. Beck, J. Derouillat, I. Zemzemi et A. Specka, “Numerical modeling of laser tunneling ionization in particle-in-cell codes with a laser envelope model”, *Phys. Rev. E*, t. 102, p. 033 204, 3 sept. 2020. doi : 10.1103/PhysRevE.102.033204. adresse : https://link.aps.org/doi/10.1103/PhysRevE.102.033204.

[159] F. contributors, *FBPIC*, https://github.com/fbpic, 2023.

[160] R. Lehe, M. Kirchen, I. A. Andriyash, B. B. Godfrey et J.-L. Vay, “A spectral, quasi-cylindrical and dispersion-free Particle-In-Cell algorithm”, *Computer Physics Communications*, t. 203, p. 66-82, 2016.

[161] A. Lifschitz, X. Davoine, E. Lefebvre, J. Faure, C. Rechatin et V. Malka, “Particle-in-Cell modelling of laser–plasma interaction using Fourier decomposition”, *Journal of Computational Physics*, t. 228, n° 5, p. 1803-1814, 2009, issn : 0021-9991. doi : https://doi.org/10.1016/j.jcp.2008.11.017. adresse : https://www.sciencedirect.com/science/article/pii/S0021999108005950.

[162] P.-L. Bourgeois et X. Davoine, “New mitigation approach to numerical Cherenkov radiation in PIC simulations of wakefield accelerators”, en, *Journal of Computational Physics*, t. 413, p. 109 426, juill. 2020, issn : 00219991. doi : 10.1016/j.jcp.2020.109426. adresse : https://linkinghub.elsevier.com/retrieve/pii/S002199912030200X (visité le 07/01/2023).

[163] M. Kirchen, R. Lehe, S. Jalas, O. Shapoval, J.-L. Vay et A. R. Maier, “Scalable spectral solver in Galilean coordinates for eliminating the numerical Cherenkov instability in particle-in-cell simulations of streaming plasmas”, en, *Physical Review E*, t. 102, n° 1, p. 013 202, juill. 2020, issn : 2470-0045, 2470-0053. doi : 10.1103/PhysRevE.102.013202. adresse : https://link.aps.org/doi/10.1103/PhysRevE.102.013202 (visité le 07/03/2023).

[164] M. Kirchen et al., “Stable discrete representation of relativistically drifting plasmas”, *Physics of Plasmas*, t. 23, n° 10, p. 100 704, 2016.

[165] J.-L. Vay, “Noninvariance of space-and time-scale ranges under a Lorentz transformation and the implications for the study of relativistic interactions”, *Physical review letters*, t. 98, n° 13, p. 130 405, 2007, Publisher: APS.

[166] R. Trebino et al., “Measuring ultrashort laser pulses in the time-frequency domain using frequency-resolved optical gating”, *Review of Scientific Instruments*, t. 68, n° 9, p. 3277-3295, 1997.

[167] T. Audet et al., “Electron injector for compact staged high energy accelerator”, *Nuclear Instruments and Methods in Physics Research Section A: Accelerators, Spectrometers, Detectors and Associated Equipment*, t. 829, p. 304-308, 2016.

[168] J. Björklund Svensson, “Extreme Electron Beams and Brilliant X-rays: Generation, Manipulation and Characterization of Relativistic Electron Beams for and from Plasma-Based Accelerators”, Defence details Date: 2020-09-25 Time: 9:15 Place: Lecture hall Rydbergsalen, Fysiska institutionen, Professorsgatan 1, Faculty of Engineering LTH, Lund University, Lund., thèse de doct., Lund University, sept. 2020, isbn : 978-91-7895-618-0.

[169] J.-L. Vay, “Noninvariance of space-and time-scale ranges under a Lorentz transformation and the implications for the study of relativistic interactions”, *Physical review letters*, t. 98, n° 13, p. 130 405, 2007.

[170] P. Lee, G. Maynard, T. L. Audet, B. Cros, R. Lehe et J.-L. Vay, “Dynamics of electron injection and acceleration driven by laser wakefield in tailored density profiles”, *Phys. Rev. Accel. Beams*, t. 19, p. 112 802, 11 nov. 2016. doi : 10.1103/PhysRevAccelBeams.19.112802. adresse : https://link.aps.org/doi/10.1103/PhysRevAccelBeams.19.112802.

[171] P. San Miguel Claveria et al., “Betatron radiation and emittance growth in plasma wakefield accelerators”, en, *Philosophical Transactions of the Royal Society A: Mathematical, Physical and Engineering Sciences*, t. 377, n° 2151, p. 20 180 173, août 2019, issn : 1364-503X, 1471-2962. doi : 10.1098/rsta.2018.0173. adresse : https://royalsocietypublishing.org/doi/10.1098/rsta.2018.0173 (visité le 03/03/2023).

[172] T. Mehrling, J. Grebenyuk, F. Tsung, K. Floettmann et J. Osterhoff, “Transverse emittance growth in staged laser-wakefield acceleration”, *Physical Review Special Topics-Accelerators and Beams*, t. 15, n° 11, p. 111 303, 2012.

[173] R. Lehe, C. Thaury, E. Guillaume, A. Lifschitz et V. Malka, “Laser-plasma lens for laser-wakefield accelerators”, *Phys. Rev. ST Accel. Beams*, t. 17, p. 121 301, 12 déc. 2014. doi : 10.1103/PhysRevSTAB.17.121301. adresse : https://link.aps.org/doi/10.1103/PhysRevSTAB.17.121301.

[174] X. Li, A. Chancé et P. A. P. Nghiem, “Preserving emittance by matching out and matching in plasma wakefield acceleration stage”, *Phys. Rev. Accel. Beams*, t. 22, p. 021 304, 2 fév. 2019. doi : 10.1103/PhysRevAccelBeams.22.021304. adresse : https://link.aps.org/doi/10.1103/PhysRevAccelBeams.22.021304.

[175] W. Lu et al., “A nonlinear theory for multidimensional relativistic plasma wave wakefields”, *Physics of Plasmas*, t. 13, n° 5, p. 056 709, 2006.

[176] D. Jasrasaria et E. O. Pyzer-Knapp, “Dynamic control of explore/exploit trade-off in bayesian optimization”, in *Science and Information Conference*, Springer, 2018, p. 1-15.

[177] B. S. Rao, A. Moorti, P. A. Naik et P. D. Gupta, “Effect of chirp on self-modulation and laser wakefield electron acceleration in the regime of quasimonoenergetic electron beam generation”, en, *Physical Review Special Topics - Accelerators and Beams*, t. 16, n° 9, p. 091 301, sept. 2013, issn : 1098-4402. doi : 10.1103/PhysRevSTAB.16.091301. adresse : https://link.aps.org/doi/10.1103/PhysRevSTAB.16.091301 (visité le 15/12/2022).

[178] I. Roman, R. Santana, A. Mendiburu et J. A. Lozano, “Dynamic kernel selection criteria for Bayesian optimization”, in *BayesOpt 2014: NIPS Workshop on Bayesian Optimization*, 2014.

[179] W. Wang et al., “Free-electron lasing at 27 nanometres based on a laser wakefield accelerator”, *Nature*, t. 595, n° 7868, p. 516-520, 2021.

[180] G. Sarri et al., “Generation of neutral and high-density electron–positron pair plasmas in the laboratory”, *Nature communications*, t. 6, n° 1, p. 1-8, 2015.

[181] *Wizzler - ultrafast pulse measurement - Fastlite*, fr-FR. adresse : https://fastlite.com/produits/wizzler-ultrafast-pulse-measurement/ (visité le 23/01/2023).

[182] T. L. Audet et al., “Ultrashort, MeV-scale laser-plasma positron source for positron annihilation lifetime spectroscopy”, *Physical Review Accelerators and Beams*, t. 24, n° 7, p. 073 402, 2021.

[183] H. Choi, M. Chae, S. Park et H. Kang, “Introduction to the Test Result of Turbo-ICT in PAL-ITF”, *Proc. of IBIC*, 2014.

[184] F. Stulle, J. Bergoz, W. Leemans et K. Nakamura, “Single pulse sub-picocoulomb charge measured by a turbo-ICT in a laser plasma accelerator”, *IBIC2016 Proc., JACoW Publishing*, p. 119-22, 2016.

Appendix

Preprint : *Realistic driver modelling of laser wakefield electrons acceleration at APOLLON Research Facility*, I. Moulanier, L. T. Dickson *et al.*

Modelling of the driver transverse profile for laser wakefield electron acceleration at APOLLON Research Facility

I. Moulanier[1], L.T. Dickson[1], C. Ballage[1], O. Vasilovici[1], A. Gremaud[1], S. Dobosz Dufrénoy[2], N. Delerue[3], L. Bernardi[4], A. Mahjoub[4], A. Cauchois[4], A. Specka[4], F. Massimo[1], G. Maynard[1], B. Cros[1]
1 LPGP, CNRS, Université Paris Saclay, 91405 Orsay, France
2 CEA, CNRS, LIDYL, Université Paris Saclay, 91190 Gif sur Yvette, France
3 IJCLAB, CNRS, Université Paris Saclay, 91405 Orsay, France
4 LLR, CNRS/IN2P3, Ecole Polytechnique, Institut Polytechnique de Paris, 91120 Palaiseau, France and
*Corresponding author : I. Moulanier, ioaquin.moulanier@universite − paris − saclay.fr
(Dated: April 13, 2023)

The quality of electron bunches accelerated by laser wakefields is highly dependant on the temporal and spatial features of the laser driver. Analysis of experiments performed at APOLLON PW-class laser facility shows that spatial instabilities of the focal spot, such as shot-to-shot pointing fluctuations or asymmetry of the transverse fluence, lead to charge and energy degradation of the accelerated electron bunch. It is shown that PIC simulations can reproduce experimental results with a significantly higher accuracy when the measured laser asymmetries are included in the simulated laser's transverse profile, compared to simulations with ideal, symmetric laser profile. A method based on a modified Gerchberg-Saxton iterative algorithm is used to retrieve the laser electric field from fluence measurements in vacuum in the focal volume, and accurately reproduce experimental results using PIC simulations, leading to simulated electron spectra in close agreement with experimental results, for the accelerated charge, energy distribution and pointing of the electron beam at the exit of the plasma.

I. INTRODUCTION

In the process of Laser WakeField Acceleration (LWFA) [1, 2], an ultra-high intensity laser is focused inside a gas target, ionises the medium and creates a trailing perturbation in its wake in an underdense plasma. The generated plasma cavity sustains intense longitudinal and transverse electric fields that can trap, accelerate and focus bunches of electrons to the GeV range [3] within a few cm. Injection of plasma electrons makes LWFA a compact option for the generation of relativistic electron sources. However, despite numerous studies, the use of electron beams from LWFA for application is impeded by insufficient beam quality and stability. Therefore, detailed diagnostics, realistic modelling and analysis are needed to achieve a precise understanding of the key mechanisms controlling laser plasma interaction in experiments.

The main schemes for injection of plasma electrons into the plasma wave are self-injection [4] and ionization injection [5–8]. In LWFA experiments with PW-class laser drivers, both injection schemes can occur in the so-called bubble regime [9], in which the ponderomotive force of the laser repels plasma electrons from its propagation axis, generating an electron-free cavity behind the laser pulse. In the process of self-injection, a portion of the expelled plasma electrons travels around the cavity before getting trapped in the wakefield [10]. In ionization injection, the gas target is a mixture of light atomic species, typically hydrogen, ionized early before the peak of the laser pulse, and of a dopant species, e.g. nitrogen, presenting an energy-gap in its ionization potential structure [7], leading to ionization of some electrons close to the peak of the laser pulse.

With peak intensities above $I_0 = 10^{18}$ W/cm^2, the pulse temporal front ionises hydrogen and nitrogen up to N^{5+}. Remaining nitrogen L-shell electrons are primarily born around laser peak intensities, inside the bubble [11]. Ionization injection has several properties of interest for tuning electron injection and trapping, and favors highly charged electron beams. It operates at an intensity below self-injection [8] and the two mechanisms can be optimized in different parameter areas. As ionization injection depends on the local intensity of the laser pulse, it can be particularly sensitive to laser beam quality and its evolution during propagation in the evolving plasma density. These properties can be used to control the injection process in electron density tailored profile or diagnose laser beam quality. The electron beam charge can be increased by increasing the driving laser power, providing a large range of parameters to explore for optimising the properties of laser driven electron sources with PW class short pulse laser facilities.

This complex nonlinear physics is described using particle in cell (PIC) simulations [12], using as input parameters the laser temporal and spatial shapes, and the gas density profile. Experimentally achieved laser beams often differ from perfectly symmetrical distributions. So, in order to understand the role of laser imperfections on the quality of the produced electron bunches, and compare to experimental results, refined PIC simulations describing realistically the injection and acceleration physics occurring at the ps scale were performed. These realistic

simulations require a proper description of the gas density profile, as well as of the driver (laser profile transverse asymmetries) to accurately reproduce laser-plasma interactions affecting the electron beams characteristics. For instance, laser asymmetries have been shown to lead to asymmetric wakefields affecting the output accelerated electron beam, with characteristics directly correlated to the laser stability and quality [13–17].

In this paper the method used to analyze characteristic results obtained during commissioning experiments at APOLLON PW facility [18] is presented. Focusing the F_2 laser beam at 0.4 PW in the long focal area inside a gas cell [19], experiments were performed to characterize laser beam quality and evaluate its impact on electron properties.

It is shown that PIC simulations can reproduce experimental results with a significantly higher accuracy when the measured laser asymmetries are included in the simulated laser's transverse profile. This enhanced agreement is meant in comparison with simulations with an ideal, axisymmetric laser profile, which is often used in the design stage of LWFA experiments and in preliminary experimental analyses. The results described in this work thus show the importance of more realistic initial conditions in numerical modeling used for these studies. The simulation results shown in this work were obtained with the quasi-3D PIC code FBPIC [20], but the same method can be applied with other PIC codes in quasi-3D [21] or full 3D geometry.

In comparison to previous investigations made with realistic PIC simulations in [14], this work uses an alternative fast Gerchberg-Saxton algorithm [22] based on mode decomposition to reconstruct the laser field, which allows to simulate with accuracy an experimental electron bunch spectrum in the energy-angle plane. This method has already been used to present experimental results in [15], in a regime with a lower peak laser intensity and characterised by a more stable transverse laser profile from shot-to-shot. Besides, in this work the physical effects of the realistic laser driver (in particular its asymmetries) on the electron injection in the bubble are described. An agreement between realistic numerical modeling and experiment is obtained also in the electron beam spectra in the energy-angle plane. Furthermore, the realistic simulations in [14] have been performed in 3D, while the realistic simulations of this work were performed in quasi-3D geometry [21], highlighting that high-fidelity simulations can be obtained also with this less computationally-demanding technique for preliminary analyses.

The remainder of this paper is organized as follows. Characteristic experimental results are presented in section II. The method used to retrieve the laser electric field from experimentally recorded fluence images is described in section III, followed by the description of the method to generate data to initialize FBPIC simulations. A comparison of experimental and numerical electron spectra is discussed in section IV.

II. EXPERIMENTAL RESULTS

An experiment was performed in April 2021 during the commissioning phase of the long focal area of APOLLON facility, to characterize laser beam quality inside the experimental area and evaluate its impact on electron beam quality.

After compression, the F_2 laser beam was transported into the experimental area and focused in vacuum using an on-axis spherical mirror 3 m focal length), after reflection from a turning mirror with a hole, as illustrated in Fig. 1.

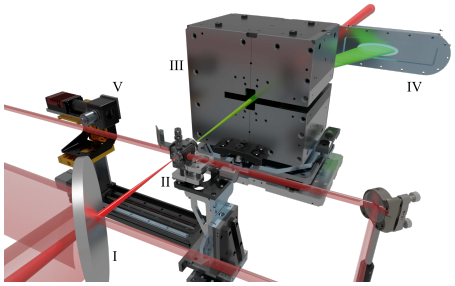

FIG. 1 : Schematic of experimental set-up : the driver laser beam (in red) is focused through the turning mirror (I) at the entrance of the gas cell (II), generating a diverging electron bunch (in green) at the exit. The electron bunch is then deflected by a magnetic dipole (III) and sent onto a LANEX screen (IV) to measure its Energy-Angle distribution. A small percentage of the laser driver is used to probe the plasma density transversely. Vacuum imaging of the focal volume is completed with a CCD (V).

The central part of the laser beam incident on the turning mirror was collected and used partly to monitor the laser beam energy from shot-to-shot using a leak through a wedge and a calorimeter. The remainder of the laser beam was used as a probe laser to diagnose plasma density transversely to the main pulse. The relative probing time was controlled by an in vacuum delay stage.

For this experiment, the APOLLON F_2 Ti : Sa laser with a central wavelength $\lambda = 0.8$, μm was measured to deliver a pulse with a FWHM intensity duration $\tau_{FWHM} = 25$ fs, a post-compression energy from $E_l = 5$ to 10 J, with a repetition rate of 1 shot per minute. The peak intensity estimated in the ideal Gaussian transverse profile approximation in vacuum is 5×10^{19} W/cm^2. The laser beam was focused inside a 6 mm long gas cell [19] filled with a mixture of 99% H_2 and 1% N_2. Electrons were trapped through ionization, accelerated in the wakefield. After plasma exit, their energy was measured using a dipole magnet and LANEX screen imaged onto a CCD camera. The spectrum was recorded in the $300 - 900$ MeV energy range within a ± 20 mrad viewing angle.

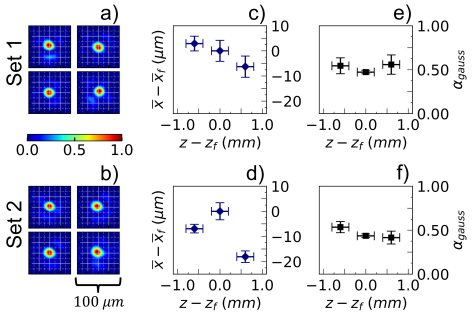

FIG. 2 : Measured laser beam stability during 2 sequences of multiple vacuum shots taken on 2 separate days with laser settings 1 and 2: (a) and (b) laser fluence of 4 consecutive shots measured in the focal plane; (c) and (d) $\overline{x} - \overline{x}_f$, laser beam relative centroid in the xOz plane, with respect to the focal plane centroid, for three positions $z - z_f$ along the laser propagation axis; the data for $z = z_f$ is from the 4 fluence images of (a) and (b), while the other points are data collected from 2 separate shots at each position; (e) and (f) fraction of energy α_{gauss} inside a Gaussian fit of waist w_0. Error bars along z come from the determination of the focal plane z_f.

The laser beam was characterized in detail in the focal volume every day prior to shots on the gas-filled target. Using a movable CCD camera in vacuum, the laser energy distribution was measured inside the interaction chamber before, at and after focus. The Rayleigh length in vacuum, defined as $z_R = (\pi w_0^2)/\lambda$, with w_0 the $1/e^2$ radius of the focal plane intensity, was $z_R = 1$ mm. The waist of a Gaussian best fit in the focal plane is $w_0 = 16.6 \pm 0.3$ μm. Fig. 2 shows 2 sets of data taken on two different days, illustrating instabilities both in laser pointing and in spatial fluence symmetry between consecutive shots and for different days. Fig. 2.(a) and (b) show the fluence distribution in the focal plane $z = z_f$. Fig. 2.(c) and (d) show the shot-to-shot transverse centroid displacement fluctuations $\overline{x} - \overline{x}_f$ in the focal volume (vertical error bars). The horizontal error bars come from the determination of the focal plane z_f. The xOz plane is the plane where electrons centroid fluctuations have been measured, perpendicularly to the laser polarisation plane yOz. Fig. 2.(c) and (d) underline instabilities of the laser centroid in both cases. For Set 1 data the centroid is moving linearly, going from $+3$ μm at $z - z_f = -0.6$ mm to -6 μm at $z - z_f = +0.6$ mm. Set 2 data show larger fluctuations $\overline{x} - \overline{x}_f = -7$ μm at $z - z_f = -0.6$ mm and $\overline{x} - \overline{x}_f = -18$ μm at $z - z_f = +0.6$ mm. Multi-directional fluctuations of the centroid around the focal plane are the signature of a non zero temporal phase and the asymmetry of the laser fluence.

In Fig. 2.(e) and (f), α_{gauss}, defined as the fraction of total energy inside a Gaussian fit with waist w_0, is plotted as a function of position in the focal volume. Values of α_{gauss} at $z \neq z_f$ are calculated using a waist $w(z) = w_0[1+(z/z_R)^2]^{1/2}$ for the Gaussian fit. At $z = z_f$, α_{gauss} is averaging 46 % for Set 1 and 40 % for Set 2. This demonstrates that the experimental fluence departs significantly from a perfect Gaussian approximation in both cases.

Figure 3 shows the average of 10 consecutive electron bunch spectra measured on the same day as Fig. 2 Set 1, in yOx, also defined as the $Energy - \theta_x$ angle plane. The average bunch charge measured between 300 and

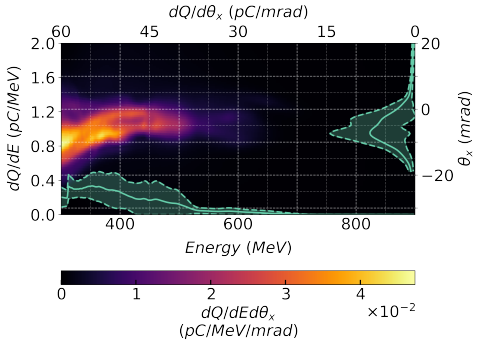

FIG. 3 : Average electron spectrum of 10 consecutive shots acquired the same day as Fig. 2 Set 1 laser measurements for an average plasma electron density $\overline{n}_0 = 2.2 \times 10^{18}$ cm^{-3}. The color scale shows the spectral charge density in the $Energy - \theta_x$ angle plane. The full green line along the $Energy$ axis is the average spectral charge density, dQ/dE, profile (scale on left vertical axis) calculated within ± 3 mrad around each individual maximum $dQ/d\theta_x$. The full green line along the θ_x axis (right-handside vertical axis) represents the average $dQ/d\theta_x$ profile (scale on the top horizontal axis) integrated over energy. The green areas are the confidence intervals bounded by the standard deviation extremes (dashed curves). $\theta_x = 0$ corresponds to the laser axis alignment position in vacuum.

900 MeV and within ± 20 mrad is $\overline{Q}_{tot} = 95 \pm 46$ pC. For this sequence, the mean measured laser energy is $\overline{E}_l = 4.8 \pm 0.2$ J, and average plasma electron density $\overline{n}_0 = 2.2 \pm 0.2 \times 10^{18}$ cm^{-3}. The measured charge fluctuations are $\delta\overline{Q}_{tot}/\overline{Q}_{tot} = 47$ %, which shows a clear sensitivity to input parameters.

III. MODELLING OF THE LASER BEAM

The analysis and implementation of the laser experimental data into PIC simulations are performed in three steps. First, the laser electric field is retrieved from of the measured fluence data. Then, the reconstructed laser electric field is represented as a mode sum of fields that are used as parameters at the start of PIC simulations.

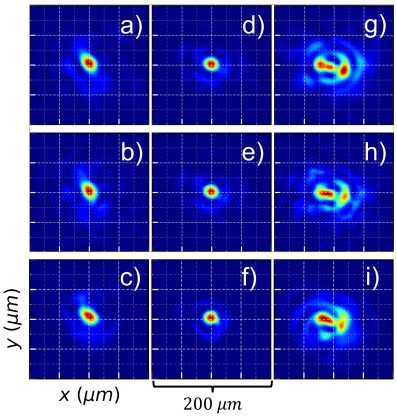

FIG. 4 : Experimental laser fluence measured in the focal volume (upper row), corresponding Hermite-Gaussian reconstruction (middle row), Laguerre-Gauss fit with $L = 3$ and $M = 40$ used in simulations (lower row): (a), (b) and (c) $z - z_f = -1.8$ mm - (d), (e) and (f) $z - z_f = +0$ mm - (g), (h) and (i) $z - z_f = +1.2$ mm. Each distribution has been normalized by its peak fluence.

Finally, the calculated electron parameters at the end of each simulation are compared with measured results.

A. Fit of the laser electric field

A modified version of the reconstructive Gerchberg-Saxton algorithm (GSA) [22], described in Appendix A, was used to retrieve the laser electric field corresponding to the laser fluence measured at 3 positions : $z - z_f = 0, +1.2, -1.8$ mm.

The algorithm was used in particular to retrieve an unknown phase map, $\psi(x, y)$, associated to a set of fluence images measured at different positions $(z_0, z_1 ... z_{k_{max}})$.

We selected laser data from the same day as Fig. 2 Set 1, which exhibit better focal spot stability than Set 2, to reconstruct a realistic laser electric field distribution. For each position, the corresponding fluence distribution has been re-centered around the origin in order to reduce in advance the shot-to-shot fluctuations error. The selected experimental distributions (upper row) and results of the fit algorithm (middle row) are plotted in Fig. 4.

Using a combination of low order fit to establish an educated guess, then refining the optimization with a higher order Hermite-Gaussian modes projection, a realistic reconstructed distribution is calculated as represented in Fig.4, (middle row).

The laser fluence reconstructed with Laguerre-Gauss modes is plotted in Fig. 4 (lower row) and shows a relatively good agreement between the reconstructed Laguerre-Gauss distribution and the experimental laser data.

B. PIC Simulation set-up

Due to the cylindrical representation used in FBPIC, the reconstructed Hermite-Gauss laser electric field $\mathrm{E_{HG}}(r, \theta, z_f)$ is projected on Laguerre-Gauss modes [23] in the focal plane $z = z_f$:

$$C_{l,m} = \int_{r=0}^{r_{max}} \int_{\theta=0}^{2\pi} r\, dr\, d\theta \;\; \mathrm{E_{HG}}(r, \theta, z_f) \times \mathrm{LG}^*_{l,m}(r, \theta, z_f)(r, \theta, z_f, r_{0,opt}, \theta_{0,opt}, w_{0r}) \quad (1)$$

with $C_{l,m}$ the complex amplitudes of the $\mathrm{LG}_{l,m}$ Laguerre-Gauss modes, l the azimuthal order, m the radial order, * the complex conjugate operator, $w_{0r} = (w_{0x}^2 + w_{0y}^2)^{1/2}$ the projection waist, $(r_{0,opt}, \theta_{0,opt})$ the GSA cycle optimized origins in cylindrical coordinates at $z = z_f$ and $r_{max} = \min(\Delta X/2, \Delta Y/2)$. The rectangular grid length along each axis is denoted by $(\Delta X, \Delta Y)$.

For a given number M of radial modes, the quality of the Laguerre-Gauss projection as a function of the number of azimuthal modes taken into account (azimuthal order L) is evaluated by calculating ϵ_{fit}, the integral error, defined as :

$$\epsilon_{fit} = \frac{\int_{r=0}^{r_{max}} \int_{\theta=0}^{2\pi} r\, dr\, d\theta\, |F_{\mathrm{HG}}(r, \theta, z_f) - F_{\mathrm{LG}}(r, \theta, z_f)|}{\int_{r=0}^{r_{max}} \int_{\theta=0}^{2\pi} r\, dr\, d\theta\, F_{\mathrm{HG}}(r, \theta, z_f)} \quad (2)$$

with $F_{\mathrm{LG}}(r, \theta, z_f)$ the normalized fluence of the Laguerre-Gauss modes, $F_{\mathrm{HG}}(r, \theta, z_f)$ the normalized fluence of the Hermite-Gauss modes from the laser electric field fit, both in the focal position $z = z_f$.

The integral error ϵ_{fit} decreases with the integration radius r_{max} for a fixed set of LG modes. ϵ_{fit} was calculated for an effective interaction radius, r_{eff}, to evaluate the quality of the Laguerre-Gauss fit near the peak fluence of the reconstructed profile. As injection and acceleration of electrons both occur within a characteristic radius around the laser centroid, on a scale of the order of the bubble radius $R_b \propto w_0$ [24], we set $r_{eff} = R_b$ and evaluate the error for $r \leq r_{eff}$ to measure the accuracy of the fit. In PIC simulations performed with a perfect Gaussian laser, the plasma cavity has values of R_b ranging from 15 to 20 μm. Therefore, we set $r_{eff} = 20$ μm as the value corresponding to the maximum observed bubble radius.

Figure 5 shows the evolution of ϵ_{fit} for $M = 40$ and L ranging from 0 to 10. The error of the fit converges towards $\epsilon_{fit} = 0$ both within r_{eff} and $r_{max} = 200$ μm as the number of azimuthal modes used for projection increases. A share of 43 % of the total energy is contained within the first mode $L = 0$ within a radius r_{eff},

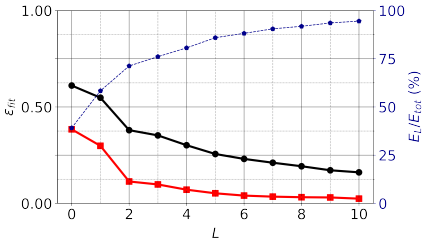

FIG. 5 : Integral error ϵ_{fit} for $M = 40$ radial modes, as a function of the maximum number of azimuthal modes L. Red squares: ϵ_{fit} calculated in a disk of radius $r_{eff} = 20$ μm; black circles: ϵ_{fit} calculated in a disk of radius $r_{max} = 200$ μm; blue diamonds (vertical axis on the right): cumulative energy fraction included in each configuration.

which shows that the remainder is contained within non-symmetrical azimuthal modes.

The number of azimuthal modes for the Laguerre-Gauss harmonics needs $N = 5$ azimuthal modes to be simulated with the azimuthal harmonics of type $\exp\{-in\theta\}$ used in quasi-3D geometry [21]. In addition, the number of macro-particles per cell in the simulations in this work has been increased with the number of azimuthal modes to maintain a constant signal to noise ratio (whose value in quasi-3D simulations is discussed in [21]). As a result, the computational time required for a simulation with a Laguerre-Gauss laser field is increased due to the increased number of modes and of macro-particles per cell. Every simulation in this work with a Laguerre-Gauss sum laser profile used $L = 3$ and $M = 40$, which reproduces 75% of the total energy according as shown in Fig. 5. For $L >3$, the fit error ε_{fit} decreases slowly compared to the increase in computational time associated to the corresponding number of modes.

All numerical results presented in this paper were obtained with input parameters in the same range as those of the data shown in Fig. 3. The simulated laser beam has a FWHM duration $\tau_{FWHM,sim} = 25$ fs (Gaussian temporal profile) and the focal plane fluence is fitted with a Gaussian waist $w_{0,sim} = 16$ μm. The laser is propagated over 10 mm in a gas cell filled with $99\,\%H_2 - 1\,\%N_2$ gas, including a starting 1.4 mm up-ramp from $n = 0$ to a density plateau of $n = n_{0,sim}$, as well as a down-ramp to $n = 0$ from $ct = 7.4$ mm to $ct = 10$ mm. The plasma density longitudinal profile profile is inferred from OpenFOAM simulations [19]. For both Gaussian and realistic simulations, the laser driver is focused onto the start of the density plateau at $z_f = 1.4$ mm.

For simulations using the Gaussian profile, the energy was fixed at $E_{l,sim} = \alpha_{gauss} \times E_l$, with $\alpha_{gauss} = 0.46$ the value calculated in Fig. 2.(e) at $z = z_f$. For simulations using the Laguerre-Gauss profile, simulated with $L = 3$ and $M = 40$, $E_{l,sim} = 0.75 \times E_l$.

The simulation grid is represented along z by $N_z = 3000$ points with an increment $\Delta z = 0.025$ μm, and along r by $N_r = 1100$ points with an increment $\Delta r = 0.2$ μm.

In the simulations with the reconstructed laser field profile, each population of H_2 and N_2 was simulated with $[P_z, P_r, P_\theta] = [2, 2, 16]$ macro-particles per cell along z, r and θ respectively. In the following, these simulations will be referred to as "realistic simulations".

Instead, every simulation using a perfect Gaussian laser profile was performed with $N_m = 2$ azimuthal modes. For these simulations, each population of H_2 and N_2 was simulated with $[P_z, P_r, P_\theta] = [2, 2, 4]$ macro-particles per cell.

IV. REALISTIC PIC SIMULATIONS RESULTS

A. Influence of Laser Asymmetry on Electron Beam Spectra

To understand the physical impact of laser asymmetry on the electron bunch quality, realistic simulations were performed with FBPIC using the reconstructed laser driver retrieved from fluence distributions shown in Fig. 4. Input parameters were set as described in the previous section, and the electron density was fixed to $n_{0,sim} = 2.1 \times 10^{18}$ cm^{-3}.

For the sake of comparison between simulation and experimental results, 5 electron spectra are shown in Fig. 6: (a) simulation with a Gaussian laser driver, (b) simulation with a Laguerre-Gauss laser driver using distribution described by Figs. 4 and 5, both with electron density $n_{0,sim} = 2.1 \times 10^{18}$ cm^{-3}, and (c) to (e) experimental spectra (single instances of the data shown in Fig. 3) measured with electron densities $n_0 = 2.1 \times 10^{18}$ cm^{-3} for (c) and (e), $n_0 = 2 \times 10^{18}$ cm^{-3} for (d) and laser energy $E_l = 4.7$ J for (c) to (e). The total charge of the average of the experimental spectra from (c) to (e) is 111 pC, and their average central divergence is -6.6 mrad.

These results show that a Gaussian driver Fig. 6.(a) gives rise to a wide, high-energy, high-charge electron spectrum, peaked spatially on the laser axis. Using a realistic laser driver generates an off-axis electron beam with lower energy, lower charge, a structure in agreement with experimental results as shown in Fig. 6.(b) and (c) to (e), where all these spectra exhibit an off-axis $dQ/d\theta_x$ profile centered towards negative values. The final spectrum contains 20 % (0 %) of self-injected electrons for the Gaussian case (realistic cases).

Table I provides quantitative data for comparison of electron beam properties for the 3 cases shown in Fig. 6.(a) to (c). The total charge Q_{tot} is summed between ± 20 mrad and $300 - 900$ MeV. We define the exit angle $\theta_{x,max}$ as the angle at which the maximum $dQ/d\theta_x$ is reached. Within ± 3 mrad, peaks with center energy E_{peak}, FWHM width $\Delta E_{peak}/E_{peak}$, and FWHM charge Q_{peak}, are identified based on minimum peak prominence

Spectrum	Q_{tot}	$\theta_{x,max}$	Peak Label	E_{peak}	$\Delta E_{peak}/E_{peak}$	Q_{peak}	$dQ/dE\,max.$
Units	pC	mrad		MeV	%	pC	pC/MeV
Simulation Gauss	174	-0.3	**1**	556	3.2	7	0.38
			2	629	3.3	8	0.41
Simulation Laguerre-Gauss	109	-4.7	**1**	466	23.2	18	0.23
			2	632	8.6	5	0.11
Experimental Data	96	-3.8	**1**	424	20.3	17	0.21
			2	653	9.8	5	0.10

TABLE I : Comparison of electron properties retrieved from simulated (with ideal Gaussian and reconstructed laser profile) and experimental $\theta_x - E$ spectra shown in Fig. 6. Q_{tot} is the total charge on each Fig. 6 spectrum, $\theta_{x,max}$ the central divergence of the angular distribution, while the "peak" labelled quantities refer to the dQ/dE profiles that result from selection of $dQ/dEd\theta_x$ within a ± 3 mrad range around the maximum $dQ/d\theta_x$. $\Delta E_{peak}/E_{peak}$ is the energy spread FWHM for each peak, Q_{peak} is the FWHM charge contained within each peak and $dQ/dE\,max.$ is the maximum dQ/dE value reached within each peak.

$\delta_{dQ/dE} = 0.05$ pC/MeV and minimum base to base width $\delta_E = 45$ MeV. Values of Table I show that the results of the simulation with reconstructed laser field profile are in good agreement with the detailed electron beam structure measured in experiment, while the Gaussian simulation results in electron beam characteristics significantly different from the measured ones. Two major differences are Q_{tot} value, which is 45 % higher than the experimental data for the Gaussian case, and the overall dQ/dE structure which has a highest peak energy of 875 MeV against 653 MeV in the experimental data. The charge difference stems from the quality of the laser angular intensity profile as it is the only input difference between Gaussian and Laguerre-Gauss simulations.

The analysis of the evolution of laser symmetry during the propagation coupled to electron injection is discussed in the next section.

B. Evolution of the laser asymmetry and effects on electron dynamics

Figure 7 shows the simulated evolution of the laser beam and electron bunch characteristics in the xOz plane for the case with ideal Gaussian laser profile (left-hand column) and the case with the reconstructed laser field (right-hand column). It can be inferred from Fig. 7 that the evolution of laser asymmetry and maximum field amplitude define the conditions for electron injection and the dynamics of electron during the acceleration process in the plasma cavity.

Figures 7.(a) and (b) show the evolution of the laser driver in the plasma density profile. As the realistic simulated transverse distribution is asymmetric with respect to the focal plane and changes before and after $z = z_f$ (see Fig. 4), different spatial distortions occur during non-linear self-focusing inside the plasma.

To quantify the deviation from cylindrical symmetry of the transverse fluence $F(r,\theta)$ and track its evolution throughout the simulated propagation, we define an asymmetry coefficient σ_l [15] as :

$$\sigma_l = \int_{r=0}^{r_{max}} r\,dr \sqrt{\int_{\theta=0}^{2\pi} \left(d\theta \left(f(r,\theta) - \overline{f}(r)\right)\right)^2}, \qquad (3)$$

where the normalized laser fluence $f(r,\theta)$ is defined as

$$f(r,\theta) = \frac{F(r,\theta)}{\int_{r=0}^{r_{max}} \int_{\theta=0}^{2\pi} r\,dr\,d\theta\,F(r,\theta)}, \qquad (4)$$

and $\overline{f}(r)$ is the mean normalized fluence over θ. The integral origin $r = 0$ is defined as the position of the fluence maximum. By definition, σ_l converges towards 0 for a cylindrically symmetric fluence profile.

This asymmetry coefficient σ_l is plotted for the Gaussian laser profile and realistic laser profile in Fig. 7.(a) and (b) respectively as a function of position along propagation axis. Figure 7.(a) confirms that the Gaussian profile is angularly symmetric. In this ideal case σ_l undergoes variations between $0.5e{-}5$ and $2.5e{-}5$. In comparison, its variations in the simulation with realistic laser field profile are on a scale 10^2 times larger. In the realistic case (Fig. 7.(b)), the amplitude of the symmetry coefficient drops by 67 % between 600 μm and 2000 μm, the focal plane in the plasma being in the middle of this area. This reduction of σ_l is simultaneous with the increase of a_0, showing that tight focusing of the laser reduces its imperfections. In the realistic case, a_0 reaches values similar to the Gaussian a_0 through the first self-focusing due to a near Gaussian shape in its focal plane (Fig. 4.(d)). However, the asymmetry of the intensity around the focal plane and relatively short typical variation length ($z_R = 1$ mm) are responsible for a 1 mm shift of the maximum in comparison to the Gaussian symmetric pulse (Fig. 7.(a) and (b)).

Figures 7.(c) and (d) show line profiles of injected charge Q_{inj} (right hand-side vertical axis), and spectral

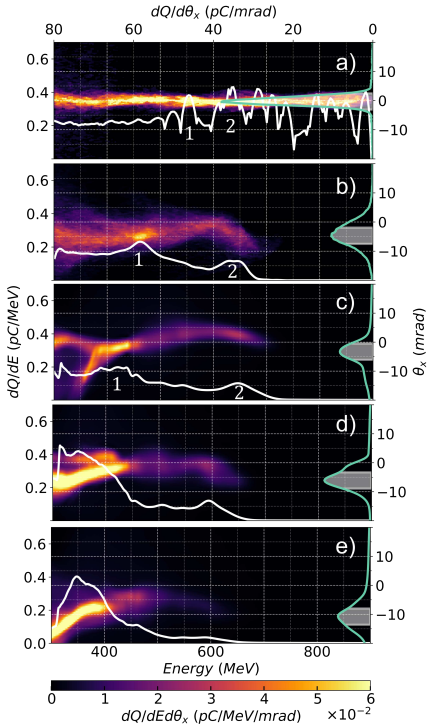

FIG. 6 : Electron bunch $dQ/dEd\theta_x$ spectral density in the energy θ_x divergence plane for 3 different cases : (a) Simulated Gaussian spectrum - (b) Simulated Laguerre-Gauss spectrum - (c) to (e) Single experimental spectra from Fig. 3.(a) sequence. White (green) lines represent spectral charge, dQ/dE, (divergence charge density $dQ/d\theta_x$) integrated over the divergence (energy) respectively. The shaded area under the green $dQ/d\theta_x$ line shows the range ± 3 mrad around the peak of $dQ/d\theta_x$, used to produce the dQ/dE curve and calculate the spectrum peaks properties. The label 1 and 2 reference specific peaks within the dQ/dE profiles corresponding to Table I.

charge density $dQ/dE_{end}dz$ of electrons (black-red-yellow histogram) with final energy E_{end}, as functions of injection position z. In other words, this spectrum describes distribution of the initial z positions of electrons for given final energies E_{end}.

The simulation with ideal Gaussian laser profile (Fig. 7.(c)) shows a correlation between final energy and injection position as electrons trapped earlier gain more energy over the interaction distance. The injection of electrons in ± 3 mrad around axis (green line) occurs inside a 400 μm window centered around the maximum laser amplitude a_{max} at $ct_1 = 1800$ μm. The green injected charge in this region (Fig. 7.(c)) is maximal because the process occurs over $0.4z_R$ within the density plateau, in the portion where $a_0 \simeq a_{max}$. Electrons injected at the start of this region see a longer accelerating length than the ones at the end, which results in decreasing final energy in function of the injection position. The resulting spectrum is evenly spread between 300 and 900 MeV as observed in Fig. 6.(a).

For a realistic laser driver, the injected charge spectrum (Fig 7.(d)) exhibits multiple injection positions. The higher energy electrons are injected 1 mm after ct_1, when a_0 has dropped to 2.5, and contribute to the high energy peak centered on 632 MeV in Fig. 6.(b). The lower energy peak at 466 MeV in Fig. 6.(b) is composed of electrons trapped at different positions: 1 mm after ct_1 and at ct_2, which explains why this peak (Index 1 of Figs. 6.(b) and (c)) has a relatively higher energy spread than peak 1 for Gaussian driver (see Table I).

The dynamics of electron injection results from the evolution of the laser and plasma cavity. Snapshots of the first plasma cavity behind the laser pulse are shown for the Gaussian driver in Fig. 7.(e) and (g), and for a realistic driver in Fig. 7.(f) and (h), at $ct_1 = 1800$ μm and $ct_2 = 4000$ μm respectively. At ct_1, for the ideal Gaussian laser simulation, injection of electrons on axis has just begun in a perfectly symmetric bubble, while for the realistic case most of the already injected electrons are greatly defocused and spread from -30 to 30 μm. The accelerating fields are similar for Fig. 7.(e) and (f). However, in the realistic case, electrons ionized early are desynchronized with the trapping portion of the bubble due to off axis laser fluence fluctuations resulting in a 3 μm shorter bubble compared to the Gaussian case. This prevents continuous injection and the generation of electrons with energy above 700 MeV (see Fig. 6.(a)).

Comparison of the two cavity structures at ct_2 (Fig. 7 (d) and (h)), provides insight on the effects of transverse asymmetry evolution on the acceleration process. In the ideal Gaussian laser case, most of the initially injected charge is accelerated, and the injection process remains continuous. The transverse centroid variations and stronger defocusing with the realistic laser profile induce important losses throughout the interaction process, which enables trapping of up to 10 pC around ct_2, in an off-axis bubble with half of the accelerating maximum compared to a Gaussian cylindrically symmetric driver.

Laser and electron beam positions in the xOz transverse plane are plotted in Fig. 8 as functions of the position along the propagation axis in vacuum. The ideal Gaussian laser trajectory is centered on the laser axis in vacuum, closely followed by the electron beam trajectory. The electron beam transverse size remains relatively constant in the plasma and grows symmetrically around $x = 0$ after plasma exit. For a realistic laser driver, the laser trajectory (see Fig. 8.(b)) in vacuum oscillates around the $x = 0$ axis. Self-focusing in the plasma lowers the amplitude of the displacement off-axis (compare red line and black dashed line). After electron

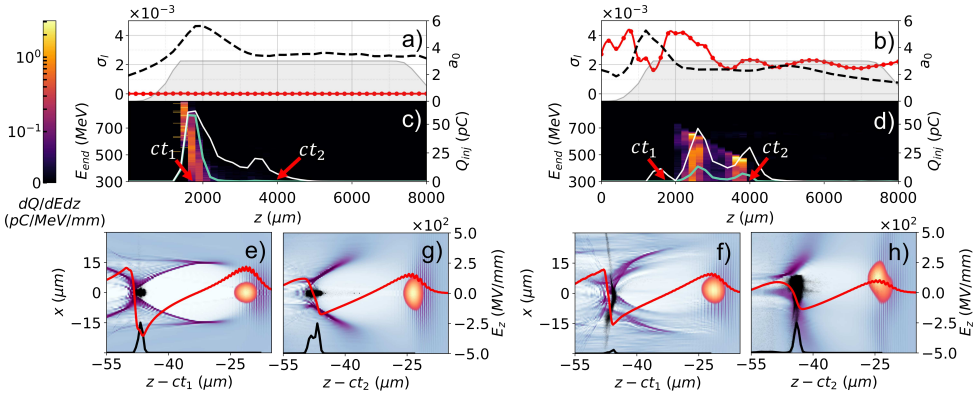

FIG. 7 : Simulated evolution of laser pulse and electron bunch characteristics for the ideal Gaussian laser profile (columns on the left) and the realistic laser field profile [columns on the right]. Panels (a) and (b): laser asymmetry function σ_l (red dots) and spline approximated asymmetry function curve (red curve) as functions of position on the propagation axis; peak normalized laser potential a_0 (black dashed-line), and normalized longitudinal unperturbed plasma density profile (grey area). Panels (c) and (d): injected charge Q_{inj} (vertical axis on the right) as function of position (all electrons plotted as a white line, and angularly selected ± 3 mrad electrons as green line); The panels (c) and (d) also show the spectral charge density $dQ/dE_{end}dz$ of electrons (black-red-yellow colormap) with final energy E_{end} for the angular selection as a function of the injection position z. Panels (e) and (g) [(f) and (h) for the simulation with realistic laser field]: transverse slice of the normalized charge density perturbation ρ/en_0 on the $z-x$ plane at $ct_1 = 1800$ μm and resp. $ct_2 = 4000$ μm; in these panels the electron macro-particles positions are shown as small black dots (with their size pondered by their individual charge). Superposed in these panels is the laser driver intensity's normalized envelope (orange colormap); in the same panels, the black and red lines correspond respectively to the density and the longitudinal electric field E_z on the axis of maximum laser intensity.

trapping, $z > 2000$ μm, the electron bunch trajectory is centered on the laser centroid, and its standard deviation reaches up to 10 μm. This behavior clearly demonstrates the impact of the asymmetry of the transverse laser driver on the pointing of the electron beam at the exit of the plasma.

C. Charge fluctuations due to laser intensity distribution

Simulations were performed to analyze the effects of variations of the intensity profile on the resulting charge. The laser electric field was reconstructed for 3 reference profiles with the modified GSA algorithm described in Appendix A and the remaining simulation input parameters are the same as in Fig. 6.(b) (reported in section IV A). The density was varied between 1.7×10^{18} cm^{-3} and 2.3×10^{18} cm^{-3}.

To characterize the laser energy distribution for each profile, we define the following effective energy ratio :

$$E_{ratio} = \frac{1}{N_z} \sum_{z=-z_R}^{+z_R} \frac{\int_{r=0}^{r_{eff}} \int_{\theta=0}^{2\pi} r\, dr\, d\theta\, F(r,\theta,z)}{\int_{r=0}^{r_{max}} \int_{\theta=0}^{2\pi} r\, dr\, d\theta\, F(r,\theta,z)}, \quad (5)$$

with z the propagation position of the laser with respect to z_f, N_z the number of evenly spaced positions z used to perform the summation in the Rayleigh range $[-z_R, ..., 0, ..., z_R]$ and $F(r,\theta,z)$ the fluence at each propagation position in vacuum. The integral origin is defined as the position of the fluence maximum. This ratio quantifies the average effective energy in the characteristic divergence boundaries $[-z_R,\ z_R]$ of the laser propagation axis, and within an area of radius r_{eff}. Improving this ratio increases the portion of energy usable for the injection of electrons.

The total accelerated charge Q is calculated within the whole $E - \theta_x$ space and plotted in Fig. 9 as a function of n_0 for the 3 laser profiles and densities ranging from 1.7 to 2.3×10^{18} cm^{-3}. In this regime, within the chosen set of parameters, the total charge Q remains lower than the theoretical value calculated for a matched laser for most of the input densities n_0. This is a consequence of the non-Gaussian laser transverse distributions, and of the fact that the laser spot size is not matched with the bubble radius. Comparing the 3 values simulated for $n_0 = 2.1 \times 10^{18}$ cm^{-3}, while E_{ratio} fluctuates between 0.47 and 0.52, the total charge Q varies from 198 to 434 pC. A relative effective energy fluctuation $\delta E_{ratio}/E_{ratio} = 5\,\%$ leads to a relative charge fluctuation $\delta Q/Q = 38\,\%$. For the laser profile resulting in the highest total charge, i.e. $E_{ratio} = 0.48$, increasing the density n_0 from 1.9×10^{18} cm^{-3} to 2.1×10^{18} cm^{-3} increases Q from 295 to 434 pC. A relative den-

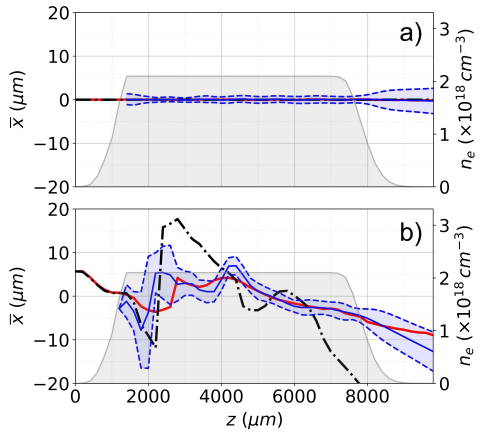

FIG. 8 : Laser beam (solid red line) and electron bunch (solid blue line) positions in the xOz plane for (a) Gaussian case and (b) Laguerre-Gauss case. The blue dashed lines are the ± RMS σ_x size of the selected bunch. The laser position is defined as the centroid of the fluence distribution in an area of radius r_{eff} around the fluence maximum. For reference, the dash-dotted black line represents the position of the laser beam in vacuum and the grey area is the longitudinal density profile (right-end side vertical axis scale).

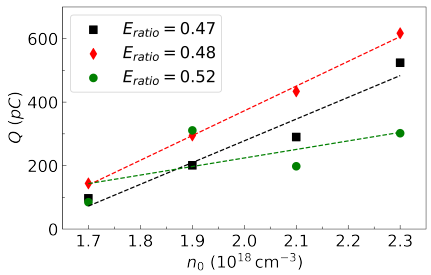

FIG. 9 : Total injected bunch charge Q for 3 different simulated laser profiles as a function of n_0. For each profile, the corresponding E_{ratio} is calculated by eq. (5), setting $N_z = 21$: black squares profile with $E_{ratio} = 0.47$ - red diamonds profile with $E_{ratio} = 0.48$ - green circles profile with $E_{ratio} = 0.52$. For each profile, the dashed curve is the linear regression of the data points.

sity fluctuation of 5 % leads to a relative charge fluctuation $\delta Q/Q = 19\,\%$. This shows that taking into account small errors either on the gas density value or on the calculated effective energy ratio leads to significant charge fluctuations, of the same order of magnitude as the one measured experimentally (see Fig. 3).

The averaged calculated charge measured within the same boundaries as experimental data is 113 pC ($\overline{Q}_{tot}$ = 95 pC in experiment), with an RMS relative charge fluctuation of 56% ($\delta\overline{Q}_{tot}/\overline{Q}_{tot}$ = 47 % in experiment). There is a good agreement between the average simulated and experimental charge for the same central density $\overline{n}_0 = 2.2 \times 10^{18}$ cm^{-3}. In conclusion, this analysis shows that improving the quality and the stability of the laser energy distribution and the stability of the plasma density are crucial to achieve stable and high-energy, high charge electron spectra.

V. CONCLUSIONS

Experiments were carried out during the commissioning phase in the long focal area of the APOLLON laser facility, to study the influence of the laser beam properties on the quality of electron beams generated by ionization injection and laser wakefield acceleration in a gas cell. A detailed analysis of the laser beam in the transverse plane was performed using fluence measurements in the focal volume. Particle in Cell simulations were performed with a reconstruction of the measured laser field profile as input, leading to electron spectra in close agreement with experimental results, for the accelerated charge, energy distribution and pointing of the electron beam at the exit of the plasma. The presented results also show that this degree of quantitative agreement can be found without using computationally demanding full 3D simulations.

These high fidelity simulations rely on the calculation of the laser electric field from experimental data providing the fluence at different positions along the propagation in vacuum. An iterative method based on a modified version of the Gerchberg-Saxton algorithm [22], which allows the reconstruction of a realistic laser electric field based on a collection of fluence images in vacuum (Fig. 4), was used. The implementation of asymmetric laser drivers leads to better agreement of the simulation output bunch characteristics to measured experimental data in comparison to simulations using a perfect Gaussian driver (Fig. 6 and Table I).

These realistic simulations highlight the effects of laser field spatial characteristics (centroid fluctuations and asymmetry quantified by σ_l) on the injection and acceleration of the electrons (Fig. 7 and Fig. 8). The symmetry degradation from a Gaussian laser driver leads to a loss of both peak energy and total accelerated bunch charge (Table I), which could be mitigated through optimization of the gas cell density characteristics.
The impact of shot-to-shot fluctuations of the laser transverse distribution and of plasma density on the accelerated bunch charge, have been quantified and the source of charge fluctuations in experiments identified. The stabilization of these fluctuations would lead to an improved stability of the produced electron spectra.

ACKNOWLEDGMENTS

We acknowledge the resources and assistance of the computing center MesoLUM managed by ISMO (UMR8214) and LPGP (UMR8578), University Paris-Saclay (France). Experimental results were achieved using APOLLON Research Infrastructure and we gratefully acknowledge the work of the Laboratoire pour l'Utilisation des Lasers Intenses (UMR7605) staff during planning and execution of the experiment. APOLLON facility was partially funded by Equipex Cilex (Centre interdisciplinaire lumière extrême) grant N° ANR-10-EQPX-25-01, and by region Ile-de-France.

Appendix A: Modified Gerchberg-Saxton algorithm (GSA) to model the laser driver

In the experimental campaign described in this work, only the fluence maps $F(x,y,z)$ of the laser pulse at specific distances z_k, with $k = 0, 1, ..., k_{\max}$ from the focal spot were measured.

A Gaussian temporal profile was assumed for the laser pulse, with the measured FWHM duration in intensity τ_{FWHM}. Under this hypothesis, the linear relation between the peak fluence F_0 and peak intensity I_0 is :

$$F_0 = \frac{\tau_{FWHM}}{2}\sqrt{\frac{\pi}{\log 2}} I_0. \tag{A1}$$

Given this linear relation between fluence $F(x,y,z)$ and intensity $I(x,y,z)$, an electric field at position z can be defined from a phase map $\psi(x,y)$ and a fluence $F(x,y,z)$:

$$\begin{aligned} \mathrm{E}(x,y,z) &= \mathrm{E}[F(x,y,z), \psi(x,y)] = \\ &= \sqrt{I(x,y,z_0)}\exp\{i\psi(x,y)\}. \end{aligned} \tag{A2}$$

To initialize the realistic PIC simulations of this work, a reconstruction of the laser electric field at a given plane was necessary. Since only the fluence (and thus intensity) maps at multiple planes were known experimentally, to reconstruct the laser electric field using Eq. A2 the field phase map had to be reconstructed.

For this purpose, a modified implementation of the Gerchberg-Saxton algorithm (GSA) [22] was used to find the field phase $\psi(x,y)$ at z_0 and thus the laser electric field $\mathrm{E}_{GSA,z_0}(x,y,z_0) = \mathrm{E}[F(x,y,z_0), \psi(x,y)]$, from the available data on the the fluence $F(x,y,z_0)$ at z_0 and other planes, each referred to as z_k.

In the following a simplified description of the field reconstruction algorithm used in this work is reported.

This version of the GSA aims at finding a reconstruction of the laser field at z_0 through an expansion in Hermite-Gauss (HG) modes [23], using the measured $F(x,y,z_k)$ fluence maps. Since the propagation of the HG modes $\mathrm{HG_{n,p}}$ at z_k is analytically known, this reconstruction is equivalent to finding the estimated HG expansion coefficients $D_{n,p}$ (and thus the corresponding field phase map). The indices n,p denote the order of the HG mode along the x, y axis respectively.

At each iteration *iter* of the algorithm, the estimated expansion in HG modes is propagated from the position z_0 to $z_{k_{\max}}$, with an improvement of the estimate at each of the intermediate positions z_k. This update of the estimated coefficients for the HG expansion uses the estimated coefficients from the previous measurement plane at z_{k-1} and the measured fluences $F(x,y,z_k)$. As in the original GSA formulation [22], the estimated propagated phase is combined with the fluence at the measurement planes in the calculations.

After one iteration ends, the procedure is repeated starting from z_0, using the coefficients (and thus the phase map) estimated from the previous iteration.

The implementation of the modified GSA used for this work can be described by the following pseudocode:

- Find an initial estimate of the coefficients $D_{n,p}$ projecting the intensity corresponding to the fluence $F(x,y,z_0)$ on the $\mathrm{HG_{n,p}}(x,y,z_0)$ modes at z_0. In the following we denote the projection of a function $f(x,y,z)$ on the HG modes with the notation Proj:

$$D_{n,p} = \mathrm{Proj}[f(x,y,z), \mathrm{HG_{n,p}}(x,y,z)]. \tag{A3}$$

- For $iter = 0 \to N_{\mathrm{iter}}$ and for $k = 0 \to k_{\max}$:
  - define the propagated field as

$$\mathrm{E}_{GSA,z_k}(x,y,z_k) = \sum_{n,p} D_{n,p} \cdot \mathrm{HG_{n,p}}(x,y,z_k); \tag{A4}$$

  - find the phase map ψ as:

$$\psi(x,y) = \arg\left(\mathrm{E}_{GSA,z_k}(x,y,z_k)\right); \tag{A5}$$

  - combine the measured fluence $F(x,y,z_k)$ with the phase $\psi(x,y)$ to find the function $\mathrm{E'}_{GSA,z_k}$ using Eq. A2:

$$\mathrm{E'}_{GSA,z_k}(x,y,z_k) = \mathrm{E}[F(x,y,z_k), \psi(x,y)]; \tag{A6}$$

  - combine the previous estimate of the HG coefficients with those obtained from the projection of $\mathrm{E'}_{GSA,z_k}$ on the HG modes at z_k:

$$\begin{aligned} D_{n,p} &= (1-\alpha)\cdot D_{n,p} + \\ &+\alpha \cdot \mathrm{Proj}[\mathrm{E'}_{GSA,z_k}, \mathrm{HG_{n,p}}(x,y,z_k)]; \end{aligned} \tag{A7}$$

For this work the number of iterations was chosen as $N_{\mathrm{iter}} = 10$. The coefficient α for the weighted sum of the previous and new HG expansion coefficients are chosen in order to obtain convergence.

Once the algorithm has performed the iterations passing through the measurements planes, using Eq. A2 the estimated field phase $\psi(x,y)$ can be easily found and combined with the measured fluence $F(x,y,z_0)$ of the laser to reconstruct its field $\mathrm{E}_{GSA,z_0}(x,y,z_0) = \mathrm{E}[F(x,y,z_0), \psi(x,y)]$.

In this algorithm, the mentioned projection of a function $f(x, y, z_k)$ on the HG modes at z_k was defined as:

$$\begin{aligned}&\mathrm{Proj}[f(x,y,z_k), \mathrm{HG_{n,p}}(x,y,z_k)] = \\ &= \int_{-\Delta X/2}^{\Delta X/2}\int_{-\Delta Y/2}^{\Delta Y/2} dx\, dy\;\; f(x,y,z_k) \times \\ &\qquad \times \mathrm{HG}^*_{n,p}(x,y,z_k), \end{aligned} \tag{A8}$$

where $(\Delta X, \Delta Y)$ are the data rectangular grid length along each axis. The HG modes at z_k are defined also using the origins $(x_{0,k}, y_{0,k})$ and the projection waists $w_{0x,y}$. The latter are set sufficiently small to make the Hermite-Gauss modes decay within the projection integral boundaries, and sufficiently large to fit the part of the transverse intensity map further away from the origin. The values of $(x_{0,k}, y_{0,k})$ are optimized to improve the quality of the laser field reconstruction, as will be described in a future work.

The field reconstruction obtained with described phase retrieval algorithm would be sufficient to initialize the laser pulse in a realistic PIC simulation in 3D Cartesian geometry. However, for the simulations in quasi-3D geometry [21] of this work, which use a cylindrical grid, a further decomposition in Laguerre-Gauss modes is necessary, as described in Section III B.

[1] T. Tajima and J. M. Dawson, Phys. Rev. Lett. **43**, 267 (1979).
[2] E. Esarey, C. Schroeder, and W. Leemans, Reviews of modern physics **81**, 1229 (2009).
[3] F. S. Tsung, R. Narang, W. B. Mori, C. Joshi, R. Fonseca, and L. O. Silva, Physical Review Letters **93**, 185002 (2004).
[4] S. Corde, C. Thaury, A. Lifschitz, G. Lambert, K. Ta Phuoc, X. Davoine, R. Lehe, D. Douillet, A. Rousse, and V. Malka, Nature Communications **4**, 1 (2013).
[5] M. Chen, E. Esarey, C. Schroeder, C. Geddes, and W. Leemans, Physics of Plasmas **19**, 033101 (2012).
[6] C. McGuffey, A. Thomas, W. Schumaker, T. Matsuoka, V. Chvykov, F. Dollar, G. Kalintchenko, V. Yanovsky, A. Maksimchuk, K. Krushelnick, *et al.*, Physical Review Letters **104**, 025004 (2010).
[7] A. Pak, K. Marsh, S. Martins, W. Lu, W. Mori, and C. Joshi, Physical Review Letters **104**, 025003 (2010).
[8] M. Mirzaie, S. Li, M. Zeng, N. Hafz, M. Chen, G. Li, Q. Zhu, H. Liao, T. Sokollik, F. Liu, *et al.*, Scientific reports **5**, 1 (2015).
[9] A. Pukhov and J. Meyer-ter Vehn, Applied Physics B **74**, 355 (2002).
[10] I. Kostyukov, E. Nerush, A. Pukhov, and V. Seredov, Physical review letters **103**, 175003 (2009).
[11] F. Massimo, A. Beck, J. Dérouillat, I. Zemzemi, and A. Specka, Physical Review E **102**, 033204 (2020).
[12] C. K. Birdsall and A. B. Langdon, *Plasma Physics via Computer Simulation* (Taylor and Francis Group, 2004).
[13] B. Beaurepaire, A. Vernier, M. Bocoum, F. Böhle, A. Jullien, J.-P. Rousseau, T. Lefrou, D. Douillet, G. Iaquaniello, R. Lopez-Martens, A. Lifschitz, and J. Faure, Phys. Rev. X **5**, 031012 (2015).
[14] J. Ferri, X. Davoine, S. Fourmaux, J. Kieffer, S. Corde, K. T. Phuoc, and A. Lifschitz, Scientific reports **6**, 1 (2016).
[15] L. T. Dickson, C. I. D. Underwood, F. Filippi, R. J. Shalloo, J. B. Svensson, D. Guénot, K. Svendsen, I. Moulanier, S. D. Dufrénoy, C. D. Murphy, N. C. Lopes, P. P. Rajeev, Z. Najmudin, G. Cantono, A. Persson, O. Lundh, G. Maynard, M. J. V. Streeter, and B. Cros, Phys. Rev. Accel. Beams **25**, 101301 (2022).
[16] W. Leemans, A. Gonsalves, H.-S. Mao, K. Nakamura, C. Benedetti, C. Schroeder, C. Tóth, J. Daniels, D. Mittelberger, S. Bulanov, *et al.*, Physical review letters **113**, 245002 (2014).
[17] A. Popp, J. Vieira, J. Osterhoff, Z. Major, R. Hörlein, M. Fuchs, R. Weingartner, T. Rowlands-Rees, M. Marti, R. Fonseca, *et al.*, Physical review letters **105**, 215001 (2010).
[18] D. Papadopoulos, J. Zou, C. Le Blanc, G. Chériaux, P. Georges, F. Druon, G. Mennerat, P. Ramirez, L. Martin, A. Fréneaux, *et al.*, High Power Laser Science and Engineering **4** (2016).
[19] T. Audet, P. Lee, G. Maynard, S. D. Dufrénoy, A. Maitrallain, M. Bougeard, P. Monot, and B. Cros, Nuclear Instruments and Methods in Physics Research Section A: Accelerators, Spectrometers, Detectors and Associated Equipment **909**, 383 (2018).
[20] R. Lehe, M. Kirchen, I. A. Andriyash, B. B. Godfrey, and J.-L. Vay, Computer Physics Communications **203**, 66 (2016).
[21] A. Lifschitz, X. Davoine, E. Lefebvre, J. Faure, C. Rechatin, and V. Malka, Journal of Computational Physics **228**, 1803 (2009).
[22] R. W. Gerchberg, Optik **35**, 237 (1972).
[23] F. Pampaloni and J. Enderlein, arXiv preprint physics/0410021 (2004).
[24] W. Lu, M. Tzoufras, C. Joshi, F. Tsung, W. Mori, J. Vieira, R. Fonseca, and L. Silva, Physical Review Special Topics-Accelerators and Beams **10**, 061301 (2007).

Physics of Plasmas

PLEASE CITE THIS ARTICLE AS DOI: 10.1063/5.0142894

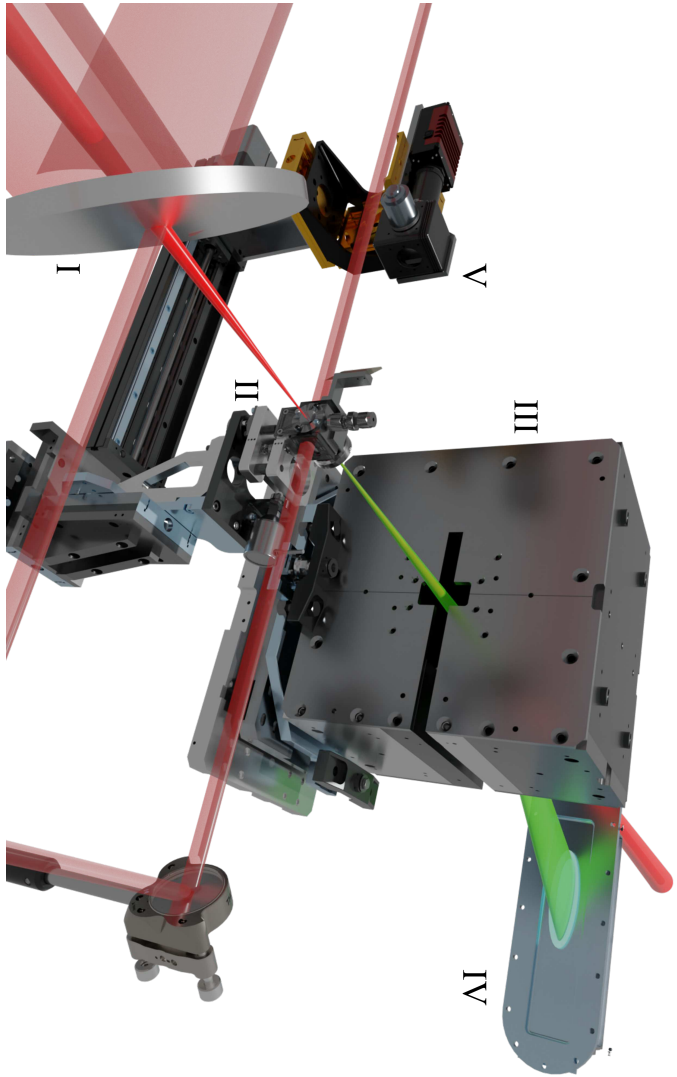

PLEASE CITE THIS ARTICLE AS DOI: 10.1063/5.0142894

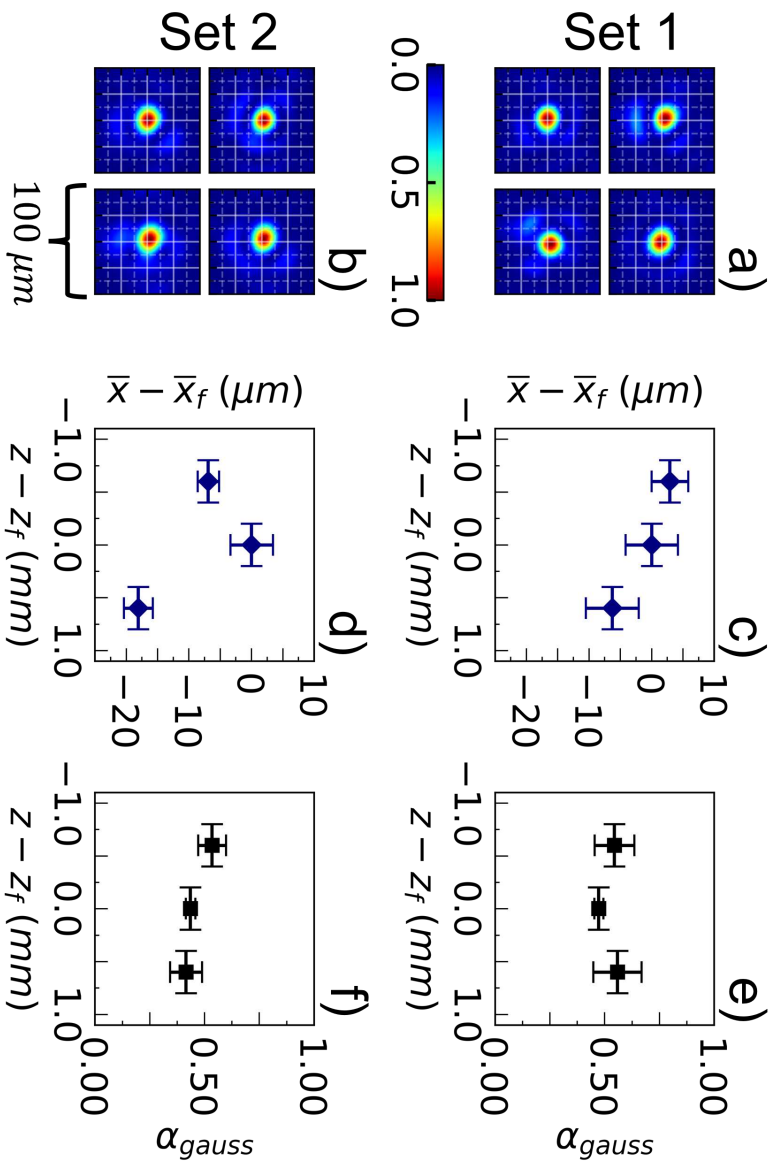

PLEASE CITE THIS ARTICLE AS DOI: 10.1063/5.0142894

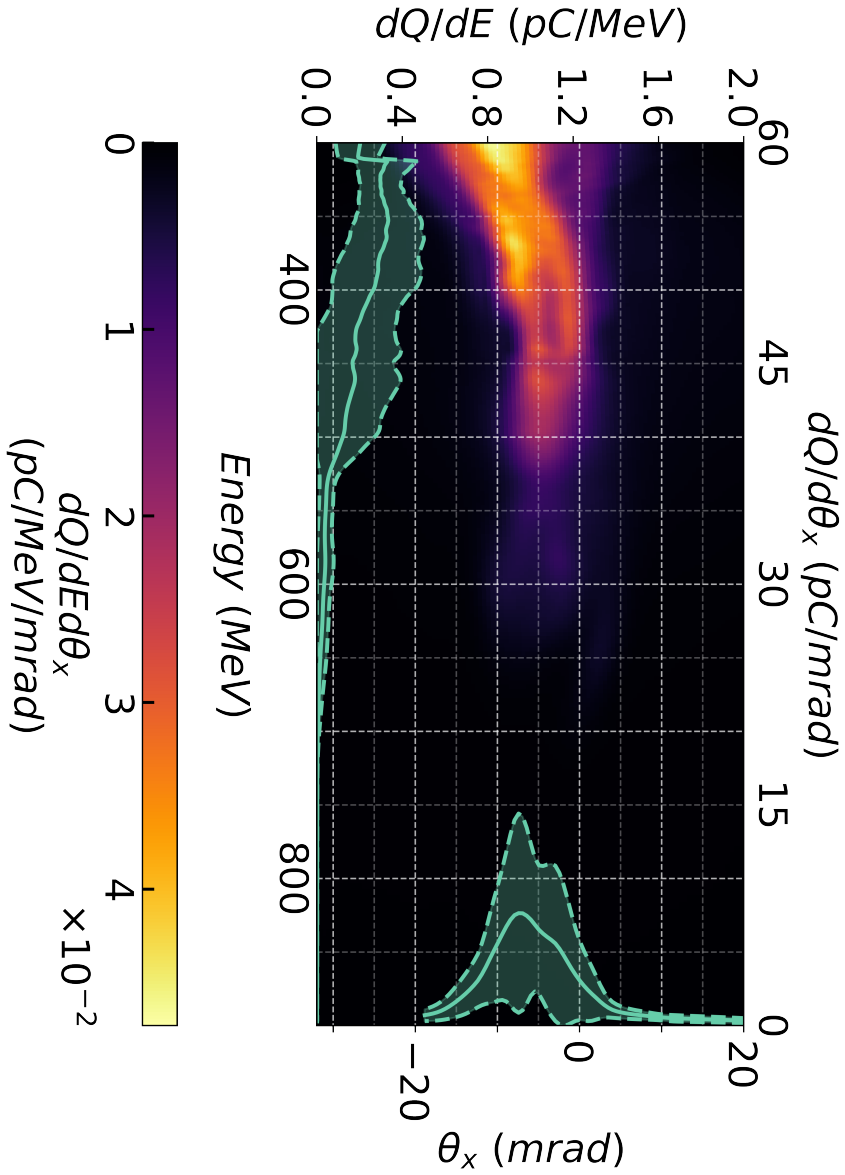

Physics of Plasmas

PLEASE CITE THIS ARTICLE AS DOI: 10.1063/5.0142894

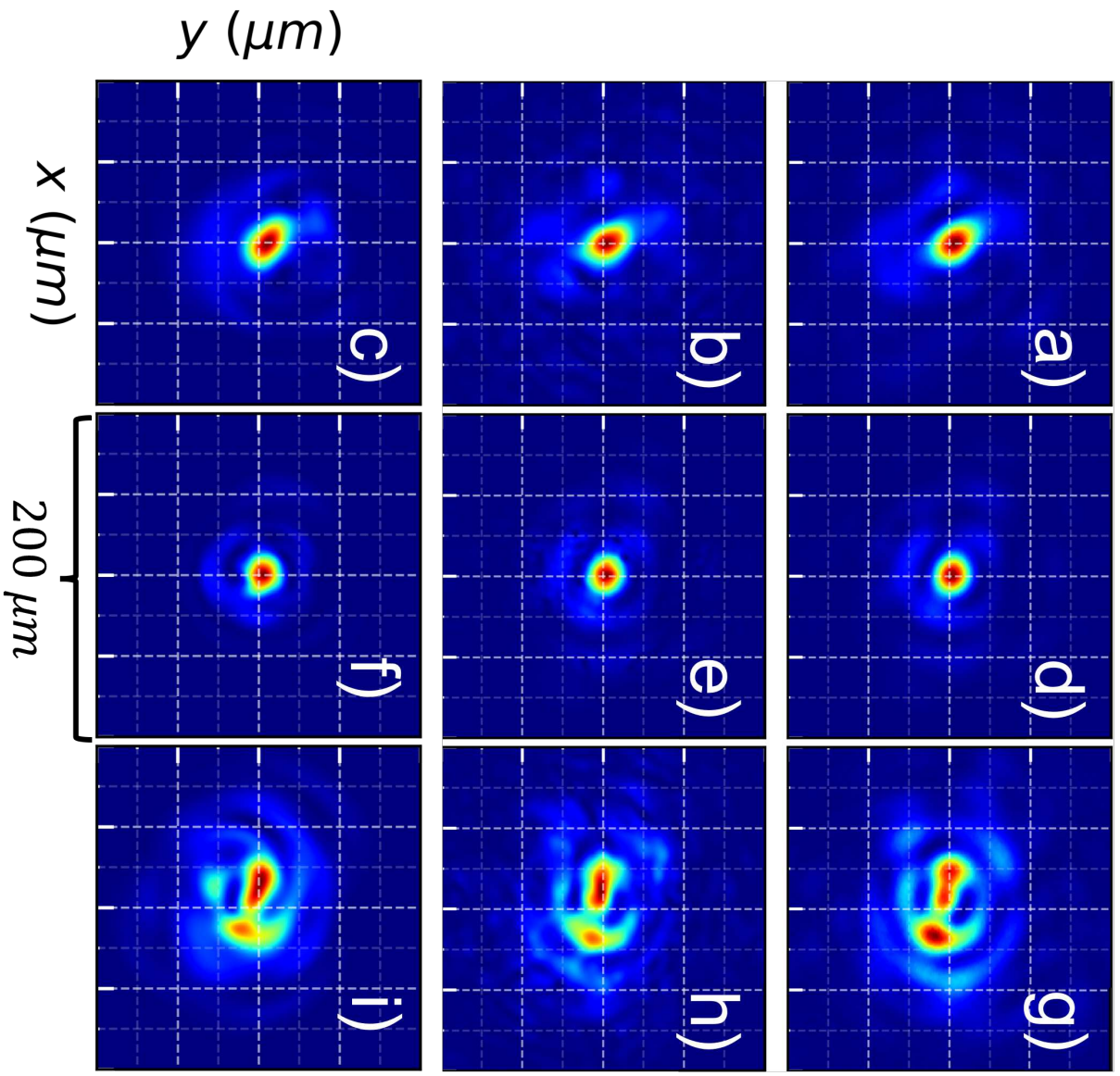

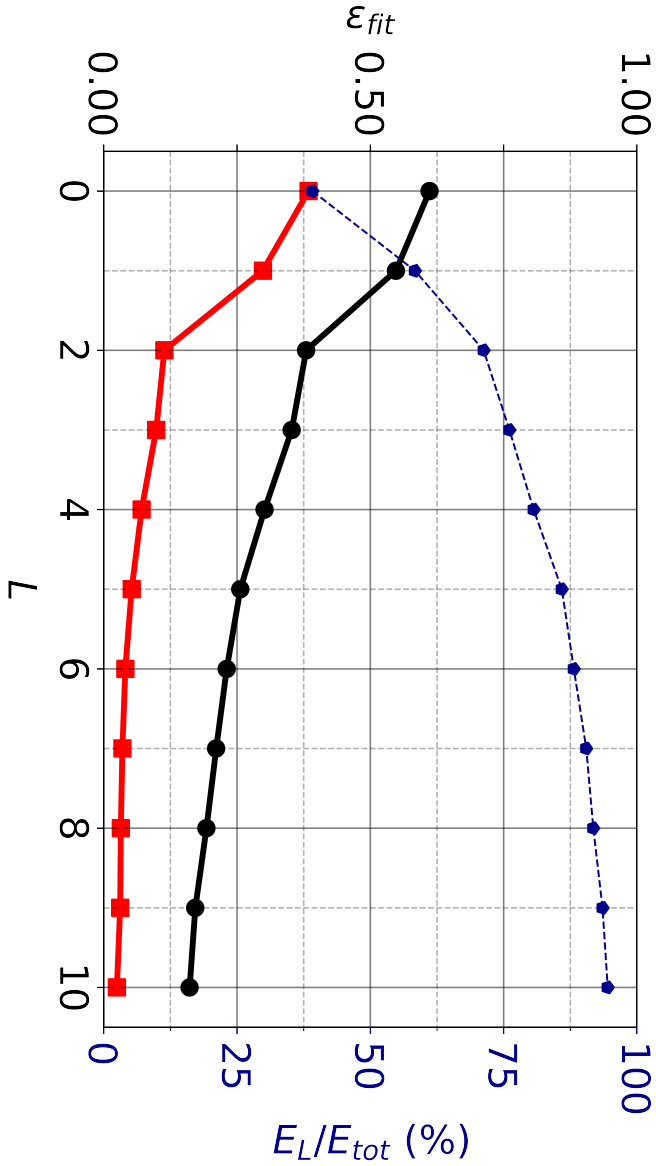

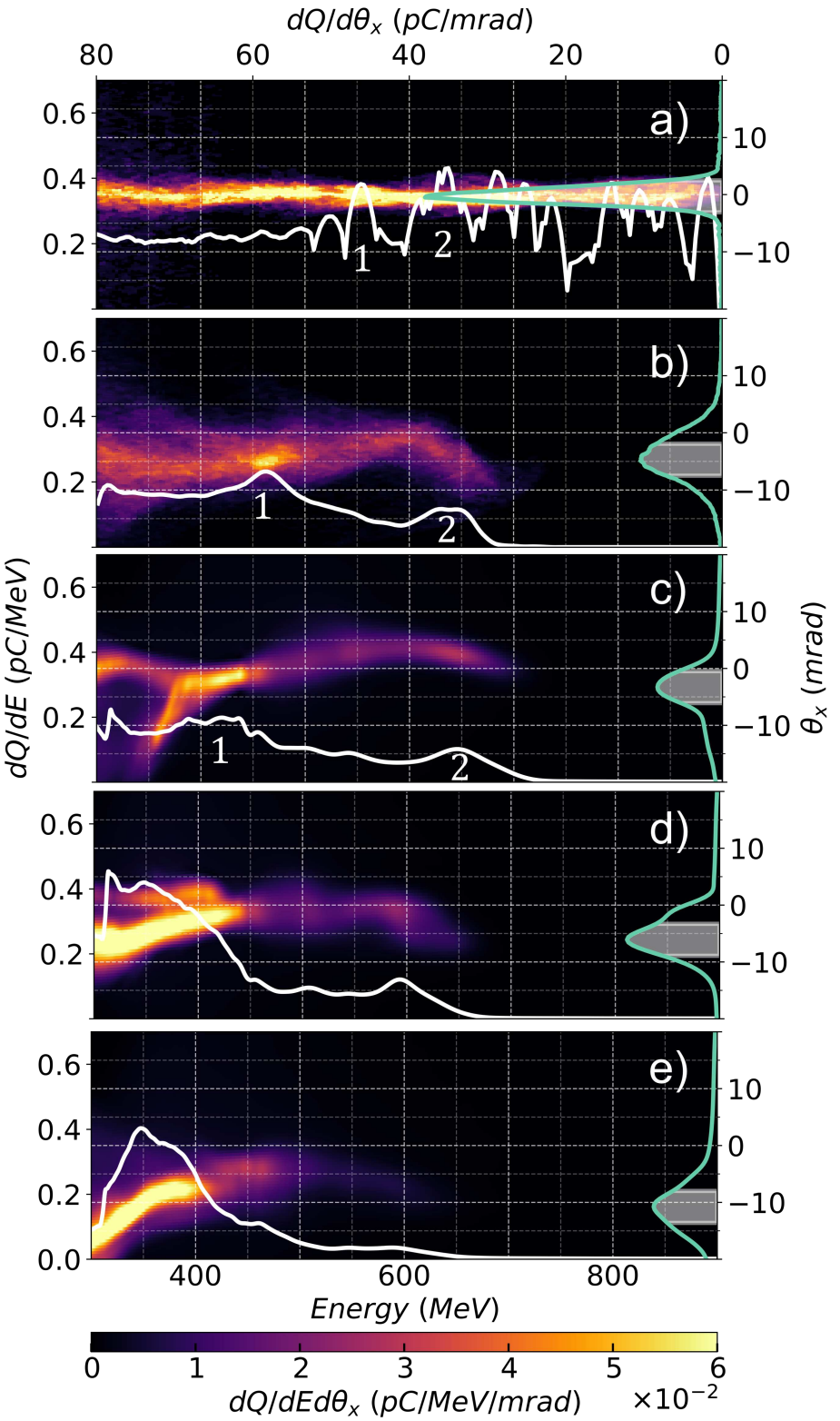

PLEASE CITE THIS ARTICLE AS DOI: 10.1063/5.0142894

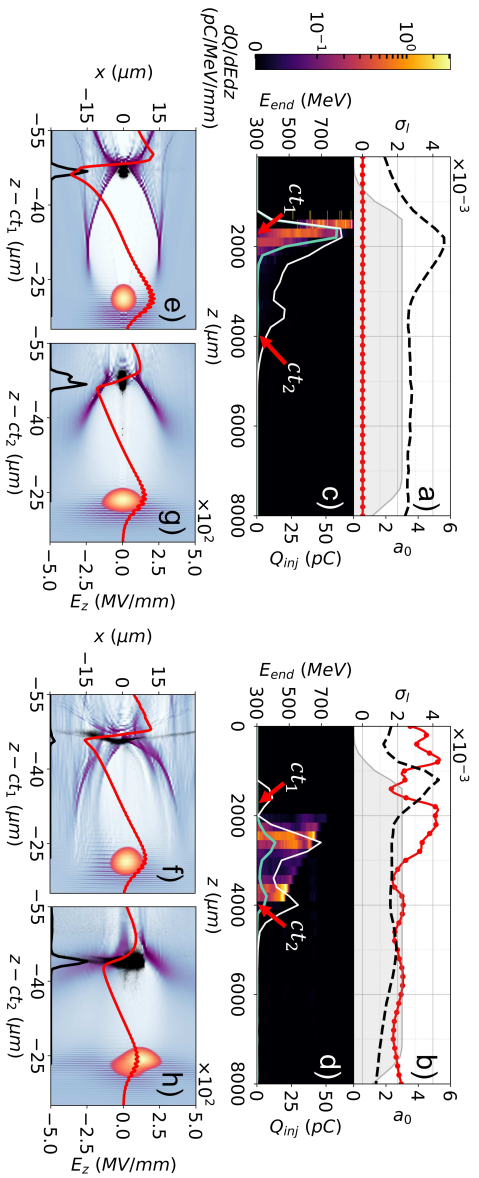

PLEASE CITE THIS ARTICLE AS DOI: 10.1063/5.0142894

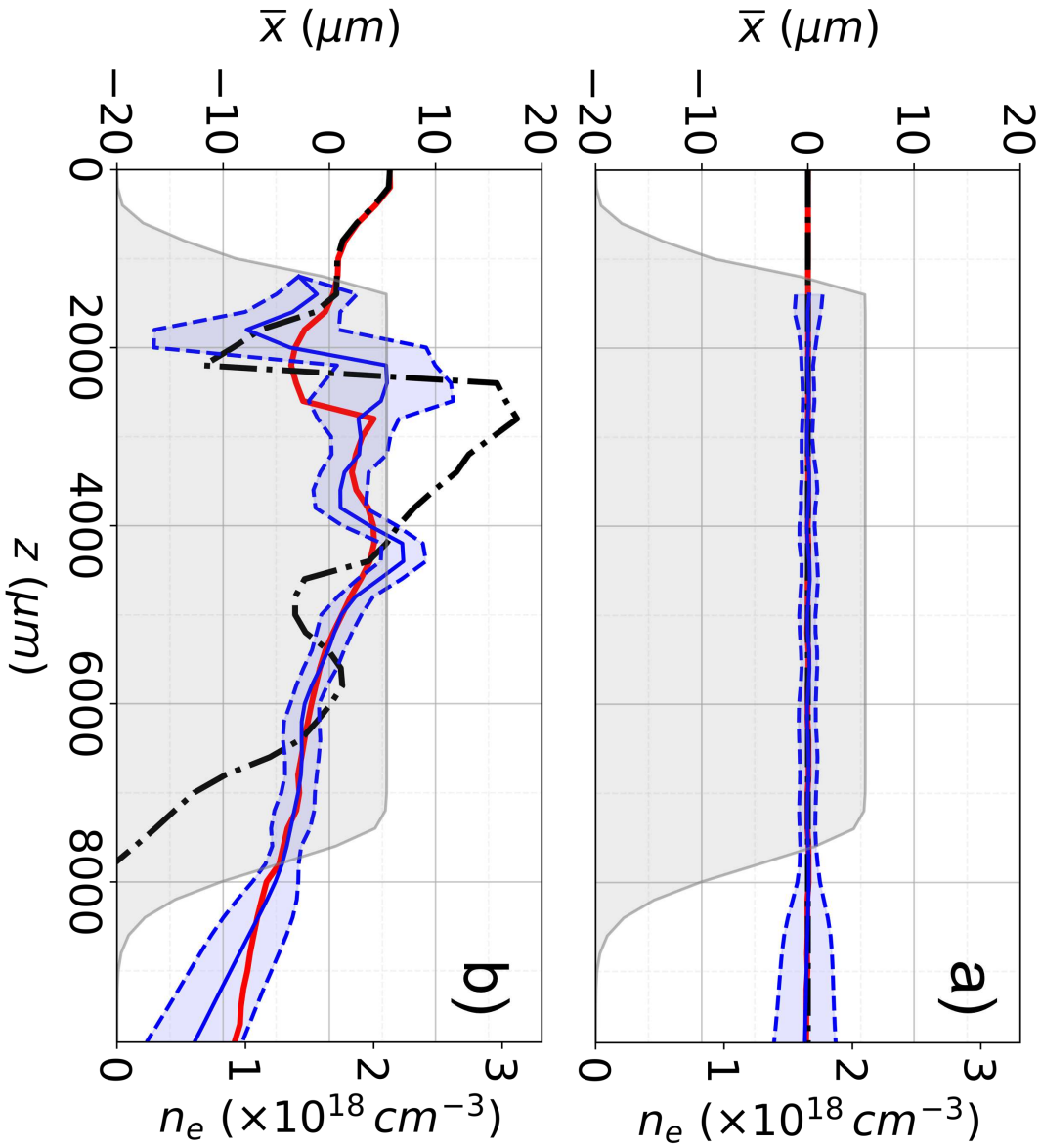

PLEASE CITE THIS ARTICLE AS DOI: 10.1063/5.0142894

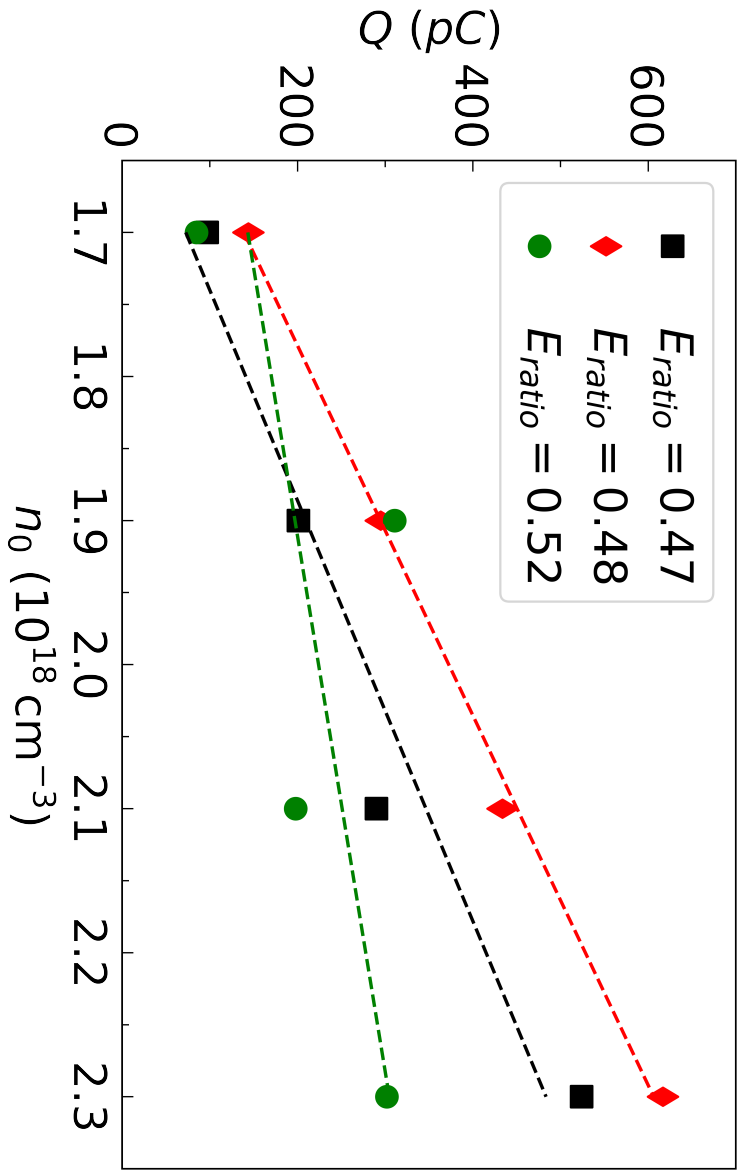

Titre : Accélération d'électrons par sillage laser-plasma
Mots clés : sillage laser plasma, accélération d'électrons, expériences laser plasma, optimisation numérique, diagnostic plasma

Résumé : L'accélération par sillage laser plasma fournit des gradients accélérateurs plusieurs ordres de grandeur au dessus de ceux des accélérateurs actuels, mais la stabilité et la qualité des faisceaux d'électrons accélérées doivent être améliorées. Ce travail est centré sur l'étude d'injecteurs laser-plasma (LPI) à basse ($150\,\mathrm{MeV}$) et haute énergie ($1\,\mathrm{GeV}$) créés en cellule de gaz. Des outils expérimentaux et numériques ont été développés pour l'optimisation et le diagnostic de l'interaction laser-plasma. Une nouvelle méthode de mesure monocoup de la densité plasma en cellule de gaz a été mise au point et utilisée. Des méthodes d'intelligence artificielles ont été mises en oeuvre pour l'automatisation, le diagnostic et l'optimisation d'une expérience de sillage laser plasma. Les effets du front d'onde du laser, de la position focale, et de la densité du plasma ont été mesurés et comparés à des simulations. Des profils laser réalistes, utilisés comme données d'entrée, ont permis d'améliorer fortement la précision des simulations et d'expliquer l'impact de l'asymétrie du laser sur les propriétés des électrons. Une expérience de qualification utilisant une cellule à gaz dans la zone focale longue de l'installation laser Apollon a permis d'obtenir des électrons jusqu'au GeV. Une deuxième campagne a permis d'améliorer la stabilité et la qualité des faisceaux d'électrons jusqu'à 1.8 GeV.

Title : Laser wakefield acceleration of electrons
Keywords: laser plasma wakefield, electron acceleration, laser plasma experiments, optimisation by machine learning, plasma diagnostic

Abstract: Laser Wakefield Acceleration (LWFA) provides orders of magnitude higher accelerating gradients than current accelerator designs, but the stability and quality of the accelerated electron bunches require improvement. This work focuses on the development of low ($150\,\mathrm{MeV}$) and high energy ($1\,\mathrm{GeV}$) laser-plasma injectors (LPI) in gas cells. Experimental and numerical tools have been developed for the optimisation and diagnosis of the laser-plasma interaction. A novel method for single-shot plasma density measurement in a gas cell was developed and implemented. Bayesian optimisation and automation of an LWFA experiment were completed. The effect of laser wavefront and focal position and plasma density in a low-energy LPI were explored experimentally and compared to simulations. Realistic laser profiles were used as input data and shown to explain otherwise overlooked effects on electron properties arising from laser asymmetry. The first gas cell experiment in the long focal area of the Apollon laser facility achieved electron bunches with energy up to 1 GeV. A second experiment at Apollon was performed leading to $1.8\,\mathrm{GeV}$ electrons with improved stability and quality.